AN ABSTRACT OF THE DISSERTATION OF

Charles McLouth Culbertson for the degree of Doctor of Philosophy in Chemistry presented on June 8, 2020.

Title: The Local Structure of Functional Electroceramics

Abstract approved:

_____

Michelle R. Dolgos

This work investigates the relationship between the local structure and physical properties of a set of classical ($MgTiO_3$, $CaTiO_3$, $SrTiO_3$, and $BaTiO_3$) and complex ((1-*x*)$Ba(Zr_{0.2}Ti_{0.8})O_3$-*x*$(Ba_{0.7}Ca_{0.3})TiO_3$[BZT-BCT], $Na_{0.5}Bi_{0.5}TiO_3$ [NBT]) perovskite electroceramics. The materials in this work were synthesized via standard solid state ceramic synthesis, the structure was investigated through a number of different scattering methods to probe different aspects of the unique atomic arrangements in these materials, and the electrical properties of the materials were characterized.

Although the properties of $MgTiO_3$, $CaTiO_3$, $SrTiO_3$, and $BaTiO_3$ are well documented, there have been no comprehensive investigations of the local structure. These foundational materials are an important component in current electronic devices either as the host or a dopant, and it is therefore vital to understanding more complex materials. Neutron total scattering data was collected for these materials, and the local structure of $MgTiO_3$ was well described by the reported ilmenite average structure with rhombohedral $R\bar{3}$ symmetry. Similarly, the local structure of both $CaTiO_3$ and $SrTiO_3$ showed no deviation from the average structure (with orthorhombic *Pbnm* symmetry for $CaTiO_3$, and cubic $Pm\bar{3}m$ symmetry for $SrTiO_3$). However, the local structure of $BaTiO_3$ was found to be rhombohedral (*R*3*m*), whereas the average structure was best fit as tetragonal (*P*4*mm*). This difference between the local and average structure is due to order-disorder behavior where the locally ordered rhombohedral unit cells are disordered relative to one another, and bulk probes reveal the average structure which is the vector sum of the ionic displacements.

The major component of this work is focused on understanding both the origin of piezoelectricity and the local structure of the lead-free piezoelectric material (1-*x*)$Ba(Zr_{0.2}Ti_{0.8})O_3$-*x*$(Ba_{0.7}Ca_{0.3})TiO_3$ (BZT-*x*BCT). For these studies, a range of compositions were synthesized and X-ray total scattering data was collected during the application of an electric field. From the pair distribution function (PDF) data, it was found that the electric field caused the peaks to shift towards higher-*r*, indicating a lattice expansion. The PDF peak shift was quantified and the intrinsic contribution to the piezoelectricity was calculated. Surprisingly, the intrinsic contributions to the

macroscopic piezoelectric were found to be minimized at the morphotropic phase boundary composition (x = 0.50). Furthermore, the <200> diffraction reflections, on the BCT-rich tetragonal side, were investigated and it was found that domain wall motion (extrinsic contributions) is the dominating factor for the enhanced piezoelectricity observed. Neutron total scattering and X-ray absorption spectroscopy were also collected on the x = 0.50 sample at room temperature. The local structure was not orthorhombic (*Amm*2) as was expected. Instead, the titanium ions were found to be distorted along the [111] direction with rhombohedral symmetry, whereas the zirconium ions were found to be undistorted with cubic symmetry. Incorporating these findings into the small-box modeling yielded a two-phase BCT-BCZ (*R*3*m*-*Pm*$\bar{3}$*m*).

The final study in this work investigates the ionic conductivity and structure of $Na_{0.5}Bi_{0.5}TiO_3$ (NBT). Stoichiometric, non-stoichiometric (bismuth deficient and excess), and magnesium-doped samples were synthesized. Synchrotron X-ray diffraction, synchrotron X-ray total scattering, neutron total scattering, and physical property measurements were performed. Both the average and local structure showed changes in symmetry with increasing temperature from monoclinic *Cc* to tetragonal *P*4*bm* to cubic *Pm*$\bar{3}$*m*, with only minor variations between the different compositions. However, non-stoichiometry and magnesium doping did cause the cubic phase to appear at lower temperatures (~500 °C) as evidenced by diffraction. Although the structure did not show many changes, the physical properties from the dielectric and electrical impedance measurements showed dramatic differences. The excess bismuth decreased the high temperature leakage current and created a much better insulator,

whereas the bismuth deficiency slightly increased the conductivity. The magnesium doped sample showed greatly enhanced conductivity at even lower temperatures. The slopes of the Arrhenius plots for all the compositions were very similar, yielding activation energies on the order of ~0.74 eV.

©Copyright by Charles McLouth Culbertson

June 8, 2020

All Rights Reserved

The Local Structure of Functional Electroceramics

by

Charles McLouth Culbertson

A DISSERTATION

submitted to

Oregon State University

in partial fulfillment of

the requirements for the

degree of

Doctor of Philosophy

Presented June 8, 2020

Commencement June 2021

Doctor of Philosophy dissertation of Charles McLouth Culbertson presented on June 8, 2020

APPROVED:

Major Professor, representing Chemistry

Head of the Department of Chemistry

Dean of the Graduate School

I understand that my dissertation will become part of the permanent collection of Oregon State University libraries. My signature below authorizes release of my dissertation to any reader upon request.

Charles McLouth Culbertson, Author

ACKNOWLEDGEMENTS

I would like to acknowledge my principal advisor Michelle Dolgos for helping me begin this journey and guiding me throughout it. Thank you for pushing me and creating the environment that allowed me to succeed. To my adoptive advisor Dave Cann, thank you for providing the resources and guidance for me to finish my PhD at Oregon State, your sage advice, and showing me how to fly with style. To the both of you and Oregon State University, thank for the amazing opportunities and trips I have been able to be a part of.

To the original members of the Dolgos group, Dylan Fast, Ryan McQuade, Wesley Surta, thank you for accepting me and welcoming me in. Your support and friendship over the years has been invaluable, and with your help we are able to determine that I am statistically funny. To Alicia Manjón-Sanz, thank you for your patience and wisdom as we worked together. Your dedication and enthusiasm motivated me to always be the best scientist I could be. To my college-bound summer worker Alex Flak, thank you for putting up with me and working hard.

To my collaborators, thank you for everything, you all have inspired me and produced excellent work. In particular, thank you Dong Hou for teaching me everything I know about the pair distribution function, Alisa Paterson for her help in all things NBT related, and Anton Goetzee-Barral for his insightful discussions. Thank you all for sharing your expertise, wisdom, and knowledge freely and graciously.

I would also like to acknowledge my committee members, Michael Lerner, Kim Anderson, and Brady Gibbons, for their time, commitment, helpful feedback, and for their generosity over the years.

Thank you to my family, Lib, Cub, Ed, and Max. Without you all I certainly wouldn't be where I am today and I certainly wouldn't be the person I am. To my extended family, Mark Olin, J Dunn, Colin Ward, Jacob Rothschild, and Liz Knorr you all inspire me daily to be the best person I can be. Thank you for your love, dedication, and patience with me over the years.

CONTRIBUTION OF AUTHORS

Dr. Michelle Dolgos provided guidance on the experimental design, data analysis and interpretation, and writing of everything presented in this dissertation. Dr. Cann performed a similar role for Chapters 1, 2, and 5. Alexander T. Flak assisted in the synthesis of $ATiO_3$ materials for Chapter 2. Dr. Alicia Manjón-Sanz assisted in the experimental design, synthesis, property measurement, data analysis and interpretation, and writing for Chapters 3 & 4. Marcos Lucero and Dr. Zhenxing Feng collected, interpreted, and helped analyze the X-ray absorption spectroscopy data in Chapter 4. For Chapter 5, Dr. Ryan R. McQuade helped with the experimental design and data collection, and Dr. Alisa R. Paterson aided in the data collection, interpretation, and writing.

TABLE OF CONTENTS

Page

TABLE OF CONTENTS (Continued)

Page

TABLE OF CONTENTS (Continued)

Page

TABLE OF CONTENTS (Continued)

Page

TABLE OF CONTENTS (Continued)

Page

LIST OF FIGURES

Figure Page

LIST OF FIGURES (Continued)

Figure Page

Figure Page

Figure Page

Figure Page

Figure Page

Figure Page

LIST OF TABLES

Table Page

LIST OF APPENDIX FIGURES

Figure Page

Figure Page

LIST OF APPENDIX TABLES

Table Page

LIST OF APPENDIX TABLES (Continued)

Table Page

Chapter 1: Introduction of Solid State Chemistry, Structural Characterization, and Property Measurements

1.1. Scope and Motivation

Electroceramics are ceramic materials that perform an electronic function. Their electronic functionality is fundamentally related to the fact that ceramics are bound together by ionic bonds. Therefore, external electric fields are able to interact directly with the crystal structure through a Coulombic force with the ions that make up the ceramic. These materials have a wide range of electrical, magnetic, and optical properties that are used in a wide array of applications and devices.[1] For example, in a single a circuit board there are resistors, transistors, capacitors, inductors, diodes, and switches which can all be made from electroceramics. Due to the ubiquity and importance of these materials, the market share for electroceramics is estimated to reach $11.5 billion dollars by 2022.[2] As the demand for electronic miniaturization grows, there is also a demand for sustainability, thus creating the need for new materials and innovative solutions that are both smaller (or possess stronger properties) and are more environmentally friendly.

In regards to these motivating factors, this work investigates the local structure and properties of lead-free electroceramics. Understanding the structural origins of the physical properties is critical to the design and synthesis of novel materials and technologies.

More specifically, the work described here covers the study of the local structure and properties of functional electroceramics with dielectric, piezoelectric, ferroelectric, and ionic conducting properties. Chapter 1 will present an introduction to the perovskite structure and the applications of perovskites, it will outline the different material classes under study, then detail the structural characterization methods, and describe how the physical property measurements and how they are performed. In Chapter 2, a detailed investigation into the local and average structure of $A^{2+}TiO_3$ (A = Mg, Ca, Sr, Ba) is presented. Chapter 3 and 4 investigate the structure and properties of the lead-free piezoelectric material barium calcium zirconium titanate (1-x)$Ba(Zr_{0.2}Ti_{0.8})O_3$-$x(Ba_{0.7}Ca_{0.3})TiO_3$ (BZT-BCT) through a number of techniques. Chapter 5 changes tack and address the structure and ionic conductivity properties of sodium bismuth titanate $Na_{0.5}Bi_{0.5}TiO_3$ (NBT). Finally, a summary of this work and concluding remarks are made in Chapter 6.

1.2. Perovskites

The perovskite structure, of the form ABX_3, has endured the test of time and proven to be one of the most technologically important material structures due to its stability and relative flexibility (or tunability). The name perovskite is shared by the mineral form of calcium titanate ($CaTiO_3$), discovered by Gustav Rose in the Ural Mountains in 1839 and named after the Russian mineralogist Lev Aleksevich von Perovski.[3] During World War II, the material $BaTiO_3$ was discovered by Wainer and Salomon in the US (1942), Ogawa in Japan (1942), and Vul in Russia (1944).[4] Since

then, the perovskite structure has been found to accommodate a wide array of elements in the *A*-, *B*-, and *X*-sites as shown in Figure 1.1.

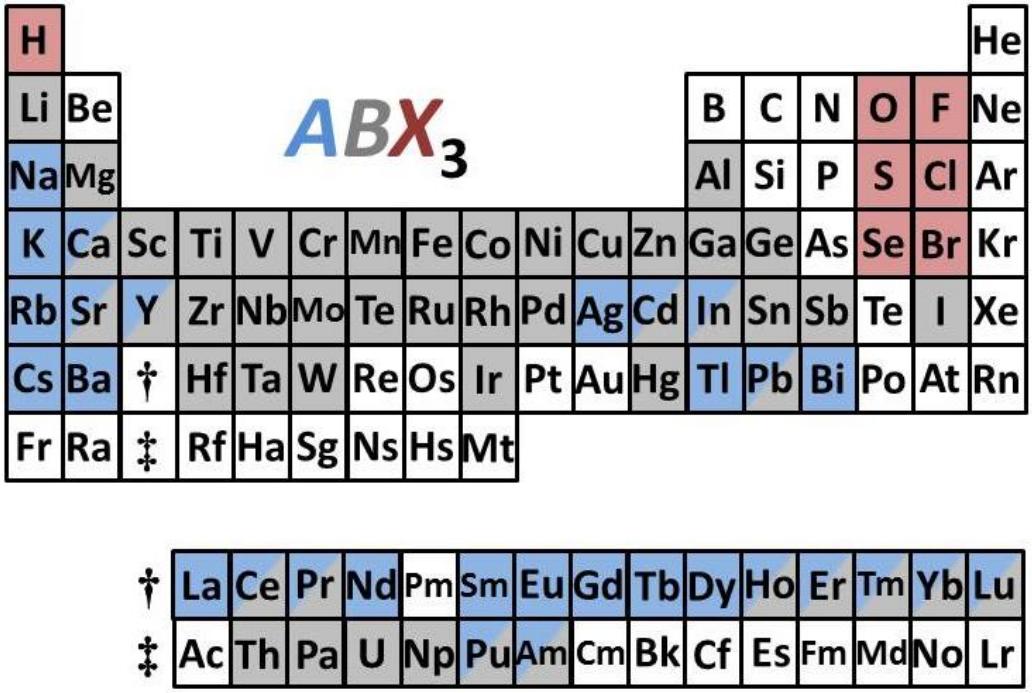

Figure 1.1. Perovskite forming elements, adopted from Dr. Richard McQuade.[5]

The elemental diversity the perovskite structure is capable of hosting has led to a range of structural modifications (Section: 1.2.1) that make the perovskite structure technologically useful for many different applications (Section: 1.2.2).

1.2.1. Perovskite Structure

The perovskite structure, ABX_3 (for typical oxide perovskites $A^{2+}B^{4+}O_3$, $A^{3+}B^{3+}O_3$, or $A^{1+}B^{5+}O_3$), is generally described as a network of corner sharing BX_6 octahedra, with a 12-coordinate cubo-octahedral *A*-site formed from the center of eight BX_6 octahedra.[6] Larger cations prefer the 12-coordinate *A*-site, and relatively smaller cations prefer the 6-coordinate *B*-site.

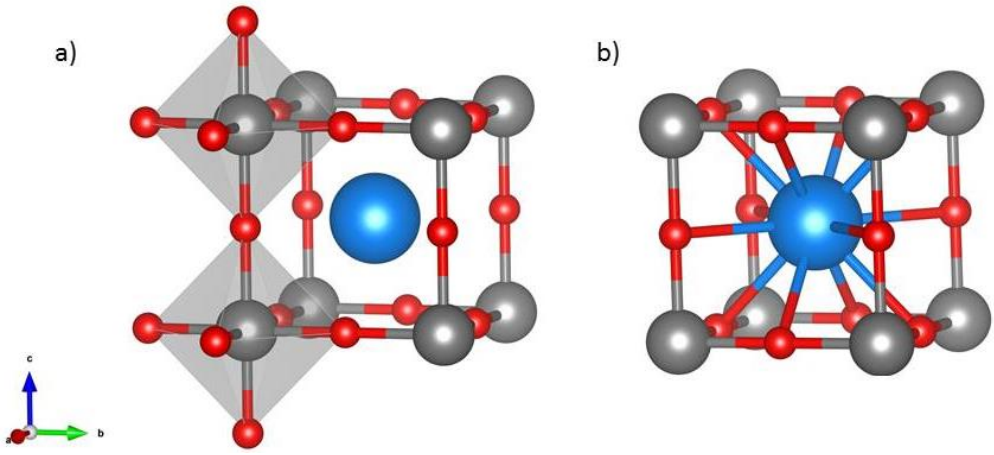

Figure 1.2. Cubic perovskite structure showing a) six coordinate *B*-site (BX_6 octahedra) and b) 12 coordinate *A*-site (AX_{12} cubo-octahedra) with the *A*-site shown in blue, *B*-site in grey, and *X*-site in red.

Although the archetypical perovskite is historically $CaTiO_3$, $SrTiO_3$ has become the de facto ideal perovskite structure. The cubic $Pm\bar{3}m$ structure of $SrTiO_3$ is shown in Figure 1.2, with the strontium cations in blue, titanium cations in grey, and oxygen anions in red. The relative size of the strontium, titanium, and oxygen ions lead to this highly symmetric and stable structure. In other perovskites, the relative size of the cations can lead to different structure types. The Goldschmidt tolerance factor (*t*) derives from the relationship between the edge and the body diagonal of the unit cell:

$$\frac{\sqrt{2}a}{2} = (r_A + r_X) = \sqrt{2}(r_B + r_X)$$

where *a* is the cubic lattice parameter, where r_A is the ionic radius of the *A*-site cation, r_B of the *B*-site cation, and r_X of the *X*-site anion.[7]

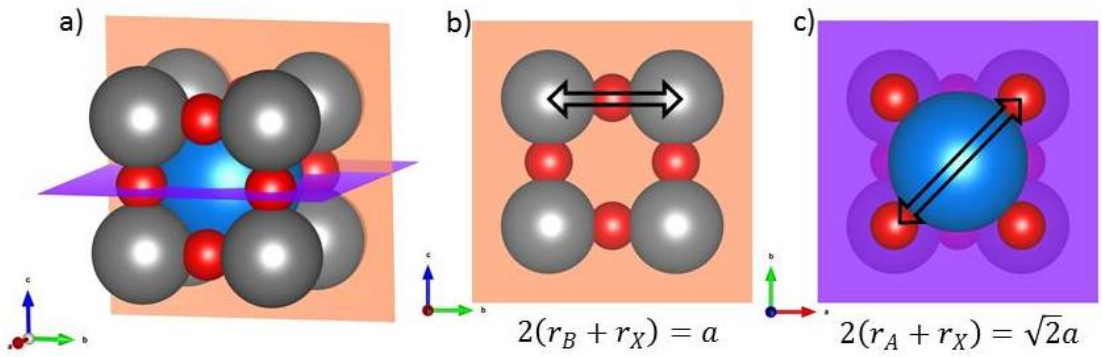

Figure 1.3. The a) perovskite structure with the mid (orange) and basal (purple) planes shown. The geometric edge length for the b) mid plane and c) basal plane are shown as they relate to the unit cell parameter, *a*.

The ratio between these lengths yields the Goldschmidt tolerance factor (*t*):

$$t = \frac{r_A + r_X}{\sqrt{2}(r_B + r_X)}$$

The tolerance factor (*t*) can then be used to predict the structure (Table 1-1).[7] If the *A*-site ions are too small ($t < 1$) the BX_6 octahedra will tilt to mitigate the void space leading to orthorhombic or rhombohedral symmetry. Conversely, if the *B*-site ion is too small, it will no longer be able to fit in the BX_6 octahedral and will displace leading to tetragonal or hexagonal symmetry.

Table 1-1. Approximate Goldschmidt tolerance factors ranges and the predicted structures with literature examples[7], with ionic radii from Shannon et al[8].

Tolerance Factor (*t*)	Predicted Structure	Example
< 0.85	Non-perovskite	$MgTiO_3$ (*t* = 0.81)[6]
0.85~0.9	Orthorhombic/Rhombohedral	$CaTiO_3$ (*t* = 0.97)[7], $GdFeO_3$ (*t* = 0.87)[11]
~1	Cubic	$SrTiO_3$ (*t* = 1.0)[12]
> 1	Tetragonal/Hexagonal	$BaTiO_3$ (*t* = 1.06)[13]

However, the Goldschmidt tolerance factor was put to the test in a recent study and was only able to predict between perovskite and non-perovskite with 74% accuracy

for 576 compounds tested.[14] The classical tolerance factor also assumes spherical ions, which isn't as accurate for larger ions with lone pairs (i.e. Pb^{2+}: $[Xe]5d^{10}6s^{2}6p^{0}$).

The perovskites outlined above are known as single and there are also layered perovskites such as Ruddleson-Popper[15–17], Dion-Jacobson[18–20], and Aurivillius phases.[21–23]

1.2.2. Applications of Perovskites

The diverse elemental components and adaptable structure, have led to a whole host of applications. This work will focus on perovskites with interesting dielectric, piezoelectric, and ferroelectric in Chapter 2:, Chapter 3:, and Chapter 4:, and ionic conducting perovskites in Chapter 5:.

Perovskites with dielectric properties are primarily used as capacitors. These materials include $CaTiO_3$, $SrTiO_3$, $BaTiO_3$, and $LaAlO_3$to name only a few. For example, $BaTiO_3$ is used in multilayer ceramic capacitors (MLCC) where the capacitance (C) is:

$$C = \frac{N\varepsilon_r' A\varepsilon_0}{d}$$

where N is the number of capacitive layers, ε_r' is the dielectric permittivity, A is the area, ε_0 is the permittivity of free space, and d is the distance (thickness) of each layer.

Piezoelectric and ferroelectric perovskites such as $PbZr_{1-x}Ti_xO_3$ (PZT) are used in a number of applications, typically as sensors and actuators. Piezoelectrics are used in devices for fuel-ignition, solid state batteries, ultrasonic applications (cleaning

devices, transmitters, receivers), medical and surgical instruments[24], sonar technology, biomedical sensors[4,24], actuators for nano- and micro-positioning, transportation applications[25], and more recently energy harvesting applications[25,26].

Perovskites with ionic and electronic conducting properties like $Na_{0.5}Bi_{0.5}TiO_3$ (NBT) and $LaMnO_3$ are viable for solid oxide fuel cell applications (SOFC).[27] Other applications of ionic conducting perovskites include varistors, thermistors, among others[28].

Other applications of perovskites include devices based on the photovoltaic effect[3], superconductivity[29], and magnetoresistance[30].

1.3. Structure-Property Relationships

Much of this work focuses on determining the structure of materials that possess interesting properties to develop a structure-property relationship. For crystalline or polycrystalline materials there is a clear link between the symmetry of the unit cells (local structure), the way those unit cells are arranged relative to one another (meso-scale or domains), and how those regions of domains (grains) contribute to the various physical properties measured (density, dielectric, piezoelectric, ferroelectric, impedance, etc.). The relationship is best defined by Neumann's principle which states that the of any physical property of a crystal must include the symmetry elements of the point group of the crystal.[31] However, the opposite is not true, where the symmetry of the physical property may be much higher than that of the crystal structure.[32] Understanding the structure-property

relationships in a material can reveal the origin of physical properties and thus allow for the intelligent design of new higher performance materials.

1.4. Material classes

Materials are generally grouped into three categories: insulators, semiconductors, and conductors. The work described here, focuses on insulating materials, namely dielectric, piezoelectric, and ferroelectric materials. Additionally, this includes the investigation of high temperature ionic conductors, therefore conducting materials in general will be covered briefly.

1.4.1. Dielectrics

As the name implies, dielectric materials are insulators that restrict the movement of electrons and oppose an external electric field. When two parallel plates are connected to a power supply, charge will accumulate on the plates. When the plates are separated by air, the charge on the plates (q) is represented by the following:

$$q = \frac{\varepsilon_0 A V}{d}$$

where ε_0 is the permittivity of free space, A is the area of the plates, V is the voltage applied, and d is the distance between them. Furthermore, the capacitance (c) is simply the charge per applied volt.

$$c = \frac{q}{V} = \frac{\varepsilon_0 A}{d}$$

More interestingly, if a dielectric material is placed between the plates the charge and therefore the capacitance increase by a factor of the relative permittivity (ε_r).

$$c' = \frac{\varepsilon_0 \varepsilon_r A}{d}$$

This accumulation of charge, when a dielectric material is placed between two parallel plates is shown in in Figure 1.4.

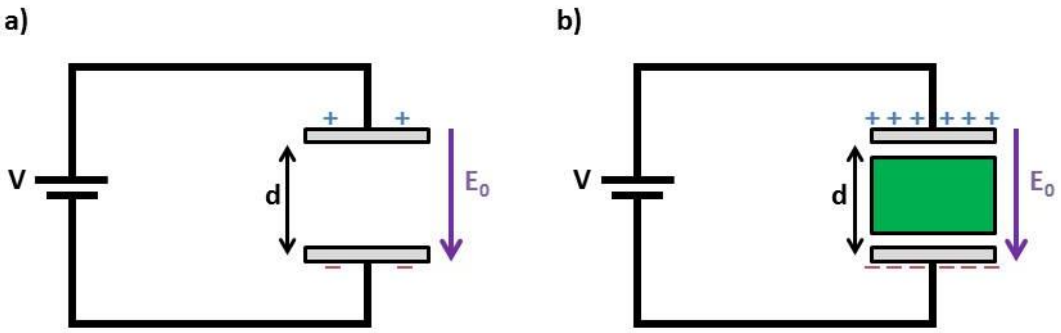

Figure 1.4. When two conductive plates are placed in parallel (at a distance *d*) and a voltage is applied, charge will accumulate on the plates, a) if no material is placed between the plates, the charges accumulated are related to the permittivity of free space, however b) if a dielectric material is placed between the plates, additional charges will accumulate on the conductive plates based on the dielectric permittivity of the material.

In general, the relative permittivity represents a materials response to an electric field. Unlike a conducting material, when an electric field is applied to a dielectric material the charges in that material are accelerated and come to a steady state displacement or polarization. These internal electric dipoles (p) create an electric field that opposes the original electric field that allows additional charge to accumulate (Figure 1.5).

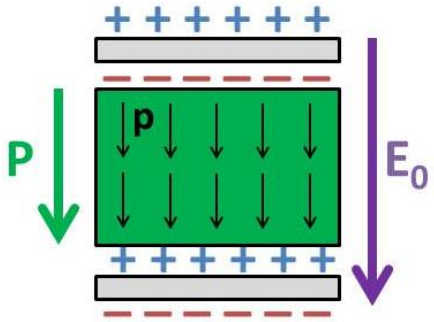

Figure 1.5. The application of an electric field (E_0) across a dielectric material results in a polarization (P) that is the summation of internal electric dipoles (p) that will oppose the external field and lead to the accumulation of additional charge on the conductive plates.

The polarization (P) can also considered as the electric dipole moment per unit volume.

$$P = (\varepsilon_r - 1)\varepsilon_0 E_0$$

However, in real materials the relative permittivity is made up of several different frequency dependent contributions. Furthermore, due to the alternating electric fields used, some energy is lost as heat. Therefore the complex dielectric constant (ε_r') is used:

$$\varepsilon_r = \varepsilon' + i\varepsilon''$$

the energy loss in a capacitor is known as the loss tangent ($\tan\delta$), which is defined as:

$$\tan\delta = \frac{\varepsilon''}{\varepsilon'}$$

The contributions to permittivity include electronic, ionic, dipolar, and space charge:

$$\varepsilon_r' = \varepsilon_{r,electronic} + \varepsilon_{r,ionic} + \varepsilon_{r,dipolar} + \varepsilon_{r,space\ charge}$$

The electronic polarization is due to the displacement of the electron cloud around the nucleus of the atoms and has a high resonance frequency typically in the ultraviolet spectrum, $\omega_{electronic}$ ~10^{15} Hz. The ionic polarization is from the movement and displacement of the cations and anions in the material relative to one another. Ionic polarization has a relatively lower resonance frequency compared to electronic polaraziation typically in the infrared spectrum, ω_{ionic} ~10^{13} Hz. Dipolar polarization occurs in polar materials, where the poles can be reoriented. The resonance frequency for dipolar polarization can occur over a much larger range, typically in the microwave spectrum, $\omega_{dipolar}$ ~$10^{3\text{-}10}$ Hz. The last contributing polarization is space charge polarization, which involves the movement of mobile defects that interact at interfaces and barriers in a material. Space charge has the lowest resonance frequency, typically in the radio frequency range, $\omega_{space\text{-}charge}$ ~10^{3} Hz. The dielectric permittivity measured is the combination of these factors, shown in Figure 1.6.

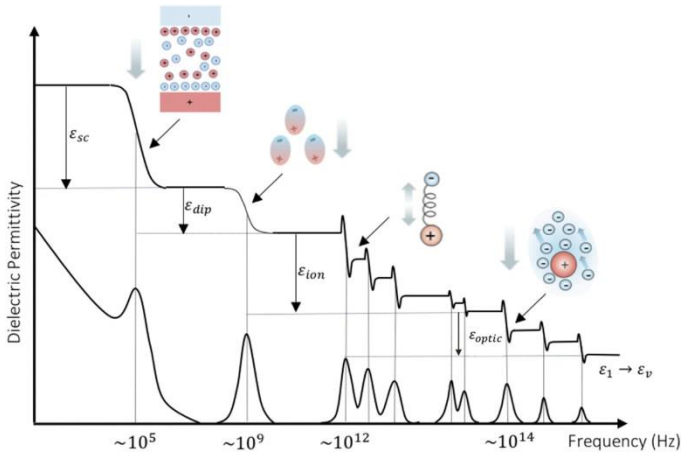

Figure 1.6. Contributions to the dielectric permittivity from space-charge (ε_{sc}), dipolar (ε_{dip}), ionic (ε_{ion}), and electronic (ε_{optic}) polarization. This figure has been reprinted with permission under the Creative Commons Attribution (CC BY) license from Wilson et al.[34]

Depending on the crystallographic symmetry, in particularly the point group, of dielectric materials there are additional properties that arise, namely piezoelectricity and ferroelectricity (Figure 1.7a and b).

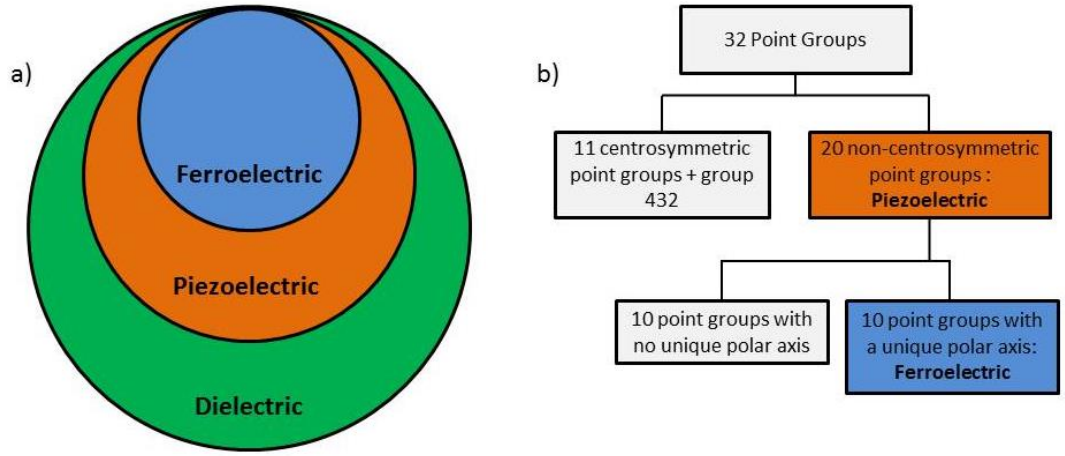

Figure 1.7. a) Relationship between dielectric, piezoelectric, and ferroelectric materials and b) point group symmetry requirements for piezo- and ferroelectricity.

1.4.2. Piezoelectrics

Piezoelectric materials are a subset of dielectric materials that do not possess a center of symmetry. In other words, only materials that crystallize in the 20 non-centrosymmetric space groups can exhibit piezoelectricity. The non-centrosymmetric unit cells in the material, under no field or stress, are randomly oriented and thus no net polarization is observed. However, an applied mechanical stress or electric field can induce a dipole to create a unique polar axis within each unit cell. The dipole moments in these now-polar unit cells can align to form a net polarization and cause a strain to occur or an electric potential to accumulate. This effect is expressed in two forms, the direct and indirect piezoelectric effect, depending on whether a stress or a field is applied to the material, as depicted in Figure 1.8.

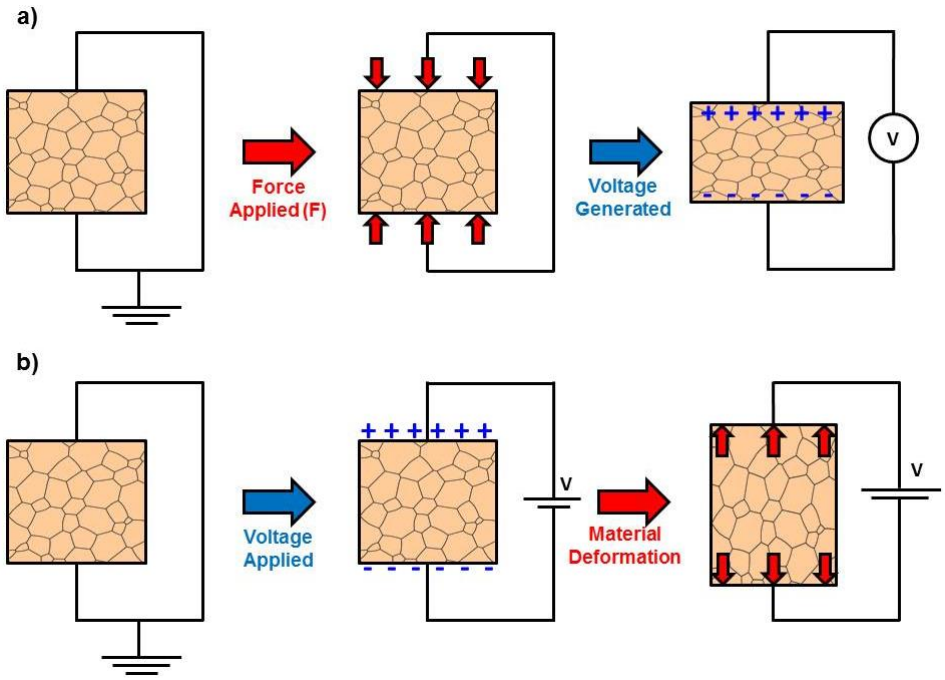

Figure 1.8. General schematic for a) direct piezoelectric effect where a force (*F*) is applied to a material, and a voltage is generated in response, and b) inverse or indirect piezoelectric where a voltage is applied that results in deformation.

The direct piezoelectric effect is when a force is applied to a solid which causes a voltage to accumulate across the material. The polarization (*P*) is proportional to the materials response and the applied stress:

$$P_i = d_{ijk} X_{jk}$$

where *d* is the piezoelectric coefficient in pC/N and *X* is the mechanical stress in N/m^2. Due to the 3-dimensional nature of the material, the piezoelectric properties depend on the direction of the stress. For a polarization in the i^{th} direction, the field (*X*) defined as:

$$X_{jk} = \frac{F_j}{A_k}$$

where *F* is the force oriented in the *j* direction and *A* is the area upon which the force acts where *k* is the vector normal to the plane. For example, a normal stress occurs

when $j = k$, and a shear stress occurs when $j \neq k$. The matrix for the piezoelectric coefficient can be dramatically simplified due to the symmetry constrains of piezoelectric materials. For a poled polycrystalline ceramic material such as those that are the subject of this study, the piezoelectric coefficient matrix is represented by:

$$d_{ijk} = \begin{pmatrix} 0 & 0 & 0 & 0 & d_{15} & 0 \\ 0 & 0 & 0 & d_{15} & 0 & 0 \\ d_{31} & d_{31} & d_{33} & 0 & 0 & 0 \end{pmatrix}$$

where the d_{33} refers to a polarization in the same direction as the applied force, d_{31} is a polarization induced perpendicular to the stress, and d_{15} relates the polarization generated by a shear stress. The most commonly used piezoelectric coefficient is the d_{33} which is known as the piezoelectric figure of merit.

As mentioned previously, the indirect piezoelectric effect occurs when an electric field is applied to a material and the material mechanically deforms or strains. The material strain (S) is proportional to the effective piezoelectric coefficient (d^*) in pm/V and the applied electric field (E).

$$S_{jk} = d^*_{ijk} E_i$$

Just like the direct piezoelectric effect, the inverse piezoelectric effect is also a tensor property that is simplified by the symmetry of the crystal system. The strain (S) can be written as:

$$\begin{pmatrix} S_1 \\ S_2 \\ S_3 \\ S_4 \\ S_5 \\ S_6 \end{pmatrix} = \begin{pmatrix} 0 & 0 & d^*_{31} \\ 0 & 0 & d^*_{31} \\ 0 & 0 & d^*_{33} \\ 0 & d^*_{15} & 0 \\ d^*_{15} & 0 & 0 \\ 0 & 0 & 0 \end{pmatrix} \begin{pmatrix} E_1 \\ E_2 \\ E_3 \end{pmatrix}$$

where the d^*_{33} refers to a strain in the same direction as the applied field, d^*_{31} is a strain perpendicular to the field, and d^*_{15} is a shear coefficient.

There are two primary contributors to the piezoelectric effect observed: intrinsic and extrinsic. Intrinsic contributions refer to atomic displacements in individual unit cells which can lead to changes in symmetry, whereas extrinsic contributions refer to the reorientation of domains or domain wall motion inter-phase boundaries, and defect-dipole rotation. The ability of piezoelectric materials to transduce electrical and mechanical energy makes them uniquely suited for many applications, such as: sensors, actuators, transducers, and microelectromechanical systems (MEMS).

1.4.2.1. Lead Zirconate Titanate (PZT)

The current industry standard piezoelectric material is lead zirconate titanate, $PbZr_{1-x}Ti_xO_3$ (PZT), which shows a strong piezoelectric response at the $x = 0.48$ MPB composition. At low titanium (x) content PZT adopts rhombohedral $R3m$ symmetry, and at high titanium (x) content tetragonal $P4mm$ symmetry. Like many piezoelectric materials, the high temperature structure for all compositions is a paraelectric cubic phase. An adapted phase diagram from Noheda et al. is shown in Figure 1.9.[35]

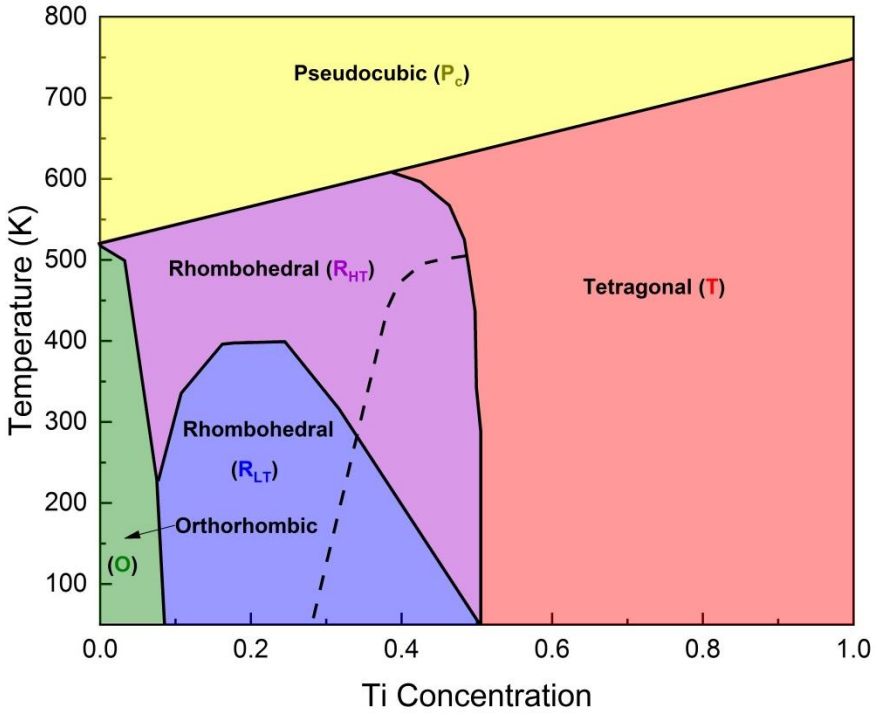

Figure 1.9. Phase diagram for lead zirconate titanate (PZT), adapted from Noheda et al.[36]

Like many perovskite materials, as time advances additional complexities continue to be found. When the electromechanical properties of PZT were first discovered in 1954 by Jaffe et al., the corresponding phase diagram was simply rhombohedral at low (*x*), tetragonal at high (*x*), and cubic at high temperatures.[37] However, since then a more complicated system was proposed by Noheda et al where a monoclinic phase was found at the MPB.[36] Furthermore this monoclinic phase served to "bridge" the dissimilar symmetries on either side of the MPB and allow for the enhanced properties observed.[35] This theory was challenged by Schönau et al. who used TEM to discover rhombohedral nanodomains that lead average structure-type refinements to yield a monoclinic structure.[38] Additionally, a more recent report has been published that investigate both the local and average structure of PZT using

total scattering. They found significant evidence for the existence of two monoclinic phases at the MPB composition.[39]

However, the interest in PZT-based research has waned in recent years due to environmental concerns over the toxicity of lead and a push by the European Union to restrict the use of lead in consumer electronics in the Restriction of Hazardous Substances initiative (Directive 2002/95/EC).[40] This has led to the development of lead free alternatives which will be discussed in the next section (1.4.2.2).

1.4.2.2. Lead Free Piezoelectrics

With the rise of demand for new materials to replace PZT, three main lead-free families of materials have emerged: niobium, bismuth, and barium titanate based materials.[41–45] As the demand has risen, so too has the amount of research and subsequent publications (shown in Figure 1.10 for the years 1994 to 2012).

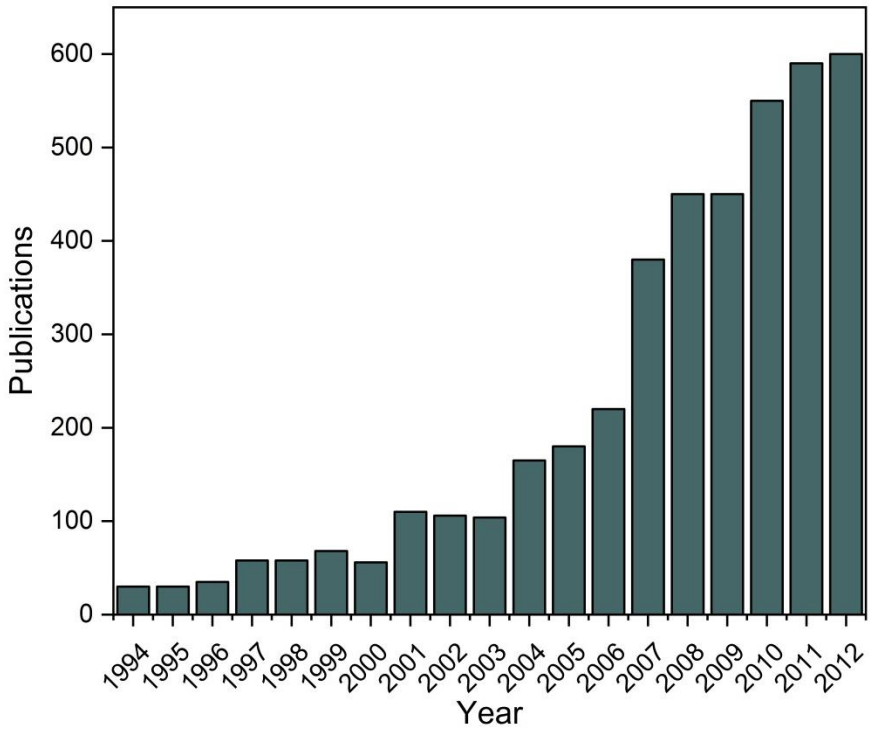

Figure 1.10. Number of publications on lead-free piezoceramics from 1994 to 2012, reproduced from Coondoo et al.[41]

The bismuth based materials are largely focused around sodium bismuth titanate, $Na_{0.5}Bi_{0.5}TiO_3$ (NBT), and bismuth potassium titanate, $Bi_{0.5}K_{0.5}TiO_3$ (BKT), and derivatives thereof. However, layered bismuth titanate ($Bi_4Ti_3O_{12}$) based materials have been investigated for high temperature applications. The sodium bismuth titanate (NBT) system will be described in greater detail in Section: 1.4.2.2.1.

Barium titanate has remained a steadfast staple in the field of piezoelectrics however the low Curie temperature (T_c ~120 °C) has limited its use in applications.[41] This has led to the discovery of a number of barium titanate based materials (including solid solutions with NBT and KNN), the most notable materials are barium zirconate titanate – barium calcium titanate, $Ba(Zr_{0.2}Ti_{0.8})O_3$-$(Ba_{0.7}Ca_{0.3})TiO_3$ (BZT-BCT), and barium stannate titanate – barium calcium titanate, $Ba(Sn_{0.12}Ti_{0.88})O_3$-

$(Ba_{0.7}Ca_{0.3})TiO_3$ (BTS-BCT).[41] This work focuses on the most promising barium titanate derivative, BZT-BCT, which will be discussed thoroughly in Section: 1.4.2.2.2.

1.4.2.2.1. Sodium Bismuth Titanate (NBT)

Sodium bismuth titanate, $Na_{0.5}Bi_{0.5}TiO_3$ (NBT, although sometimes referred to as "BNT"), was first reported in 1961 by Smolenskii et al.[46] but remained largely understudied until the early 2000s as the push for lead-free materials began.[42]

Some of the early work on the properties of NBT began in the 1990s with the work of Suchanicz among others, who studied the optical and dielectric properties of NBT.[47–49] NBT was found to possess a high Curie temperature (T_C ~325 °C) and a piezoelectric figure of merit of 73 pC/N.[50] Some limitations found were that NBT requires a high sintering temperature (> 1200 °C), a high coercive field (E_C = 73 kV/cm), and a large conductivity at high temperatures.[41]

Like the properties, the preliminary work on the structure of NBT was also conducted by Suchanicz in the 1990s, who reported the structure as a combination of rhombohedral and tetragonal phases over a wide temperature range.[51] However, in 2000 Jones and Thomas used the Rietveld method on high quality neutron powder diffraction data on relatively high temperature sample (698 K) to discover a tetragonal P4bm phase of NBT[52], which corroborated the single crystal work of Soukhojak et al.[53] To better elucidate the structural transitions in NBT, Jones and Thomas performed a follow up study in 2002, where they investigated the structure of polycrystalline NBT over a range of temperatures.[54] At high temperatures (above 813

K) the structure is cubic, then tetragonal (673-773 K), then rhombohedral (5-528 K). There are also regions of two symmetry phases, at high temperatures (773-813 K) there is a coexistence of tetragonal and cubic phases, and then rhombohedral and tetragonal phases (528-673 K).[54] However, there were a number of studies published that were inconsistent with the findings of Jones and Thomas, particularly with the result of a rhombohedral *R*3*c* symmetry phase.[55–57]

In 2011, Aksel et al. discovered evidence for the existence of a monoclinic *Cc* phase from high resolution X-ray diffraction refinements.[58] This study was followed up by two studies on the local structure of NBT using the pair distribution function, found evidence of a large amount of local disorder present, particularly related to the *A*-site cations.[59,60] The bismuth ions were found to be locally distorted in different directions, leading to a bifuricated polarization that enables the unique physical properties.[60]

Solid solutions between NBT and other materials have also been synthesized and widely tested, such as NBT-BT[61], KNN-NBT[62], and NBT-KBT[63], to name only a few.

The high leakage current in NBT was investigated and in 2013 Li et al. found strong ionic conductivity.[64] The leakage current was reported to be due to bismuth deficiencies and oxygen vacancies that are induced during the high temperature calcination and sintering steps.[64] Since then, the electrical and ionic conductivity in NBT has been found to be highly dependent on both the *A*- and *B*-site occupancy and the sintering conditions.[27] The work reported herein, investigates the structure and properties of non-stoichiometric NBT in Chapter 5:.

1.4.2.2.2. Barium Zirconate Titanate – Barium Calcium Titanate (BZT-BCT)

As mentioned previously, one of the most promising lead-free alternatives is barium calcium zirconate titanate, (1-*x*)$Ba(Zr_{0.2}Ti_{0.8})O_3$-*x*$(Ba_{0.7}Ca_{0.3})TiO_3$ (BZT-*x*BCT). The material BZT-BCT was discovered in 2009 by Liu and Ren and found to possesses strong piezoelectric properties, d_{33} ~ 620 pC/N at the MPB (x = 0.50).[65,66] The BZT-BCT system was found to adopt the perovskite structure with rhombohedral *R*3*m* symmetry at low BCT content (x), tetragonal P4mm symmetry at high BCT content (x), and cubic $Pm\bar{3}m$ symmetry above the Curie temperature (T_c ~ 350 K).[65,67] Since then, the physical properties and structure have been studied extensively to determine the structure-property relationships.

Optimized synthesis routes and the properties of BZT-BCT have been investigated in a number of studies.[68–70] These studies, among others, are well summarized in the review by Liu et al.[71]

As mentioned previously, a number of structural studies have been reported since the discovery of BZT-BCT in 2009. In 2012, Jeong and Ahn performed variable temperature neutron total scattering measurements for BZT-0.5BCT at 150 and 300 K[72] using reverse Monte Carlo modeling (RMC) and found that the local structure is relatively independent of temperature, even though the average structure (long range order) clearly refines to different space groups at different temperature regimes (see Figure 1.11).[65] They concluded that the substitution of calcium on the barium site promotes octahedral tilting of ZrO_6 octahedra while leaving the titanium distortion

relatively unaffected.[72] In 2013, two additional structure studies investigating the average structure of BZT-*x*BCT were published.[73,74] The first study, published by Jones et al., used high energy synchrotron radiation X-ray powder diffraction (SR-XRPD) on BZT-0.5BCT, from low (~175 K) to high (~425 K) temperatures. Employing the Rietveld method,[75] they found strong evidence, largely based on the fitting of the $(220)_{pc}$, $(222)_{pc}$, $(400)_{pc}$, and $(411)_{pc}$ pseudocubic reflections, that the structure was a mixture of R (*R*3*m*) and T (*P*4*mm*) from ~250 K (95.2% *R*3*m*, 4.8% *P*4*mm*) to ~290 K (57.7% *R*3*m*, 42.3% *P*4*mm*).[74] The second study by Keeble et al. also reported the use of SR-XRPD analyzed with the Rietveld method to investigate the structure of BZT-*x*BCT across a range of compositions, $x = 0.20$, 0.32, 0.40 and 0.50 and temperatures (~80 to 450 K). They found evidence for the existence of an orthorhombic (O) *Amm*2 phase between the R and T phases in the range $0.45 \leq x \leq 0.51$.[73] They reported the structure of BZT-0.5BCT as a mixture of *R*3*m* (48.22%) and *Amm*2 (51.78%) symmetries at a low temperature of 250 K, then single phase orthorhombic, and at 280 K a mixture of *Amm*2 (66.50%) and *P*4*mm* (33.50%) phases. Finally the structure goes to $Pm\bar{3}m$ above the Curie temperature around 375 K. The phase diagram from Keeble et al. has been adapted in Figure 1.11.

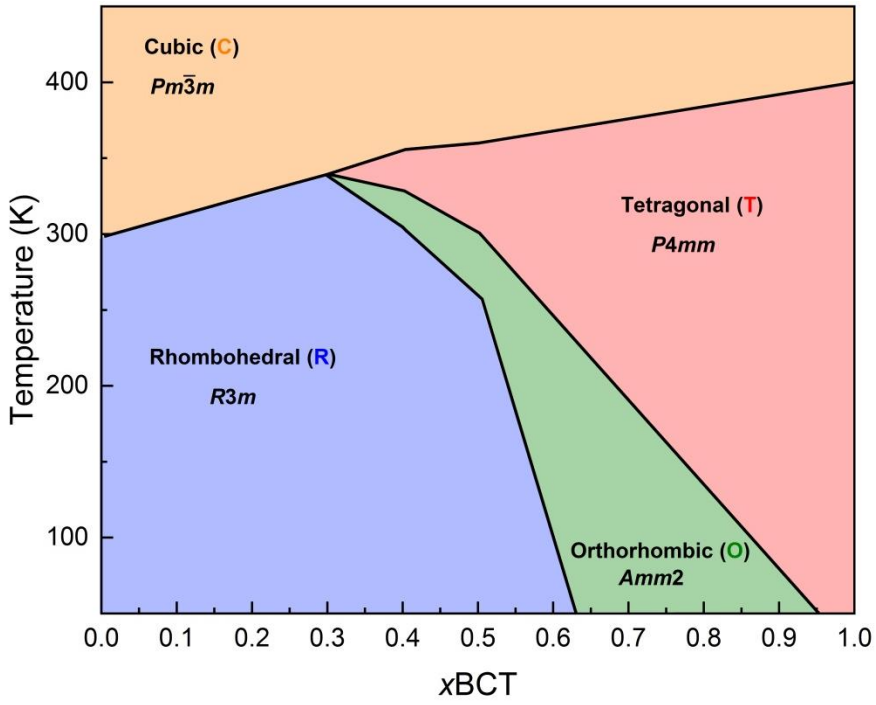

Figure 1.11. Phase diagram of BZT-*x*BCT system adapted from Keeble et al.[73]

Additionally, other methodologies and techniques have been used to determine the local symmetry and bonding environment of the BZT-BCT system. In 2014, a study using convergent beam electron diffraction (CBED) on BZT-0.5BCT which found both 3 *m* and 4 *mm* point group symmetries present at the local scale.[76] Another study, using multi-edge X-ray absorption spectroscopy (XAS) analysis was conducted on $Ba_{0.9}Ca_{0.1}Ti_{1-x}Zr_xO_3$ which concluded that the local ordering of Ti-O_6 is largely unaffected by the increasing substitution of zirconium and that the zirconium ions reside in the center of the Zr-O_6 octahedra.[77] The results of these literature studies including BZT-0.5BCT are summarized in Table 1-2.

Table 1-2. Summary of the literature structure of BZT-0.5BCT using various techniques from Ren, Jeong and Ahn, Keeble, Jones, and Gao et al.[65,72–74,76] *Entries estimated from published phase diagrams.

Composition: BZT-0.5BCT	Literature Reference and Methodology

	Ren et al. (2009)[65]	Jeong and Ahn (2012)[22]	Keeble et al. (2013)[73]	Jones et al. (2013)[74]	Gao et al. (2014)[26]
Temperature (K)	Dielectric measurements	Neutron total scattering	SR-XRPD	SR-XRPD	CBED
210	*R*3*m**	*R*3*m* (at 150 K)	*R*3*m* + *Amm*2	*R*3*m* + *P*4*mm*	
287	*R*3*m*		*Amm*2	*R*3*m* + *P*4*mm*	
305	*R*3*m* + *P*4*mm*	*P*4*mm*	*Amm*2 + *P*4*mm*	*R*3*m* + *P*4*mm*	3 *m* + 4 *mm* symmetry elements
425	$Pm\bar{3}m$*		$Pm\bar{3}m$	$Pm\bar{3}m$	

In 2014, Gao et al. performed Rayleigh analysis under subswitching-electric-field in combination with high field strain measurements to determine the cause of the enhanced piezoelectric properties in BZT-BCT to be domain wall motion.[78] This foundational work led the efforts of this work (Chapter 3:) to investigate the contributions to the piezoelectric effect from a structural stand point. The findings of that work aligned with that of Gao et al and prompted the further investigation into the local structure of BZT-BCT which is described in Chapter 4:.

1.4.2.2.3. The Future of Lead-Free Piezoelectrics

Although there have been great strides in the field of lead-free piezoelectrics, there has yet to be a breakthrough in the electromechanical properties that would allow for the replacement of PZT in modern applications. Furthermore, there is a

concern over the life cycle (mining, processing, and synthesis) of some lead-free materials.

The pertinent parameters for the replacement of PZT with lead-free piezoelectrics are: cost, reproducibility, mechanical and thermal properties, electrical conductivity, and lifetime.[45]

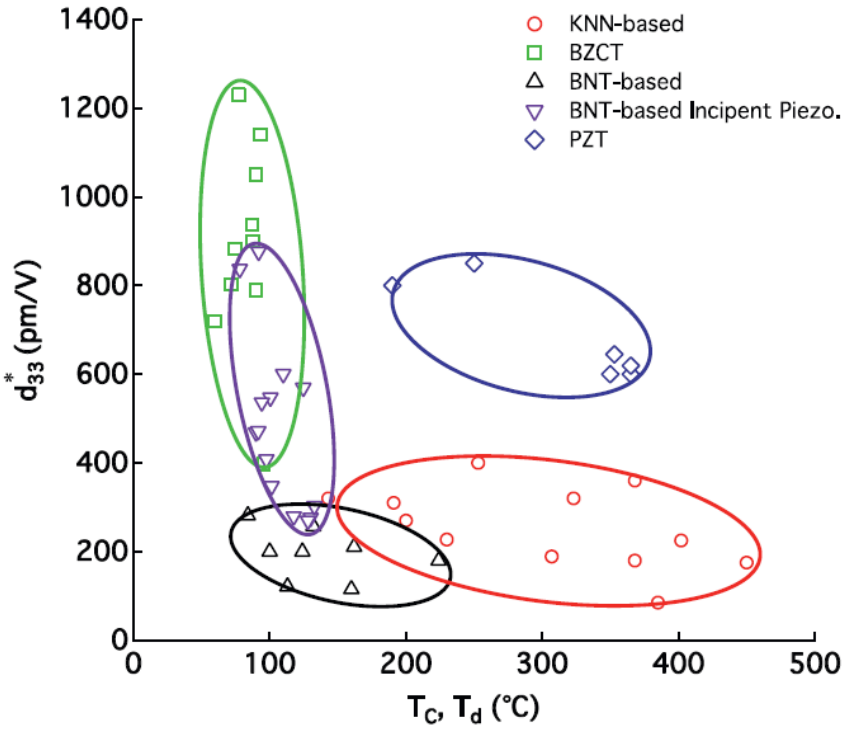

Figure 1.12. The large field (inverse) piezoelectric figure of merit versus the depolarization temperature for KNN-based, BZCT-based, BNT-based, and PZT-based families of lead-free piezoelectrics, reproduced with permission from Rödel et al.[79]

As mentioned previously, there are some environment concerns with the use of lead-free piezoelectric materials. In particular, the mining, chemicals involved in synthesis, and processing can have a large footprint on our climate than for PZT.[80] Furthermore, for the bismuth based systems, the primary source of bismuth currently is a byproduct from lead smelting.[80]

The future of lead-free piezoelectric materials remains unclear. Lead-free materials will certainly be able to find a role in niche applications. However, the ability for lead-free materials to replace PZT has yet to be seen.

1.4.3. Ferroelectrics

Ferroelectrics are a subset of piezoelectric materials that contain a unique polar axis. As a result, the individual unit cells will be polar and this causes a polarization in the material with stress or field, that is known as a spontaneous polarization (P_s). There are two sub-classifications of ferroelectrics: canonical and relaxor ferroelectrics.

Canonical ferroelectrics undergo a phase transition from a high temperature, high symmetry, paraelectric phase to a lower symmetry ferroelectric phase. The temperature at which the paraelectric to ferroelectric transition occurs is known as the Curie temperature (T_c). In the ferroelectric phase, the dipoles moments from the polar unit cells congregate in regions where the dipole moments are aligned, known as domains. However, in the absence of an electric field the domains are randomly oriented and net polarization is zero. Under an electric field, the domains can reorient into a lower energy configuration with the dipole moments preferentially aligned with the external electric field, through the mechanism of domain wall motion. Furthermore, the reorientation causes the alignment of neighboring domains and thus the domains combine and grow larger in size. There are two types of domain walls defined by the relationship between their respective polarization states, 90° and 180°, shown in Figure 1.13.

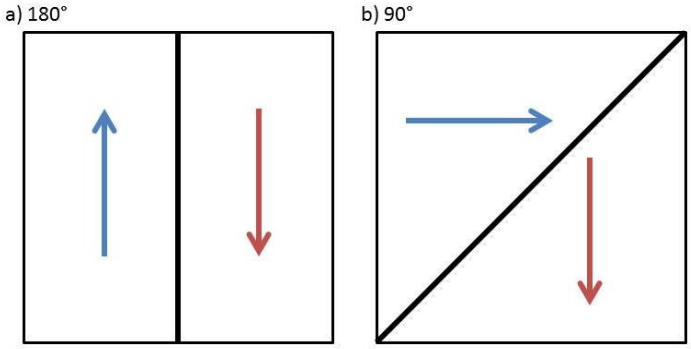

Figure 1.13. Schematic examples of a) 180° and b) 90° domain walls.

The domain wall motion in ferroelectrics leads to ferroelectric hysteresis, shown in Figure 1.14. Initially the material, under no field, has no polarization as the domains are randomly oriented. As the field is increased the material becomes directionally polarized or poled. When the field is removed, the polarization does not go back to zero, the material remains in a poled state with a remenant polarization (P_r). With the application of an electric field in the opposite direction, the domains can be reoriented in the opposite direction.

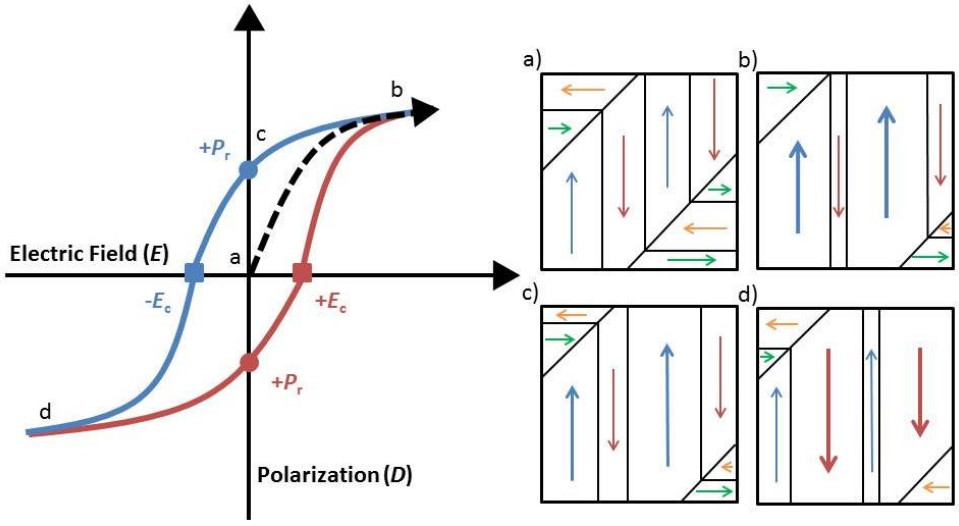

Figure 1.14. Ferroelectric hysteresis (left) and the domain state (right) where a) represents the material under no field where the domains are randomly oriented, b) shows the growth of domains leading to a net polarization, c) shows the removal of the field where the structure remains in a poled state with a remenant polarization (P_r), and d) where the field is reversed and the 180° domains grow.

The second type of ferroelectrics are relaxor ferroelectrics, which are differentiated from canonical ferroelectrics by three main criteria. The primary identifier for relaxor ferroelectrics is a diffuse and frequency dependent permittivity. These materials do not follow the Curie Law and no sharp phase transition is observed. Secondly, the hysteresis behavior of relaxors shows thinner, pinched loops. Finally, the crystal structures of relaxors are typically cubic. Although the term pseudocubic is often employed, where the cubic structure that is obtained from standard methods is the result of the averaging of disordered unit cells. Relaxor ferroelctrics generally consist of a large number of highly charged ions in a disordered matrix where the degree of cation ordering greatly influences the properties. For example, in lead scandium tantalate, $Pb(Sc_{1/2}Ta_{1/2})O_3$ (PST), if the *B*-site cations are ordered then ferroelectric behavior is observed, whereas is the *B*-site cations disordered relaxor behavior is observed.[81]

The cause of the relaxor behavior is attributed to polar nanoregions (PNR) where there are locally ordered regions in a randomly orientated matrix. The temperature at which these regions develop a measurable polarization is referred to as the Burns temperature (T_B).

1.4.4. Conductors

Unlike insulating materials, conductors and semiconductors allow an electric current to flow when a voltage is applied. For this to occur there must be charge carriers present in the material, such as electrons, holes, or highly mobile ions (H^+, O^{2-}). Conductivity (σ) therefore can be expressed simply as:

$$\sigma = \frac{1}{\rho} = nq\mu$$

where ρ is the resistivity (in ohm-m), *n* is the number of charge carriers, *q* is the charge, and μ is the mobility of the carrier. The mobility is:

$$\mu = \frac{q\tau}{m^*}$$

where *q* is the charge of the carrier, τ is the mean time between collisions, and *m** is the effective mass. The charge and the effective mass are constants; therefore the resistance is largely based on the mean time between collisions (τ). The temperature (atomic disorder and phonons) and impurities (point defects, dopants, grain boundaries, and surfaces) can greatly affect the mean collision time.

Due to the nature of the charge carrier, conductors are subdivided into electronic, mixed, and ionic conductors. Depending on whether the primary charge carriers are electrons/holes (electronic), electrons/holes/ions (mixed), or ions (ionic). The work presented here, particularly in Chapter 5, will focus on mixed and ionic conductors.

The ratio between the electronic and ionic conductivity creates several categories: solid electrolytes (regions 2, 4, 6, and 8 in Figure 1.15), mixed ion-electron conductors (1, 3, 5, and 7 in Figure 1.15). These regions are also classified as: superionic conductors (regions 3 and 4), advanced superionic conductors (5 and 6) and hypothetical advanced superionic conductors (7 and 8).

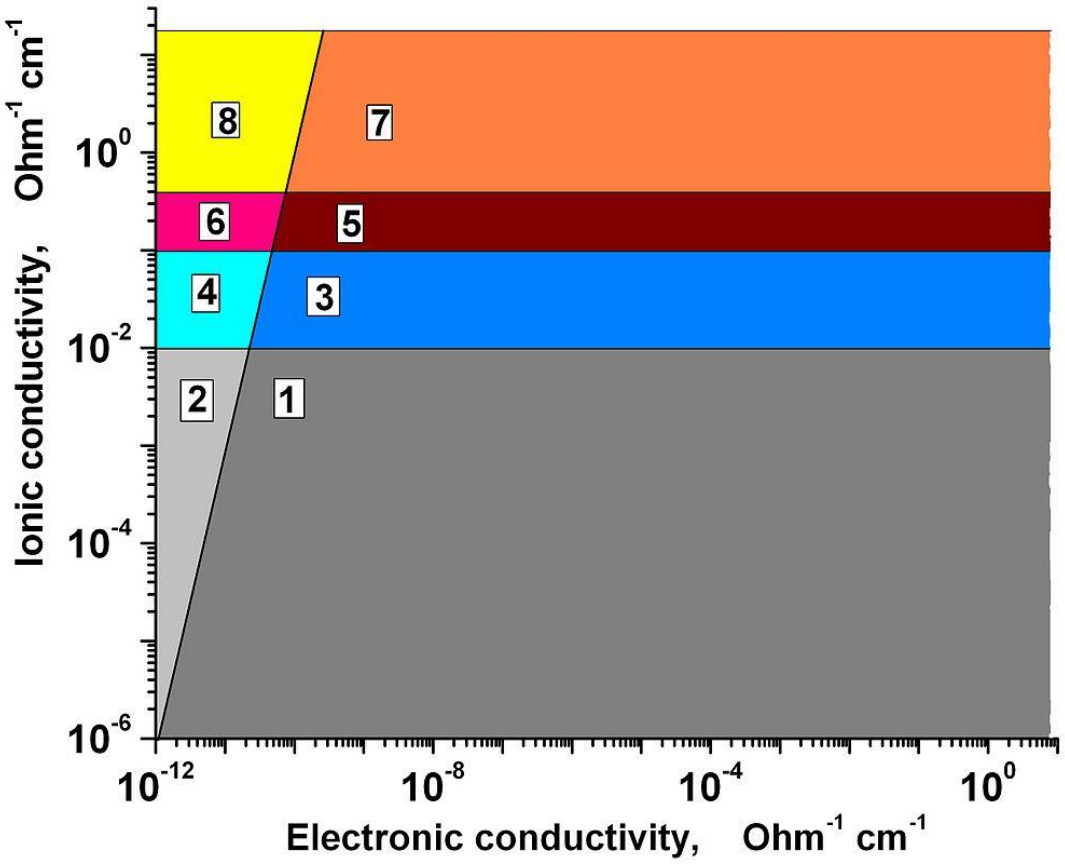

Figure 1.15. Classification of solid-state ionic conductors by the ionic versus the electronic conductivity: mixed ion-electron conductors (regions 1, 3, 5, and 7), and solid electrolytes (regions 2, 4, 6, and 8) (Image created by Despotuli).

Impedance spectroscopy is used to measure the conductivity of relatively resistive materials and is described in further detail in Section: 1.6.4 "Impedance Spectroscopy."

1.4.5. Synthetic Techniques

Materials in the solid state have several additional barriers to overcome compared so liquid and gas reactions. In general, mixing is a problem as entropic forces are unable to overcome strong electrostatic interactions. To overcome these large energy barriers, high temperature, pressure, or a reaction medium are used.

Modern solid state synthesis methods include: standard solid state synthesis, hydrothermal, solvothermal, deposition methods, and cold sintering. This section of the dissertation will focus on the standard state synthesis methods used in this study, as the type of synthesis used can have a dramatic impact on the structure and properties of the material.

1.4.6. Standard Solid State Synthesis

Standard solid state synthesis or direct synthesis involves mixing, pressing, and heating at high temperatures, sometimes in an iterative process.

The mixing step is usually performed in tandem with grinding or agitation to reduce the particle size and therefore dramatically increase the reaction surface area. This effect is shown in Figure 1.16, where the reaction surface area is calculated for particles with decreasing edge length (a) for a 1 cm^3 volume. The simplest approach to the mixing step is to use a mortar and pestle, however high speed ball-mills and powerful vibratory mills are routinely used. The loose powders are pressed into pellets using a uniaxial or isostatic press to reduce the void space between particles. The reduction in void space again increases the reaction surface area. The unfired pellets are typically referred to as green bodies.

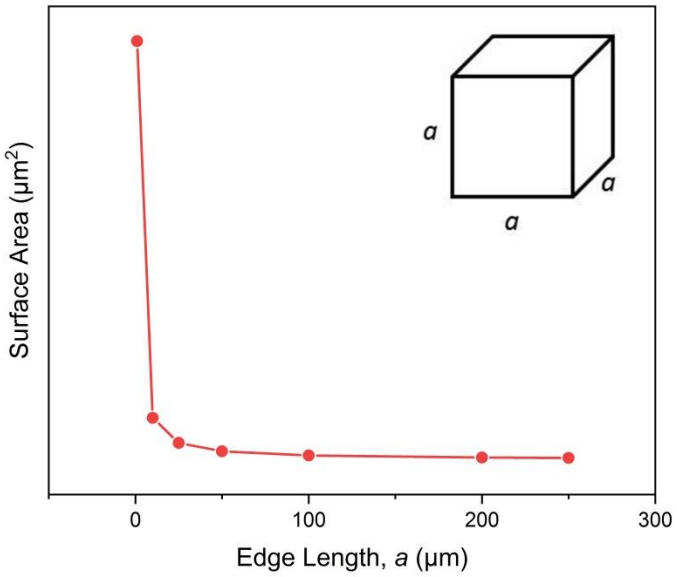

Figure 1.16. Hypothetical relationship between the edge length (*a*) of cube-like particles in 1 cm volume and the resulting reaction surface area.

The heating step is performed in high temperature ovens typically with a slow increase in the temperature (ramp rate), then dwelling or holding at high temperatures to allow the chemical reactions to occur. More specifically, the high temperature conditions are needed to accelerate the slow diffusion rate of ions as they overcome the relatively large Coulombic attraction forces.[82]

As mentioned previously, this process is iterative and a general schematic is shown in Figure 1.17. The first heating step is known as a calcination, which involves growing small portions of the desired phase at relatively lower temperatures. The sample is then re-ground and mixed. Then heated to high temperatures once more in what is known as the sintering process, to allow the growth of larger grains of the desired chemical phase.

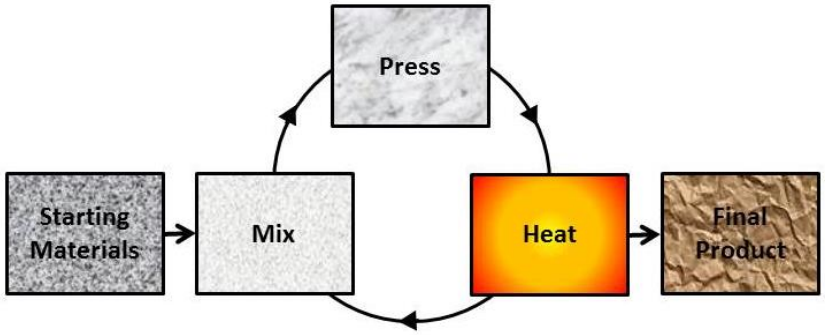

Figure 1.17. General work flow for solid state synthesis.

There are some limitations to the temperature and dwell time that are available to use. The most obvious limitation is the furnace capacity. However, for some materials with relatively volatile cations like lead or bismuth, additional considerations are necessary. These volatile ions readily volatilize at the high temperatures (lead above 500 °C, bismuth above 400 °C).[83] Therefore there is a trade-off between heating conditions and the loss of volatile cations, namely bismuth in this study.

1.5. Structural Techniques

The next section of this dissertation focuses on understanding the structure of solids through several techniques, namely diffraction, total scattering, and X-ray absorption spectroscopy. Understanding the bond structure, atomic positions, and unit cell symmetry is critical to developing structure-property relationships and designing new materials.

1.5.1. Diffraction

Diffraction is the primary tool used in this work to investigate the structure of materials and in general, involves particles or waves interacting with a solid and diffracting or scattering off of the solid at particular angles. Crystalline solids, by definition, are arranged of atoms in a pattern that repeat periodically in three-dimensional space, where the smallest repeatable unit is called the unit cell. Due to the periodic structure, there are regular planes of atoms that can be defined. This holds true for both single crystals and polycrystalline samples. For this work, only diffraction as it pertains to polycrystals will be described.

Diffraction occurs when the incident waves are diffracted from planes of atoms in the solid. The diffracted waves interfere with one another, and the conditions to achieve constructive interference are described by Bragg's Law:

$$n\lambda = 2d \sin\theta$$

where n is an integer representing the order of the diffraction, λ is the wavelength, d is the distance between the planes (d-spacing), and θ is the angle of the diffraction. A common convention is report the diffraction that occurs at the angle between the transmitted and diffracted beam, 2θ. Bragg's Law is depicted in Figure 1.18.[84]

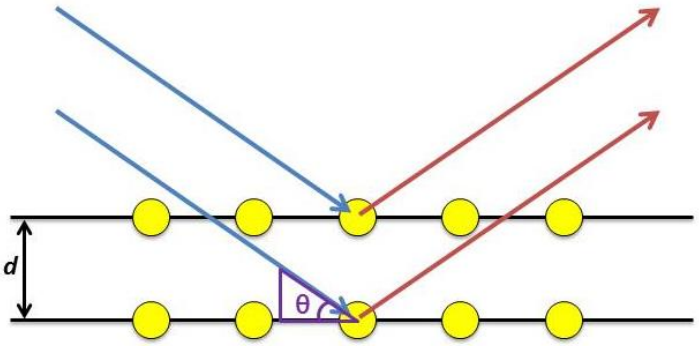

Figure 1.18. Representation of Bragg's Law where two incident beams scatter from planes with a *d*-spacing (*d*).

When λ is an integer (*n*) multiple of the *d*-spacing, the Bragg conditions are satisfied and the diffracted waves are in-phase and constructively interfere. However, if the Bragg conditions are not satisfied the waves destructively interfere. The waves that satisfy the Bragg conditions are therefore at specific angles and are detected. It is important to note that the diffraction from specific planes (real-space) gives rise to peaks in diffraction or reciprocal space. Furthermore, the λ is critical as it must be of the same magnitude of atoms (sub-Angstrom to Angstrom scale) to detect minor variations in the crystal structure.

There are three types of diffraction that are related to what waves are used to probe the solid: electron, X-ray, and neutron diffraction. The key differences between these types of waves are the specific mechanisms in which the incident beam interacts with the solid being characterized. Electrons and X-rays both scatter from the electrons in the solid, although X-rays penetrate further. Therefore, electron diffraction is commonly used to investigate the surfaces of materials, whereas X-ray diffraction is used for bulk characterization. Like X-rays, neutrons are highly penetrative, but scatter from the nucleus of atoms. Neutrons also possess a magnetic moment that can interact with the magnetic moments in the electron cloud

surrounding an atom and lead to additional scattering. The differences between these types of diffraction are shown in Figure 1.19.

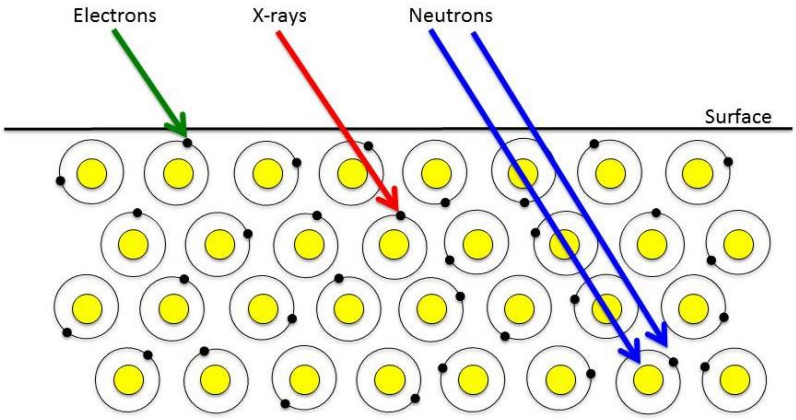

Figure 1.19. Types of diffraction and how they interact with a solid. Figure was created and used with permission from Dr. Todd Wesley Surta.

For any diffraction experiment, there are four principle components used: particle source, optics, sample, and detector. The particle source, for examples an X-ray tube for X-rays, generates the scattering particles. The optics typically filter and focus the incident wave into monochromatic radiation. The sample is the solid that will diffract the particles, which for this study will be a pelletized or powder polycrystalline material. The detector then detects the diffracted particles. Due to wave-particle duality, the scattering particles also act as waves. As such, it is more convenient to describe the nature of the scattering in wave terms. The incident wave (k_i) interacts with the solid and the diffraction wave (k_f) is detected. The difference between the diffracted wave and the incident wave is the momentum vector (Q).

$$Q = k_f - k_i$$

The momentum vector is also related to Bragg's Law by:

$$|Q| = \frac{4\pi \sin\theta}{\lambda}$$

A general schematic for a scattering experiment is shown in Figure 1.20. For the work presented here, only X-ray and neutron diffraction were performed, and therefore will be explained in greater detail.

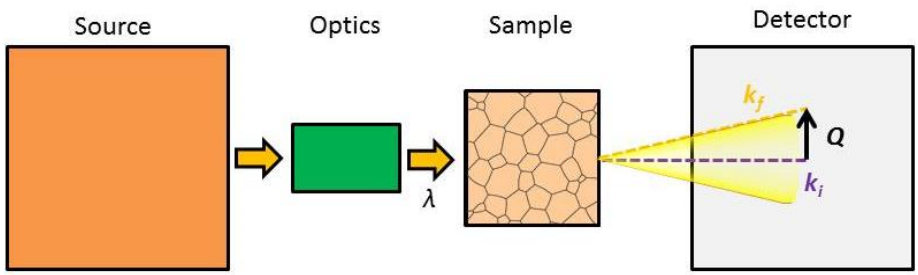

Figure 1.20. Principle components of a diffraction experiment where the incident waves/particles are generated by a source, filtered and focused with optics, interact with the sample – are diffracted, and are detected.

During scattering, there is also a chance that the particles can lose or gain energy. If the energy of the particle changes during scattering then the scattering is said to be inelastic, if the energy remains constant - elastic. Furthermore, coherent scattering occurs if the scattered waves are in phase, whereas incoherent scattering refers to out of phase waves. This work will focus on elastic, coherent scattering.

1.5.1.1. X-ray Diffraction

X-ray diffraction is the most widely used type of diffraction due to the cost of the equipment used to generate X-rays. Lab diffractometers are commonly equipped with copper sources that utilize Cu Kα radiation (λ = 1.541 Å). As X-rays scatter from the electrons in a solid, the more electrons an atom has the stronger it scatters X-rays. More specifically, the form factor (*f*) or scattering efficiency of an atom scales linearly with the atomic number (Z).

As mentioned previously, the planes of atom in a solid give rise to peaks in the diffraction pattern or diffractogram. The position of the peak is determined by the size and shape (symmetry) of the unit cell. The intensity of the peaks (I_{hkl}) that is measured depends on a number of factors, such as: the structure factor (F_{hkl}), the multiplicity (M_{hkl}), the Lorentz and polarization factor ($LP(\theta)$), absorption ($A(\theta)$), and thermal parameters ($TF(\theta)$):

$$I_{hkl} = |F_{hkl}| \cdot M_{hkl} \cdot LP(\theta) \cdot A(\theta) \cdot TF(\theta)$$

The structure factor accounts for the scattering of waves by the electrons in the structure and is based on the individual scattering of atoms and the atomic planes. More specifically the structure factor is defined as:

$$F_{hkl} = \sum_j f_j \, e^{2\pi i(hx_j + ky_j + lz_j)}$$

where *f* is the atomic scattering factor, *x*, *y*, and *z*, are the atomic coordinates of the reflection (*hkl*). The multiplicity accounts for the number of planes contributing to the same reflection. The Lorentz and polarization factor account for geometric factors that influence the intensity:

$$LP(\theta) = \frac{1 + \cos 2\theta}{8 \sin^2 \theta \cos \theta}$$

The absorption correction is used to account for the loss of intensity from absorption. The thermal factors account for the thermally induced atomic vibrations that cause the intensity to smear over a larger range in 2θ:

$$TF(\theta) = e^{\left[-B_j\left(\frac{\sin\theta}{\lambda}\right)^2\right]}$$

where *B* is proportional to the mean square displacement of atom *j* from its equilibrium position.

Although, there are many different experimental setups and geometries that can be used for X-ray diffraction experiments, prevailing geometry is known as Bragg-Brentano geometry. Bragg-Bretano involves moving both the source and detector radially at a fixed distance from the sample, thereby changing the incident angle (ω) and the angle of diffraction (2θ), this geometry is shown in Figure 1.21.

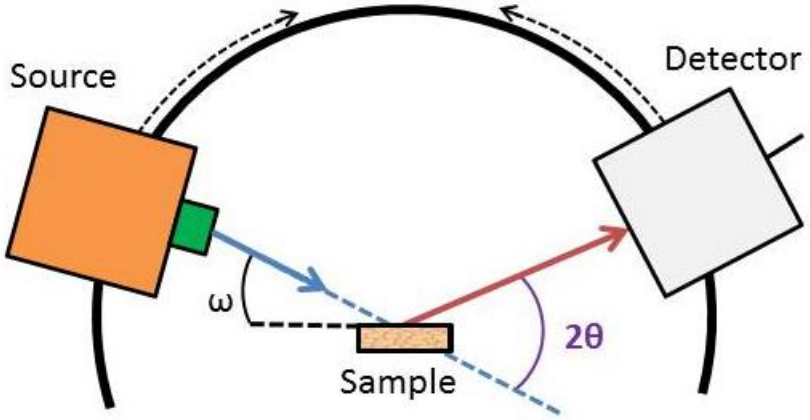

Figure 1.21. Schematic representation of Bragg-Brentano geometry.

Additionally, there are various optics used to tune the incident and diffracted beams, most notably: divergent and Soller slits. Divergent slits are used to limit the divergence of the incident X-rays, whereas Soller slits limit the axial divergence but do not restrict the illumination length. Furthermore some atoms fluoresce when irradiated with Cu Kα X-rays, such as vanadium, chromium, manganese, iron, cobalt, nickel, copper, and zinc. To correct for fluorescence a monochromater can be placed in front of the detector to only allow X-rays waves with the specific wavelengths to pass.

Aside from the weak scattering of lighter elements, another drawback to laboratory-scale X-ray diffraction is limited resolution. This problem can be largely mitigated with the use of high resolution synchrotron light sources in the US alone,

such as: the Advanced Photon Source (APS) at Argonne National Labs, the National Synchrotron Light Source (NSLS-II) at Brookhaven National Labs, and the Synchrotron Ultraviolet Radiation Facilities (SURF and SURF II) at the National Institute of Standards and Technology. Synchrotron sources are made of roughly six components: a linear accelerator, a booster ring, a storage ring, an insertion device, experiment halls, and beamlines. Basically, electrons are accelerated in the linear accelerator into the booster ring where an additional electric field and magnets focus the electrons further. The electrons are deposited into the storage ring where they maintain a current velocity. The insertion devices pull electrons out of the storage rings tangentially, into the various experiment halls where the beam is divided into beamlines that are used by staff and users. A schematic of a synchrotron source is shown in Figure 1.22.

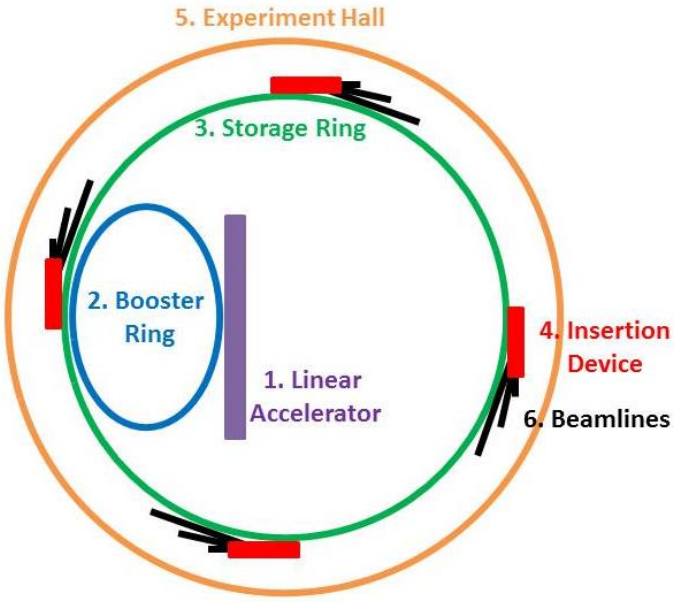

Figure 1.22.General layout of a synchrotron light source.

There are several advantages and disadvantages to using a synchrotron source. As mentioned previously, synchrotron sources are capable of collecting higher

resolution data, which can be particularly useful for material systems that show weak reflections or are have split peaks. Additionally, synchrotron sources have many beamlines that provide the choice of mode of radiation – monochromatic or continuous, varying wavelengths, and more sample environments are available (variable temperature, pressure, gas flow, electric field, etc.). Therefore synchrotron sources are particularly useful for high absorbing samples, time resolved measurements, in situ experiments, and high resolution structure solution. However, the cost of the higher resolution is accessibility. To perform these experiments it can take months to apply for time, get accepted, and go do the experiment. While many facilities do not charge for this service, the travel fees can make these measurements prohibitively expensive.

1.5.1.2. Neutron Diffraction

Similar to synchrotron experiments, neutron diffraction involves large scale government experiment halls, where, as the name implies, neutrons are generated, accelerated, and diffracted from samples. Therefore, from a logistical standpoint, many of the drawbacks of synchrotron sources hold true for neutron diffraction experiments.

However, unlike the X-rays used in synchrotron sources, neutrons scatter very differently from materials. Neutrons scatter from the nucleus and magnetic moment of solid, so they are able to penetrate the material further. Unlike X-rays, the efficiency of atom to scattering neutrons, known as the neutron scattering length, is not dependent on the atomic number. This means that some lighter elements, such as

oxygen, are able to scatter neutrons strongly which provide more reliable diffraction information. The scattering length is also related to the isotope of the atom. The relationship between the neutron scattering, represented as the scattering cross section, versus the atomic number is shown in Figure 1.23.

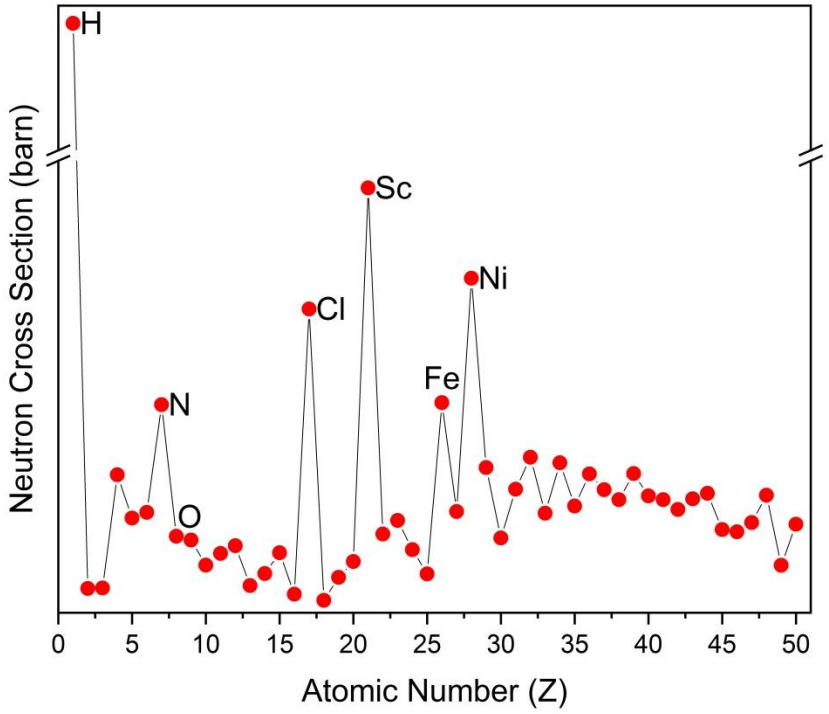

Figure 1.23. Neutron cross section (in barns) versus the atomic number (Z) of various elements.

The two different types of generating neutrons are spallation sources and nuclear reactors. Nuclear reactors deliver a continuous stream of neutrons whereas spallation sources generate bursts of neutrons. As a result, spallation sources are preferred due to the high flux inherent to the technique. Spallation sources also utilize the time of flight (TOF) technique using a complex series of detector banks that record the time and angle at which a neutron arrives. The time of flight is inversely proportional to the diffraction vector *Q* (for elastic scattering):

$$Q = \frac{2mL}{\bar{h}t}\sin\theta$$

where *m* is the mass of a neutron, *L* is the path length, θ is the scattering angle, and *t* is the time of flight.

In general, neutrons have several advantages over X-rays for diffraction purposes. Namely, neutrons scatter strongly from particular light atoms and neutrons penetrate further into the material. Having said that, these measurements are not mutually exclusive and neutron diffraction can be used effectively to complement X-ray data. The main drawback to neutron diffraction is the requirement of a nuclear reactor to generate neutrons.

1.5.2. Total Scattering and the Pair Distribution Function

Scattering data is collected in diffraction or reciprocal space. However, the information about the position, bonding, and structure of solids that is desired is in real space. Furthermore, there is a lot of important information outside of and underneath the Bragg peaks that are collected. This information is known as diffuse scattering. The total scattering technique involves collecting both the Bragg and the diffuse scattering which can then be transformed to a real-space data set known as the pair distribution function (PDF). Where the pair distribution function represents the interatomic distances in a solid, in real space.

More specifically, total scattering data is collected with a large *Q*-range, this raw data is known as the intensity, *I*(*Q*). One can account for the background and instrumental effects in the *I*(*Q*) data to yield the total scattering structure function

S(*Q*). Recall from the section on diffraction that *Q* is a wavevector with magnitude and direction, however, for polycrystalline materials the ensemble average of the scattering direction is isotropic.[85] The total scattering structure function *S*(*Q*) can be transformed to the reduced pair distribution function, *G*(*r*):

$$G(r) = \frac{2}{\pi} \int_{Q_{min}}^{Q_{max}} Q[S(Q) - 1] \sin(Qr)\, dQ$$

where Q_{min} is the lower limit (in theory 0), and Q_{max} is the upper limit (in theory ∞) of the measured *Q*-range, and *r* is the distance in real space.[85] However, the pair distribution function, *g*(*r*), is a true atomic probability function is related to the reduced pair distribution function by:

$$G(r) = 4\pi\rho_0(g(r) - 1)$$

where ρ_0 is the number density of a material (in $Å^{-3}$).[85] An example of an archetypical cubic ABO_3 perovskite and the resulting simulated PDF and the contributing partial PDFs are shown in Figure 1.24.

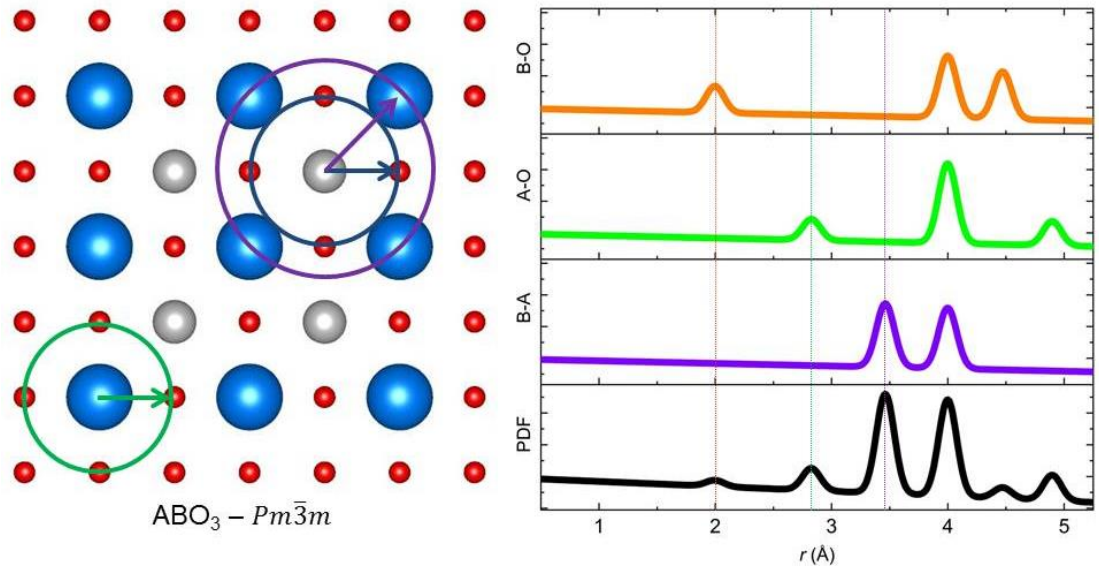

Figure 1.24. Schematic representation of interatomic distances in a solid (left), the partial PDFs from those distances (right, top three panels), and the summed PDF (right, bottom panel) for a theoretical cubic ABO_3 perovskite.

The resulting $G(r)$ or $g(r)$ will both contain peaks that correspond to the interatomic distances in the measured solid. The key difference is that the $g(r)$ is a true probability function where the integrated intensity of each peak will correspond to the number of atoms at that distance, whereas the intensity for the reduced $G(r)$ will be a relative intensity. The $G(r)$ is the most easily accessed pair distribution function as it is simply a direct Fourier transform from the $S(Q)$. Furthermore, the number density of a material is not always easily or accurately obtained. Additionally, because the $G(r)$ is calculated directly from the intensity data, any random uncertainties will be constant with r. Finally, the amplitude of the oscillations in the $G(r)$ give a direct measurement of the structural coherence in the sample, where the intensity will drop off only due to the finite Q-range measured. One issue contained within both pair distribution functions are termination ripples or low-r noise. These

ripples/noise emanate from the non-zero Q_{min} that is used in the integration. These ripples have a wavelength of approximately $\sim 2\pi/Q_{max}$.[85]

Similarly to diffraction, total scattering can be performed with X-rays and neutrons and many of the same advantages and disadvantages hold true. For high quality total scattering data two things are needed: a large *Q*-range (Q_{min} to Q_{max}), and a high flux. Experimentally the value of Q can be varied by monochromatic angle-dispersive diffraction, changing the scattering angle (θ), or by polychromatic (white) beam energy-dispersive diffraction, changing the wavelength $k(\lambda)$. Although some new lab X-ray diffractometers are capable of PDF measurements, synchrotron and neutron sources are preferred. Some requirements for high quality PDF measurements are: high energy (> ~60 keV), large *Q*-range (≥ ~20 Å), high flux (>10^{10} photons/sec), high resolution ($\Delta E/E \sim 1x10^{3}$ or better), and large solid state area detectors.

1.5.3. Structure Refinement

Once diffraction or total scattering data has been collected, the next step is to figure out what the various peaks and oscillations can tell us and we rely on structure refinements to do so. The basic idea here is that we take a model and calculate a diffraction pattern (or PDF) and compare the calculation to the observed data. Then, we tweak parameters such as the background, peak shape, lattice parameters, atomic positions, atomic displacement parameters, occupancy, among others until the calculated matches the observed in an iterative process. Refinements must be done with great care as many parameters can be correlated and can lead to local minima.[86] There are different types of refinements that are useful for different types of data or

steps in the process. This section will cover the Pawley and Rietveld methods as they apply to diffraction data, and small and large box modelling for PDF data.

For all refinement techniques there are many ways to determine the quality of a fit, however there are several statistical quantities that are the accepted standards in the crystallographic community: weighted profile *R*-factor (R_{wp}), goodness of fit (gof), and the chi-squared (χ^2).[87]

The most straightforward of these quantities to understand is the weighted profile *R*-factor (R_{wp}) which is the square root of the quantity minimized scaled by the weighted intensities:

$$R_{wp} = \sqrt{\frac{\sum_i w_i \left(y_{c,i} - y_{o,i}\right)^2}{\sum_i w_i \left(y_{o,i}\right)^2}}$$

where w is the weight, y_c is the calculated intensity, and y_o is the observed intensity at the i^{th} data point. More specifically, the weight (w):

$$w_i = \frac{1}{\sigma^2\left[y_{o,i}\right]}$$

is the inverse of the uncertainty estimate (σ) squared, of the observed intensity ($y_{o,i}$). The "best" possible R_{wp} is known as the expected *R*-factor (R_{exp}):

$$R_{exp} = \sqrt{\frac{N}{\sum_i w_i \left(y_{o,i}\right)^2}}$$

where N is the number of data points. The chi-squared (χ^2) mentioned earlier is the ratio between the weighted and expected *R*-factors:

$$\chi^2 = \left(\frac{R_{wp}}{R_{exp}}\right)^2 = \left(\frac{1}{N}\right)\frac{\sum_i w_i \left(y_{c,i} - y_{o,i}\right)^2}{\sigma^2\left[y_{o,i}\right]}$$

At the end of the day, regardless of the statistics, the most important way to analyze a fit will always be to inspect the fit visually and to determine if the model makes chemical sense.

1.5.3.1. Average Structure Refinement

To model the average structure of a material from X-ray or neutron diffraction, the Pawley and Rietveld methods are used. Both methods involve a least squares refinement of the structural model where the goal is to minimize the difference between the model-calculated pattern and the observed data.

The Pawley method is a whole pattern fitting method where only the background, lattice parameters and position of the reflections (*hkl*), and peak profile parameters are refined, however the intensity is arbitrary.[88] This method is particularly effective at yielding a superior background function and peak profile parameters and is generally recognized as the first half of any structure refinement.

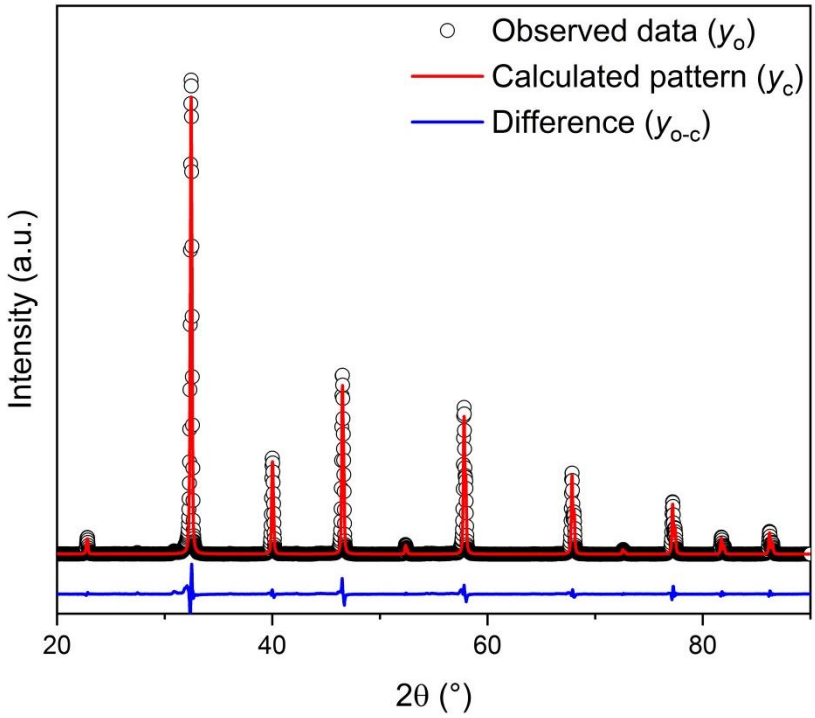

Figure 1.25. Example of a Pawley fit performed on laboratory X-ray diffraction data (Cu Kα, λ = 1.541 Å) of a polycrystalline $SrTiO_3$ sample at room temperature, revealing cubic symmetry.

Like the Pawley method, the Rietveld method parameterizes the background, lattice parameters and peak positions, profile parameters, but it also accounts for the contents of the unit cell such as the atoms, atomic coordinates, displacement parameters, occupancy, and a scale factor which account for the intensity of the peaks.[75,89] The calculated intensity (y_c) at each point (i) in a Rietveld refinement is determined by:

$$y_{c,i} = s_j \sum_k L_k |F_k|^2 \Phi(2\theta_i - 2\theta_k) P_k A + y_{B,i}$$

where s is the scale factor for the j^{th} phase, k is the Miller indices, L_k is the Lorezentian and Polarization factor, F is the structure factor, $\Phi(2\theta_i\text{-}2\theta_k)$ is the peak profile function, P_k accounts for preferred orientation, A for absorption, and y_B is the intensity calculated from the background polynomial function. For all the projects in

this work the software Topas is used to perform Pawley fittings and Rietveld refinements.[90]

An important thing to remember is that the refined model from the Rietveld method can always be improved. Around 2013 at a conference at Duquesne University, I recall Brian Toby once saying, "*A Rietveld refinement is never finished, only abandoned.*"

1.5.3.2. Local Structure Refinement

Similar to a Rietveld refinement, a model can be constructed and iteratively refined based on pair distribution function data to determine the local structure of a material. Typically there are two approaches to modeling PDF data, using a large box or a small box model.

Large box modelling or Reverse Monte Carlo (RMC) modeling involves generating a super cell of atoms and then using a fit criterion to iteratively move individual atoms. Alternatively, small box modelling is colloquially referred to as "real-space Rietveld" refinement, where a unit cell model is generated, parameterized, and iteratively refined. The parameters in a small box model include some familiar entities like scale factor, lattice parameters, atoms, atomic positions, atomic displacement parameters, occupancy, and also some PDF-specific parameters such as Q_{broad} and Q_{damp}. The large box model tends overestimate the atomic disorder in a system and the resulting model can be difficult to analyze. Whereas, the small box model can be overly constrained but is much easier to interpret. For the work presented here, small box modeling was used.

Due to complexities in PDF data, such as order-disorder behavior, it is not always appropriate to model large *r*-ranges with small box modeling but to break up the data into segments and perform many refinements at different sampling ranges. This is generally known as the "box-car" method, where fixed sampling ranges are conceived and propagated from low to high *r*-ranges. This type of sampling is important in materials where the long range (average) structure is different from the short range (local) structure. This method has been used effectively by (XXX).

1.5.4. X-ray Absorption Spectroscopy

In this work, X-ray absorption spectroscopy was also used, where, unlike diffraction, the energy of the X-rays is chosen carefully such that it has a range that is centered just above the absorption edge for a single element within the solid. This leads to an absorption event, and then a series of energy dependent oscillations. The absorption event and nearby oscillations are known as the X-ray absorption near edge structure (XANES), whereas the further out oscillations are known as the X-ray absorption fine structure (XAFS), shown in Figure 1.26.

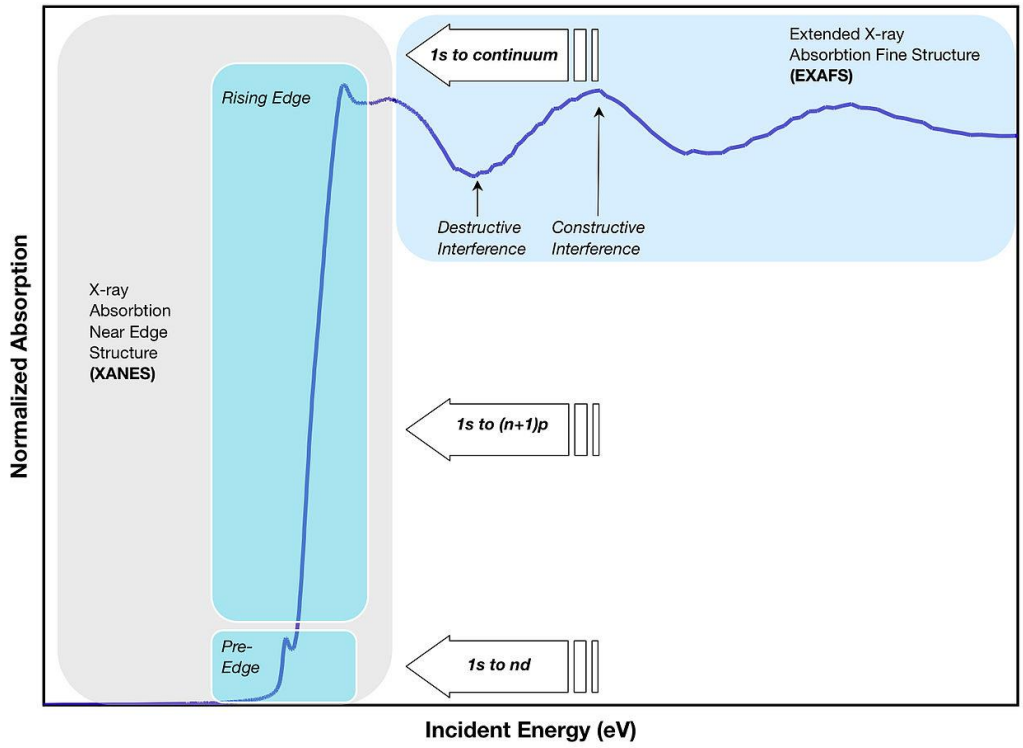

Figure 1.26. Representation of X-ray Absorption near Edge Structure (XANES) and Extended X-ray Absorption Fine Structure (EXAFS) from M. Blank, reproduced with permission under CC BY-SA 3.0.

The XAFS is a result of interference between the wavefunction of outgoing photoelectrons and photoelectrons scattered by neighboring atoms (known as backscattering). Through careful analysis, these oscillations can be used to determine the distance of neighboring atoms around the particular element to which the energy is tuned. The process of converting the scattered data to real space data is remarkably similar to that of the pair distribution function.[85]

More specifically, the X-ray absorption coefficient μ(*E*) can be expressed in terms of the momentum for the outgoing photoelectrons (*k*):

$$\mu(k) = \frac{\sqrt{m(E - E_{edge})}}{\bar{h}}$$

where m is the mass of an electron, E is the incident energy, and E_{edge} is the absorption edge energy. This is then normalized against a single atom, $\mu_0(k)$:

$$\mathrm{X}(k) = \frac{\mu(k)}{\mu_0(k)} - 1$$

Finally, the Fourier transform of this, results in a reduced pair distribution function (also $G(r)$, but adapted to $G_x(r)$ for clarity):

$$G_x(r) = \int e^{2ikr}\mathrm{X}(k)k^n dk$$

when n = 2 or 3.[85] In this way, EXAFS can be used as a complementary local structure probe for elements that are particularly difficult to resolve (due to low scattering intensity or a low molar percent). This technique will be shown in detail in Chapter 4.

1.6. Property Characterization

The other half of understanding the structure-property relationship in a material is measuring and characterizing the physical properties. In many cases, the properties are more important for applications and real world use. This section will briefly cover the various methods and techniques to characterize the physical properties of the materials studied. These properties include: density, dielectric permittivity and loss, direct and indirect piezoelectric properties, ferroelectric hysteresis, and impedance measurements.

1.6.1. Density Analysis

One of the simplest physical properties of a sample one can measure is the density. Typical lab samples are finely ground powders or ceramic pellets. The density of a powder sample is referred to as the packing fraction and is calculated by weighing the sample and determining the volume the powder occupies. Due to the large volume of void spaces in the powder, this method is prone to error and the volume is largely overestimated.

To determine the density of a ceramic pellet, the Archimedes method, also known as Hydrostatic Weighing, is employed. This method involves weighing the pellet in air (m_1), then weighing the object is submerged in a liquid (m_2). The volume of the pellet (v_{pellet}) can be determined by calculating how much liquid was displaced and accounting for the density of the liquid (ρ_{liquid}). This simple calculation is shown below.[91]

$$\rho_{pellet} = \frac{m_1}{v_{pellet}} = \frac{m_1}{(m_1 - m_2) * \rho_{liquid}}$$

1.6.2. Dielectric Permittivity and Loss

To collect dielectric measurements, a dense ceramic pellet with ≥ 85% of the theoretical crystallographic value is needed. The dense pellet must then be polished to a mirror finish on both sides. Electrodes are then applied (typically silver, gold, or platinum) to the polished sides and then heat treated. The prepared samples are then placed into a high-temperature measurement cell (typically connected to an impedance analyzer) with platinum wires attaching to the electrodes. The cell is then

placed within a protective ceramic cover and the entire setup is placed within a tube furnace. The dielectric permittivity and loss are then collected over a range of frequencies (~1 kHz to 1 MHz) upon heating and cooling. An example of dielectric data collected for this work is shown in Figure 1.27.

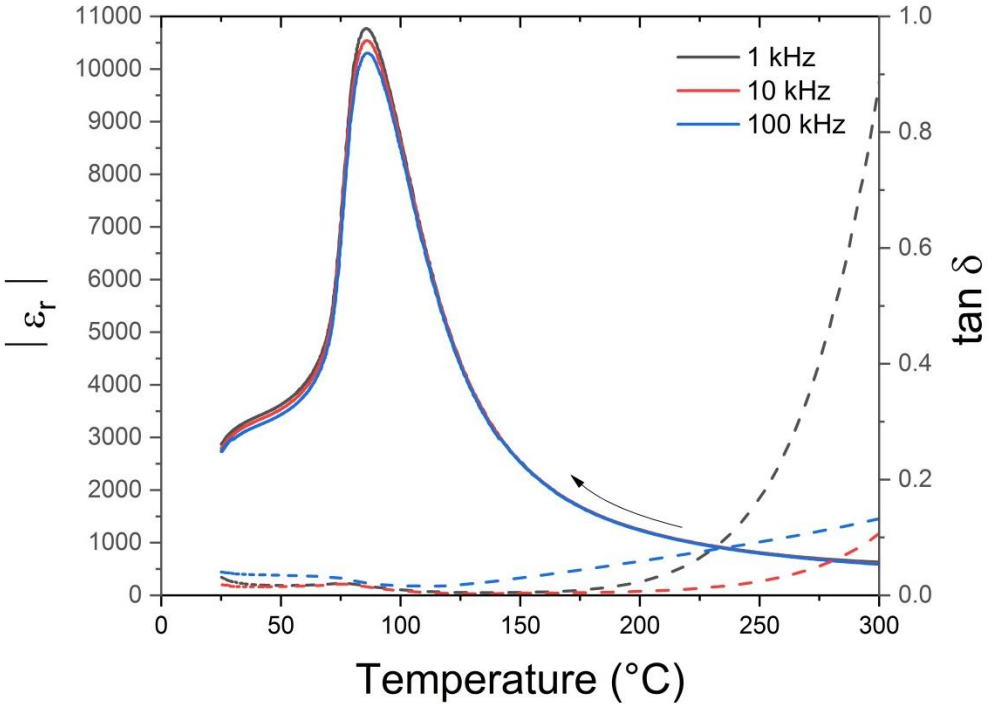

Figure 1.27. Example of dielectric permittivity (left) and loss (right) measurements for BZT-0.50BCT at 1 (black), 10 (red) and 100 (blue) kHz, tan δ shown as dotted line. Data was collected upon cooling from 300 °C to 25 °C at 3 °C/min.

1.6.3. Piezoelectric Measurements

Similar to dielectric measurements, ceramic samples must be carefully prepared to measure the direct and indirect piezoelectric effect. First, pellets must be densified, polished, and coated with electrodes.

To measure the direct piezoelectric effect, the sample is simply placed in between probes, the probes are fastened securely. The bottom probe is attached

directly to a vibrating diaphragm that vibrates resulting in the generation of a voltage (displayed on an electronic output). This type of measurement is typically performed on a Berlincourt d_{33} meter and is known as a Quasi-Static Piezoelectric (Berlincourt) Measurement.[92]

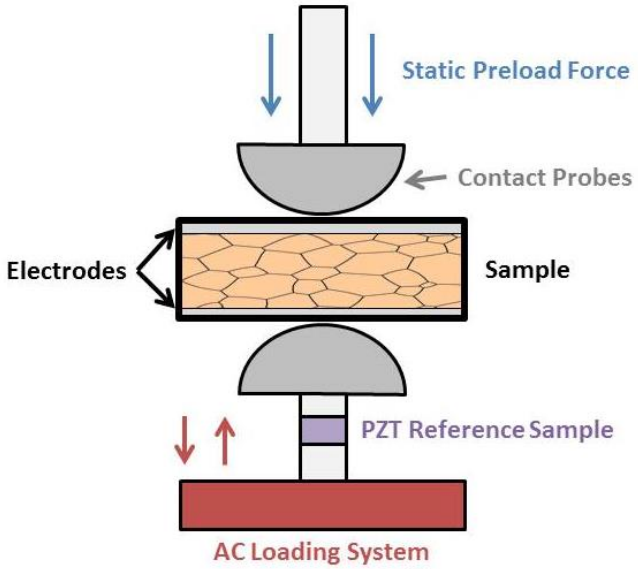

Figure 1.28. Quasi-static piezoelectric (Berlincourt) measurement setup, reproduced from Stewart et al.[92]

However, although the Berlincourt measurement is well documented and easily understood, in practice the measurements can be unreliable.[92] The accepted methodology by the community is to measure the indirect (inverse) piezoelectric effect. To do so, the prepared pellets (described above) are immersed in a non-conductive liquid and placed between two electrodes. These electrodes are connected to a high voltage (HV) supply. Furthermore, the top electrode is not secured and can be moved by the deformation of the sample. The precise position of the top electrode is monitored by an optical probe. The strain measured (as a percent) is the total displacement of the top electrode relative to the original height of the sample pellet, as a function of the applied electric field. This setup is shown in Figure 1.29.

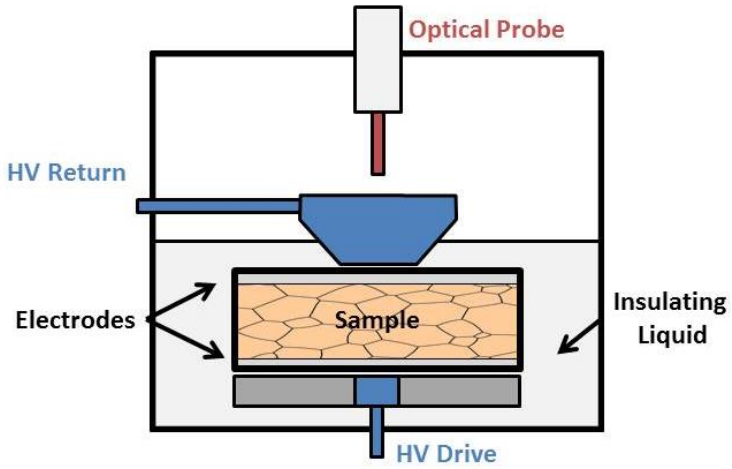

Figure 1.29. Schematic of the test setup for the measurement of the indirect (inverse) piezoelectric effect based on the Radiant Technology High Voltage Text Fixture.[93]

The advantages of this setup are that it allows for more precise measurements and more reliable data. The large field strain can be collected in both directions (bipolar) which are known as "butterfly" loops or in one direction (unipolar) as functions of the applied electric field. Examples of these loops are shown in Figure 1.30(a,b) for BZT-0.5BCT.

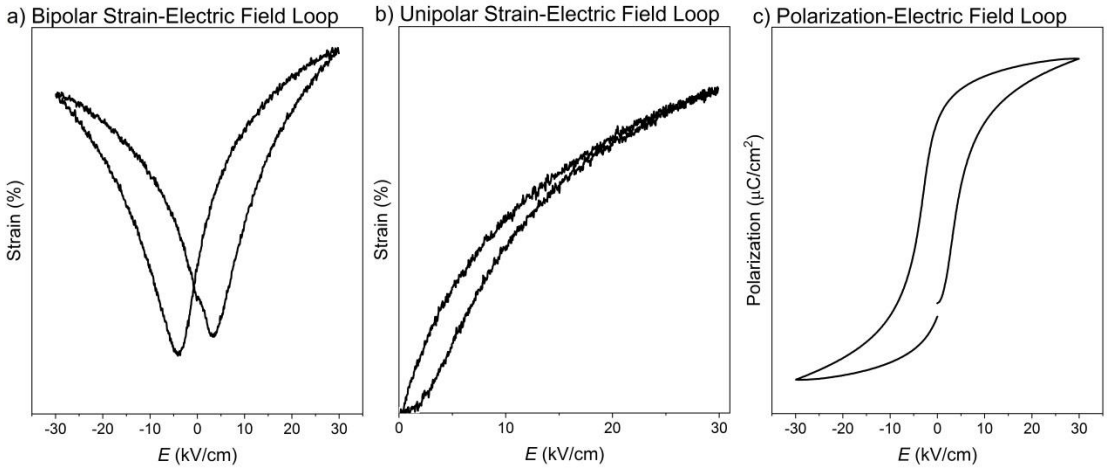

Figure 1.30. Characteristic a) bipolar S-E, b) unipolar S-E, and c) P-E loops for the disordered ferroelectric material BZT-0.5BCT at room temperature (E_{max} = 30 kV/cm).

Another advantage to the indirect piezoelectric setup is that ferroelectric hysteresis loops of polarization versus electric field (P-E) can be measured simultaneously, Figure 1.30(c).

1.6.4. Impedance Spectroscopy

Impedance spectroscopy (or electrochemical impedance spectroscopy) is a frequency dependent measurement on the electrical impedance of a sample. Impedance (*Z*), more generally, is a measure of the opposition to a current that a circuit presents when an AC voltage is applied. Impedance spectroscopy allows for the contributions to the dielectric and resistive properties of a sample to be separated and characterized independently. The dielectric constant and charge transport properties in a material are determined by many factors, such as the sample-electrode interface, and the bulk and grain boundary resistance (capacitance).[94] Impedance is defined as:

$$Z = \frac{V_o}{I_o}$$

where *V* is the voltage, and *I* is the current.[95] Due to the AC voltage, impedance has both a magnitude and a phase. Under a DC field the impedance and resistance are the same, and the impedance can be thought of as possessing a zero phase angle ($\gamma = 0°$). Impedance is also a vector quantity and can be expressed as a complex number:

$$Z^* = Z' - iZ''$$

where *Z'* is the resistive component, *Z''* is the reactive component, and *i* is the imaginary unit ($j = \sqrt{-1}$).[95] It is sometimes useful to analyze impedance data in

other terms such as the admittance (Y^*), the capacitance (C^*), or the modulus (M^*) so the relationship between these terms is summarized in Table 1-3.

Table 1-3. Complex relationships between the impedance (Z^*), admittance (Y^*), the capacitance (C^*), and the modulus (M^*) from Schmidt.[94] Where ω is the angular frequency and C_0 represents the capacitance of the cell in a vacuum ($C_0 = \varepsilon_0 A/D$) in which ε_0 is the permittivity of free space, A is the current cross section, and d is the distance.

	Z^*	Y^*	C^*	M^*
$Z^* =$	Z^*	$\frac{1}{Y^*}$	$\frac{1}{i\omega C^*}$	$\frac{M^*}{i\omega C_0}$
$Y^* =$	$\frac{1}{Z^*}$	Y^*	$i\omega C^*$	$\frac{i\omega C_0}{M^*}$
$C^* =$	$\frac{1}{i\omega Z^*}$	$\frac{Y^*}{i\omega}$	C^*	$\frac{C_0}{M^*}$
$M^* =$	$i\omega C_0 Z^*$	$\frac{i\omega C_0}{Y^*}$	$\frac{C_0}{C^*}$	M^*

In a polycrystalline ceramic, there are insulating regions and semiconducting regions. The semiconducting regions are due to chemical doping or defects, like oxygen loss. Each region can then be represented as a single parallel resistor-capacitor (RC) circuit element. The brick layer model is shown in Figure 1.31.

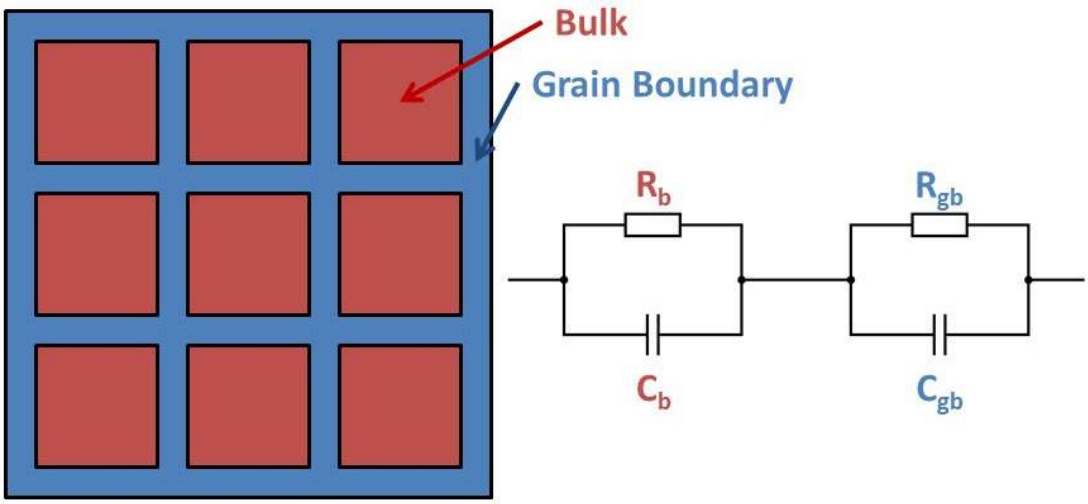

Figure 1.31. Brick layer model of a polycrystalline sample and the ideal equivalent circuit for each component.

In a polycrystalline sample, the brick layer model has three primary components: bulk (intra-granular), grain boundaries (inter-granular), and the sample-electrode interfaces. Typically the resistance and capacitance of the grain boundaries are significantly larger than the bulk ($R_{gb} >> R_b$ and $C_{gb} >> C_b$). The relaxation time (τ):

$$\tau = RC$$

where *R* is the resistivity and *C* is the capacitance, can be used to determine the species of the measured quantity (i.e. bulk versus grain boundary, etc.).

The impedance in a sample can be measured in the time- or frequency-domain, although time-domain measurements are commonly converted to frequency anyways. It is therefore practical to measure the impedance in the frequency-domain directly.[94] The impedance in a sample is typically measured over a wide frequency range ~10^{-2} to 10^{7} Hz.[96]

The common ways to visualize the measured impedance data is through impedance (*Z'* or *Z''*) versus frequency in a Bode plot and plotting the complex impedance (*Z''*) versus the real impedance (*Z'*) in a Cole-Cole plot.

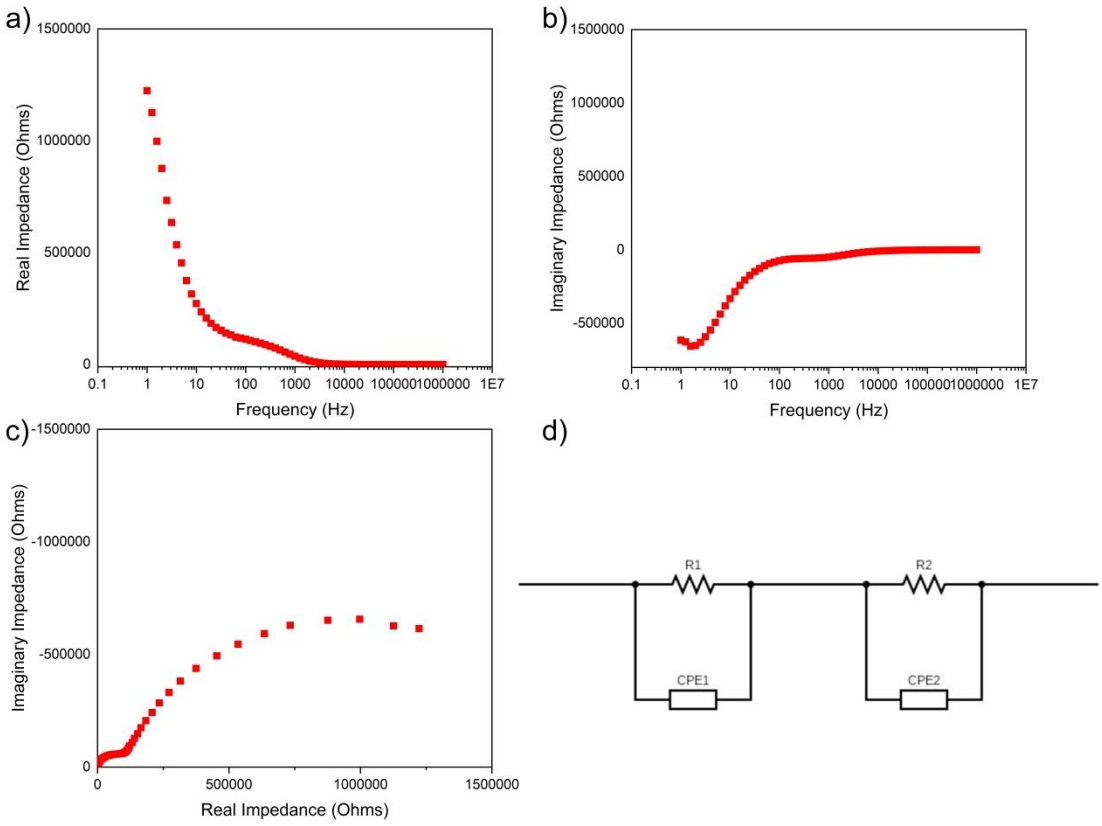

Figure 1.32. Impedance data with the a) Bode plot of the real impedance, b) Bode plot of the imaginary impedance, c) Cole-Cole plot, and d) an example of the circuits used to fit the data using constant phase elements for NBT-49 at 250 °C.

To extract the pertinent data and parameters from impedance measurements, fitting is performed by creating an equivalent circuit with resistors, capacitors, and inductors that are directly related to physical and chemical characteristics within the material. However, most real systems do not show ideal Debye behavior and therefore constant phase elements (CPE) are used to model the non-ideality.[94]

Chapter 2: Neutron Total Scattering Studies of Group II Titanates ($ATiO_3$, A^{2+} = Mg, Ca, Sr, Ba)

Charles M. Culbertson,[1,*] Alexander T. Flak,[1] Michael Yatskin,[1] Paul H.-Y. Cheong,[1] David P. Cann,[2] and Michelle R. Dolgos[3,*]

[1]*Department of Chemistry, Oregon State University, Corvallis, Oregon, 97331, USA*
[2]*Material Science, School of Mechanical, Industrial & Manufacturing Engineering, Oregon State University, Corvallis OR 97331, USA*
[3] *Department of Chemistry, University of Calgary, Calgary, Alberta, Canada T2N 1N4, Canada*

Published in Scientific Reports

C. M. Culbertson, A. T. Flak, M. Yatskin, P. H.-Y. Cheong, D. P. Cann, and M. R. Dolgos, "Neutron Total Scattering Studies of Group II Titanates ($ATiO_3$, A^{2+} = Mg, Ca, Sr, Ba)," Sci. Rep., vol. 10, no. 1, Dec. 2020, doi: 10.1038/s41598-020-60475-8.

2.1. Abstract

Neutron total scattering measurements were conducted on $MgTiO_3$, $CaTiO_3$, $SrTiO_3$, and $BaTiO_3$ to simultaneously investigate the local and average structure of these materials. The local structures of $MgTiO_3$, $CaTiO_3$, and $SrTiO_3$ were well modelled using the refined average structural models: trigonal $R\bar{3}$, orthorhombic *Pbnm*, and cubic $Pm\bar{3}m$ respectively. However the local structure for $BaTiO_3$, at both temperatures where the average structure is orthorhombic *Amm*2 (at 225 K) and tetragonal *P*4*mm* (at 290 K), was best described by the rhombohedral *R*3*m* model. Only the *R*3*m* model was able to account for the observed displacement of titanium in the [111] direction. Furthermore, box-car type refinements were conducted. These refinements show that the coherence length of the rhombohedral distortion is around 10 Å, at larger *r*-ranges the local distortions become misaligned and average out to *Amm*2 and *P*4*mm*.

2.2. Introduction

Alkaline earth metal (Group II) titanates of the form $ATiO_3$ (A^{2+} = Mg, Ca, Sr, and Ba) are both technologically important and increasingly relevant for new material applications. These compounds are generally parent structures for complex materials that are used in a variety of applications. Magnesium titanate ($MgTiO_3$) is a component in low-loss dielectric compositions for microwave applications, with a variety of uses including band-pass filters, communication antennas, direct broadcasting satellite and global positioning systems among others. Although an effective synthetic route has yet to be found for $MgTiO_3$, limiting its current

usage.[97,98] Calcium titanate ($CaTiO_3$) is used in numerous applications, such as: optics, magnetics, electronics, and superconductors.[99] Most recently $CaTiO_3$ has found renewed interest in hybrid organic-inorganic perovskites for solar cell applications.[99] Both strontium titanate ($SrTiO_3$) and barium titanate ($BaTiO_3$) are widely used in dielectric and ferroelectric applications.[100] The remaining group II elements beryllium and radium were not considered due to their toxicity and radioactivity, respectively.

Magnesium titanate crystallizes in the ilmenite structure which has the form $A^{2+}B^{4+}X_3^{2-}$. In general, the ilmenite structure is a layered derivative of the corundum structure where the cations are ordered into two nonequivalent octahedral A- and B-sites. The A and B sites are ordered along the hexagonal *c* direction in alternating layers of face shared A-X_6 and B-X_6 octahedra. The structure of $MgTiO_3$ was first found to be $R\bar{3}$ by Posnjak and Barth in 1934.[101] A more recent study using neutron diffraction was conducted by Wechsler and Von Dreele in 1989.[9] This neutron diffraction study confirmed the average structure of $MgTiO_3$ to be trigonal $R\bar{3}$ and found complete ordering of the Mg-O_6 and Ti-O_6 layers. The structure of $MgTiO_3$ is stable over a wide range of temperatures (25-1025 °C) as no phase transitions have been reported.[102]

The rest of the materials ($CaTiO_3$, $SrTiO_3$, and $BaTiO_3$) crystallize in the perovskite structure. The general perovskite structure is ABX_3, where the A-site cations surrounded by 12 anions in cubo-octahedral coordination and the B-site cations are surrounded by 6 anions in octahedral coordination. The B-O_6 octahedra form a network of corner sharing octahedra that surround the larger A-site cubo-

octahedra. In the perovskite structure the B-site cations and anions are generally similar in size, whereas the A-site cations are relatively large in comparison. The relative size of the cations and anions can be used to predict the stability and distortions within the perovskite structure according to the Goldschmidt tolerance factor (*t*):

$$t = \frac{r_{A+} r_O}{\sqrt{2}(r_{B+} r_O)}$$

where r_A is the ionic radius of the A-site cation, r_B the radius B-site cation, and r_O the radius of oxygen. The value of the tolerance factor *t* can be used to predict the structure, for $t < 0.71$ the structure is generally not a perovskite, for $t = 0.71$-0.9 orthorhombic/rhombohedral symmetry is preferred, for $t = 0.9$-1 cubic is stable, and for $t > 1$ hexagonal or tetragonal distortions are preferred.[7] It should be noted that these tolerance factor (*t*) ranges are guidelines based on observations.

Most materials with the perovskite structure are not cubic, mainly due to cation displacements and octahedral rotations. The archetypical perovskite $CaTiO_3$ is orthorhombic *Pbnm* ($t = 0.97$) from room temperature until 1375 K. At 1375 K the structure begins to undergo a phase transition to tetragonal *I*4/*mcm* and becomes single-phase tetragonal at 1425 K. The final structural transition from tetragonal to cubic $Pm\bar{3}m$ occurs at 1525 K.[103]

At low temperatures the average structure of $SrTiO_3$ is tetragonal *I*4/*mcm*, and around 100 K the structure transitions to the room temperature phase cubic $Pm\bar{3}m$ ($t = 1.00$).[12] It has been reported that a lower temperature (35-55 K) orthorhombic phase exists.[104] Although, a pair distribution function study of $SrTiO_3$ at 5 and 293 K found only cubic symmetry present for the local structure.[105]

The average structure of $BaTiO_3$ (t = 1.06) has been reported to undergo several phase transitions. Below 190 K, the structure is rhombohedral *R*3*m*. From 190 to 280 K the structure is orthorhombic *Amm*2, from 280 to 360 K the structure is tetragonal *P*4*mm*, and the structure finally becomes cubic $Pm\bar{3}m$ above 360 K.[13,106] These reported structures are all related to the undistorted cubic phase and characterized by the direction of the B-site titanium atoms (*R*3*m* – [111], *Amm*2 – [011], *P*4*mm* – [001]). In general, these materials undergo displacive phase transitions, where the structure changes as atoms move due to increased thermal energy. Another type of phase transition is an order-disorder transition, where the structure of a material changes due to a change in the degree of positional or orientational ordering/disordering.

In 1968, an order-disorder model was proposed by Comes et al. for $BaTiO_3$ based on the diffuse scattering from single crystals.[107] In this model, only the rhombohedral phase was considered ordered and the orthorhombic, tetragonal or cubic phases observed were the result of an averaging of titanium atom displacements in disordered rhombohedral directions.[107] Since then, many studies have been conducted on $BaTiO_3$ using a variety of methods and techniques to explain the complex local and average structures. The methods and summarized results of these studies are listed in Table 1. The most recent study from Senn et al.[108] describes the order-disorder behavior observed in $BaTiO_3$ as emanating from local titanium displacements along the <111> directions associated with rhombohedral *R*3*m* symmetry. At low temperatures, these rhombohedral displacements are all aligned (along the [111] direction), but as the temperature increases they become disordered

(i.e. [111] and [$\bar{1}$11]) to a vector average associated with orthorhombic *Amm*2 symmetry ([011] direction). At higher temperatures, the Ti displacements disorder along four possible directions ([111], [$\bar{1}$11], [1$\bar{1}$1] and [$\bar{1}\bar{1}$1]) to a vector average associated with tetragonal *P*4*mm* symmetry ([001] direction). The structure appears cubic *Pm*$\bar{3}$*m* at higher temperatures when the local rhombohedral displacements are completely disordered relative to one-another (eight possible displacement directions so that the net Ti displacement is localized in the center of the oxygen octahedron).

Table 2-1. Summary of literature studies on the structure of barium titanate.

Methodology	Conclusion	Date	Reference
X-ray Diffuse Scattering of Single Crystals	The rhombohedral phase is ordered, the other phases are partially ordered. The diffraction results are average structures	1968	Comes et al.[107]
Neutron Powder Diffraction	The structure was well fit with the average structure models and the anisotropic thermal parameters do not support the order-disorder model	1993	Kwei et al.[106]
Neutron Total Scattering	Local rhombohedral symmetry was found in rhombohedral and orthorhombic phases, but the average structure described the tetragonal and cubic phases well	1995	Kwei et al.[109]
Extended X-ray Absorption Fine Structure (EXAFS) and X-ray Absorption Near Edge Structure (XANES)	The local structure is rhombohedrally distorted at all temperatures, the average structures observed were explained by the disordering of domains	1998	Ravel et al.[110]

Nuclear Magnetic Resonance of Single Crystal	Satellite peaks were observed in the cubic phase that were attributed to tetragonal symmetry	2003	Zalar et al.[111]
Synchrotron Total Scattering of Nanocrystals	Tetragonal local symmetry with cubic average symmetry	2006	Petkov et al.[112]
RMC Modeling of Neutron PDF, EXAFS, and Diffuse Scattering	Tetragonal phase shows four displacements and cubic phase shows eight displacement directions for titanium atoms	2014	Levin et al.[113]
RMC Modeling of Neutron PDF	Local rhombohedral titanium distortions are correlated and lead to experimentally observed average structures	2016	Senn et al.[108]

Additionally, the local structures of nanocrystalline $Ba_xSr_{1-x}TiO_3$ (x = 1, 0.5, 0) have also been investigated by synchrotron total scattering. For nanocrystalline $SrTiO_3$ the local and average structure were found to be cubic. However for nanocrystalline $BaTiO_3$ the local structure was found to possess tetragonal distortions in the 10-15 Å regime, whereas the average structure of the nanocrystals was best described as cubic.[112]

In the present work, to provide insight into the local and average structure of these materials, neutron total scattering measurements of bulk ceramics were conducted. The advantage of collecting neutron total scattering is two-fold. Firstly, using total scattering one can study both the average and local structures of a material simultaneously. The process of simultaneous data collection is important, as a single model must be able to explain the apparent discrepancy between both coherent data sets. The second key advantage is intrinsic to neutron scattering, where neutron scattering is not dependent on the elemental number (Z) as is the case for X-ray

scattering. In particular, oxygen ions scatter neutrons strongly (oxygen coh b = 5.80 fm) and titanium ions have a negative scattering lengths (titanium coh b = -3.438 fm) which provide better signal and contrast respectively for accurate refinements.[114] The advantages of neutron total scattering can be seen in the work of Page et al[115] who employed the technique on niobium doped $SrTiO_3$ ($SrTi_{0.875}Nb_{0.125}O_3$) and $BaTiO_3$ ($BaTi_{0.875}Nb_{0.125}O_3$). At room temperature the local structure of niobium doped $SrTiO_3$ remains cubic like the parent structure of $SrTiO_3$. For niobium doped $BaTiO_3$, the local structure appears to possess rhombohedral symmetry.[115]

The purpose of this work is to provide the community with structural refinements on high resolution neutron total scattering measurements to clearly define both the local and average structure of the accessible group II titanates. In particular, the focus of this work is to present the refined structures of $MgTiO_3$, $CaTiO_3$, and $SrTiO_3$, to serve as a reference point to understand the structural details in $BaTiO_3$. Furthermore, this work seeks to provide a summarization of the literature studies on $BaTiO_3$ to contextualize these nuances. To accomplish these goals, phase pure samples were synthesized, and neutron total scattering data were collected at both 225 and 290 K (particularly to show the phase sequence of $BaTiO_3$) for all compositions.

2.3. Results

2.3.1. Magnesium Titanate

As discussed in the introduction, $MgTiO_3$ crystallizes in the ilmenite structure with trigonal $R\bar{3}$ symmetry at room temperature. In the ilmenite structure both magnesium and titanium are in 6-coordinate octahedral oxygen environments. [9]

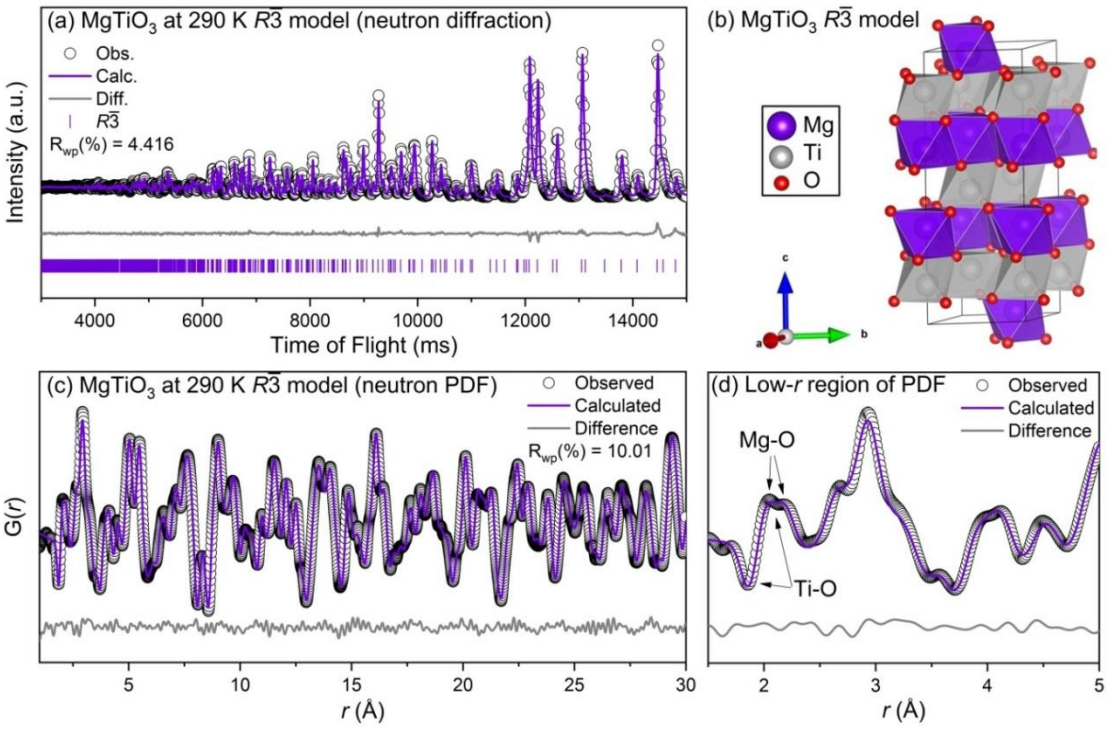

Figure 2.1. (a) Rietveld refinement of neutron diffraction, (b) refined model, (c) small-box modeling of neutron PDF, and (d) zoom-in of neutron PDF for MgTiO3 at 290 K with the R$\bar{3}$ space group. Data (identified by black circles) and refined models (continuous lines) are shown, along with the difference pattern and hkl indices below (diffraction data only).

From the initial X-ray diffractograms there was a minor $MgTi_2O_5$ phase observed in the $MgTiO_3$ sample. However this phase was not observed in the neutron total scattering data. The results of the diffraction and PDF refinements of $MgTiO_3$ at 290 K with the $R\bar{3}$ space group in the equivalent hexagonal setting ($a = b$, $\alpha = \beta = 90°$, $\gamma = 120°$) are shown in Figure 2.1. The tabulated results for the refinement at 290 K and the complete results for the refinement at 225 K are included in the supplemental information. The diffraction refinement converged on a fit criterion, $R_{wp} = 4.146$ %, with all reflections well modelled. The crystal structure of the refined structure is shown in Figure 2.1(b), with magnesium shown as purple, titanium as grey, and oxygen as red spheres. The neutron PDF, shown in Figure 2.1(c), was also

well fit with the $R\bar{3}$ space group, R_{wp} = 10.012 %. The titanium- and magnesium-oxygen bonds for the first coordination sphere are labelled in the low-*r* region of the PDF (Figure 2.1(d)). Both titanium and magnesium are displaced in their respective oxygen octahedral, resulting in three short bonds at 1.8656 Å for titanium and at 2.0497 Å for magnesium and three long bonds at 2.0940 Å for titanium and 2.1660 Å for magnesium. Although there are A- and B-site displacements in the $MgTiO_3$ structure, the $R\bar{3}$ space group is centrosymmetric and thus not a ferroelectric phase.

The negative scattering length of titanium mentioned previously manifests in negative peaks (or wells) for titanium correlations in the PDF. The diffraction and PDF refinements were conducted independently, but converged on the same model with slight discrepancies. Overall, both the long range average and short range local structure refinements clearly support literature reports describing the ilmenite structure for $MgTiO_3$ at these temperatures.[9]

2.3.2. Calcium Titanate

At room temperature $CaTiO_3$ crystallizes in the perovskite structure with *Pbnm* (or the equivalent *Pnma* and *Pcmn*) symmetry.[10] As discussed in the introduction, the perovskite structure is a network of corner shared B-site octahedra titanium atoms surrounding the 12-coordinate cubo-octahedral A-site calcium ions.

The results of the neutron diffraction, R_{wp} = 3.11 %, and neutron pair distribution function data, R_{wp} = 8.05 %, for $CaTiO_3$ at 290 K are shown in Figure 2.2(a,b) and Figure 2.2(c,d) respectively. The refinements for $CaTiO_3$ at 225 K are included in the supplementary information. Both independent refinements at 290 K

converged on the same *Pbnm* model where a = 5.38, b = 5.44, and c = 7.64 Å. Titanium is displaced towards an edge of the Ti-O_6 octahedra, yielding two bonds at 1.9514, two at 1.9530, and two at 1.9643 Å. The calcium-oxygen cubo-octahedra is more complex in the refined model, with 8 unique bond distances ranging from 2.3379 to 3.2311 Å. The major peaks that result from these bonds are labelled in the low-r region of the PDF (Figure 2.2(d)). Similarly to the results for $MgTiO_3$, the average and local structure of $CaTiO_3$ are well described at 290 K with the *Pbnm* space group as has been reported in the literature.[10] The *Pbnm* space group is centrosymmetric and thus $CaTiO_3$ does not display ferroelectric properties.

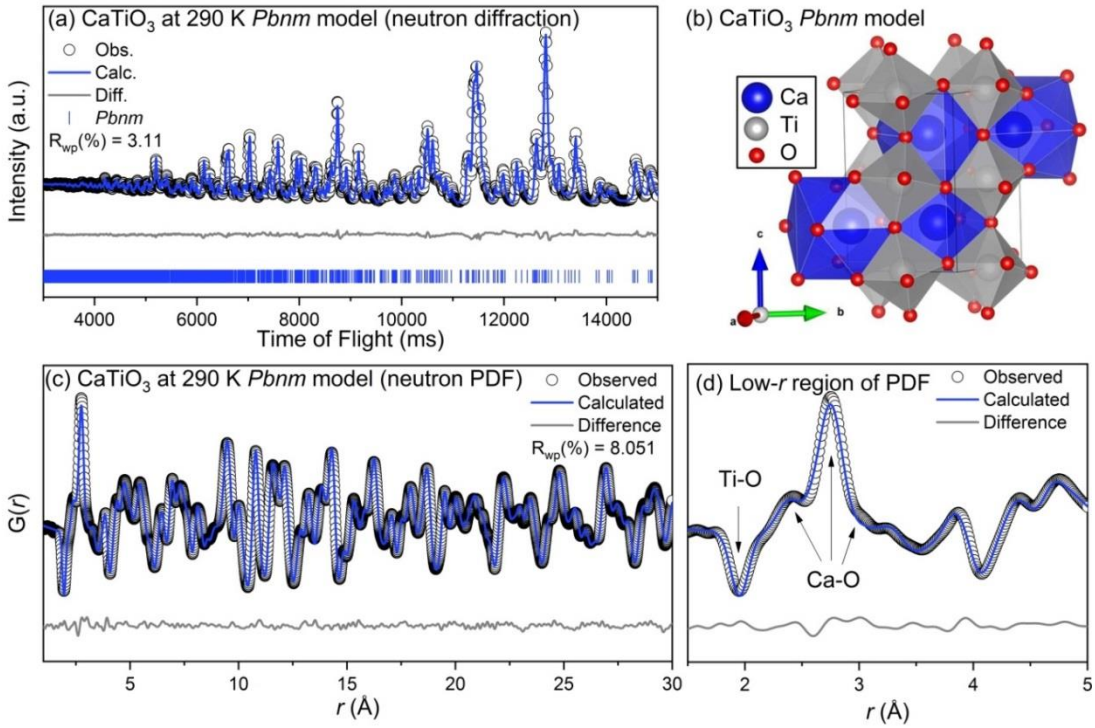

Figure 2.2. (a) Rietveld refinement of neutron diffraction, (b) refined model, (c) small-box modeling of neutron PDF, and (d) zoom-in of neutron PDF for $CaTiO_3$ at 290 K with the *Pbnm* space group. Data (black circle's) and refined models (continuous lines) are shown, along with the difference pattern and hkl markers below (diffraction data only).

2.3.3. Strontium Titanate

Across a large temperature regime $SrTiO_3$ crystallizes in the perovskite structure with cubic $Pm\bar{3}m$ symmetry.[104]

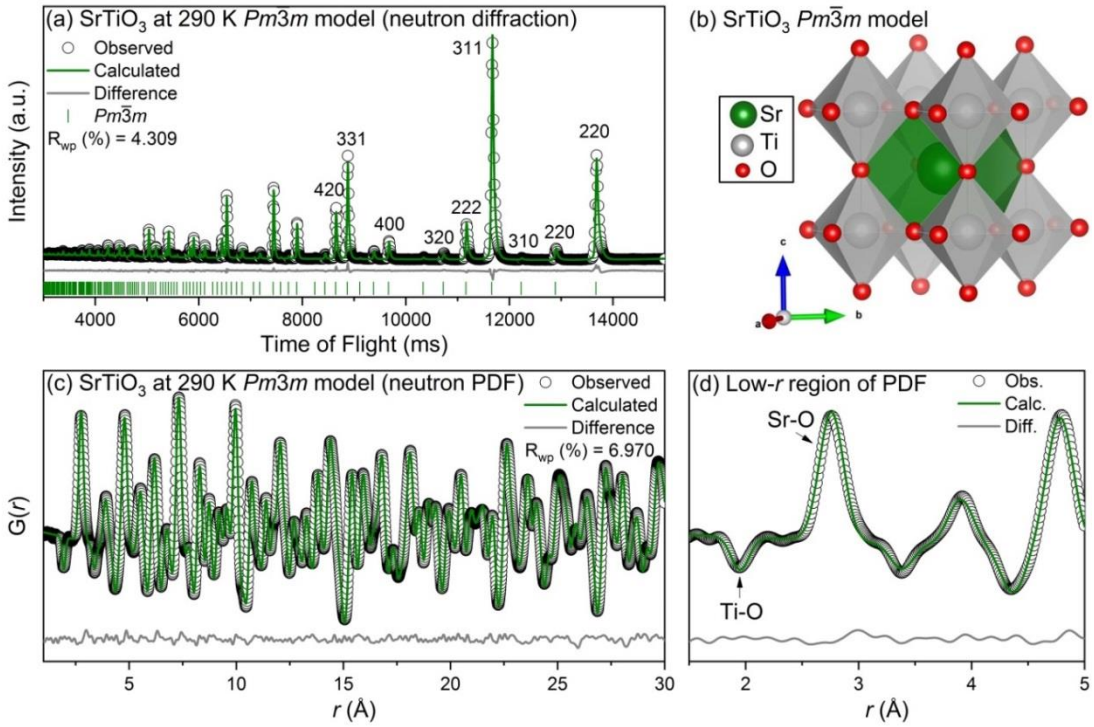

Figure 2.3. (a) Rietveld refinement of neutron diffraction, (b) refined model, (c) small-box modeling of neutron PDF, and (d) zoom-in of neutron PDF for $SrTiO_3$ at 290 K with the $Pm\bar{3}m$ space group. Data (black circles) and refined models (continuous lines) are shown, along with the difference pattern and hkl markers below (diffraction data only).

At 290 K the diffraction, R_{wp} = 4.309 %, and PDF, R_{wp} = 6.970 %, refinements results are shown in Figure 2.3(a,b) and Figure 2.3(c,d) respectively. The results of the refinement at 225 K are similar to those at 290 K and are included in the supplementary information. Due to the cubic symmetry of $SrTiO_3$, the diffraction data shows only a few sharp peaks of which the 420 through 220 reflections are labelled. All of the observed reflections were well fit by the model, with no additional reflections observed. There was some observed peak asymmetry which is

characteristic of the NOMAD beamline and spallation sources more generally. Similarly, all of the peaks in the PDF data (Figure 2.3(c) and (d)) were well modelled. The titanium-oxygen and strontium-oxygen bonds are labelled in Figure 2.3(d). The width of the single Ti-O peak is a result of the thermal disorder present even though all six Ti-O bonds are equivalent with a bond distance of 1.9534 Å. Similarly, strontium is positioned at the center of the Sr-O_{12} cubo-octahedra, with twelve Sr-O bonds at 2.7625 Å. The refined models for the average and local structure of $SrTiO_3$ are consistent with what has been reported in the literature.[104]

2.3.4. Barium Titanate

The structure of $BaTiO_3$ is much more complicated than the other titanates in its group, although it still crystallizes in the perovskite structure. The reported phase sequence for $BaTiO_3$, from low to high temperature, is *R*3*m* to *Amm*2 to *P*4*mm* to $Pm\bar{3}m$. In this study data was collected at 225 K in the orthorhombic *Amm*2 region, and at 290 K in the tetragonal *P*4*mm* region.[106]

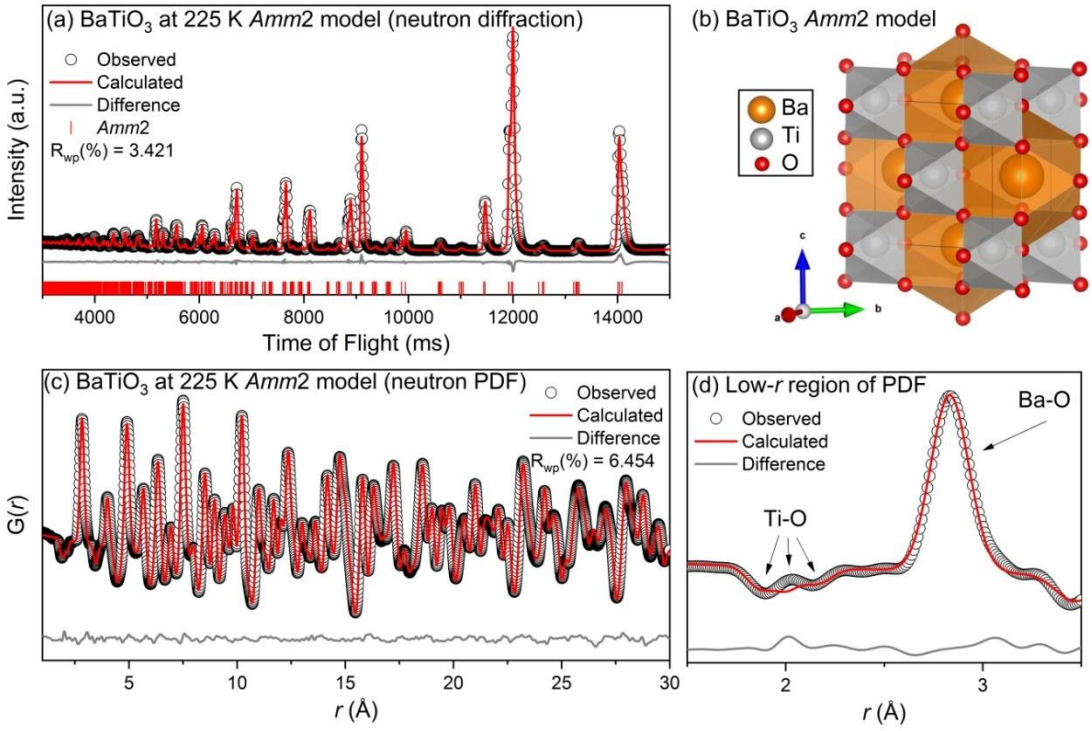

Figure 2.4. (a) Rietveld refinement of neutron diffraction, (b) refined model, (c) small-box modeling of neutron PDF, and (d) zoom-in of neutron PDF for $BaTiO_3$ at 225 K with the *Amm2* space group. Data (black circles) and refined models (continuous lines) are shown, along with the difference pattern and hkl markers below (diffraction data only).

The results of the refinements for $BaTiO_3$ at 225 K are shown in Figure 2.4. For the Rietveld refinement, as expected, the *Amm2* model fit all of the observed reflections well, with R_{wp} = 3.421 %. At first glance the PDF refinement seems equally successful, R_{wp} = 6.454 %, however upon closer inspection it becomes clear that the *Amm*2 space group does not adequately model the first two Ti-O bonds at ~2 Å (Figure 2.4(d)). The orthorhombic *Amm2* symmetry, which corresponds to a titanium displacement in the [011] direction, would result in a broad set of three shallow peaks in the PDF data for the Ti-O correlations (2 short bonds, 2 medium bonds, and 2 longer bonds) – which is not observed in the experimental data. In the data there are two equivalent negative peaks at ~1.9 and ~2.1 Å.

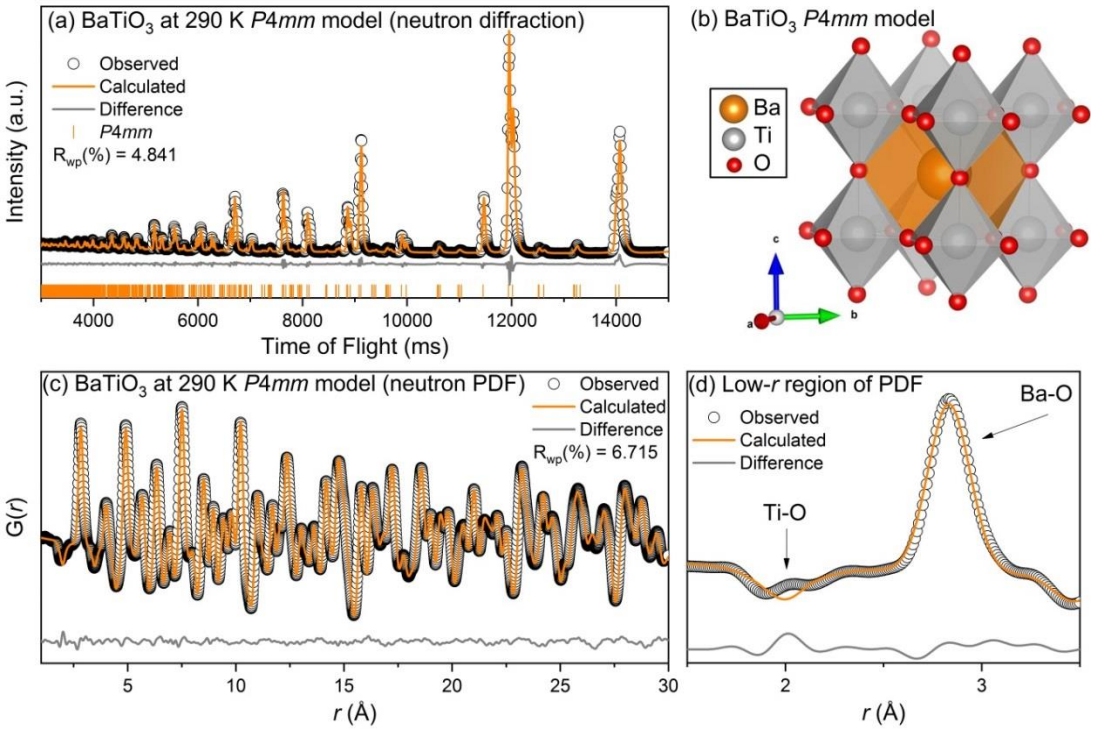

Figure 2.5. (a) Rietveld refinement of neutron diffraction, (b) refined model, (c) small-box modeling of neutron PDF, and (d) zoom-in of neutron PDF for $BaTiO_3$ at 290 K with the *P*4*mm* space group. Data (black circles) and refined models (continuous lines) are shown, along with the difference pattern and *hkl* markers below (diffraction data only).

Similarly, the results for the refinements of $BaTiO_3$ at 290 K in the tetragonal *P*4*mm* space group are shown in Figure 2.5. The refinement of the diffraction data, Figure 2.5(a), yielded a good fit where all of the observed reflections were modeled. The diffraction data showed peak splitting in the (220), (310), (311), (400), and (420) pseudocubic reflections, which are indicative of a tetragonal distortion in the [001] direction. As was the case with the refinement at 225 K, the *P*4*mm* model at 290 K does not adequately model the two Ti-O peaks in the PDF data. A [001] tetragonal titanium distortion would result in three Ti-O peaks (1 short bond, 4 medium bonds, 1 long bond), which was not observed.

To account for the two Ti-O peaks around 1.9 and 2.1 Å that were poorly fit by both the *Amm2* space group at 225 K and *P*4*mm* space group at 290 K, further refinements were conducted using each of the reported space groups for $BaTiO_3$ (*R*3*m*, *Amm2*, *P*4*mm*, *Pm*$\bar{3}$*m*). The first two Ti-O correlations could only be modelled with the *R*3*m* space group. The results of the low-*r* region refinement at 290 K are shown in Figure 2.6(a). The refinement at 225 K yielded an analogous fit and the tabulated results at both 225 K and 290 K are presented in the supplementary information. The bond structure and theoretical neutron PDFs of the reported average structures of $BaTiO_3$ are shown in Figure 2.6(b). The double peaks observed are characteristic of a rhombohedral distortion in the [111] direction, as the titanium atoms are displaced toward the face of the Ti-O_6 octahedra. The face-displaced titanium octahedra results in 3 short bonds (~1.9 Å) and 3 longer bonds (~2.1 Å).

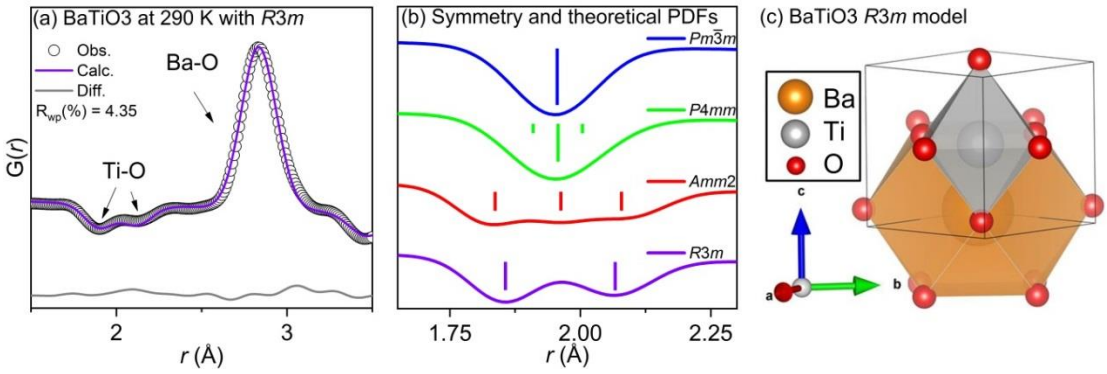

Figure 2.6. Small-box modeling of local structure (a) for $BaTiO_3$ at 290 K using the *R*3*m* space group. Data (black circles) and refined model (continuous line) are shown with the difference pattern below. Correlation labels are provided for clarity within 1 unit cell. Calculated PDF (b) for *Pm*$\bar{3}$*m*, *P*4*mm*, *Amm*2, and *R*3*m* models with bond distances shown as tick lines. (c) Refined local structure R3m model.

In the literature, there are two distinct methods that have been used to model local deviations from an average structure with small box models. The first method, henceforth referred to as the variable range refinement method, involves including an

adjustable range of data (*x*-range) for each refinement from a fixed starting point (typically ~1 Å). For example, Smith et al. investigated $BaTiO_3$ nanoparticles and refined the PDF data set from 1 to 28 Å, with varying refinement lengths (ranging from 1-8, 1-12, 1-16… 1-28 Å, etc.).[116] The second method, known as the box-car method, involves taking fixed-length boxes and performing sequential refinements from low to high *r*-ranges. For example, in the study of $BaTiO_3$-$Bi(Zn_{1/2}Ti_{1/2})O_3$ by Usher et al., a fixed refinement range of 10 Å was used to refine the structure from 1 to 80 Å (over proscribed ranges of 1-10, 5-15, … 70-80 Å, etc.).[117] Both methods were utilized in this study to provide a more complete analysis.

The results of the variable range refinements and box-car refinements are shown in Figure 2.7 and Figure 2.8 for $BaTiO_3$ at 225 and 290 K, respectively. The calculated fit criterion (R_{wp}) values for each refinement are plotted as a function of the refinement range for the variable range refinement and as a function of the larger edge of the box for the box-car method. For each method insets are provided to show an example of a characteristic refinement.

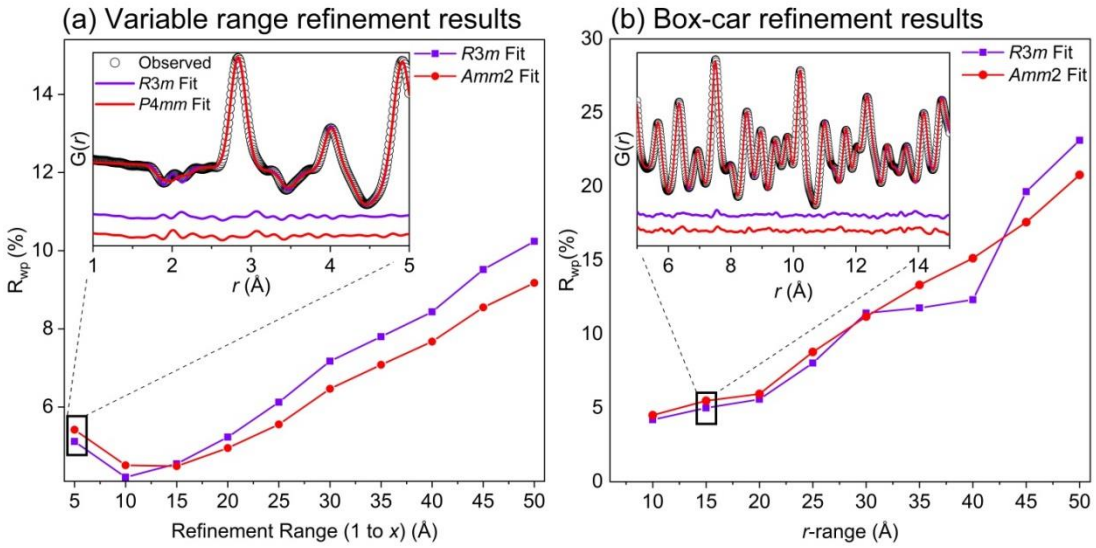

Figure 2.7. Results (R_{wp}) of the small-box analysis using the (a) variable range refinement method (refinement range shown as x-axis, i.e. x = 5 corresponds to 1-5 refinement, x = 10 to 1-10, … x = 50 to 1-50 Å, etc.) and (b) box-car refinement method (r-range shown on the x-axis corresponds to the high-r edge of box, i.e. x = 10 corresponds to the 0-10 Å box, x = 15 to the 5-15 Å box, …, x = 50, the 40-50 Å box, etc.) for neutron PDF data of $BaTiO_3$ at 225 K using the *R*3*m* (violet squares) and *Amm*2 (red circles) space groups. The insets for each method show an example of one refinement distance or box.

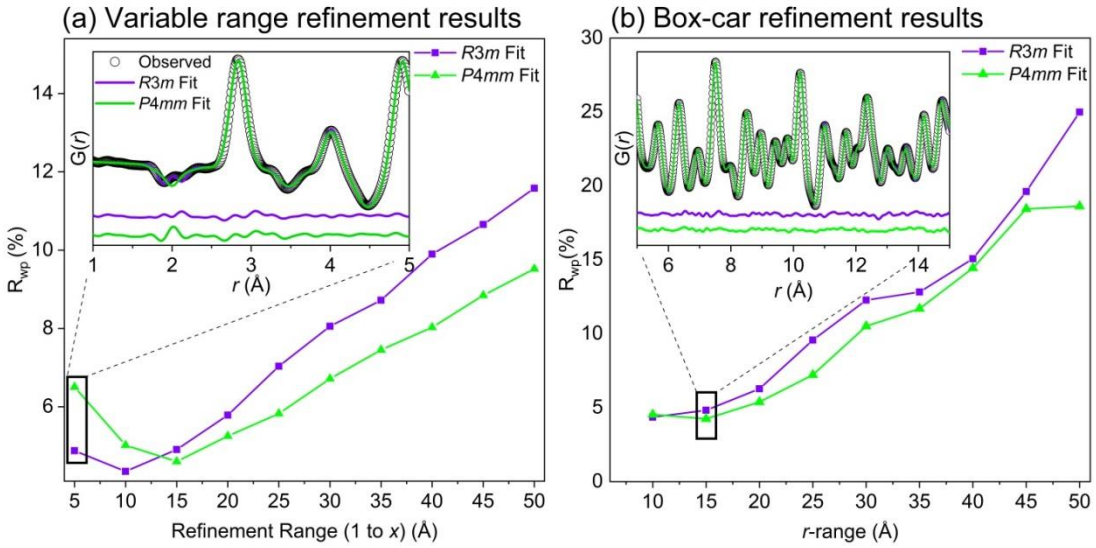

Figure 2.8. Results (R_{wp}) of the small-box analysis using the (a) variable range refinement method and (b) box-car refinement method for neutron PDF data of $BaTiO_3$ at 290 K using the *R*3*m* (violet squares) and *P*4*mm* (green triangles) space groups. The insets for each method show an example of one refinement distance or box.

From the variable range refinement method, at both temperatures the *R*3*m* fit yields the lowest R_{wp} for the 1-5 Å and 1-10 Å refinements where the local Ti-O distortions dominate the fit quality. At larger length scales the *Amm*2 (for 225 K) and *P*4*mm* (for 290 K) average structures yield the best fits for as the penalty from the poorly fit local Ti-O peaks are overcome by a better overall fit to the high-*r* data. The comparatively larger R_{wp} values in the first box from 1 to 5 Å for each data set are due to the larger influence of low-*r* noise on the refinement.

The box-car method refinements results can be used to determine the coherence length of the rhombohedral distortions. For the box-car refinements at 225 K the rhombohedral *R*3*m* space group fits the data better than the *Amm*2 space group until the 15-25 Å box. At higher *r*-ranges the refinement results are less clear, initially the *Amm*2 yields a lower R_{wp} for the 20-30 Å refinement, then the *R*3*m* fit 25-35 and 30-40 Å boxes, then the *Amm*2 at 35-45 and 40-50 Å. The box-car method refinements at 290 K are more clear and the coherence length of the local rhombohedral distortions can be estimated to be around ~10 Å. At larger distances, the distortions are misaligned relative to one another resulting in the *P*4*mm* average structure yielding the superior fit. This observed phenomenon is formalized as the order-disorder model for $BaTiO_3$. An example of the order-disorder model is well visualized in Figure 3 within the work by Senn et al.[108]

2.4. Discussion

For $MgTiO_3$, $CaTiO_3$, and $SrTiO_3$ the refinements average and local structures were internally consistent at each temperature. However the average structures for

$BaTiO_3$ (*Amm*2 at 225 and *P*4*mm* at 290 K) show distinct features with a different symmetry than the symmetry observed at the local structure. There are clear rhombohedral distortions present in the PDF data at both temperatures which are consistent with the order-disorder model for $BaTiO_3$. The local titanium octahedra distortions are only observed in the first Ti-O correlations around 2 Å. Furthermore, these distortions average out above 10 Å in the PDF data and are not observable in the neutron diffraction data.

The contrast in local structure versus long range average structure observed in $BaTiO_3$ has profound impacts on the physical properties of the material. The other compounds in this study, $MgTiO_3$, $CaTiO_3$, $SrTiO_3$, show a clear correlation between the local and average structure and all exhibit a linear dielectric response. In contrast, in $BaTiO_3$ the unique structural features detailed in this work are linked to its strong non-linear characteristics which are observed in physical phenomena in which there is a correlation between the local structure and the long-range structure. One example includes the occurrence of ferroelectricity in $BaTiO_3$, in which the local dipole moments interact to form a spontaneous polarization. Another consequence of the variable local structural distortions in $BaTiO_3$ is the resultant flat potential energy landscape that leads to the high polarizability and ease of switching of the Ti^{4+} ion.[118] Macroscopically, this is observed in $BaTiO_3$ ceramics as large relative permittivities, large polarizations, and large field induced electromechanical strains. This is also clearly relevant to other systems where these contrasting structural length scales influence the material response such as in relaxor ferroelectrics.[119] Thus, materials

systems in which there is a disconnect between the long-range average structure and local structural arrangements are of both scientific and technological interest.

In this work, we present the average and local structure of group II titanates, $ATiO_3$ (A^{2+} = Mg, Ca, Sr, Ba). For all materials except $BaTiO_3$, there are no observed differences between the local and average structures. It was shown that $MgTiO_3$ crystallizes into the ilmenite structure with trigonal $R\bar{3}$ symmetry. Both $CaTiO_3$ and $SrTiO_3$ crystallize in the perovskite structure with orthorhombic *Pbnm* and cubic $Pm\bar{3}m$ symmetry, respectively. The average structure of $BaTiO_3$ at 225 K is orthorhombic *Amm*2 and tetragonal *P*4*mm* at 290 K. However, the local structure at both temperatures is best described with small box modeling as rhombohedral *R*3*m* when the refinements were confined to data below ~10 Å, showing that the coherence length of the distortions is limited to only one to two unit cells in the structure. At larger length scales, the PDF data statistically fits the average structural model better, as the vector sum of the local titanium displacement appears to be in the [011] direction at 225 K and the [001] direction at 290 K corresponding to the orthorhombic *Amm*2 and tetragonal *P*4*mm* average structures, respectively.

2.5. Methods

Polycrystalline samples of $MgTiO_3$, $CaTiO_3$, $SrTiO_3$, and $BaTiO_3$ were prepared via standard solid-state synthesis. For each compound, stoichiometric amounts of the component oxide and carbonate reagents were mixed. The reagents MgO (Alfa Aesar 99.95%), $CaCO_3$ (Alfa Aesar 99.997%), $SrCO_3$ (Alfa Aesar 99.994%), $BaCO_3$ (Strem Chemicals Inc. 99.9%), and TiO_2 (Sigma Aldrich 99.997%) were used. The carbonate

powders ($CaCO_3$, $SrCO_3$, and $BaCO_3$) were heated at 110 °C for 24 h before being weighed. After the initial mixing of powder reagents the mixtures were ground well with a mortar and pestle. The homogenized samples were then ball milled for 4 h in a planetary micromill (Pullverisette 7 Classic Line, Fritsch). For the milling process, each sample mixture was placed in a sealed container with 20 mL of ethanol and eight 10 mm yttria-stabilized zirconia (YSZ) balls. The milled solutions were dried in air at room temperature. Then the dried powders were calcined in alumina crucibles at 800 °C for 24 h, 900 °C for 6 h, 700 °C for 4 h, and 1100 °C for 4 h for $MgTiO_3$, $CaTiO_3$, $SrTiO_3$, and $BaTiO_3$ respectively, with a 4 h step at 450 °C (to allow for degassing of carbonates). The calcined powders were ground well and pressed, uniaxially in a 10-mm die (Carver Inc.) at 2 tons for 2 mins, into pellets. The sample pellets were placed in closed alumina crucibles and sintered at 1200 °C for 12 h, 1350 °C for 12 h, 1100 °C for 12 h, and 1250 °C for 6 h for $MgTiO_3$, $CaTiO_3$, $SrTiO_3$, and $BaTiO_3$ respectively. A heating and cooling rate of 5 °C/min was used for the calcination and sintering steps for all samples. The sintered pellets were ground well and loaded into X-ray diffraction sample holders. X-ray diffraction data was collected using a benchtop X-ray diffractometer (Miniflex 600, Rigaku) to determine the phase purity.

To collect neutron total scattering measurements, samples were loaded in 2 mm diameter quartz capillaries (Hampton) and sent to the Nanoscale Ordered Materials Diffractometer (NOMAD)[120] beam-line at the Spallation Neutron Source (SNS)[121] at Oak Ridge National Labs (ORNL). Data were collected for each sample

at 225 and 290 K with a collection time of 30 mins and a heating ramp rate of 60 K/min.

To determine the average structure, Pawley fitting[88] was performed on the collected neutron total scattering data using the Topas Academic (Version 6) software package.[90,122] The starting models for each refinement were taken from the literature.[9,10,104,123] For each Pawley fit the background terms, unit cell parameters, and peak profiles were refined. The background for each refinement was modelled with a 10 term polynomial. The results of the Pawley fits were used as starting models for Rietveld analysis[75,89] (also performed with Topas) where the scale factor, atomic positions and atomic displacement parameters were refined.

To investigate the local structure of these materials the total scattering data were transformed to the pair distribution function (PDF), $G(r)$, via a sine Fourier transform.[85] This transformation was performed with in-house software at ORNL with Q_{min} of 0.50 $Å^{-1}$ and Q_{max} of 30.00 $Å^{-1}$. Again Topas (Version 6) was used to perform small-box modeling using the refined average structure as starting models. The scale, lattice parameters, atomic displacement parameters, and atomic positions were refined. The delta2, Q_{damp}, and Q_{broad} parameters were refined from both a nickel and a silicon standard.

2.6. Author Contributions

C. M. C. initiated the project and synthesized the materials with A. T. F. The material samples were sent to ORNL for neutron total scattering measurements. C. M. C. and

M. Y. analyzed and processed the total scattering data. M. R. D., D. P. C. and P. H.-Y. C. supervised the project. All authors contributed to the writing of the manuscript.

Chapter 3: Total scattering and diffraction studies of lead-free piezoelectric (1-*x*)$Ba(Zr_{0.2}Ti_{0.8})O_3$-*x*$(Ba_{0.7}Ca_{0.3})TiO_3$ deconvolute intrinsic and extrinsic contributions to electromechanical strain

Alicia Manjón-Sanz[1,2] and Charles M. Culbertson,[1] Dong Hou,[3,4] Jacob L. Jones,[4] and Michelle R. Dolgos[1,5]

[1] *Department of Chemistry, Oregon State University, Corvallis, Oregon, 97331, USA*
[2] *CELLS-ALBA Synchrotron Light Facility, Cerdanyola del Valles, 08290 Barcelona, Spain*
[3] *Department of Materials Science and Engineering, Faculty of Natural Sciences, Norwegian University of Science and Technology, 7491 Trondheim, Norway*
[4] *Department of Materials Science and Engineering, North Carolina State University, Raleigh, North Carolina, 27695, USA*
[5] *Department of Chemistry, University of Calgary, Calgary, Alberta, Canada T2N 1N4, Canada*

Published in Acta Materialia

A. Manjón-Sanz and C. M. Culbertson, D. Hou, J. L. Jones,, and M. R. Dolgos, "Total Scattering and diffraction studies of lead-free piezoelectric (1-x)$Ba(Zr_{0.2}Ti_{0.8})O_3$-x$(Ba_{0.7}Ca_{0.3})TiO_3$ deconvolute intrinsic and extrinsic contributions to electromechanical strain" Acta Materialia., no. 171, 2019, doi: 10.1016/j.actamat.2019.04.005

3.1. Abstract

The piezoelectric material (1-*x*)Ba($Zr_{0.2}Ti_{0.8}$)O_3-*x*($Ba_{0.7}Ca_{0.3}$)TiO_3 (BZT-*x*BCT) has emerged as a leading lead-free candidate to replace Pb($Zr_{1-x}Ti_x$)O_3 (PZT) for certain applications. However, the structural response of BZT-*x*BCT to an electric field is not well understood, particularly how the local structure responds to varying electric fields. In this study, *in situ* synchrotron X-ray diffraction and total scattering measurements were performed on BZT-*x*BCT from x = 0.45 to 0.60. The lattice distortions were quantified from the unit cell parameters for the compositions in the orthorhombic (O) region (x = 0.45 to 0.50) and tetragonal (T) region (x = 0.51 to 0.60). It was found that the lattice distortion is minimized in compositions that exhibit the largest effective piezoelectric effect, particularly at the x = 0.45 composition (between the rhombohedral (R) and O regions) and at the morphotropic phase boundary (MPB) composition x = 0.50 (between O and T regions). The degree of domain wall motion was quantified, and the results indicate that as the MPB is approached, the degree of domain wall motion increases dramatically. The increase in domain wall motion also coincides with the minimization of the lattice distortion. The pair distribution functions (PDFs) were calculated from the Fourier transform of the total scattering data. Analysis of the PDF peak shifts with electric field shows nonlinear lattice strains across all compositions, which indicates a deviation from classical piezoelectric behavior. We conclude that the strong piezoelectric properties in the BZT-*x*BCT system are attributed to an increased degree of domain wall reorientation that is facilitated by a decreased lattice distortion.

3.2. Introduction

Piezoelectric materials convert electrical energy to mechanical energy and vice versa and are used in a variety of applications, namely as actuators and sensors. The industry standard is $Pb(Zr_{1-x}Ti_x)O_3$ (PZT) which displays a high piezoelectric coefficient (d_{33}) with value of 200-600 pC/N at the x = 0.48 composition[43]. This enhanced piezoelectric response occurs at the morphotropic phase boundary (MPB) over a narrow compositional range. The compositions on each side of the MPB have polar crystal structures with different polarization directions, resulting in a compositionally-driven polarization rotation at the phase boundary. Although PZT is a versatile material with tunable properties, there are environmental concerns and performance limitations which have encouraged researchers to find lead-free alternatives to PZT[124,125].

The material $(1-x)Ba(Zr_{0.2}Ti_{0.8})O_3$-$x(Ba_{0.7}Ca_{0.3})TiO_3$ (BZT-xBCT), which has a d_{33} of 620 pC/N at $x \sim 0.50$[65], is a leading lead-free piezoelectric material that could potentially replace PZT in certain applications. At room temperature and low BCT concentration, BZT-xBCT crystallizes in the rhombohedral (R) $R3m$ space group and maintains that symmetry in the solid solution until $x \sim 0.44$. From x = 0.45 to 0.51 the structure crystallizes in the orthorhombic (O) $Amm2$ space group. Above $x \sim 0.51$, the system exhibits a tetragonal (T) $P4mm$ structure.[126] The symmetry and structure at the MPB for this material is still controversial. Based on early structural analysis studies, it was reported that the average structure of BZT-xBCT at the MPB consisted of mixtures of T ($P4mm$) and R ($R3m$) phases.[74] However, an updated phase diagram characterizes the MPB as O in Ref. [73]. It has also been observed that the MPB for

BZT-*x*BCT is strongly dependent on the temperature, in contrast to PZT which is only slightly dependent on temperature. There is an anomaly where the physical properties are enhanced at $x \sim 0.45$, the boundary of the R-O phases.[126] This enhancement is not as pronounced as the one found at $x \sim 0.50$, so it is not referred to as the MPB of the system.

While BZT-*x*BCT has been extensively studied, the underlying causes of the observed macroscopic strain properties of BZT-*x*BCT are still not fully understood. A combination of local and average *in situ* structural information is necessary to identify the underlying intrinsic and extrinsic mechanisms that contribute to its high electromechanical strain. The intrinsic contribution to piezoelectricity originates from atomic displacements within individual unit cells, due to an external field, that propagate as lattice strain along different crystallographic directions. On the other hand, the extrinsic contribution to the effective piezoelectric response has been primarily associated with domain wall motion[127–129], though interphase boundary motion has also been considered.[130] The application of an electric field to a ferroelectric material induces the alignment of domains along a specific direction (i.e. polarization direction), depending on the symmetry of the material. As a consequence of this reorientation, the relative intensity ratio of characteristic Bragg reflections changes and can be used to investigate domain wall motion.[131] While piezoelectric lattice strain and domain wall motion are common contributions to electromechanical properties, the contributions of field-induced phase transitions from nonpolar to polar structures are less well-discussed, though obvious in $0.93(Na_{0.5}Bi_{0.5})TiO_3$-$0.07BaTiO_3$

(NBT-0.07BT) [132] and $0.70Pb(Mg_{1/3}Nb_{2/3})O_3{-}0.30PbTiO_3$ (PMN-0.30PT) based piezoceramics.[133]

Detailed structural studies play a key role in understanding the underlying mechanisms that contribute to the effective piezoelectric coefficient. Piezoelectric ceramics often have complicated structures that possess a local, short-range structure that is different from the average, long-range structure[115,117,134–138]. To illustrate a simple example, the classical ferroelectric and piezoelectric material $BaTiO_3$ (BT) adopts a T average structure with space group *P*4*mm,* but the local structure is more closely described as R, *R*3*m*[108,139]. Jeong *et al*. proposed a similar T order-disorder model for the BZT-*x*BCT structure based on a neutron pair distribution function (PDF) study of the $x = 0.50$ composition[72]. The study showed that the B-site titanium atoms distort in the [111] direction accompanied by a small tilting of the TiO_6 octahedra, whereas the zirconium atoms do not distort and the ZrO_6 octahedra tilt dramatically. The ordered local structure remains consistent from 150 to 300 K, even though the average structure appears R and T respectively.

Identifying local deviations and understanding how both the local and average structure change under the conditions in which the high piezoelectric response is observed (i.e. under an electric field) will lead to a greater understanding of properties at and near MPBs. One method to study the local structure of piezoelectrics is the total scattering technique. In total scattering studies, the PDF is analyzed to determine the local structure from diffuse scattering. The PDF provides the probabilities of atom-atom correlation distances as a function of distance, *r*, and is highly sensitive to local ionic displacements and short-range order. The PDF technique has been used to

study piezoelectric materials before and is an efficient way to characterize the local structure of materials under the application of external electric fields[140–145].

For BZT-*x*BCT, Gao *et al*. suggested that the cause of the strong piezoelectricity at the MPB is because of an easy polarization rotation mechanism between nanodomains of coexisting R and T symmetries [76,146] as in PZT[147]. Moreover, they used Raman spectroscopy and dielectric measurements to claim that a structural phase transition just below room temperature could take place apart from the two transitions at higher temperatures, as previously reported by Ren *et al.*[65]. They predicted that this anomaly close to room temperature contributes to the large electromechanical response observed at the MPB. However, Damjanovic *et al*. proposed that the nanodomains could emerge from a coexistence of the T and the intermediate O phases, based on the new and revised phase diagram. Damjanovic *et al*. also suggested that this anomaly could be due to relaxation processes related to interaction of domain walls with defects[148]. In another work, Damjanovic *et al*. also proposed that the high piezoelectric performance at the MPB could be attributed to the increase of intrinsic piezoelectric activity due to free energy flattening of the landscape at this region[149]. In a later study, Gao *et al.* used small-field Rayleigh analysis under electric field to suggest that the main contributor to the high piezoelectric response at the MPB is the extrinsic reversible domain wall motion (67%), while the intrinsic contribution from the lattice deformation only accounts for 33% of the high performance[78]. This study, which contradicts the group's earlier studies performed at zero-field, shows the necessity of using *in situ* electric field measurements to determine the strain mechanisms under operating conditions.

Several studies have shown that *in situ* electric field X-ray diffraction (XRD) and PDF are powerful techniques to investigate lattice strain[150,151], domain wall motion[133,152], field-induced phase transitions[38,133,144,153,154], and the local structure of other piezoelectric materials[72,140–144]. *In situ* electric field XRD in the T compositional range of BZT-*x*BCT has been performed previously[155,156]. Tutuncu *et al*. demonstrated that in the region $0.60 \leq x \leq 0.90$ there is an increase in 90° domain wall motion as the composition moves closer to the MPB ($x = 0.50$). Furthermore, they observed a decrease of the T distortion or tetragonality (c/a) that results in reduced intergranular constraints which can more easily facilitate electromechanical strain[155]. On the other hand, Ehmke *et al*. observed for the composition $x = 0.60$ that the contribution of ferroelastic strain to the macroscopic strain is larger than the lattice strain[156]. In the present work, we perform high-energy XRD and total scattering measurements while applying electric fields, *in situ*, to BZT-*x*BCT compositions spanning the MPB, $0.45 \leq x \leq 0.60$, to investigate the origin of the high electromechanical strain at $x = 0.50$. The data provides insight into the extrinsic contributions of domain wall motion and the intrinsic contributions of piezoelectric strain and lattice distortion as the MPB is approached from both the O and T phases.

3.3. Experimental

Polycrystalline samples of BZT-*x*BCT were prepared via standard solid-state synthesis for compositions $x = 0.40$, 0.425, 0.45, 0.475, 0.49, 0.50, 0.51, 0.525, 0.55, 0.575 and 0.60. The reagents: $BaCO_3$ (Sigma Aldrich, 99.9%), $CaCO_3$ (Alfa Aesar, 99.0%), TiO_2 (Sigma Aldrich, 99.99%), and ZrO_2 (Alfa Aesar, 99.7%) were weighed in stoichiometric quantities. The $BaCO_3$ and $CaCO_3$ powders were heated at 110 °C

for 24 h before being weighed. The starting materials were placed in a mortar and pestle, covered in ethanol, and mixed well. The ethanol evaporated during the grinding process and the resulting mixed powder was ball milled in a planetary micromill (Pullverisette 7 Classic Line, Fritsch) for approximately 5 h to obtain a homogenous mixture. For the ball milling process, each sample was placed in a container with 20 ml of ethanol and eight 10 mm yttria-stabilized zirconia balls for 8 cycles. Each milling cycle contained three parts: 15 min forward, 10 min rest, 15 min reverse milling direction at a rate of 350 rpm. The resulting solution was dried in air at room temperature, and the milled powder was calcined in alumina crucibles at 1300 °C for 2 h, with a 4 h holding step at 450 °C to allow for degassing of carbonates. The heating and cooling rate used was 3 °C/min. The calcined powder was ball milled once more with the same conditions as the original ball mill step.

Pellets with densities ≥ 85% of the theoretical crystallographic value (as measured by an Archimedes balance) were synthesized. To achieve this density, a 1:1 ratio of 3% polyvinyl butyral (Sigma Aldrich) binder in ethanol was added to 0.3 g portions of calcined powder samples and ground well in a mortar and pestle until a homogeneous mixture was obtained. After the mixture dried, the powder was uniaxially pressed into pellets using a 10-mm die (Carver Inc.) at 2 tons for 2 min. The pellets were placed in latex bags and pressed at 210 MPa for 2 min using a cold isostatic press (YLJ-20TA, MTI). Next, they were placed in closed alumina crucibles, heated at 400 °C for 2 h to burn off binder and sintered at 1450 °C for 2 h. The heating and cooling rate used was 3 °C/min.

The phase purity of sintered pellets was determined via XRD using a benchtop diffractometer (Miniflex600, Rigaku) prior to physical properties measurements. For polarization-electric field (*P*–*E*) and unipolar strain-electric field (*S*–*E*) measurements, pellets were polished down to ≤ 0.5 mm thickness with a mirror finish using a semi-automatic polishing machine (LaboPol5, Struers) with a series of P400, P1200, and P4000 SiC foils (Struers). Electrodes were then applied to opposite faces of the polished pellets with silver conductive paint (#05002-AB, SPI supplies). The sides of the pellets were hand polished with sand paper to remove any deposited silver paint that might cause an electrical short. Prior to measurements the painted pellets were measured for conductivity using a standard ohmmeter to ensure that the electrodes functioned properly. To conduct *P*–*E* and *S*–*E* measurements, pellets were placed in a high voltage test fixture sample holder (Radiant Technologies) where the pellet was submerged in non-conductive silicon oil and connected to a standard ferroelectric test system (Radiant Technologies). For *S*–*E* measurements, an optical displacement sensor (MTI-2100, MTI Instruments, Inc., Albany, NY) was used. Both *P*–*E* and *S*–*E* measurements were conducted at 1.00 kV/mm and room temperature with a frequency of 0.1 Hz for all compositions.

For synchrotron *in situ* electric field measurements, polished ceramic pellets were cut into bars (~ 0.5 × 1.0× 5.0 mm) using a diamond saw (Isomet low speed saw, Buehler). The bars were annealed at 400 °C for 3 h to relieve stress from the polishing and cutting processes. Electrical contacts were applied in the same manner as mentioned in the physical properties measurements section.

Synchrotron X-ray diffraction (SXRD) and total scattering data were collected on the 11-ID-B beamline at the Advanced Photon Source at Argonne National Laboratory[157]. An incident X-ray wavelength of 0.1430 Å (86.70 keV) with a beam size of 0.2 × 0.2 mm was used. The design of the electric field loading stage is described by Daniels *et al*.[132], and is the same as used by Usher *et al*. [143] and Goetzee-Barral *et al*. [142] in earlier experiments. Figure 3.1 shows a schematic of the experimental setup in which the sample bars were immersed in an electrically insulating liquid Fluorinert (3M) bath in a Kapton (DuPont) tape container and connected to high voltage leads before being positioned in the X-ray beam. The sample stage was tilted an angle of φ = 4-8° towards the incident X-ray to minimize the angular variation between the scattering and electric field vectors on the detector plane, as described in the literature[143]. A flat-panel amorphous-silicon detector (Perkin Elmer)[157] was used to collect data. A high voltage amplifier (AMS-10B2, Matsusada Precision) connected to a function generator (33220A, Agilent) was used to apply the DC electric field to the sample bars. For SXRD experiments, a detector distance of 950 mm was used with an exposure time of 1 min to collect data. The electric field was increased in increments of 0.25 kV/mm from 0.00 to 2.50 kV/mm. SXRD data were also collected as the electric field was decreased from E = 2.50 kV/mm, at E = 2.00, 1.00 and 0.00 kV/mm. Total scattering data were collected using a detector distance of 250 mm, and an exposure time of 5 min. For these total scattering measurements, the electric field was increased from 0.00 to 2.55 kV/mm in smaller 0.15 kV/mm steps. The Kapton tape container and insulating liquid were measured separately then subtracted from the total signal as background scattering.

Due to the small size of the sample bars and the existence of larger crystallites, the sample stage was moved slowly right and left (perpendicular to the X-ray beam) to reduce the contribution of individual crystallites on the resulting patterns (for both SXRD and total scattering measurements). For each composition, the sample bars measured by each technique were cut from the original sintered pellet. At each detector distance, a CeO_2 standard was measured to calibrate the detector related parameters.

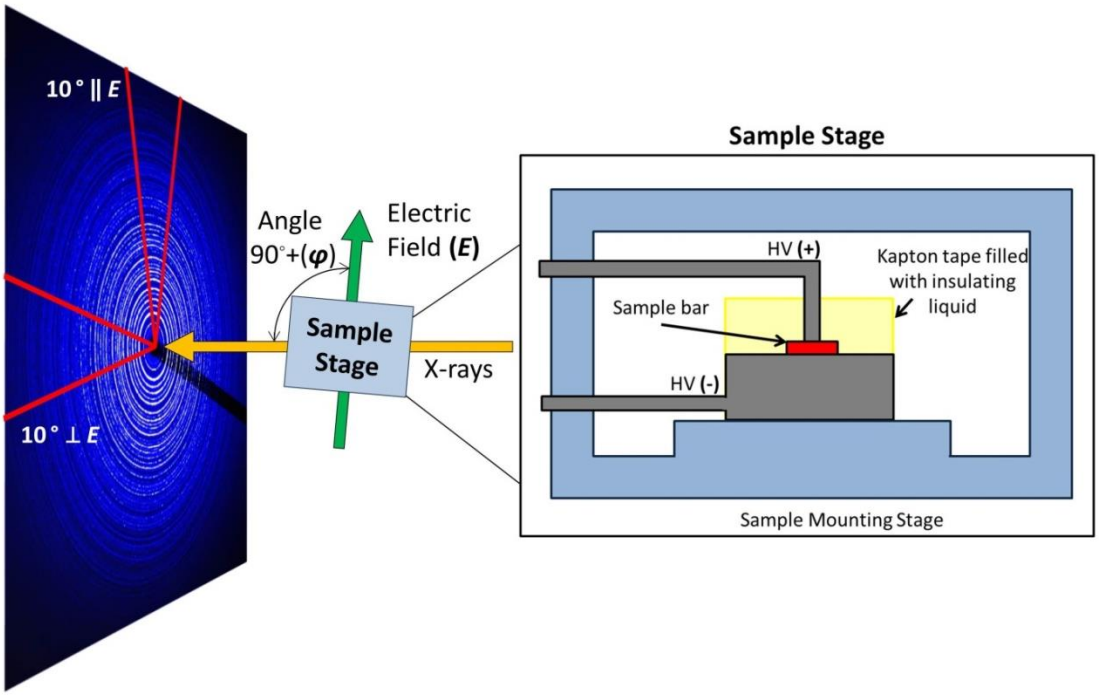

Figure 3.1. Schematic illustrating the experimental setup for synchrotron X-ray total scattering and diffraction measurements where φ = 4-8°.

The two dimensional diffraction images were converted to a one dimensional (1D) pattern of intensity (I) versus Q (the modulus of the scattering vector) and 2θ patterns using the program FIT2D[158]. More specifically, the 1D intensity data were extracted by selecting azimuthal slices (±5°) parallel and perpendicular to the electric field, as illustrated by the red lines in Figure 3.1. The parallel and perpendicular

azimuthal slices are necessary as the crystallites will respond differently for different directions of the electric field. In piezoelectric materials, the unit cell in the parallel direction is expected to expand and the perpendicular direction is expected to contract. This is because of the alignment of individual crystallites with the electric field as described in Usher *et al.*[143]. The software PDFgetX3[158] was used to perform background subtraction, correct intensity data for polarization, and extract the normalized structure factor $S(Q)$ from the $I(Q)$ data. Upon inspection of noise levels in the data, the total scattering data were cut off at a Q_{max} of 22.8 Å^{-1}. The $S(Q)$ data were then converted to the pair distribution function $G(r)$ via a sine Fourier transform as described below:

$$G(r) = 4\pi r[\rho(r) - \rho_o] = \frac{2}{\pi}\int_0^\infty Q[S(Q) - 1]\sin(Q_r)dQ$$

where r is the distance from any atom, $\rho(r)$ is the atomic pair-density function, and ρ_o is the number density of the material[85].

Pawley fits[88] were carried out against the I versus 2θ SXRD data collected to extract the lattice parameters in the 2θ range 2-12°. The software package Topas Academic (Version 6)[90] was used to perform these Pawley fits. The background of the SXRD data was modeled using 10 coefficients in the Chebyschev model. For a given space group, the lattice parameters, profile shape parameters, and background were refined.

3.4. Results and Discussion

Sample preparation can greatly affect the physical properties, so the materials were processed with the utmost care and consistency. Therefore, physical properties

measurements were performed to characterize the quality of the samples and to test whether the response is highest at the MPB, as expected. Ferroelectric *P–E* hysteresis loop measurements were collected for all compositions as shown in Figure 3.2 (a-c) and Figure A.6. The measured *P–E* loops are characteristic of a saturated ferroelectric material[65]. The highest maximum polarization (P_{max}) is achieved for composition x = 0.50 at the MPB in the O region with a value of 13μC/cm^2, as expected[65]. For compositions on either side of the MPB, the P_{max} values are lower. At x = 0.40 in the R region a P_{max} of 9.1 μC/cm^2 is observed, and on the T side, when x = 0.60, P_{max} = 9.7 μC/cm^2.

The electromechanical strain response was measured under unipolar *E* cycling at room temperature for all compositions (Figure 3.2 (d-f) and Figure A.7) at the optimum electric field of 1.00 kV/mm, as reported in the literature[67,160]. The largest strain value was obtained for x = 0.50 at 1.36%. Strain values of 0.49% and 0.34% were achieved for x = 0.40 and x = 0.60, respectively. Figure 3.2(g) shows the effective piezoelectric coefficient (d_{33}^*) calculated from unipolar *S–E* loops as a function of BCT composition. Two regions of enhanced piezoelectric response were observed, one occurring at x = 0.45 and the other at x = 0.50, corresponding to the R-O and O-T phase boundaries respectively. These results are consistent with previous studies of this material[78,126]. The maximum d_{33}^* is achieved at the MPB (~1410 pm/V), which is in reasonable agreement with previous reported compositions by Liu *et al*. (1140pm/V)[65]. The results of the *S–E* measurements agree well with the *P–E* loops, where a maximum d_{33}^* and P_{max} is observed at the MPB composition x = 0.50. The results of the observed physical properties are consistent with the literature,

indicating that the synthesized materials in this study are of the intended composition and structure.

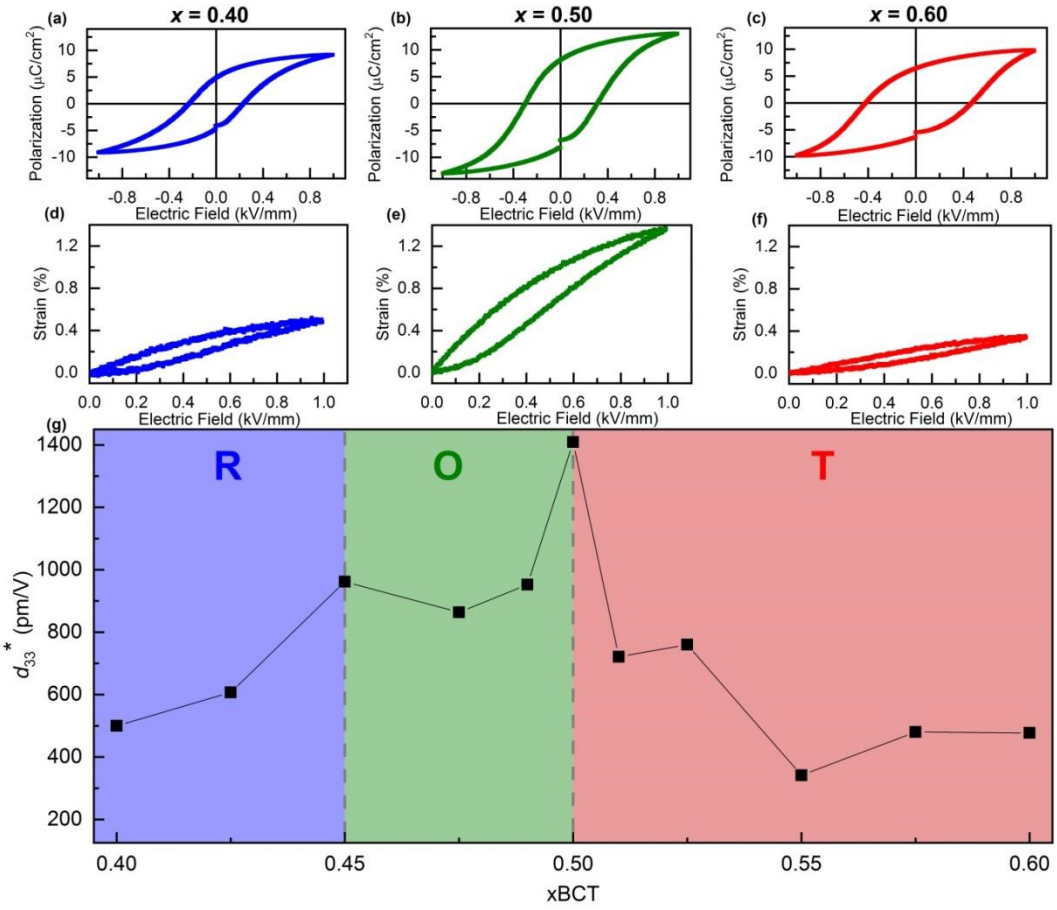

Figure 3.2. For x = 0.40 (R), 0.50 (O) and 0.60 (T): (a-c) P–E loops, and (d-f) Unipolar S–E loops, respectively. (g) Variation of the effective piezoelectric coefficient (d_{33}*) calculated from unipolar S–E loops d_{33}*(=S_{max}/E_{max}), where S_{max} is the strain observed at the maximum field E_{max}, as a function of composition (x). The gray dashed lines indicate approximate the region where a change in symmetry occurs from rhombohedral (R) to orthorhombic (O) and tetragonal (T).

3.4.1. Extrinsic contribution: Domain wall motion

When an electric field is applied across a ferroelectric ceramic, a portion of the domains within individual crystallites reorient along a specific direction, depending on the symmetry of the unit cell and the polarization direction. As a result, the relative intensity ratio of representative Bragg reflections varies and can be

analyzed to quantify the degree of domain reorientation[127]. The *in situ* electric field XRD technique has been used to study domain wall motion on several piezoelectric systems[150,151,161,162]. In this study, we investigate domain wall motion across the MPB for BZT-*x*BCT to gain a deeper understanding of the structure-property relationship in this system. Compositions with the O structure included x = 0.45, 0.475, and 0.50, while compositions on the T side included x= 0.525, 0.55, 0.575, and 0.60.

For this BZT-*x*BCT system, previous *in situ* electric field experiments were performed to study the domain wall motion of the T compositions x= 0.60, 0.70, 0.80, and 0.90[155,156]. These studies found that in BCT-rich compositions, the contributions to the macroscropic response came mainly from domain wall motion rather than lattice strain. Tutuncu *et al.* demonstrated this concept by examining the intensity variations for the $\{002\}_{pc}$ region in the SXRD pattern as a function of electric field. At the BCT-rich compositions, they found the tetragonal distortion was large, but upon application of *E*, there were only small changes in intensity of the 002 and 200 reflections, indicating little 90° domain wall motion. However, as the BCT content decreased to x = 0.60, the tetragonal distortion decreased, and the application of *E* resulted in a significant change in intensity of the 002/200 reflections, demonstrating increased domain wall motion. It is the decrease in tetragonal distortion with reduced intergranular constraints that allows for an increase in the domain wall motion. Their study showed that this increase in domain wall motion as the MPB is approached makes a significant contribution to the macroscopic strain.[155]

In our study of the T compositional range, we examined compositions even closer to the MPB. Figure 3 a-d shows sections of SXRD patterns for the peak

$\{002\}_{pc}$ collected as a function of E from 0.00 to 2.50 kV/mm for x = 0.525, 0.55, 0.575 and 0.60. The domain wall motion induced by the application of an E was investigated by analyzing the change in the relative intensity of the 002 and 200 reflections. In Figure 3.3(a), it can be observed that when x = 0.525, in the unpoled state, the 200 reflection is the most intense. At E = 2.50 kV/mm, the intensity distribution changes and both 002 and 200 reflections have similar intensities. For x = 0.55, at zero field, the 200 reflection is the most intense while above 1.00 kV/mm the 002 reflection gains intensity as the 200 reflection decreases in intensity (Figure 3.3(b)). Similar behavior is observed for compositions x = 0.575 and 0.60 (Figure 3.3(c) and (d)). It appears that the change of the relative intensity of the 002 and 200 reflections occur at a lower E as the MPB is approached. When the E is decreased, the intensity of the 200 and 002 reflections shift towards their original state which suggests back switching (Figure A.8). This domain back switching was also observed in the study by Tutuncu *et al.*[155].

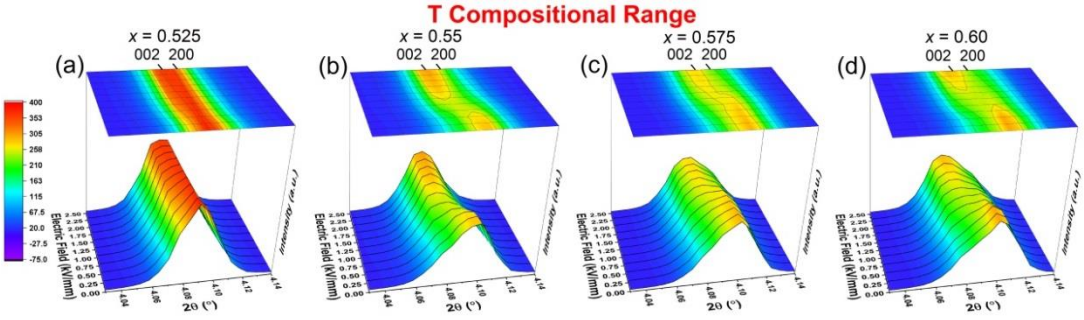

Figure 3.3. For compositions with T structure, x = 0.525, 0.55, 0.575 and 0.60: a-d) Sections of diffraction patterns for the $\{002\}_{pc}$ region as a function of electric field from 0.00 to an applied field of 2.50 kV/mm, in the parallel direction from the electric field.

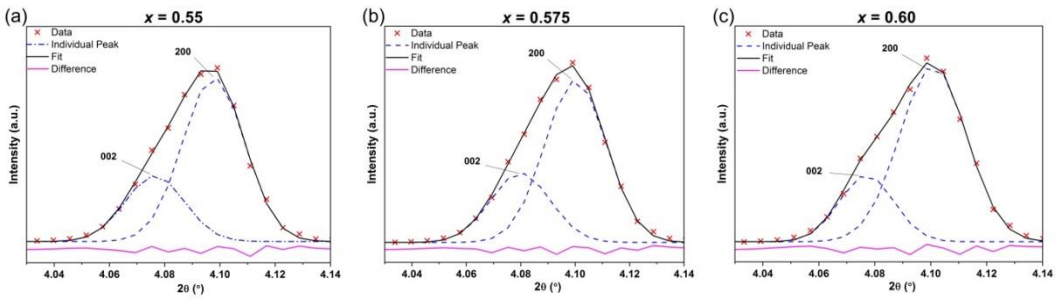

Figure 3.4. For compositions with T structure, x = 0.55, 0.575, and 0.60: a-c) Measured intensity (red triangles), Gaussian profiles fits (blue dashed lines), the overall fit (black solid line), and the difference between the measured intensity and overall fit of the$\{002\}_{pc}$ peaks (pink solid line) in the unpoled state.

In order to quantify the amount of 90° domain wall motion, the integrated intensity of the 002 and 200 reflections was determined by fitting the peaks to two Gaussian peak profile functions for x = 0.55, 0.575, and 0.60 as a function of E from 0.00 to 2.50 kV/mm. Figure 3.4 (a-c) shows for the $\{002\}_{pc}$ peaks the measured intensity, the component Gaussian profile fits, the overall fit, and the difference between the measured intensity and overall fit when x = 0.55, 0.575, and 0.60, respectively in the unpoled state. In the case of x = 0.525, it was not possible to fit the $\{002\}_{pc}$ peaks with two distinct Gaussians due to the large overlap of the peaks (Figure 3a). As previously published by Jones *et al*., the degree of domain orientation (f_{002}) can be calculated using multiples of random distribution (*MRD*).

For tetragonal systems, f_{002} can be determined from the ratio of integrated intensities with respect to the state of the unpoled sample using[131]:

$$f_{002}[MRD] = \frac{3\left(I_{002}/I_{002}^{unpoled}\right)}{\left(I_{002}/I_{002}^{unpoled} + 2I_{200}/I_{200}^{unpoled}\right)}$$

The degree of orientation can be also reported as the domain orientation volume fraction (η_{002}) in tetragonal systems.

$$\eta_{002} = \frac{f_{002}}{3} - \frac{1}{3}$$

Both the f_{002} and η_{002} values are normalized to the unpoled state, where the initial unpoled values are $f_{002} = 1$ and $\eta_{002} = 0$. Figure 3.5 shows the f_{002} and equivalent η_{002} values obtained for $x = 0.55$, 0.575, and 0.60 in the direction parallel to the electric field. The f_{002} values increase with increasing electric field as the domains rotate and orient to align with the field. As the content of BCT is decreased, the f_{002} values increase: 2.03 ($x = 0.60$), 2.16 ($x = 0.575$), and 2.64 ($x = 0.55$) when $E = 2.55$ kV/mm. These results indicate increased 90° domain wall motion as the MPB is approached. Following the trend, we can extrapolate that the $x = 0.525$ composition approaches a saturated domain orientation state in which all domains are aligned as closely as possible to the field ($f_{002} = 3$, $\eta_{002} = 0.67$).

Our findings are consistent with the trend observed in the previous study of the T side for BZT-*x*BCT in the range $0.60 \leq x \leq 0.90$ where the degree of orientation increases when approaching the MPB[155]. As the field is removed, the domains relax to an extent, (denoted by the triangles facing down in Figure 3.5), which is indicative of domain back switching. After application of the field, the structure remains in a partially domain-aligned (poled) state but does not relax completely. This behavior is characteristic of a ferroelectric material, where there is some remnant polarization after removal of an electric field. The degree of domain orientation after removal of the field is still high with values of $f_{002} = 1.54$, 1.48, and 1.74 when $x = 0.60$, 0.575, and 0.55, respectively. For $x = 0.60$, the calculated f_{002} value is 2.03 whereas the reported value in the Jones *et al.* study is 1.65[155]. One explanation for the discrepancy between these two values could be due to the different processing conditions which

could strongly influence the microstructure and thus the degree of domain wall motion.

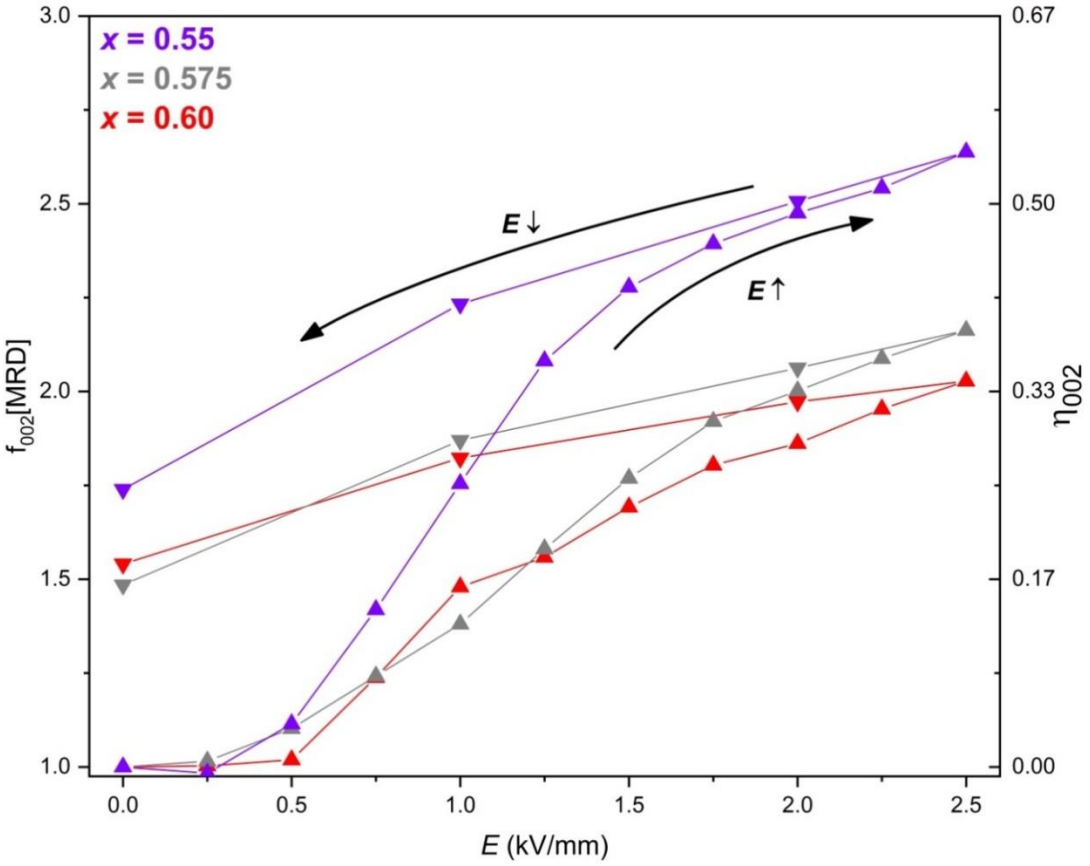

Figure 3.5. Calculated degree of domain orientation (f_{002}) in right y-axis and equivalent domain degree orientation volume fraction (η_{002}) in left y-axis values in the direction parallel to the electric field for T compositions x = 0.55, 0.575, and 0.60. Values in upward facing triangles correspond to the increase of the E from 0 to 2.55 kV/mm whereas the downward facing triangles correspond to the removal of the E.

Domain wall motion contributions to the piezoelectric response in the O compositional range have not yet been reported using the *in situ* XRD technique. SXRD patterns collected as a function of E in the O region $0.45 \leq x \leq 0.50$ are shown in Figure 3.6. For an O phase, the polarization direction is along the $[110]_{pc}$ of the primitive cell edge, so the intensity variations for the $\{440\}_{pc}$ family of peaks was investigated. The $\{440\}_{pc}$ family corresponds to the 440, 080 and 008 reflections in

the orthorhombic cell. Unfortunately, there is no observable peak splitting of the $\{440\}_{pc}$ peak for any O composition because the structure is nearly tetragonal. Based on the Pawley fits performed in the O range for unpoled samples (Table A.11), the lattice parameters *b* and *c* are very similar with values of 5.665(1) Å and 5.661(1) Å respectively, for $x = 0.50$. It is clear based on Figure 3.6 that the $\{440\}_{pc}$ peaks change intensity as a function of *E*, indicating domain wall motion. However, attempts to fit the peak using three Gaussian peak profile functions did not yield a reliable convergence, making it difficult to quantify domain wall motion based on the integrated intensity of individual reflections in the $\{440\}_{pc}$ diffraction profile. We expect the extrinsic contributions on the O side to increase as *x* approaches the MPB. This hypothesis is based on the lack of significant peak splitting in all O compositions, which indicates that only small lattice distortions are present, allowing for more domain wall motion to occur. Once the *E* is decreased, back switching is observed, as shown in Figure A.9. The same behavior was observed for the T compositional range studied in this work (Figure A.8) and when $x > 0.60$ by Tutuncu *et al.* [155].

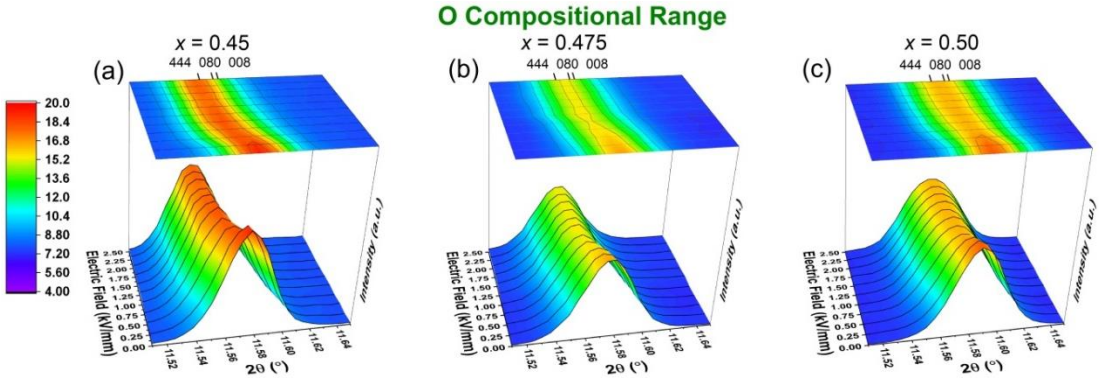

Figure 3.6. For compositions $x = 0.45$, 0.475, and 0.50 in the O compositional range: (a-c) Sections of diffraction patterns for the $\{440\}_{pc}$ region as a function of electric

field from 0.00 to an applied field of 2.50 kV/mm, in the parallel direction from the electric field.

From the measured diffraction patterns, the changes in the unit cell as a function of BCT content were also investigated. Pawley fits were performed to extract lattice parameters at zero field. The O space group *Amm*2 was used for Pawley fits with compositions $0.45 \leq x \leq 0.50$, and the T space group *P*4*mm* was used when $0.525 \leq x \leq 0.60$ as determined in previous literature[73,126]. Examples of Pawley fits obtained for selected compositions $x = 0.50$ and $x = 0.60$ are shown in Figure A.10. Table A.11 and Table A.12 list the lattice parameters obtained for O and T compositional ranges respectively in the unpoled state.

The amount of distortion from the cubic unit cell can be determined quantitatively for the different crystal systems found in BZT-*x*BCT. For compositions adopting an O structure, $0.45 \leq x \leq 0.50$, the lattice distortion can be given as:

$$\delta_O = \frac{(b - c)}{(b + c)}$$

Whereas for compositions in T compositional range, $0.525 \leq x \leq 0.60$ by:

$$\delta_T = \frac{c}{a} - 1$$

As *x* approaches the MPB at $x = 0.50$ from both the O and the T sides the distortion of the lattice decreases, as shown in Figure 3.7(a). This behavior is particularly pronounced in the T compositional range. Minimum values of the lattice distortion for $x = 0.45$ (at the R-O phase boundary) and $x = 0.50$ (at the MPB, O-T boundary) coincide with the highest d_{33}* values achieved of 962 pm/V and 1410 pm/V, respectively (Figure 3.7(b)).

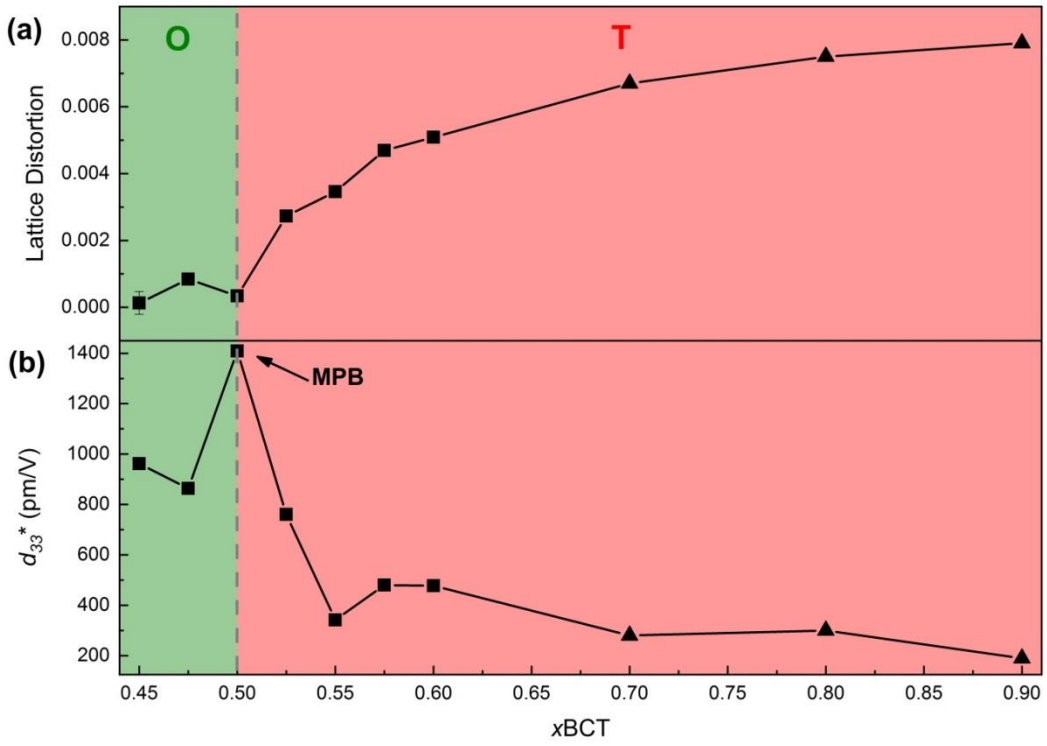

Figure 3.7. For BZT-*x*BCT ceramics as a function of composition (*x*): (a) lattice distortion calculated for the orthorhombic compositional range, $0.45 \leq x \leq 0.50$ using the equation: $\delta = (b-c)/(b+c)$, and for the tetragonal compositional range, $0.525 \leq x \leq 0.90$ using $\delta = c/a-1$. (b) Effective piezoelectric coefficient d_{33}^*. Errors bars are smaller than the data points. The data in triangles ($x = 0.70$, 0.80, and 0.90) were taken from literature[155].

We conclude that, for BZT-*x*BCT in the range $0.45 \leq x \leq 0.90$, the lattice distortion becomes smaller closer to the MPB ($x = 0.50$), which correlates to a decrease in the strain between domains and may allow for increased domain wall motion and easy switching of the domains. This observation is supported in Figure 3.8, which shows the lattice distortion and maximum degree of domain wall motion versus the composition. As the lattice distortion decreases, the degree of domain wall motion increases dramatically. On the O side, all compositions have very small lattice distortions, even a slight increase in the distortion at $x = 0.475$ coincides with a decreased piezoelectric response. This evidence of smaller lattice distortions and

overall higher d_{33}* values of the O phase compared to the T phase, indicates occurrence of significant domain wall motion in this region despite our inability to quantify the contribution using diffraction methods due to the small structural distortions. Our results agree with the observations by Gao *et al*. performing Rayleigh analysis for BZT-*x*BCT in the range $0.42 \leq x \leq 0.56$. They found that the intrinsic contributions coming from lattice distortion increase as the MPB is approached from the O and T sides[78]. For other high performing piezoelectric ceramics the lattice distortion is minimized at the MPB, such as: PZT[160,163,164], and NBT-BT[165]. This phenomenon has even been observed in systems that do not have an MPB. An enhancement of the piezoelectric properties is observed when the rhombohedral lattice distortion is minimized as for $(Bi_{0.5}Na_x)TiO_3$ at $x = 0.48$[166], and NBT-*x*Bi$(Mg_{0.5}Zr_{0.5})O_3$ when $x = 0.01$[167].

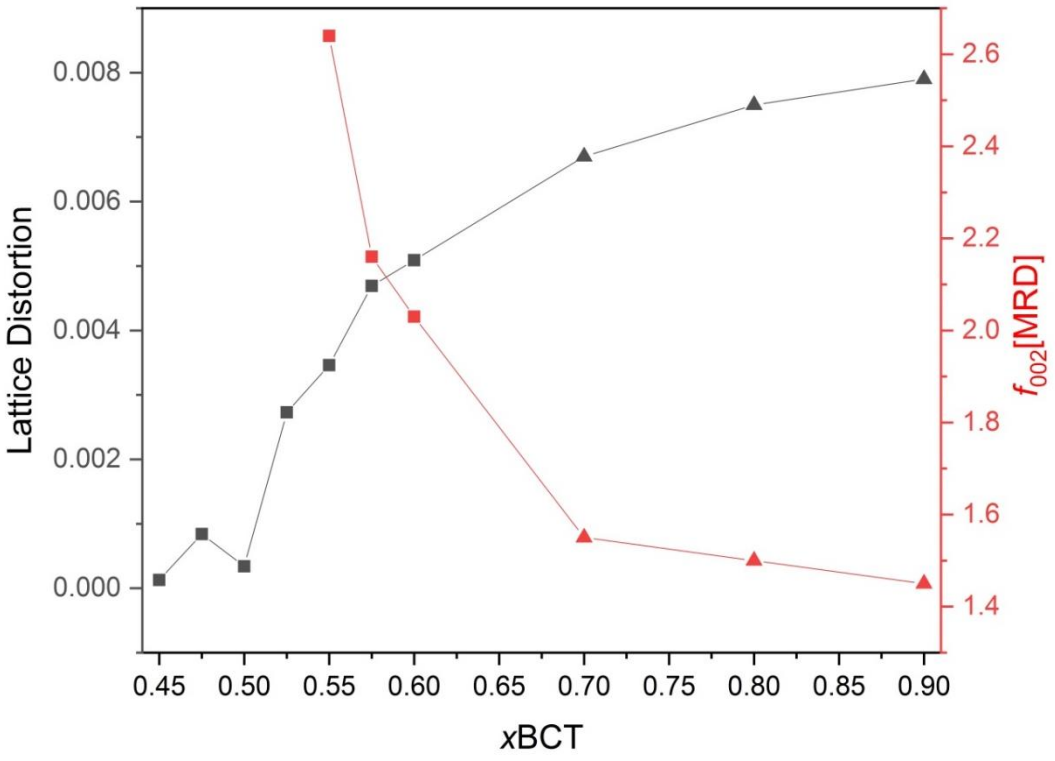

Figure 3.8. For BZT-*x*BCT ceramics as a function of composition (*x*): lattice distortion calculated for the orthorhombic compositional range, $0.45 \leq x \leq 0.50$ using the equation: $\delta = (b-c)/(b+c)$, for the tetragonal compositional range,$0.525 \leq x \leq 0.90$ using $\delta = c/a-1$ (shown in black, left y-axis). Calculated maximum f_{002} values (degree of domain wall motion) in the parallel direction to the electric field for tetragonal compositions $x = 0.55$, 0.575, 0.60, 0.70, 0.80, and 0.90 (shown in red, right y-axis). The data in triangles ($x = 0.70$, 0.80, and 0.90) were taken from literature[155].

3.4.2. Intrinsic contributions: Piezoelectric lattice strain

To investigate the intrinsic contributions from piezoelectric lattice strain we studied the local structure of the BZT-*x*BCT system in the O and T compositional ranges using the total scattering technique. As described in the experimental section, the PDF describes the distribution of all interatomic distances at some distance *r* (Å), allowing for investigation into the short, medium, and long-range ordering simultaneously. Changes in the short and medium-range order upon application of *E* may provide more insight into the strain contributions at the MPB.

A 1D PDF pattern parallel to E, $G_{||}(r)$, and perpendicular to E, $G_{\perp}(r)$, were obtained as previously described in the literature[143]. Figure 3.9 displays the $G_{||}(r)$ for two key compositions in the O range, x = 0.45 and 0.50, as well as x = 0.60 in the T compositional range at both E = 0.00 and 2.55 kV/mm. The $G_{||}(r)$ for the rest of compositions and $G_{\perp}(r)$ are shown in the supplementary information (Figure A.11-Figure A.19). To visualize the effect of the electric field on interatomic distances, the difference between the two PDFs was calculated using:

$$\Delta G_{||}(r) = G_{||}(r)_{zero-field} - G_{||}(r)_{max-field}$$

For all compositions, the peak amplitude of $\Delta G_{||}(r)$ is small below 10 Å and increases slowly as r increases, indicating that the most significant changes in the PDF occur at long-range distances upon application of an E.

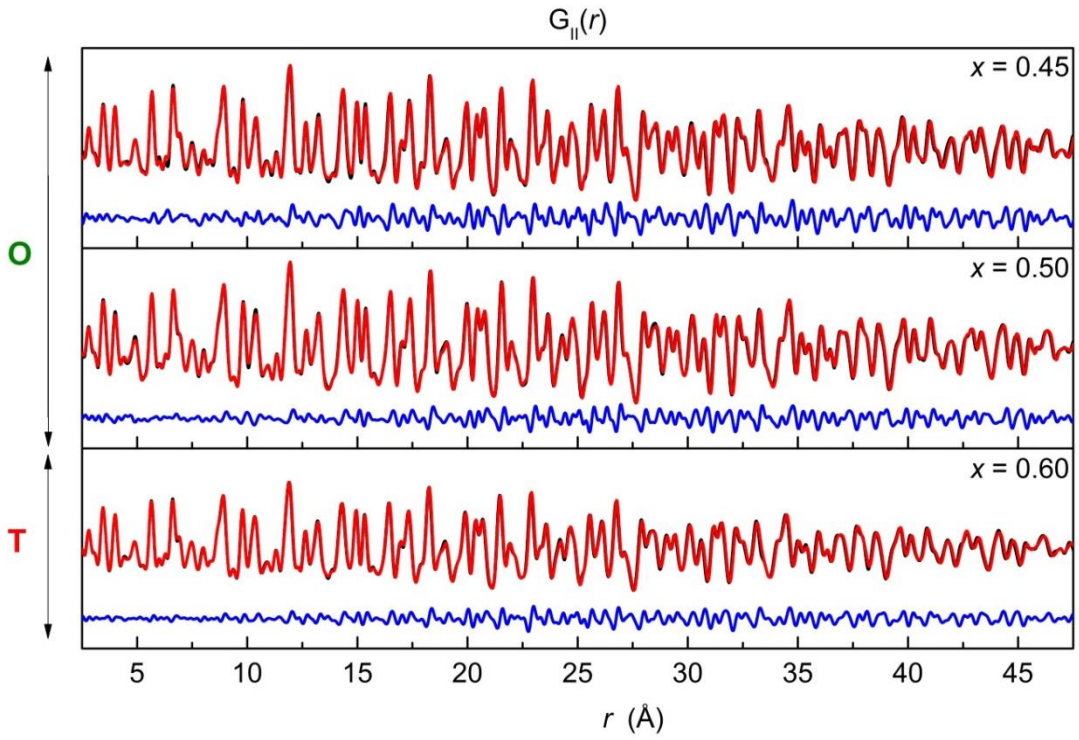

Figure 3.9. $G_{||}(r)$ for x = 0.45, 0.50, and 0.60 at E = 0.00 (black), E = 2.55 kV/mm (red), and the difference ($\Delta G_{||}(r)$) in blue.

Due to the small magnitude of $\Delta G_{||}(r)$, it is difficult to interpret the structural changes that occur as a function of *E* from the difference curves alone. It is more useful to view subsections of the PDF data as shown in Figure 3.10 to qualitatively describe what happens under field. Low (~3-4 Å) and high (~42-45 Å) *r* sections are shown at *E* = 0.00 and 2.55 kV/mm for two compositions in the O side, *x* = 0.45 and 0.50, and for *x* = 0.60 in the T compositional range. The first peak in the low-*r* range at ~3.45 Å corresponds to the *A*-*B* distances (Ba^{2+}/Ca^{2+}-Ti^{4+}/Zr^{4+}), the second peak at ~4 Å to the *A*-*A* distances (Ba^{2+}/Ca^{2+}-Ba^{2+}/Ca^{2+}), *B*-*B* distances (Ti^{4+}/Zr^{4+}-Ti^{4+}/Zr^{4+}) and *X*-*X* (O^{2-}-O^{2-}) distances. The *A*-*B* peak is the first reliable peak in the PDF data. The B-O peak at ~2.0 Å and the *A*-O peak at ~2.9 Å cannot be reliably analyzed due to the weak scattering of oxygen combined with the Fourier ripples (noise emanating from the limited *Q* range) which obscure the low-*r* region. Neutron diffraction, which scatters strongly from oxygen atoms (and generally has a larger *Q*-range), could be used to better elucidate the *B*-*O* and *A*-*O* first coordination environments (bond distances) in this material.

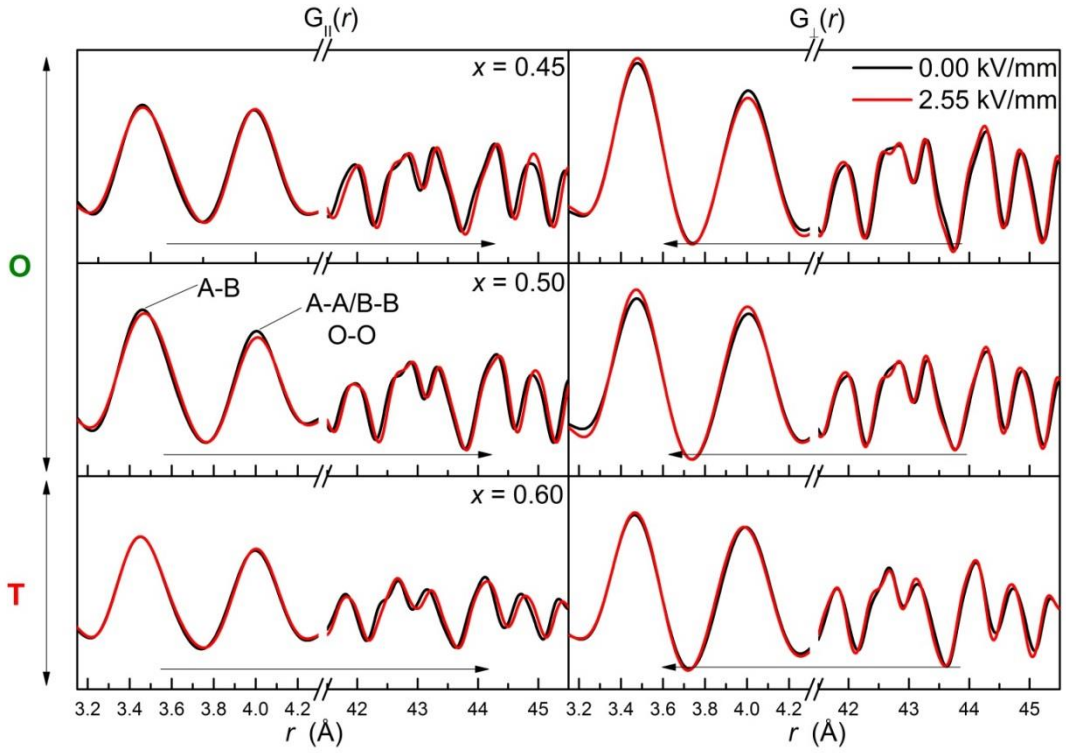

Figure 3.10. Low-*r* and high-*r* *G*(*r*) for *E* = 0.00 and *E* = 2.55 kV/mm for $G_{\parallel}(r)$ and $G_{\perp}(r)$ for *x* = 0.45, 0.50 in the O range, and 0.60 in the T range. Black arrows indicate that peaks shift to higher and lower *r* for $G_{\parallel}(r)$ and $G_{\perp}(r)$, respectively.

The PDF measurements show that there are no significant changes to the local structure in both the O and T phases, whereas the medium and long-range structures show evidence of piezoelectric strain in the parallel direction as the peaks shift to the right (higher *r* values). Perpendicular to the field, peaks at high *r* regions shift to the left (lower *r* values) indicating lattice contraction. In $G_{\parallel}(r)$, the low-*r* region of the T compositions, the *A*-*B*, *A*-*A*, *B*-*B*, and *X*-*X* peaks remain mostly unchanged, while the first two peaks in the O compositions shift slightly to low *r* and become slightly narrower. For the O compositions, the two low-*r* peaks shift and broaden slightly, with the *x* = 0.50 composition at the MPB showing a more prominent change. The increase in the width and baseline around the peak corresponds to an increase in atomic disorder as the probability function widens. The same peaks in the low-*r*

region do not appear to shift in the T compositions. In all compositions, high-*r* peaks shift to higher *r* at maximum applied *E*, indicating an expansion of the lattice in this direction (Figure 3.10, left column). The lattice strain ($\varepsilon = \Delta l/l$) from piezoelectric strain could be the same over the entire length scale, but these high-*r* peak shifts are larger due to the effect of a larger displacement (Δl) occurring at the longer distances (l).

Quantifying the peak shift, δr, is important to understanding the intrinsic contributions of the strain mechanism. To obtain this information, first the residual, R_Δ[143], was calculated from the equation below for x = 0.45, 0.475 and 0.50 in the O region, and x = 0.525, 0.55, 0.575, and 0.60 in the T region. The R_Δ is calculated over a sampling range Δ, at each electric field, $E = x$, for a range of δr values

$$R_\Delta = \frac{\sum_r^{r+\Delta} |G(r \pm \delta r)_{E=0} - G(r)_{E=x}|}{\sum_r^{r+\Delta} |G(r)_{E=0}/N|}$$

where δr is the shift in r relative to the zero field (E = 0) PDF, and N is the number of data points in Δ. Using the aforementioned equation, R_Δ values were calculated as the δr is varied from -2.5 to 2.5 (in increments of 0.01) at each sampling distance in r. The δr corresponding to the minimum R_Δ value that is calculated at each sampling range was reported. The δr represents the average distance that the peaks shift (in Angstroms) upon application of an electric field. A positive δr distance represents the expansion of the lattice, whereas a negative δr distance represents a lattice contraction[142].

Figure 3.11 displays the PDF peak shift (δr) parallel (top panel) and perpendicular (bottom panel) to E for the compositions x = 0.45, 0.475, and 0.50 in the O region. In all compositions, there is an increase in δr || as E increases, and a

decrease in $\delta r \perp$, which correspond to the observed shift in the PDF peaks in Figure 10. The magnitude of $\delta r \parallel$ approaches a maximum of ~0.05 Å and could be attributed to piezoelectric lattice strain. This value is a relatively small shift in comparison with the results obtained in the previous study by Goetzee-Barral *et al*. where the $(K_xNa_{1-x})_{0.5}Bi_{0.5}TiO_3$ system is investigated[142]. Figure 3.11 shows two distinct regions in the perpendicular direction: one at low *r*, below ~8-10 Å, where the δr is constant ~0.005 Å, and a second region when $r > 10$ Å that displays a relatively linear increase in the peak shift for all electric fields. The first region corresponds to the size of the one to two unit cells and indicates that the local structure remains stable at all *E* fields. This phenomenon is most visible for the composition at the MPB ($x = 0.50$), where the δr remains low and then increases sharply at ~10 Å.

The δr shift was also calculated for the compositions in the T region, the results of which are shown in Figure 3.12. In general, the magnitude of the maximum peak shift in both $\delta r \parallel$ and $\delta r \perp$ is similar, however the two distinct regions observed in the O compositions are not as well defined in the T compositions. The low-*r* plateau region is somewhat visible in $x = 0.525$, but is much more difficult to see with increasing BCT content. In the T region the lattice response is stronger at lower fields, indicating an increased susceptibility of the lattice to the lower fields.

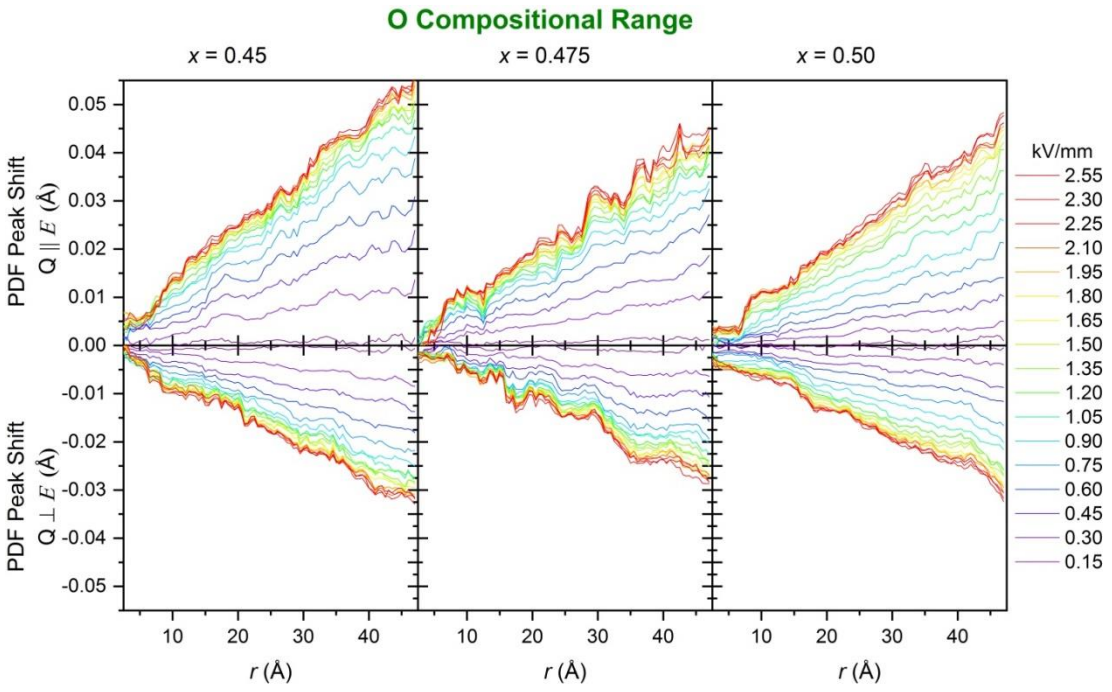

Figure 3.11. Peak shift, δ*r*, that yielded minima in R_Δ for compositions *x* = 0.45, 0.475, and 0.50 in the O region.

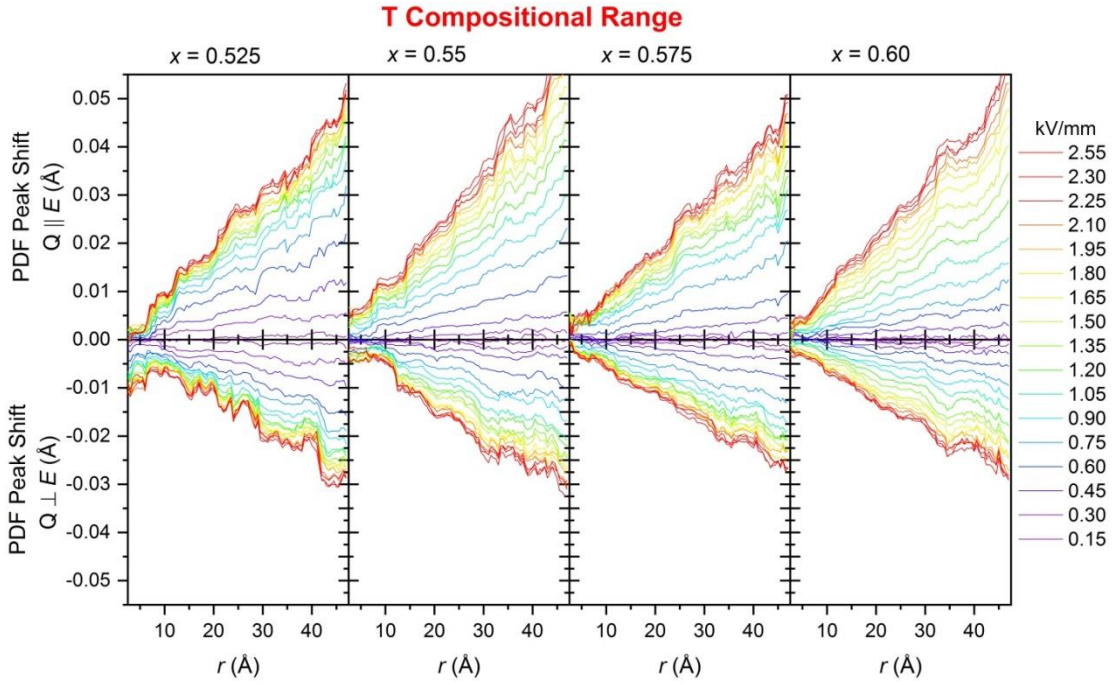

Figure 3.12. Peak shift, δ*r*, that yielded minima in R_Δ for compositions *x* = 0.525, 0.55, 0.575, and 0.60 in the T region.

To better quantify the change in δr as a function of r the gradient, $\delta r(r)$, from r = 10-40 Å, was calculated for Q||E and Q⊥E. Figure 3.13 shows the δr gradient as a function of electric field for the compositions in the O compositional range (Figure 3.13(a)) and in the T side (Figure 3.13(b)) in the parallel (top panels) and perpendicular (bottom panels) to the E. This figures shows how the magnitude of lattice strain propagates in r as E is increased, in other words how steep the δr is at different fields - which is directly related to the piezoelectric lattice strain[142]. The δr gradient shows a compositional trend, particularly noticeable at low fields, where the O compositions are initially more susceptible at lower electric fields (sharp increase in δr gradient). Whereas at higher electric fields, these compositions become less responsive and plateau at lower electric fields than the compositions in the T region. This observation indicates that in the orthorhombic compositions the mechanism is not entirely piezoelectric, as piezoelectric lattice strain is linear. The same non-linearity is observed at the MPB composition, x = 0.50, which shows relatively low susceptibility at both low and high electric fields, as it is surpassed by x = 0.45 and 0.475 compositions around 1.50 kV/mm (Figure 3.13(a)). However, the high BCT-content compositions on the T side (Figure 3.13(b)), the lattice expands more linearly from E = 0 up to 2.50 kV/mm which is indicative of linear piezoelectric lattice strain. The linearity of the lattice strain decreases as the MPB is approached from the T region, which coincides with the observed increase in domain wall from Figure 3.5.

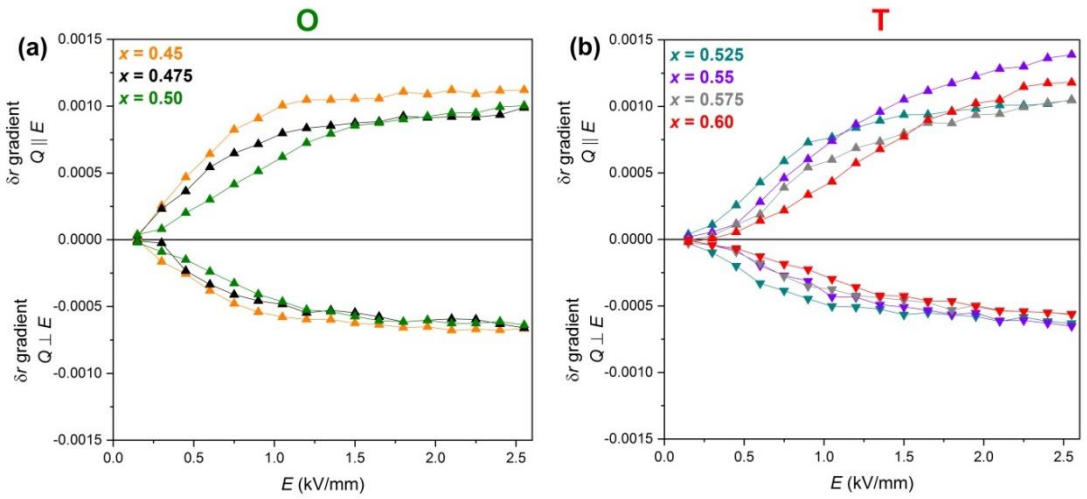

Figure 3.13. In the top panels the gradient of $\delta r(r)$ (lattice strain) parallel ($Q||E$) and in the bottom panels perpendicular ($Q \perp E$) to the electric field for: (a) compositions in the O region: x = 0.45, 0.475, and 0.50, and (b) in T region: x = 0.525, 0.55, 0.575, and 0.60.

These results suggest that the increased degree of domain wall motion suppresses the piezoelectric lattice strain, resulting in the non-linearity in the O region. A linear fit of the sloping region of the δr gradient was performed (the sloping regions fit were E = 0.00 to 0.90 kV/mm for x = 0.45, 0.475, E = 0.00 to 1.50 kV/mm for x = 0.50, 0.525, E = 0.00 to 2.10 kV/mm for x = 0.55, 0.575, and E = 0.00 to 2.55 kV/mm for x = 0.60). The resulting slopes, in mm/kV, represent the local strain coefficients (units converted to pm/V for clarity). Figure 3.14 compares the local strain coefficients (which is related to the intrinsic contribution) versus the observed macroscopic strain coefficients. There is a minima in the local strain at the x = 0.50 composition. We hypothesize that the lattice distortion in the x = 0.50 composition enables more domain wall motion, which suppresses the local strain, and results in an increased piezoelectric response dominated by extrinsic contributions. Recall that the lattice distortion decreases from both the O and T sides of the phase diagram and is minimized at the MPB. This reduced lattice distortion results in decreased strain

between the domains, which allows for increased domain wall motion and easier polarization switching. At the MPB, the piezoelectric strain is also suppressed as shown in the nonlinearity of the lattice strain (Figure 3.13). In addition, at the MPB the local strain is minimized, while the macroscopic strain is maximized (Figure 3.14). This coincides with a significant increase in domain wall motion, meaning that most of the macroscopic strain comes from this extrinsic contribution. These observations are in good agreement with previous studies by Gao *et al.*[78] where the high performance of BZT-*x*BCT at the MPB was attributed to come mostly from extrinsic reversible domain wall motion based on small-field Rayleigh analysis under electric field. This study extended the research by Tutuncu *et al.*[155] by investigating compositions across the MPB and through the O region. In addition, this work also examined the local structure of each composition as well as the average structure. The results reported here are also in agreement with this previous in-situ study of compositions from $0.60 \leq x \leq 0.90$ which demonstrated an increase in domain wall motion contributions as the MPB was approached.

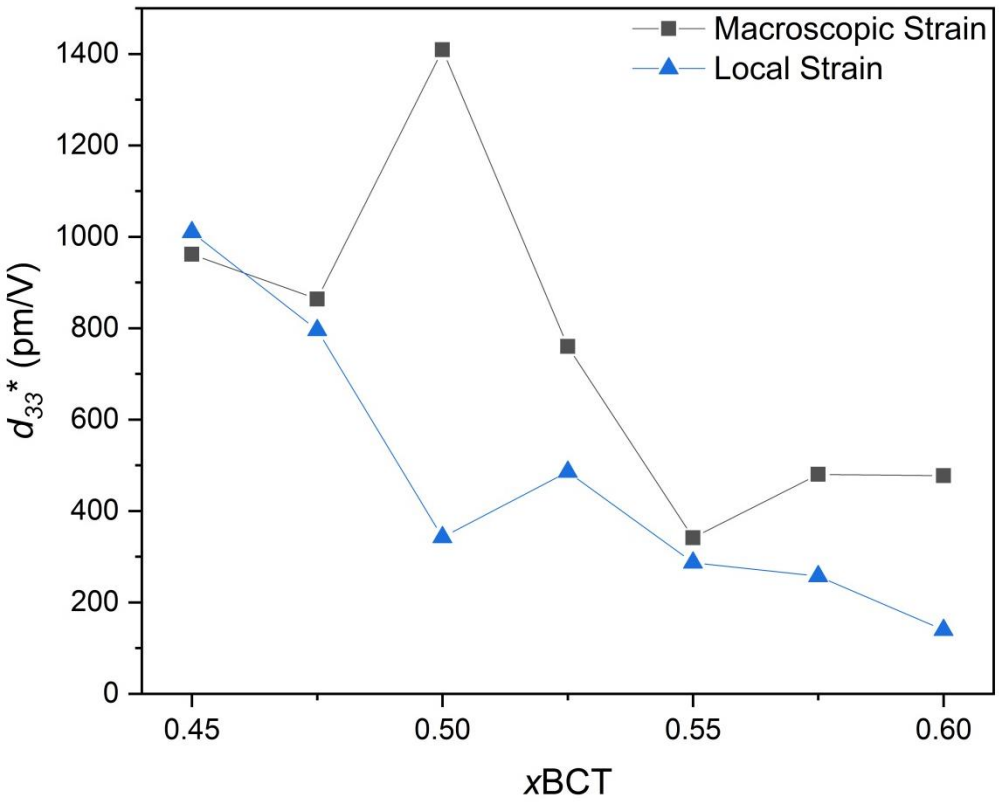

Figure 3.14. The local strain coefficient (intrinsic contribution) in blue, versus the measured macroscopic strain coefficient in black as a function of composition (x) for the BZT-*x*BCT system.

3.5. Conclusions

In summary, this work examined the combination of the average and local structure as a function of electric field at compositions ranging from $0.45 \leq x \leq 0.60$ (which includes the MPB at $x = 0.50$) and it was determined that a majority of the piezoelectric response is derived from extrinsic effects of domain wall motion. The enhancement of the domain wall motion coincides with the decreasing lattice distortions at the MPB. As mentioned previously, the PDF shows evidence of some intrinsic contributions from piezoelectric lattice strain, but the main driving force of the high piezoelectric response is clearly domain wall motion. Surprisingly, there is little to no change in the first coordination sphere of the local structure upon

increasing electric field. This is in contrast to what is observed in other well-known piezoceramics such as NBT-KBT[63] and PMN-0.30PT[144].

3.6. Acknowledgements

Michelle Dolgos, Alicia Manjón-Sanz, and Charles Culbertson would like to thank the National Science Foundation (NSF) under Grant No. DMR-1606909. This research used resources of the Advanced Photon Source, a U.S. Department of Energy (DOE) Office of Science User Facility operated for the DOE Office of Science by Argonne National Laboratory under Contract No. DE-AC02-06CH11357. Jacob Jones acknowledges support from the NSF under award number DMR-1409399. We would like to thank Kevin Beyer, Olaf Borkiewicz, and Changhao Zhao for their assistance with running the experiment on 11-ID-B at the Advanced Photon Source. In addition, we would also like to thank Anton Goetzee-Barral for insightful conversations about the PDF analysis.

Chapter 4: The Local Structure of $0.5Ba(Zr_{0.2}Ti_{0.8})O_3$-$0.5(Ba_{0.7}Ca_{0.3})TiO_3$ from Neutron Total Scattering Measurements and Multi-Edge X-ray Absorption Analysis

Charles McLouth Culbertson,[1] Alicia Manjón-Sanz,[2] Marcos Lucero,[3] Zhenxing Feng,[3] and Michelle R. Dolgos[4]

[1] *Department of Chemistry, Oregon State University, Corvallis, Oregon, 97331, USA*
[2] *Oak Ridge National Laboratory, Neutron Scattering Division, Oak Ridge, Tennessee, 37831 USA*
[3] *School of Chemical, Biological, and Environmental Engineering, Oregon State University, Corvallis, Oregon, 97331, USA*
[4] *Department of Chemistry, University of Calgary, Calgary, Alberta, Canada T2N 1N4, Canada*

Unpublished work.

4.1. Abstract

Neutron total scattering measurements and multi-edge X-ray absorption analysis were performed on a $0.5Ba(Zr_{0.2}Ti_{0.8})O_3$-$0.5(Ba_{0.7}Ca_{0.3})TiO_3$ powder sample. The Ti_{III-II} edges showed that titanium is distorted in the rhombohedral [111] direction (in a $BaTiO_3$-like chemical and bonding environment). Extended X-ray fine structure analysis (EXAFS) was performed on the zirconium K-edge and it was found that zirconium resides in the center of the Zr-O_6 octahedra in cubic symmetry. The local structure was initially modelled with the orthorhombic *Amm*2 space group with unsatisfactory results. To better model the local structure, the results from the EXAFS analysis were incorporated into the small-box pair distribution function (PDF) refinements and the best fit of the observed data was a combination of barium calcium titanate (BCT) and barium calcium zirconate (BCZ) phases.

4.2. Introduction

Due to the environmental toxicity of lead containing materials, there is a demand for new high performance lead-free piezoelectric materials to replace the current commercial standard lead zirconate titanate, $PbZr_{1-x}Ti_xO_3$ (PZT) .[37,43,124,125,168] One of the most promising lead-free alternatives is barium calcium zirconate titanate, $(1-x)Ba(Zr_{0.2}Ti_{0.8})O_3$-$x(Ba_{0.7}Ca_{0.3})TiO_3$ (BZT-*x*BCT), which possesses strong piezoelectric properties, d_{33} ~ 620 pC/N at the x = 0.50 composition (BZT-0.5BCT).[65,66]

It was reported that BZT-0.5BCT adopts the perovskite structure (ABX_3), where the *A*-site is occupied by both barium (85%) and calcium (15%), the *B*-site by

both titanium (90%) and zirconium (10%), and the *X*-site is occupied solely by oxygen. The *A*-site atoms are coordinated by 12 oxygen atoms in cubo-octahedral symmetry, and the *B*-site atoms are coordinated to 6 oxygen atoms in octahedral symmetry, forming a B-O_6 octahedra.[65] Initial studies reported an observed phase sequence from low-temperature rhombohedral (R) *R*3*m*, to tetragonal (T) *P*4*mm*, then finally to cubic (C) $Pm\bar{3}m$ above the Curie temperature (T_c ~ 350 K).[65,67] More recently, two studies have since reported the average structure of BZT-0.5BCT at room temperature, using high energy synchrotron radiation X-ray powder diffraction (SR-XRPD), as a mixture of R and T (57.7% *R*3*m*, 42.3% *P*4*mm*) phases[74] and a mixture of R and orthorhombic (O) (48.2% *R*3*m*, 51.8% *Amm*2).[73]

Additionally, there have been many studies conducted investigating the electromechanical properties[67,148] and origin of piezoelectricity[78,146,163,169] of this system. Including our previous work studying BZT-*x*BCT, where the cause of the enhanced piezoelectricity was found to be the increased domain wall motion that is accessible at the $x = 0.50$ composition . This study was performed on ceramic samples under the application of an electric field via *in situ* high resolution X-ray total scattering. In that work, we were unable to discern the symmetry and structure of local structure due to the weak signal of oxygen that is inherent to X-ray scattering.[169]

While several studies on the average structure can be found in the literature, only two reports on the local structure of BZT-0.5BCT exist, one uses neutron total scattering with large box modeling,[72] and the other utilizes convergent beam electron diffraction (CBED).[76] In the neutron total scattering study, variable temperature neutron total scattering measurements were conducted for BZT-0.5BCT at 150 and

300 K.[72] Total scattering involves collecting both Bragg and diffuse scattering that contains information about the local and the average structure simultaneously. To model the data, reverse Monte Carlo modeling (RMC) was used, which involves creating a large sample "box" of atoms and then individually moving atoms based on input fitting parameters (such as experimental diffraction measurements), and found that the local structure is relatively independent of temperature, contrary to the observed average phase sequence.[65,73,74] Furthermore, they proposed order-disorder behavior to explain the mismatch in local and average structure symmetry. They concluded that the substitution of calcium on the barium site promotes octahedral tilting of ZrO_6 octahedra (~1-3°) while leaving the titanium distortion relatively unaffected.[72]Additionally, CBED was performed and found both 3 *m* (rhombohedral) and 4 *mm* (tetragonal) point group symmetries present at the local scale.[76] Interestingly enough, these local structure studies report conflicting conclusions. RMC modeling trends toward disorder and therefore likely overestimates the atomic disorder and octahedral tilting present in the system. CBED uses a 5 nm probe which is likely approaching average structure length scales.

In all of the different literatures studies the average structure of BZT-0.5BCT has been reported with some combination of the following space groups: *R*3*m*, *Amm*2, *P*4*mm*, and $Pm\bar{3}m$. The reported space groups are related by a group-subgroup relationship where the R, O, and T space groups are all related to the C "parent" structure where each contain a *B*-site distortion of the octahedral in the [111], [011], and [001] direction respectively. This relationship is shown in Figure 4.1(a) and the distortion directions are shown visually in Figure 4.1(b).[170,171]

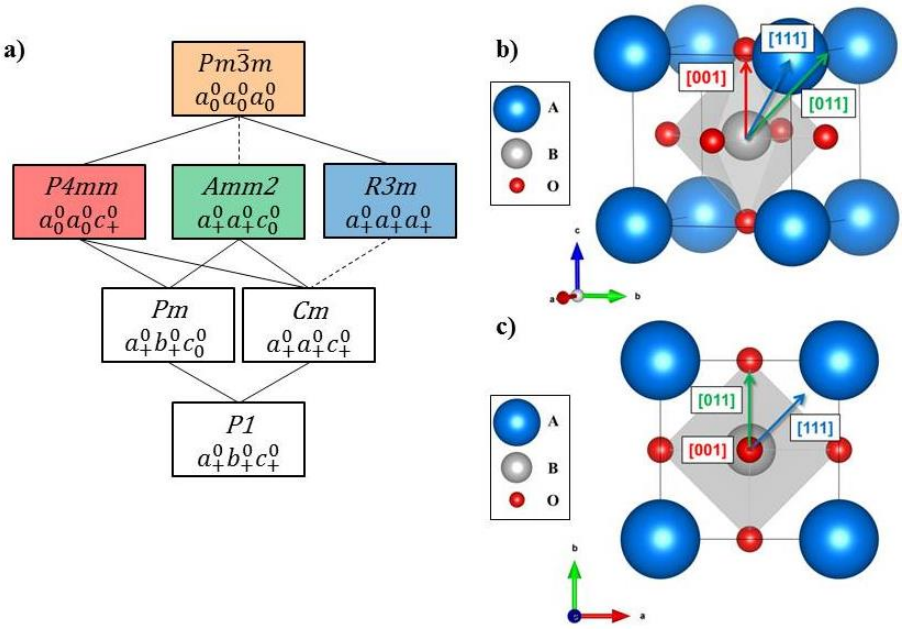

Figure 4.1. a) Subgroup relationships from $Pm\bar{3}m$ space group with modified Glazer notation.[170,171] b) The view down $[\bar{1}\bar{1}0]$ and c) along $[00\bar{1}]$ of ABO_3 unit with distortion directions for *P*4*mm* (red), *Amm*2 (green), and *R*3*m* (blue) space groups from the cubic $Pm\bar{3}m$ cell. The *A*-site cations are shown in blue, the *B*-site cations in grey, and the oxygen atoms in red.[172–175]

The goal of this project is to resolve the conflicting literature reports and to determine the true local structure of BZT-0.5BCT using X-ray absorption spectroscopy (XAS) and neutron total scattering in a complementary fashion. Additionally, small-box modeling will be used to model the neutron pair distribution function (PDF) data obtained from the total scattering experiments. The advantages to small box modeling, particularly for materials that show order-disorder behavior, are that it provides unambiguous results and can be constrained by the results from the XAS studies. It is critical to study the local structure of high-performing materials, particularly $BaTiO_3$ based materials as they are likely to show order-disorder behavior.[176] Where an ordered local structure becomes disordered at higher length scales due to the misalignment of the ordered nano-regions. Consequently the structure that is measured from average structure techniques, such as X-ray

diffraction, no longer depicts the actual chemical and bonding environment of the material.

4.3. Experimental

The polycrystalline sample of BZT-0.5BCT was prepared via standard solid-state synthesis as described by Manjón-Sanz and Culbertson et al.[169] The phase purity of the powder sample was determined via XRPD using a benchtop diffractometer (Miniflex 600, Rigaku).

Multi-edge X-ray absorption spectroscopy (XAS) experiments were performed on BZT-0.5BCT and a phase pure $BaTiO_3$ sample (sample provided from Culbertson et al.[176]) at both hard and soft X-ray regimes. Due to the inherent qualitative nature of XAS measurements, the $BaTiO_3$ sample will serve as a standard to compare and contrast with the BZT-0.5BCT sample. The titanium L-edge and oxygen K-edge (532 eV) were measured at Beamline 6.3.1 of the Advanced Light Source (ALS) at the Lawrence Berkeley National Laboratory (LBNL). Powder samples were uniformly spread on conductive carbon tape and soft XAS (sXAS) measurements were conducted in the total electron yield (TEY) mode. The pressure of the experiment chamber was in the 10^{-8} to 10^{-7} mbar range. The zirconium K-edge (17998 eV) was measured at the Experimental Station 2-2 of the Stanford Synchrotron Radiation Lightsource (SSRL). A zirconium metal reference was used as a standard to calibrate the Zr K-edge. The hard XAS (hXAS) measurements were conducted in transmission and fluorescence yield mode while a double crystal silicon (220) monochromator varied the photon energy from 17800 to 18800 eV. A Lytle

detector with a strontium filter was used to collect the fluorescence signal while ionization chambers were used to detect the incident and transmitted signal. The sample powders were spread homogenously on 25 μm Kapton tape. All XAS spectra were collected at room temperature. XAS normalization and background subtraction were performed using the software package Athena. [177] Normalization was done by fitting the pre-edge background with a linear fit and post-edge background through a cubic-spline. Shell fitting was performed using the software package Artemis[177] in both *k* and real (R) space in the ranges 3-13 $Å^{-1}$ and 1-4.3 Å, respectively. Scattering paths were generated using the feff6 code in Artemis.[177,178]

A phase pure powder sample of BZT-0.5BCT was loaded in a 2 mm diameter quartz capillary (Hampton) and taken to the Nanoscale Ordered Materials Diffractometer (NOMAD)[120] beam-line at the Spallation Neutron Source (SNS)[121] at Oak Ridge National Labs (ORNL) to perform neutron total scattering measurements. Neutron diffraction data were collected at 305 K with a collection time of 30 mins.

The average structure of BZT-0.5BCT was firstly investigated by performing Pawley fits[88] on the as collected neutron total scattering data. The refined structures from Keeble et al.[73] were used as starting models. For each Pawley fit the background terms, unit cell parameters, and peak profiles were refined. The results of the Pawley fit were used as starting models for the analysis using the Rietveld method[75,89] where the scale factor, atomic positions and atomic displacement parameters were also refined. The background was modelled with a Chebyshev polynomial with 6 terms. For Rietveld refinements, the atomic positions and atomic displacement parameters

were constrained to be the same for the *A*- (Ba^{2+} and Ca^{2+}) and *B*-site ($Ti^{4+}$and Zr^{4+}) cations as each pair shares the same crystallographic position.

To investigate the local structure of BZT-0.5BCT the total scattering data were transformed to the PDF, $G(r)$, via a sine Fourier transform as described below:

$$G(r) = 4\pi r[\rho(r) - \rho_o] = \frac{2}{\pi}\int_{Qmin}^{Qmax} Q[S(Q) - 1]\sin(Q_r)dQ$$

where r is the distance from any atom, $\rho(r)$ is the atomic pair-density function, and ρ_o is the number density of the material.[85] This transformation was performed using a Q_{max} of 34.414 $Å^{-1}$ with a software developed in-house specifically for the NOMAD beamline. Q_{max} is the maximum scattering length and functions as the upper limit of the integrand. Ideally, this integration would be performed over a *Q*-range of infinity, but there is a tradeoff between resolution and *Q*-range due to instrument detector limitations. To account for the limited *Q*-range that is experimentally accessible, the Lorch function was applied to the data to remove Fourier ripples (low-*r* oscillations that are consequences of the limited *Q*-range).[179,180] The instrumental parameters Q_{damp} and Q_{broad} used were 0.017659 and 0.0191822 $Å^{-1}$ respectively, as determined from a Nickel standard.[181,182] Furthermore, an empty capillary or blank was subtracted from the total scattering data. The software package Topas (Version 6) was used to perform the Pawley fits, Rietveld refinements, and to model the PDF data.[90,122]

4.4. Results

4.4.1. Multi-edge X-ray absorption analysis

To better understand the results from the XAS, a phase pure $BaTiO_3$ sample was measured to serve as a comparison to the spectral features observed in BZT-0.5BCT. The rational for measuring $BaTiO_3$ as a standard is twofold. Firstly, there is a wealth of literature exploring $BaTiO_3$ with XAS.[183–185] And secondly, BZT-0.5BCT is primarily composed of $BaTiO_3$ with only 15 % calcium on the *A*-site and 10 % zirconium on the *B*-site. In general, XAS is a qualitative technique where reference spectra are critical for contextualizing the observed results, although quantitative fitting can be performed. The results of this study are also compared with the findings of Mastelaro et al.[77] who also performed XAS experiments on the closely related $Ba_{0.9}Ca_{0.1}Ti_{1-x}Zr_xO_3$ (BCZT) system. Unlike the BZT-BCT system, the BCZT system has a fixed *A*-site ratio and the *B*-site occupancy is varied.

The measured titanium L-edge XAS spectra for BZT-0.5BCT and $BaTiO_3$ are shown in Figure 4.2(a). These spectral features are characteristic to Ti^{4+}.[77] More specifically, these features include two pre-edge peaks (labelled A and B) around an energy of 455 and 456 eV which are caused by forbidden dipole transitions resulting in low intensity. The main absorption features appear as four well defined peaks C, D & E, F which correspond to the L_{III} and L_{II} edges, respectively. These four peaks arise from crystal field splitting of the 3d orbitals into the t_{2g} and e_g orbitals. Peaks C and E correspond to the t_{2g} sub-band, whereas peaks D and F the e_g sub-band.[77]

The oxygen K-edge spectra for BCT-0.5BZT and $BaTiO_3$ are shown in Figure 4.2(b). The spectra is composed of six major features (labelled G through L) related

to electronic transitions from the oxygen 1s to hybridized states of the oxygen 2p with barium, calcium, titanium and zirconium character. The first features G and H, correspond to the oxygen 1s to 2p transition and oxygen 1s to titanium 3d transitions, respectively. The separation between the G and H peaks is around 2 eV which is in agreement with crystal field splitting seen in the titanium L-edge XAS spectra. On the higher energy side of feature H there are slight contributions from hybridized orbitals between the oxygen 2p and barium 5d states. Peaks I and J are composed of states with oxygen 2p and calcium 3d and barium 5d character. Finally, peaks K and L correspond to states with mixed oxygen 2p, titanium 4s and 4p and barium p character.[77] From the titanium and oxygen edges, it is clear that the TiO_6 octahedra are in the same chemical and bonding environment in BZT-0.5BCT as they are in $BaTiO_3$. Therefore the titanium must be distorted in the [111] direction within the TiO_6 octahedra in rhombohedral *R*3*m* symmetry, as is the case in $BaTiO_3$.

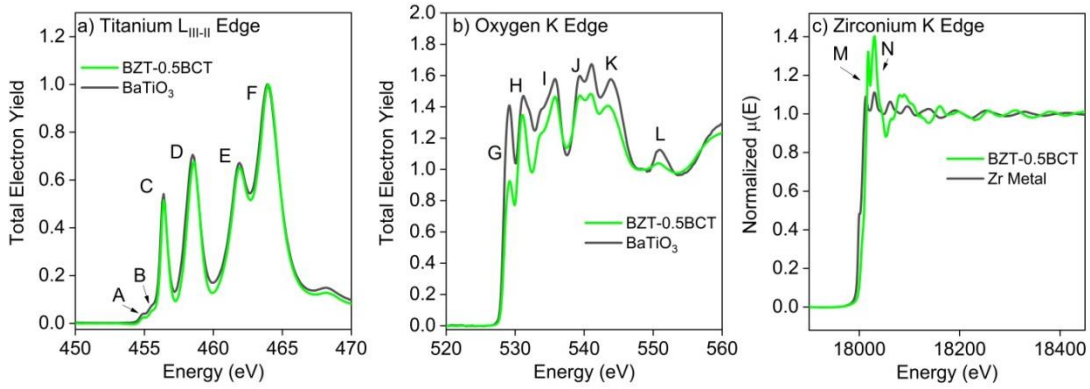

Figure 4.2. X-ray absorption spectra for: a) titanium L_{III-II} edges, b) oxygen K edge, and c) zirconium K edge of BZT-0.5BCT(green continuous line) and $BaTiO_3$(black continuous line).

From the zirconium K-edge measurements, both X-ray absorption near-edge structure (XANES) and the extended X-ray absorption fine structure (EXAFS) spectra were collected for BZT-0.5BCT. In the XANES spectra, Figure 4.2©, the

rising edges (labelled M and N) exhibit a characteristic shift to higher energy (~12 eV) for the Zr^{4+} in BZT-0.5BCT compared to the zirconium metal (Zr^{0}), revealing the increase in the valence state in the oxide sample. The real space spectrum, Figure 4.3(a), has two distinct features which correspond to the single scattering paths between zirconium and oxygen, and multiple scattering paths between Zr and other elements (i.e., Zr, Ti, Ba and O).

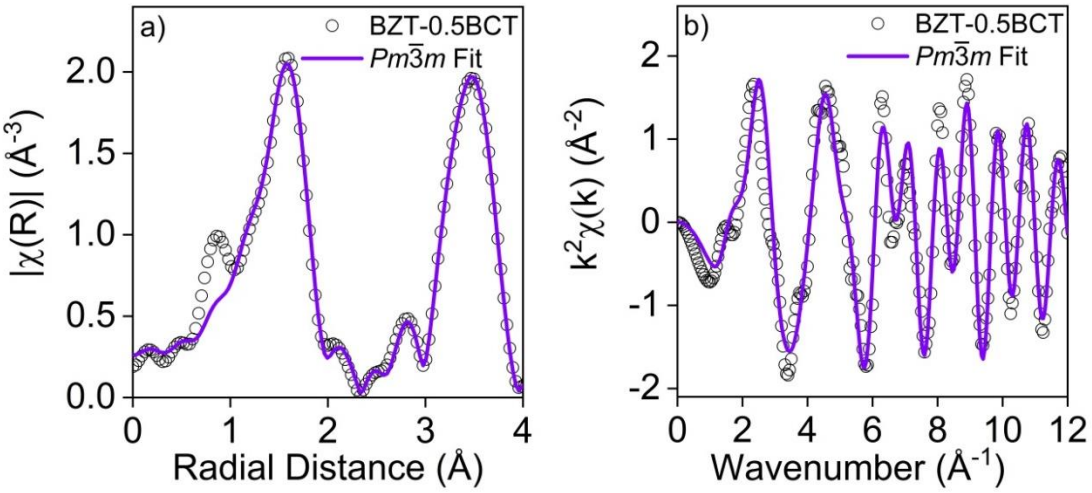

Figure 4.3. For zirconium K-edge EXAFS spectra of BZT-0.5BCT: a) real space spectra and b) *k* space spectra shown (black circles) with shell fitting results (purple continuous line).

Shell fitting and refinement was performed on the collected data from 1-4 Å using initial *R*3*m*, *Amm*2, *P*4*mm*, and *Pm*$\bar{3}$*m* average structure models obtained from the Rietveld refinements of neutron diffraction data (shown in the supplementary information Table S3-S6). For the EXAFS fitting (Figure 4.3), only the cubic model could account for the observed Zr-O bond structure observed and yielded the best fit with six equivalent Zr-O bonds of 2.09 ± 0.01 Å and no octahedral tilting. The tabulated results of the shell fittings are shown in Table 3. It should be noted that the first peak below 1 Å in Figure 4.3(a) is an artifact from the background subtraction

process used to obtain the EXAFS oscillations and was not included in the fitting. A sub-angstrom artifact peak is commonly observed in EXAFS analysis.[186,187]

Table 4-1. Summary of the EXAFS fitting results using the R, O, T, and C models where the reduced chi squared (χ_R^2), standard deviation ($\sigma^2 x10^{-3}$), and refined bond lengths (R_f) are shown.

Model:	χ_R^2	$\sigma^2 x10^{-3}$ (Å^2)	R_f Zr-O_1 (Å)	R_f Zr-O_2 (Å)	R_f Zr-O_3 (Å)
*R*3*m*	447.30	1.5(6)	2.13(4) x 3	2.03(3) x 3	
*Amm*2	584.03	1.0(8)	2.01(7) x 2	2.15(7) x 2	2.08(2) x 2
*P*4*mm*	376.92	1.9(1)	2.00(1)	2.08(1)	2.19(1)
$Pm\bar{3}m$	314.15	4.3(1)	2.09(1) x 6		

4.4.2. Local structure determination from neutron total scattering

The neutron PDF data for BZT-0.5BCT at 305 K is shown in Figure 4.4. Figure 4.4(a) shows the range *r* = 1.5-30 Å. Figure 4.4(b) shows the range *r* = 1.5-3.15 Å, low-*r* correlations, that correspond to the *B*-O bonds and the *A*-O bonds, as indicated by the black arrows.

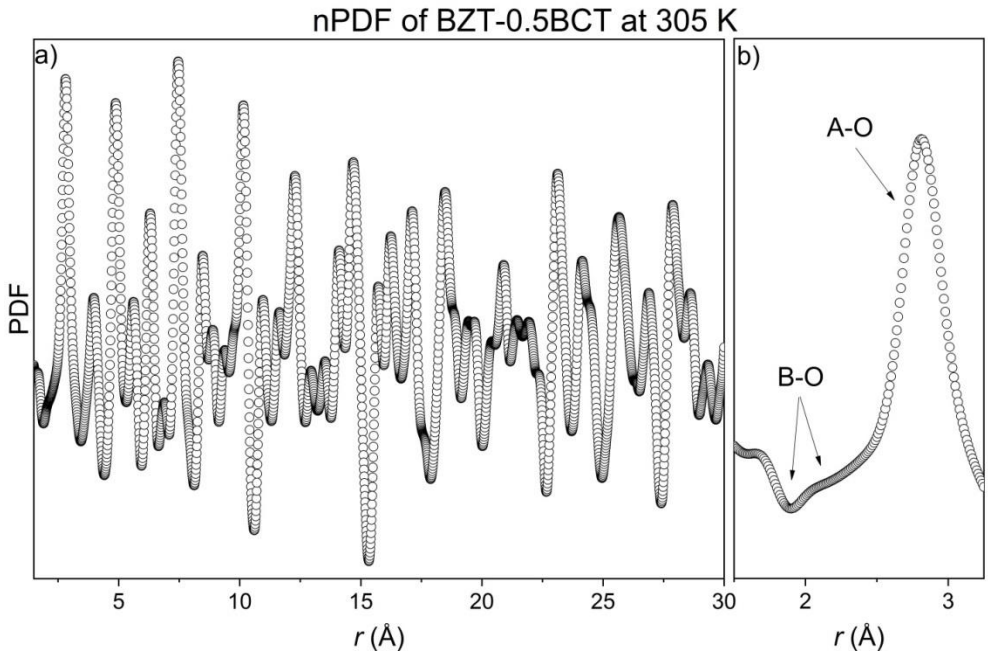

Figure 4.4. Neutron PDF data for BZT-0.5BCT at 305 K for the: a) long range PDF, and the b) low-*r* region PDF.

The PDF data collected is the summation of the partial PDF contributions from each scattering species. In BZT-0.5BCT the *B*-site ions (Ti^{4+} and Zr^{4+}) scatter neutrons very differently, where the titanium (the majority *B*-site atoms) scatters neutrons with a negative phase (titanium coherent scattering length, coh $b = -3.44$ fm) and the zirconium atoms (minority *B*-site atoms) scatter neutrons with a positive phase (zirconium coh $b = 7.16$ fm).[114] The negative scattering intensity from the titanium atoms therefore overlaps and obscures the positive scattering intensity of the zirconium atoms.

Small-box modeling or real-space Rietveld refinements were conducted to determine the structural parameters for BZT-0.5BCT. The neutron PDF data was modeled with the *R*3*m*, *Amm*2, *P*4*mm*, and $Pm\bar{3}m$ space groups from $r = 1.5$ to 35 Å, following the previous literature based on reports of the average structure. For these single phase fits, the orthorhombic *Amm*2 space group yielded the best fit, R_{wp} =

14.9 %, which is in agreement with the neutron diffraction refinement results. However, this single phase model was not able to fit the first *B*-O correlation around ~2 Å (*B*-O_6 bond distances), shown in Figure A.22. To model the low-*r* region, refinements were conducted from 1.5 to 4.5 Å. Single phase refinements in the *R*3*m*, *Amm*2, *P*4*mm*, and *Pm*$\bar{3}$*m* space groups were attempted. Additionally, single phase *R*3*m*, *Amm*2, and *P*4*mm* models with split *B*-site refinements (allowing the titanium and zirconium positions to refine independently) were considered. Two phase models of *R*3*m*-*Amm*2, *R*3*m*-*P*4*mm*, and *R*3*m*-*Pm*$\bar{3}$*m* were also attempted with similarly unsatisfactory results.

To create a model that could account for observed low-*r* peaks in the PDF, the results of the XAS experiments were used to guide and constrain the small-box model. The titanium L_{III} and L_{II} edges and oxygen K-edge indicate that the titanium atoms are displaced in the rhombohedral [111] direction, as is seen in $BaTiO_3$. Furthermore, from the shell fitting the Zr-O_6 octahedra is undistorted and no evidence of tilting was seen. The result that zirconium is undistorted in the ZrO_6 octahedra has also been reported before using neutron total scattering[72,188] and X-ray absorption spectroscopy[77] on BZT-0.5BCT-like systems.

Therefore, a two-phase *R*3*m*-*Pm*$\bar{3}$*m* (BCT-BCZ) model was created where the titanium atoms are in R *R*3*m* symmetry, and the zirconium atoms are in C *Pm*$\bar{3}$*m* symmetry. More specifically, the titanium atoms are displaced towards the faces of the Ti-O_6 octahedra in the [111] direction and the zirconium atoms were in the center of the Zr-O_6 octahedra (undistorted) with C *Pm*$\bar{3}$*m* symmetry. This initial model was constructed and refined. This refinement involved an iterative process where the PDF

of the zirconium BCZ phase was calculated, and then the lattice parameters were changed manually, until the bond lengths matched the experimentally observed bond length from the EXAFS shell fitting, Zr-O bond 2.09 Å

Table 4-2. For BZT-0.5BCT: fit criterion (R_{wp}) of single phase and two phase R-C (BCT-BCZ) refinements of neutron PDF data from r = 1.5 to 4.5 Å.

R_{wp} (%)					
r-range	$R3m$	$Amm2$	$P4mm$	$Pm\bar{3}m$	$R3m$-$Pm\bar{3}m$ (BCT-BCZ)
1.5-4.5 Å	6.14	3.97	5.96	17.2	6.10
1.5-35.0 Å	15.1	14.9	16.0	23.6	16.3

The two-phase model (90% $R3m$, 10% $Pm\bar{3}m$) refinement converged at R_{wp} = 6.10 %, the refined parameters are summarized in Table S7. The PDF refinement is shown in Figure 4.5(a) with the partial PDFs of the *B*-O bond peak for the BCT and BCZ phases shown in Figure 4.5(b). The $R3m$-$Pm\bar{3}m$ model proposed here slightly overestimates the disorder on the first Ti-O peak and slightly underestimates the disorder on the second Ti-O peak. This can be seen where the first peak at r ~1.8 Å in the model is broader than the observed data and the second peak at 2.15 Å is sharper.

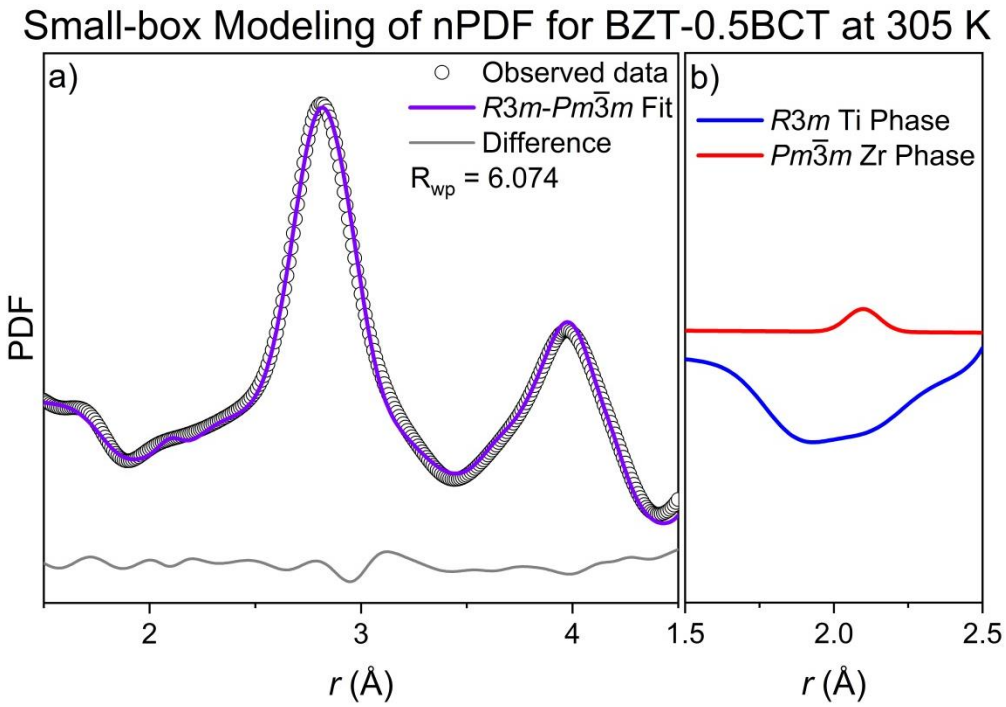

Figure 4.5. Small-box modeling of neutron PDF for BZT-0.5BCT using a two phase *R*3*m*-*Pm*$\bar{3}$*m* (BCT-BCZ) model: a) fitting at 305 K, and b) zoom in of low-*r* *B*-O correlation contributions for each space group.

4.5. Discussion

The material BZT-0.5BCT shows a number of interesting structural and property features that make it a particularly unique and challenging system to study. The structure of BZT-0.5BCT is related to the parent barium titanate structure, that, by itself is surprisingly complex and shows order-disorder behavior, where local rhombohedral titanium distortions exist at all temperatures and the observed average structures are the misalignment of those rhombohedral distortions.[107–110,113] The BZT-0.5BCT system has additional complexity with the introduction of calcium on the *A*-site and zirconium on the *B*-site, and the pseudocubic nature of the observed diffraction data. With the limited resolution inherent to PDF measurements, in this study differentiating between the conflicting literature results was unfruitful based on the results of the Rietveld refinements.

However, from the results of the titanium L_{III}-L_{II} edges and the zirconium K edge XAS measurements and subsequent fitting revealed that there was no displacement of the zirconium ions within the ZrO_6 octahedra. Using the XAS results to inform the small-box model led to the only model, a two phase BCZ-BCT model, that could reproduce the observed results where the titanium ions are distorted in the [111] direction with R symmetry and the zirconium ions are in C $Pm\bar{3}m$ symmetry.

These results fit into the broader scope of a range of literature results that indicate that the chemical stability and symmetry of titanium and zirconium ions in the perovskite structure are relatively independent of any disorder present on the *A*-site and a mixed occupancy on the *B*-site. In both $BaTiO_3$ and in the BZT-0.5BCT system (with 15% calcium on the *B*-site) the titanium ions are displaced in the [111] rhombohedral direction, even when the average structure refines to a non-R structure.[108–110,113]

4.6. Conclusions

Neutron total scattering and multi-edge X-ray absorption data were collected on the material BZT-0.5BCT. Rietveld refinements were performed on the collected diffraction data and small-box modeling was performed on the pair distribution function data. The Rietveld refinements were largely inconclusive due to the pseudocubic nature of BZT-0.5BCT. However from the X-ray absorption analysis it was found that the titanium ions are distorted in the rhombohedral direction whereas the zirconium ions are undistorted in the ZrO_6 octahedra. The XAS results were used to parameterize the small-box modeling where a two phase barium calcium titanate

and barium calcium zirconate (BCT-BCZ) model was able to fit the observed neutron PDF data. This model, which contradicts current literature, is experimentally verified using two different local structure techniques, unlike the previous studies.

4.7. Acknowledgements

Michelle Dolgos, Alicia Manjón-Sanz, and Charles Culbertson would like to thank the National Science Foundation (NSF) under Grant No. DMR-1606909. This research used resources of the Spallation Neutron Source at the Oak Ridge National Labs (IPTS 12380). The authors would like to thank Kate Page and Jue Liu for their help with the data processing, and Yang Ren for his helpful advice. Michelle Dolgos would also like to thank the Canada First Research Excellence Fund for support.

Chapter 5: The Effect of Non-Stoichiometry and B-site Doping on the Local Structure and Ionic Conductivity of Sodium Bismuth Titanate (NBT)

Charles McLouth Culbertson,[1*] Alisa R. Paterson,[2*] Ryan McQuade,[1] David P. Cann,[1] and Michelle R. Dolgos[2*]

[1] *Department of Chemistry, Oregon State University, Corvallis, Oregon, 97331, USA*
[2] *Department of Chemistry, University of Calgary, Calgary, Alberta, Canada T2N 1N4, Canada*

Unpublished work.

5.1. Abstract

Recently it has been shown that sodium bismuth titanate, $Na_{0.5}Bi_{0.5}TiO_3$ (NBT 50), based materials can exhibit strong ionic conduction behavior that could be useful for high temperature electrochemical systems. To understand the mechanism behind the enhanced ionic conductivity, a range of stoichiometric, non-stoichiometric, and doped NBT samples have been synthesized. High resolution X-ray diffraction, X-ray and neutron total scattering, and dielectric and impedance measurements have been performed. There was no observed change in the average and local structure as a function of composition. However, the structure changes rapidly with temperature undergoing the following phase transitions of monoclinic *Cc* to tetragonal *P*4*bm* to cubic $Pm\bar{3}m$. Furthermore, acceptor doping (via bismuth deficiency or magnesium doping) greatly increased the bulk conductivity. This work represents an on-going effort to determine the origin of the enhanced ionic conductivity in NBT-based materials.

5.2. Introduction

Sodium bismuth titanate, $Na_{0.5}Bi_{0.5}TiO_3$, (NBT 50) based materials have traditionally been studied for their ferroelectric and piezoelectric properties as lead free alternatives to lead zirconate titanate (PZT).[42] However, the NBT system has a high leakage current at high temperatures and has a high coercive field, which has limited its use in piezo- and ferroelectric applications.[42] Recently, NBT-based materials have been found to have promising properties as oxygen ion conductors. In 2014, Li et al. found the high temperature leakage current in the NBT system was due

to bismuth deficiencies and oxygen vacancies that are induced during the high temperature processing, particularly due to the loss of Bi_2O_3.[64] Furthermore, they reported that acceptor doping (2% magnesium on the titanium *B*-site) dramatically increased the ionic conductivity (~0.01 S cm^{-1} at 600 °C).[64]

Since then, undoped,[189] A-site non-stoichiometric (sodium non-stoichiometry[190] and bismuth non-stoichiometry[189]), acceptor doped,[189] and donor doped NBT[27] have been investigated. These various modifications change the observed electrical behavior to three observed types: oxide-ion conduction (type I), mixed ionic-electronic conduction (type II), and insulating or dielectric behavior (type III).[27] There have been various defect mechanisms proposed for each type of observed behavior.[27]

For stoichiometric NBT 50 (nominal composition $Na_{0.5}Bi_{0.5}TiO_3$), which shows type I behavior, the electrical conductivity is dominated by oxide-ions where oxygen vacancies are created from the loss of Bi_2O_3 and increased oxygen mobility is attributed to polarized Bi^{3+} ions and weak Bi-O bonds. The conductivity of this system can be increased by generating more oxygen vacancies as is observed in 1% bismuth deficient "NBT 49" (nominal composition $Na_{0.50}Bi_{0.49}TiO_3$: $NB_{0.49}T$). Conversely, bismuth excess can suppress the conductivity by compensating for the loss of Bi_2O_3. A 1% bismuth excess "NBT 51" (nominal composition $Na_{0.50}Bi_{0.51}TiO_3$: $NB_{0.51}T$) leads to type III behavior, however counterintuitively a 2% bismuth excess can reintroduce oxide-ion conductivity behavior resulting in type II behavior.[27]

Although the change in conductivity has been well evaluated from a defect and property standpoint, there has yet to be a definitive structural study that reveals the origin of the ionic conductivity in NBT-based materials. The existing structural work on NBT was mostly performed while NBT was still thought of as only a lead-free replacement and therefore the work is largely limited to the nominal stoichiometric composition. Most of the work into the structure and phase transformation sequence in the parent NBT structure was performed by Aksel et al.[58,191] The average structure was found to be monoclinic *Cc* at room temperature, tetragonal *P*4*bm* at elevated temperatures, and finally cubic $Pm\bar{3}m$ at high temperatures.[58,191] These space groups (*Cc*, *P*4*bm*, and $Pm\bar{3}m$), in general, are all part of the broader perovskite family with the form ABX_3, where the *A*-site cations are surrounded by 12 anions in cubo-octahedral coordination and the *B*-site cations are surrounded by 6 anions in octahedral coordination. The BX_6 octahedra form a corner shared 3-diemensional network that surrounds the *A*-site.

Furthermore, the local structure of NBT has been investigated by Aksel et al.[192], Rao et al.[193], and Keeble et al.[60] These works have found that the local structure has significant variance from the refined monoclinic average structure. More specifically, Aksel et al. used X-ray and neutron pair distribution function (PDF) data to find that the Na^+ and Bi^{3+} ions were found to adopt significantly different atomic positions that are averaged out as large thermal parameters in traditional diffraction refinements.[192] Rao et al. used a combination of electron, X-ray, and neutron diffraction with first-principle calculations to determine that there are locally ordered regions that average out to appear “monocliniclike” over larger sampling ranges (*r*-

ranges) and that the monoclinic structure was not the ground state structure from their calculations.[193] The work of Keeble et al. showed from large box modeling of neutron PDF data that there are two different displacement directions for the bismuth ions, which lead to the unique properties observed.[60]

The goal of this work is to determine the structural origin of the enhanced ionic conductivity observed in NBT-base materials due to non-stoichiometry and doping, by studying the both the long-range and local order, and the electrical properties of NBT. To do so, a holistic approach is needed where a number of complementary techniques are invoked. For this study, high resolution synchrotron X-ray diffraction, synchrotron X-ray total scattering, and neutron total scattering will be used to investigate the structure of NBT-based materials over a range of temperatures. The electrical properties will be determined by dielectric measurements and electrochemical impedance spectroscopy.

5.3. Experimental

Due to the complex nature of the structure of these materials several complementary techniques were employed. After synthesis of the materials and preliminary phase purity was determined (via X-ray diffraction), synchrotron diffraction data (Section 5.3.2), synchrotron total scattering data (Section 5.3.3), and neutron total scattering data (Section 5.3.4) were collected. Furthermore, dielectric and impedance measurements were performed (Section 5.3.5).

5.3.1. Solid State Synthesis

Polycrystalline samples of stoichiometric (NBT 50), 1% bismuth deficient (NBT 49), 1% bismuth excess (NBT 51), and 2% magnesium B-site doped (NBT 50 Mg 2) sodium bismuth titanate samples were synthesized via standard ceramic synthesis. The reference name and nominal stoichiometry are summarized in Table 5-1**Error! Reference source not found.** for clarity.

Table 5-1. A list of the sample reference names and nominal stoichiometry for synthesized polycrystalline NBT materials.

Reference Name	Nominal Stoichiometry
NBT 49	$Na_{0.50}Bi_{0.49}TiO_3$
NBT 50	$Na_{0.50}Bi_{0.50}TiO_3$
NBT 50 Mg 2	$Na_{0.50}Bi_{0.50}Ti_{0.98}Mg_{0.02}O_3$
NBT 51	$Na_{0.50}Bi_{0.51}TiO_3$

High purity starting materials Na_2CO_3 (Alfa Aesar 99.95%), Bi_2O_3 (Strem 99.9%), TiO_2 (Cerac 99.9%), MgO (Alfa Aesar 99.95%), and Nb_2O_5 (Alfa Aesar 99.995%) were weighed in stoichiometric amounts, mixed well, and ground into a homogenous powder in a mortar and pestle. The Na_2CO_3 was heated at 200 °C for 24 h prior to being weighed. The mixed powders were loaded into a vibratory mill with ethanol and yttrium stabilized zirconia grinding media and milled for 6 h. The milled slurry was dried at 70 °C for 24 h. The dried powder was then loaded into a 13 mm die (Carver Inc.) and pressed into pellets. The pellets were calcined at 800 °C for 2 h with ramp rate of 4 °C for heating and 5 °C for cooling. After heating, the pellets were crushed and ground well. The ground powders were then vibratory milled again, with the same conditions as before. The milled slurry was dried again at 70 °C for 24 h. The dried powder was mixed with a 2% polyvinyl butyral in ethanol binder

solution. The solution was mixed and dried. Finally, the dried powder was pressed into pellets. The pellets were heated first at 400 °C for 1 h to remove the binder and then heated at 1100 °C for 1 h (with the same heating rates as before). The phase purity of each sample was determined via X-ray diffraction, shown in Figure 5.1.

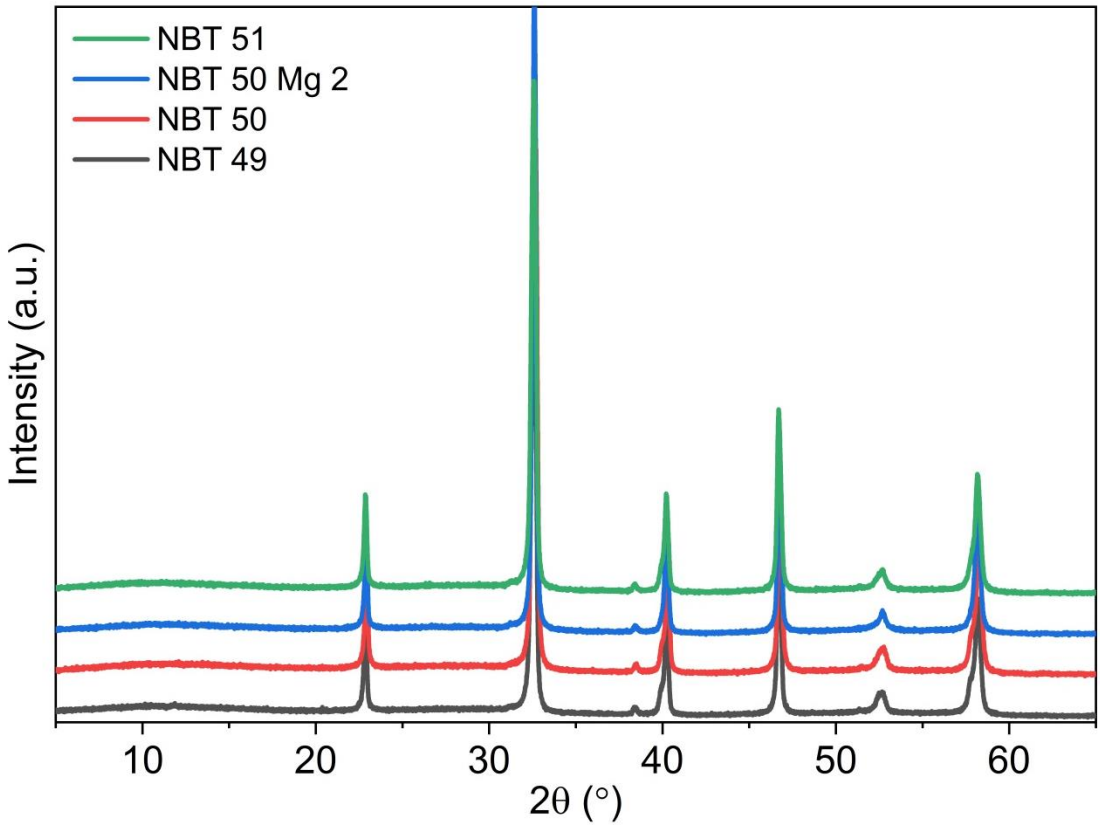

Figure 5.1. X-ray diffractograms of phase pure NBT samples from a benchtop diffractometer.

5.3.2. Synchrotron X-Ray Diffraction at 11-BM

The samples were ground into fine powders and loaded into quartz capillaries. The capillary samples were taken to the 11-BM beam line at the Advanced Photon Source (APS) at the Argonne National Labs (ANL). The 11-BM beamline utilizes 30 keV X-rays with a corresponding wavelength of 0.41283 Angstroms. The capillaries

were mounted on a rotating goniometer and placed between two resistive wire heating elements. High resolution synchrotron X-ray diffraction was collected for each sample at room temperature, 400, 500, 600 and 700 °C. The data collection time for each measurement was 30 minutes. Room temperature diffraction patterns are shown in Figure 5.2.

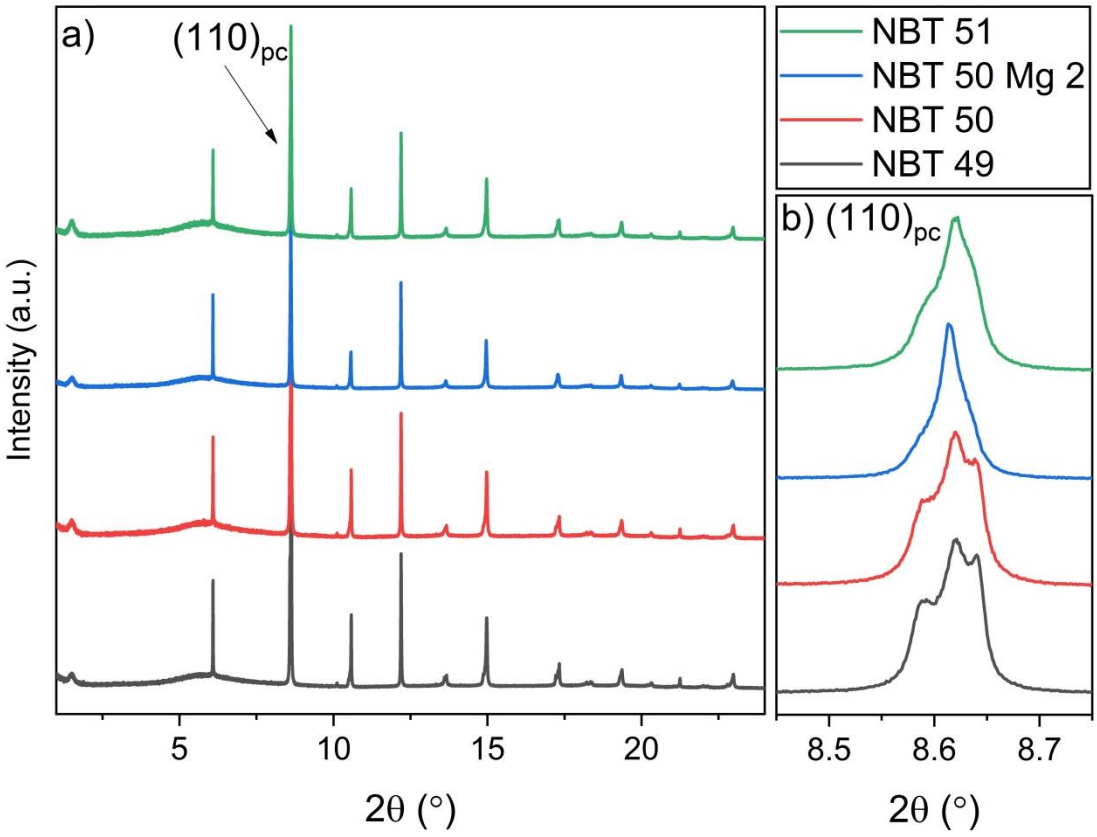

Figure 5.2. High resolution synchrotron diffraction data for a) NBT samples from the 11-BM beamline and $(110)_{pc}$ reflection at room temperature.

5.3.3. Synchrotron Total Scattering Measurements at 11-ID-B

The samples were then taken to the 11-ID-B beamline at ANL to collect synchrotron total scattering data.[157] An incident X-ray wavelength of 0.1430 Å (86.70

keV) with a beam size of 500 by 500 microns was used. Each sample was placed in a quartz capillary that was 240 mm from the detector. Resistive wire heating elements and a thermocouple were then mounted near the sample to control the temperature. The temperature was varied from 25 to 700 °C at a ramp rate of 5 °C/min with 2 minute data collection at 25, 100, 200, 300, 400, 500, 600, and 700 °C. At room temperature a CeO_2 and nickel metal standard were also measured. All total scattering measurements utilized an amorphous silicon flat-panel area detector (Perkin Elmer).

The collected image file data (.tiff format) was processed to the scattering intensity function, $I(Q)$, using the Fit2D software,[158] where the measured CeO_2 standard was used as a calibrant. The $I(Q)$ data was reduced to the PDF using the PDFgetX3 software,[159] during which the quartz capillary background was subtracted. A Q_{max} of 22 Å was used during the data reduction. The processed PDF data for all NBT compositions at room temperature is shown in Figure 5.3.

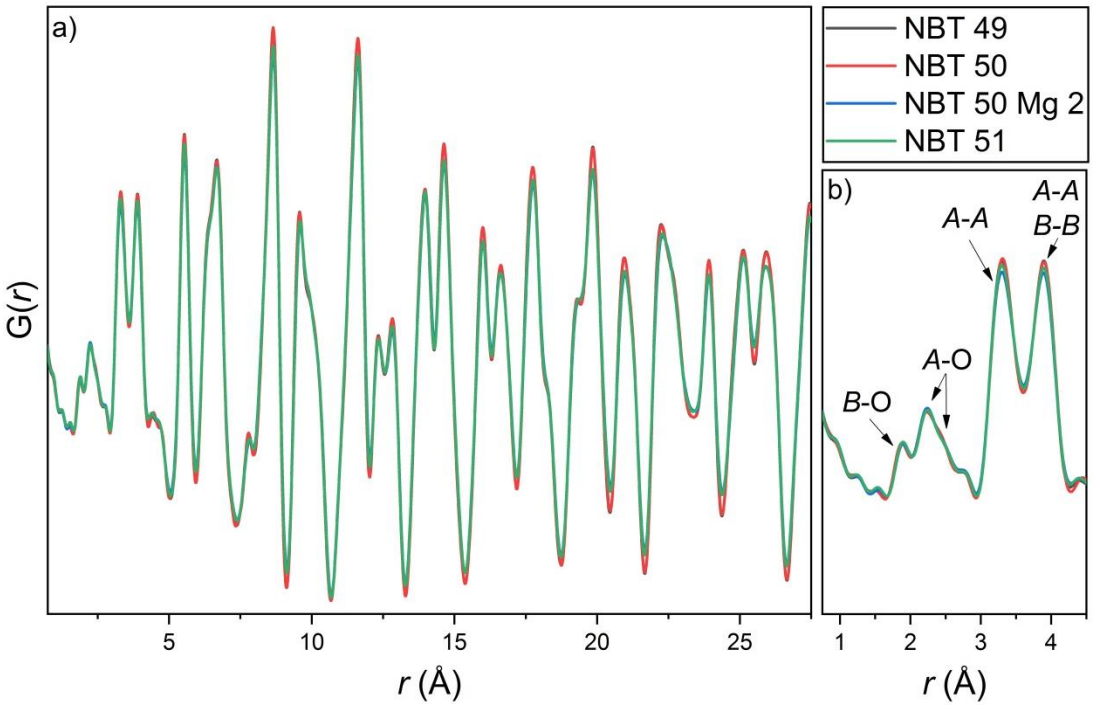

Figure 5.3. a) Long range synchrotron PDF data and b) zoom-in of low-*r* region with *B*-O and *A*-O bond lengths, and *A*-*A* and *B*-*B* correlations for all NBT compositions.

5.3.4. Neutron Total Scattering Measurements at NOMAD

The samples were also taken to the NOMAD beamline[120] at the Spallation Neutron Source[121] at Oak Ridge National labs to collect neutron total scattering data. The samples were loaded into vanadium cans and data collected for ~48 minutes at 25, 150, 400, 600 and 700 °C (with a 70 mm MICAS furnace) at a ramp rate of 10 °C/minute. The data was processed and reduced to the PDF using the Advanced Diffraction Environment (ADDIE) GUI utilizing the Mantid framework with a range of Q_{max} values (~20-50 Å). The Lorch function was applied to the data to account for low-*r* noise.[179] A comparison of the low-*r* region of the PDF with and without the Lorch function and a comparison of the different Q_{max} values used are shown in Figure 5.4. The resulting processed neutron PDF data is shown in Figure 5.5.

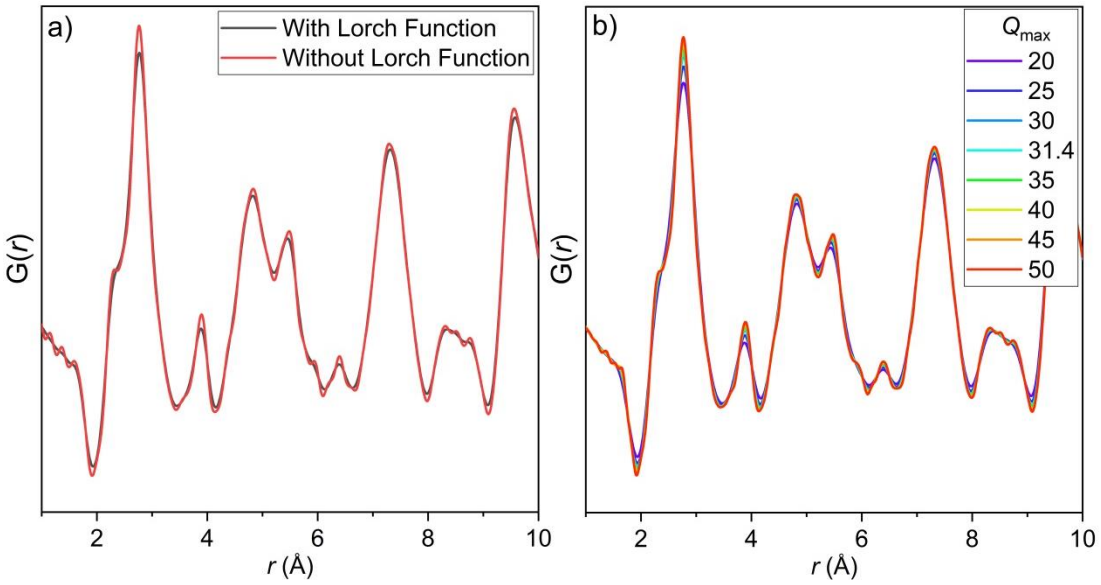

Figure 5.4. Neutron PDF data for NBT 50 at 25 25 °C showing the a) comparison between the data with and without the Lorch function, and, b) effect of the different Q_{max} values on the data processing.

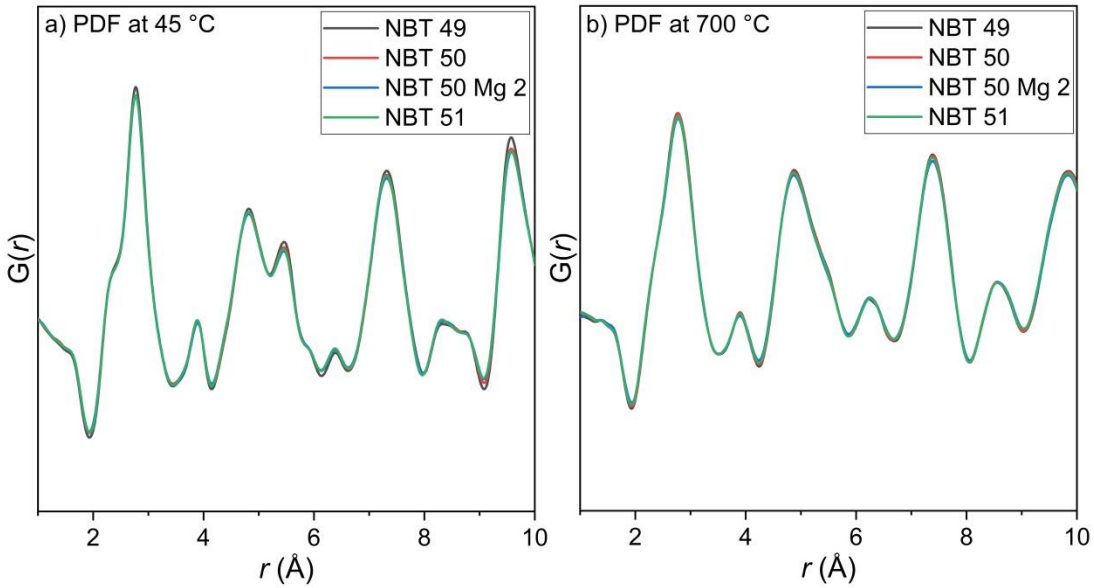

Figure 5.5. Neutron PDF data for NBT samples at a) 45 and b) 700 °C.

During cooling the NBT 50 sample was measured once more at 150 °C, to see if there were any permanent structural modifications imposed by the high temperatures. The

PDF data for NBT 50 on initial heating and then subsequent cooling at 150 °C is shown in Figure 5.6.

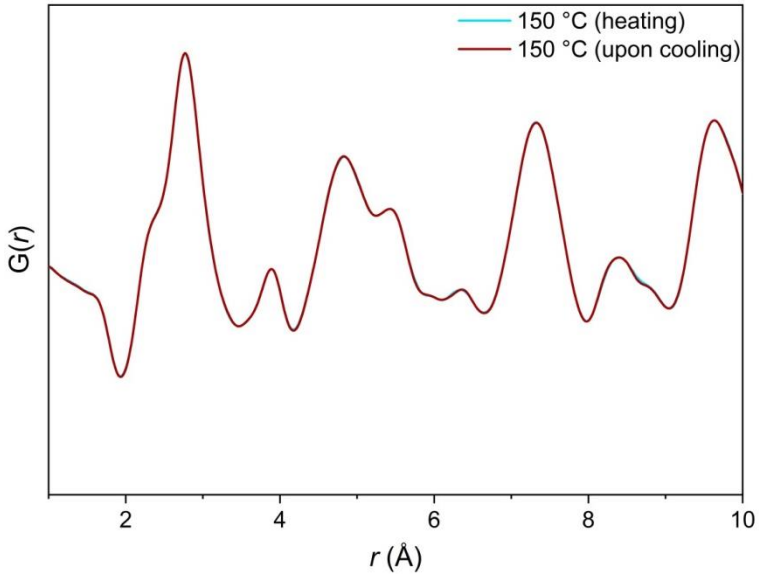

Figure 5.6. A comparison of the neutron PDF for NBT 50 upon initial heating to 150 °C and subsequent cooling to 150 °C (after T_{max} = 700 °C).

5.3.5. Dielectric and Impedance Spectroscopy Measurements

To collect dielectric and impedance spectroscopy measurements, dense pellets were required. The theoretical crystallographic density was calculated from the X-ray diffraction patterns, the calculated density for stoichiometric NBT was 5.98 g/cm^3. The density of each sample pellet was determined by an Archimedes balance. There was some variation in the measured density between individual pellets, ranging from 94 to 97% of the theoretical density. The densest pellets for each composition were polished down to ≤ 0.5 mm thickness with a mirror finish using a semi-automatic polishing machine (LaboPol5, Struers) with a series of P400, P1200, and P4000 SiC foils (Struers). The polished pellets were painted with silver electrodes (Heraeus

C1000) which were fired at 650 °C for 2 h with a heating and cooling rate of 1 °C/min. The sides of the pellets were hand polished with sandpaper to remove any deposited silver paint.

The prepared pellets were placed in a high-temperature measurement cell (NorECS Probostat) and inserted into a tube furnace equipped with a Carbolite VST 12/300 temperature controller. Capacitance and loss were collected as a function of frequency and temperature using an HP 4192A LF Impedance Analyzer. Measurements were taken from 1 kHz to 1 MHz in the temperature range of 25 to 500 °C. The heating and cooling rate used was 3 °C/min. The dielectric permittivity and loss for NBT 50 upon cooling are shown in Figure 5.7.

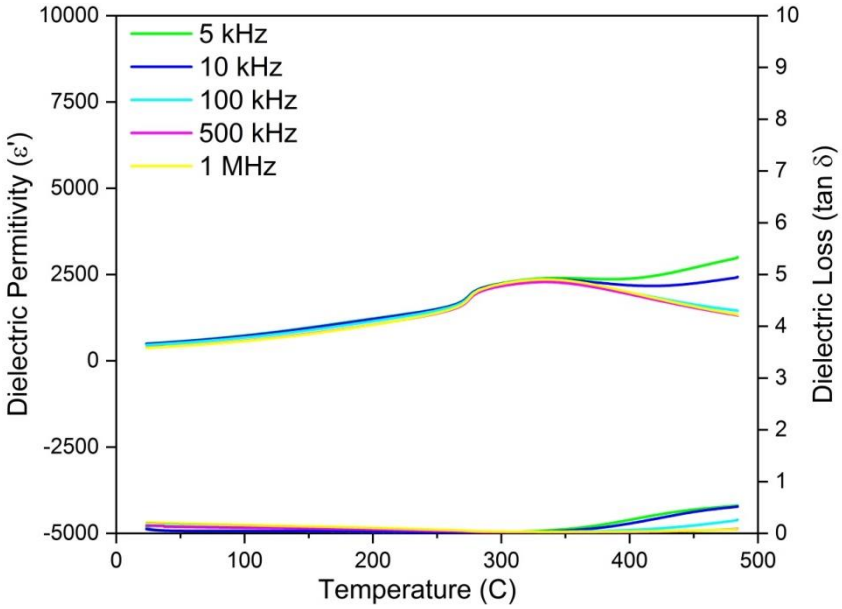

Figure 5.7. Dielectric permittivity of NBT 50 upon cooling at 5, 10, 100, and 500 kHz and 1 MHz.

Impedance spectroscopy measurements were performed using an impedance gain-phase analyzer (Solartron 1260) connected to a dielectric interface

(Solartron1296). Samples were placed in high-temperature measurement cell (NorECS Probostat) that was inserted into a tube furnace equipped with a Carbolite VST 12/300 temperature controller. Impedance data was collected from 250-550 °C in 50 °C intervals over a wide frequency range (0.1 Hz to 1 MHz). The collected impedance data, displayed as a Cole-Cole plot of the imaginary impedance (*Z''*) versus the real impedance (*Z'*), for NBT 50 is shown in Figure 5.8.

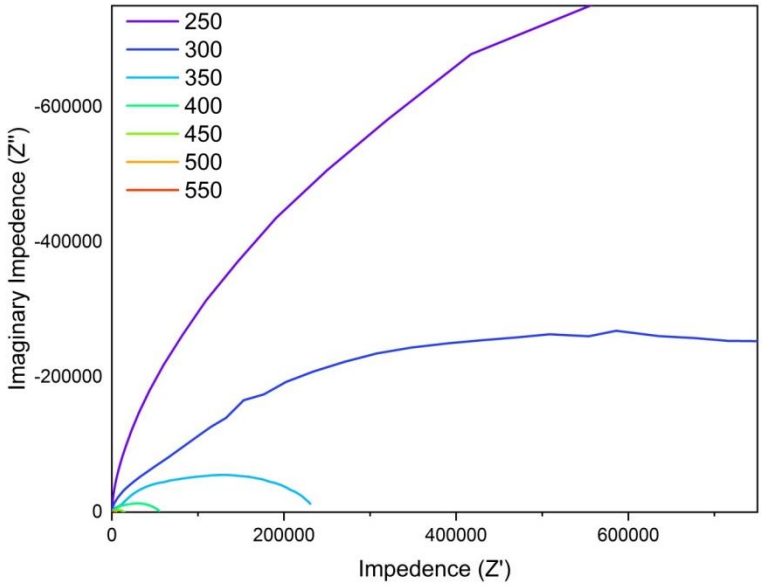

Figure 5.8. Cole-Cole plot of NBT 50 impedance data from 250 to 550 °C.

5.4. Results

The results for the average structure analysis from diffraction data (Section 5.4.1), local structure determination from total scattering (Section 5.4.2), and electrical properties from dielectric and impedance measurements (Section) are described in the following sections.

5.4.1. Average Structure of NBT

At room temperature, all of the samples appear to be monoclinic as is expected for these materials.[58] The monoclinic *Cc* space group is clear from the characteristic splitting of the $(110)_{pc}$ reflection. As the temperature is increased, the structure undergoes a phase transition to tetragonal (*P*4*bm*). Similar to the monoclinic phase, the tetragonal phase can be identified by the splitting of the $(200)_{pc}$ reflection. The high resolution X-ray diffraction from the 11-BM beamline for NBT 50 from 25-700 °C is shown in Figure 5.9a, with the $(200)_{pc}$ and $(110)_{pc}$ reflections shown in panels b) and c), respectively.

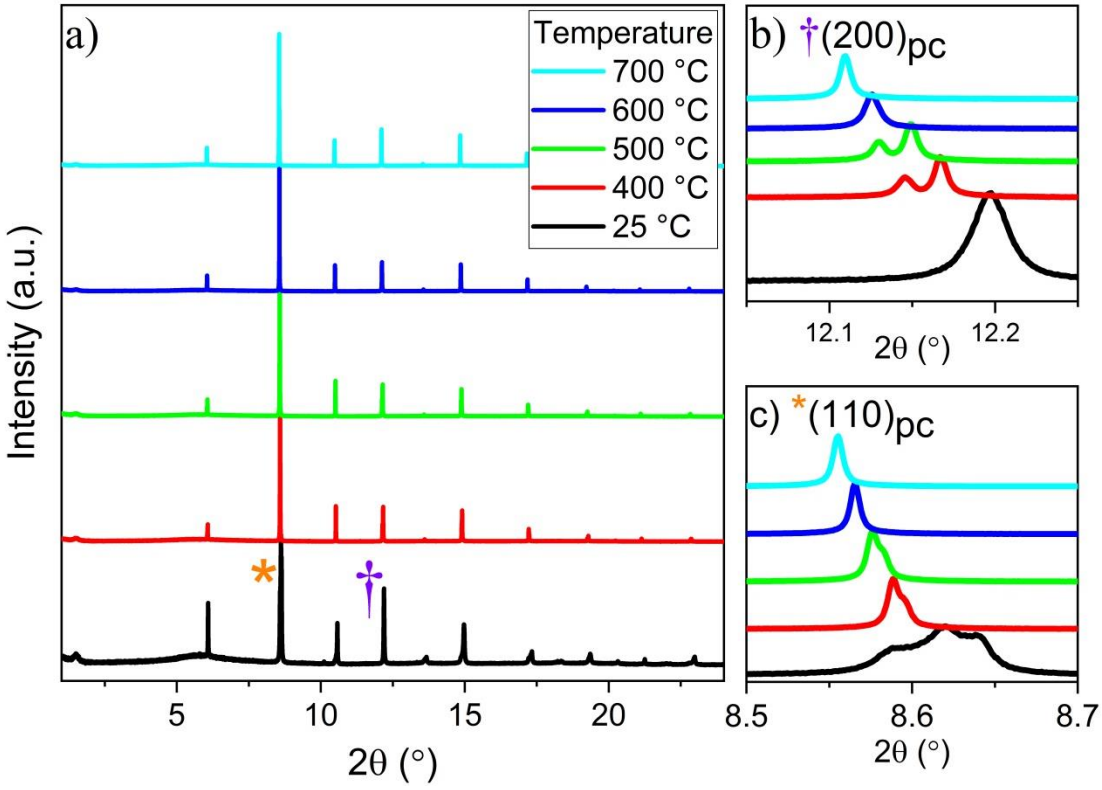

Figure 5.9. a) High resolution synchrotron X-ray diffraction data for NBT 50 showing b) $(200)_{pc}$ and c) $(110)_{pc}$ reflections from 25-700 °C.

At high temperatures, the structure transitions to cubic ($Pm\bar{3}m$). For the stoichiometric $Na_{0.5}Bi_{0.5}TiO_3$ (NBT 50) sample, the tetragonal ($P4bm$) phase is present at the 400 and 500 °C measurements and the cubic phase is observed the at 600 and 700 °C measurements. However, in the non-stoichiometric bismuth deficient NBT sample, $Na_{0.5}Bi_{0.49}TiO_3$ (NBT 49), the tetragonal phase is only present at 400 °C. The deficiency appears to destabilize the crystal structure leading to the disordered cubic phase at lower temperatures. The same effect is observed in all of the non-stoichiometric samples (NBT 51) and magnesium doped sample (NBT 50 Mg 2). Any deviation from the stoichiometric NBT parent structure leads to the early onset of the high-temperature cubic phase.

5.4.2. Local Structure of NBT

There were no significant changes observed between the PDF (both X-ray and neutron) data of the different NBT compositions (NBT 49, NBT 50, NBT 50 Mg 2, and NBT 51). It is likely that the structural changes induced by the bismuth deficiency/excess and the magnesium doping are too small to be detected by the bulk total scattering technique. The X-ray and neutron PDF for all compositions around room temperature are shown in Figure 5.10.

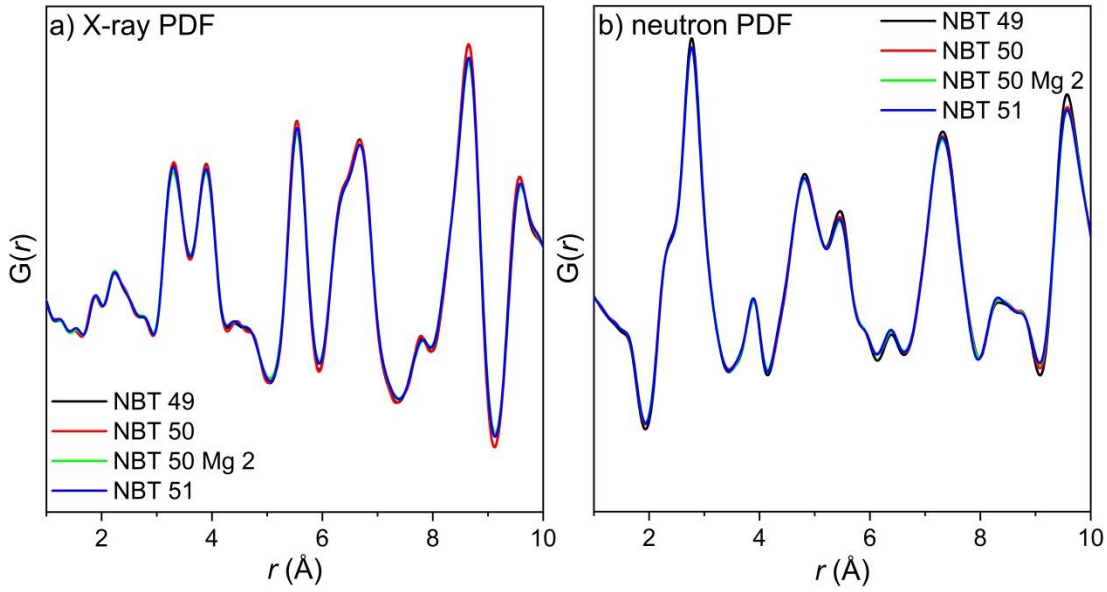

Figure 5.10. Low *r*-range a) X-ray PDF and b) neutron PDF for NBT compositions.

Due to the lack of difference in the PDF data between compositions, the differences in the local structure as a function of temperature will be discussed in reference to the NBT 50 neutron data. As neutrons are inherently more sensitive to oxygens, the neutron PDF data better shows the oxygen correlations that are critical to understand the structure. In general, as the temperature increases there is a clear change in symmetry and a dramatic increase in the atomic disorder. The symmetry change can be seen visually as the *A*-O shoulder peak at ~2.25 Å and the *A*-*A*/*B*-*B* peak at ~5.5 Å change in intensity, shown in Figure 5.11.

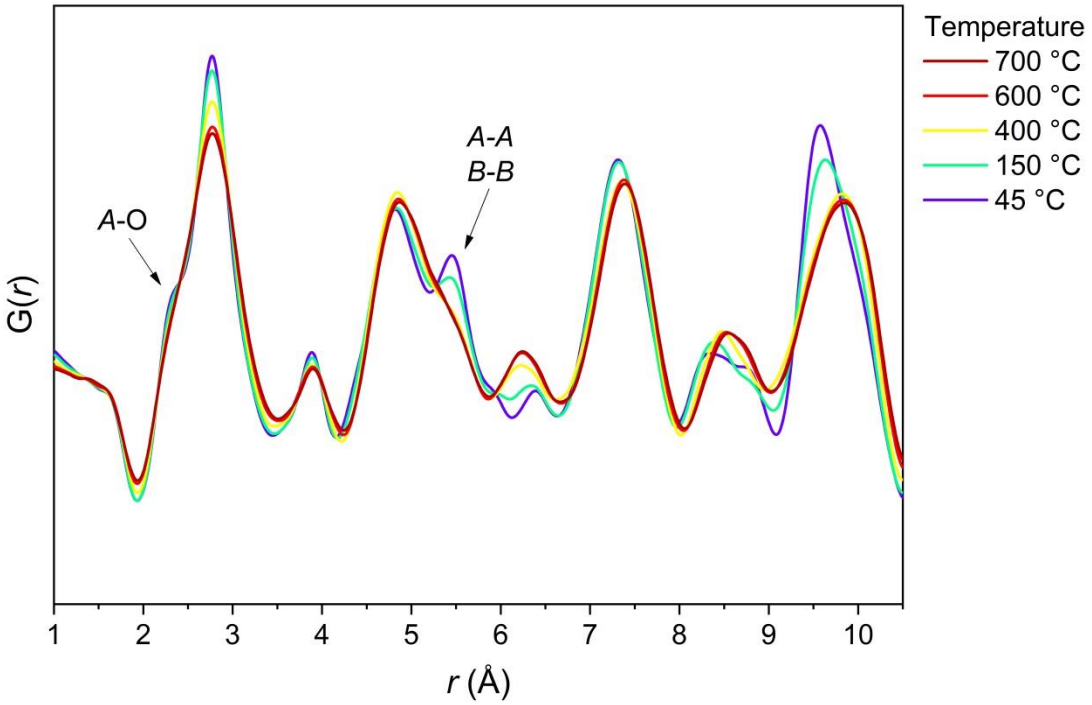

Figure 5.11. Neutron PDF data of NBT 50 at 45, 150, 400, 600, and 700 °C.

As these peaks vanish the structure changes steadily towards a highly disordered cubic phase. One clear indicator of this transition is the increase in the uniformity (or evenness) of the PDF peaks that is indicative of cubic symmetry and the disorder is visible as the peaks broaden significantly. The peaks also shift towards higher-*r* as the lattice expands at higher temperatures.

Preliminary small-box model refinements were conducted at each temperature for the NBT 50 neutron data using the TOPAS-Academic (Version 6) software.[90] Although the average structural models yielded the best fit at each individual temperature, no single average structure model was able to fully recreate the complex local structure observed. An example of a fit for NBT 50 at room temperature with the monoclinic *Cc* space group is shown in Figure 5.12. These unsatisfactory fits are expected as each model only has one bismuth distortion (or none in the cubic model)

which contradicts previous work showing that there are two clear bismuth distortion directions.[60] Furthermore, in these preliminary models the *A*-site sodium and bismuth ions were constrained to the same atomic position when it has also been reported that they inhabit different positions in the crystal structure.[192]

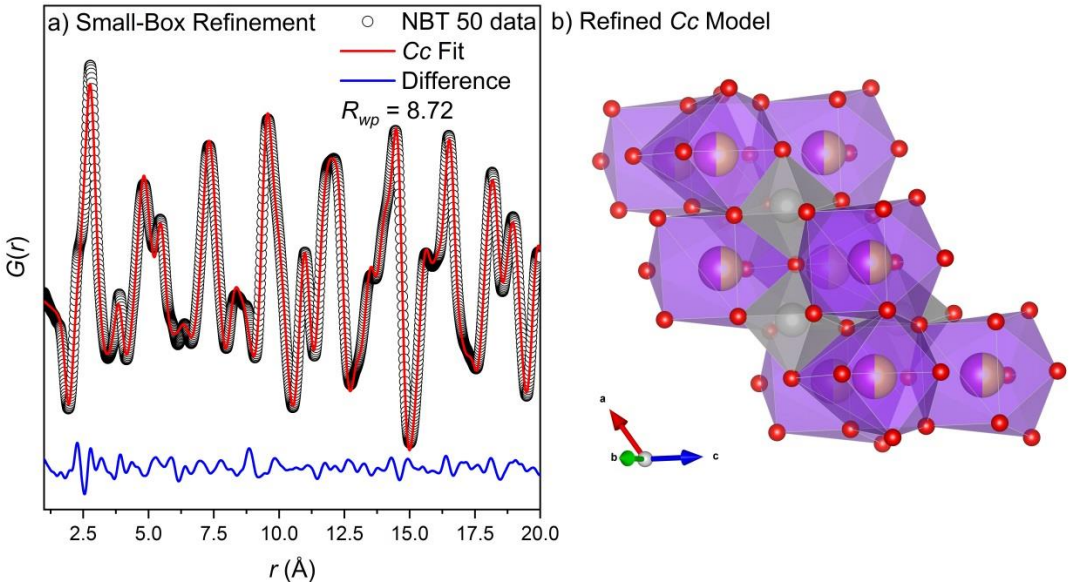

Figure 5.12. a) Small-box modeling fit and b) refined model for neutron PDF data of NBT 50 at room temperature with the monoclinic *Cc* space group.

5.4.3. The Electrical Properties of NBT

The dielectric permittivity and loss are extremely useful measurements to monitor the onset of the transition from insulator to conductor. Figure 5.13 shows the dielectric permittivity (solid lines with left axis) and the dielectric loss (dashed lines with right axis) of all compositions at 100 kHz upon cooling.

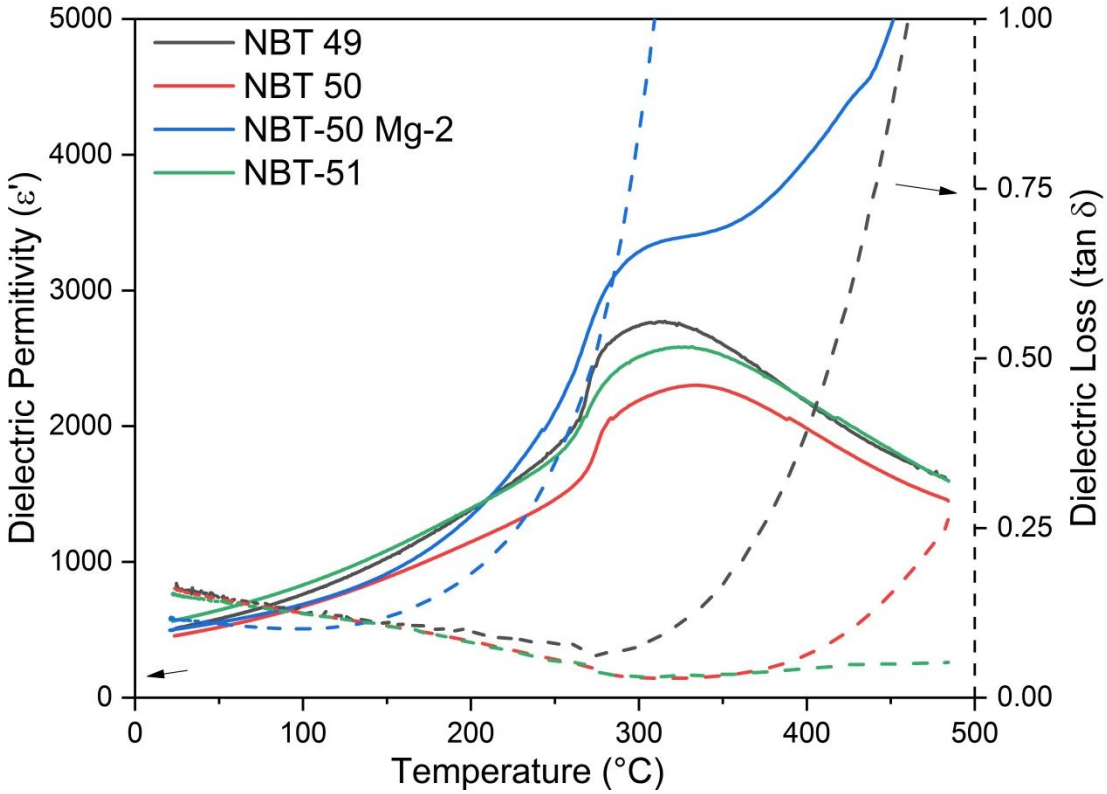

Figure 5.13. Dielectric permittivity (solid lines) and dielectric loss (dashed lines) for all NBT compositions at 100 kHz upon cooling.

For NBT 50 there is a rise in the dielectric loss starting around ~400 °C, corresponding to the leakage current that was referred to in the introduction.[42] The bismuth excess sample, NBT 51, does not show this feature and the loss remains low. The other samples, NBT 50 Mg 2 and NBT 49, show a sharp rise in the loss at ~175 and ~325 °C, respectively.

To further investigate the electrical properties, impedance spectroscopy was performed on each NBT composition from 250 to 450 °C. However, the NBT 51 sample was so resistive at the accessible temperatures that no reliable data was able to be collected. The impedance data that was collected for the remaining compositions was fit with equivalent circuits utilizing constant phase element (CPE) components

with the software ZView® (Scribner Associates, Inc.). The bulk and grain boundary conductivity values were extracted from the equivalent circuit modeling and Arrhenius-type plots were constructed (Ln(σ) versus 1000/T). From the slope of the Arrhenius plots the activation energy (E_a) was calculated for each composition. The activation energy for NBT 49, 50, and 50 Mg 2 was around 0.72-0.75 eV.

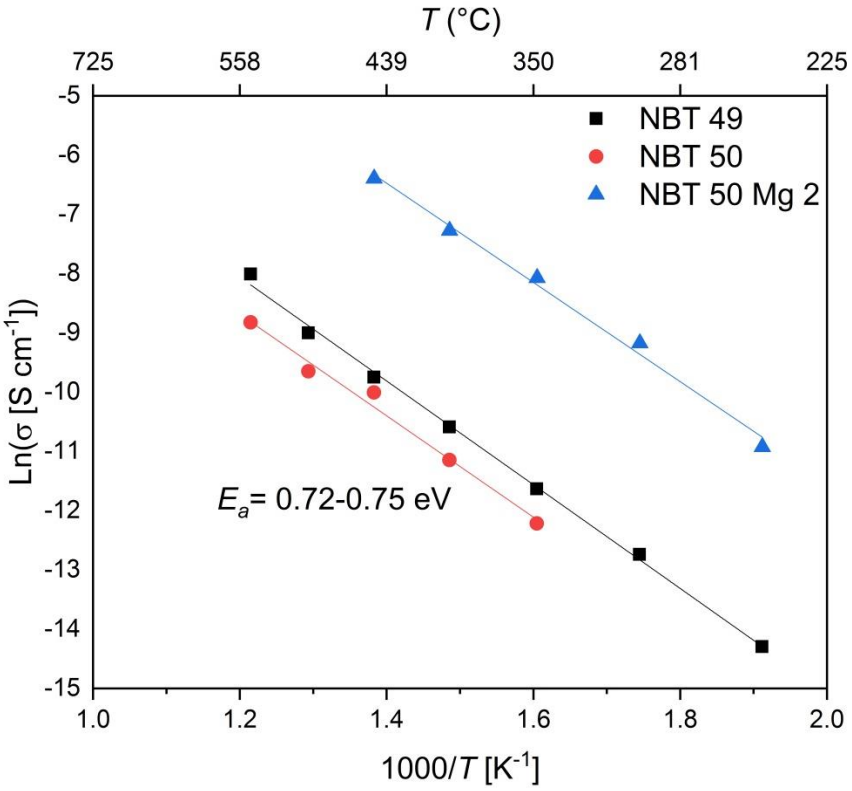

Figure 5.14. Arrhenius-type plot (Ln(σ) versus 1000/*T*) for NBT compositions.

5.5. Discussion

The average structure of the non-stoichiometric and doped NBT samples varied only slightly from the stoichiometric NBT 50. This variation was that the tetragonal (*P*4*bm*) phase transitioned to the cubic ($Pm\bar{3}m$) phase at a lower temperature. ~500 °C. The increase in atomic disorder due to the non-stoichiometry

and doping seem to destabilize the more ordered tetragonal phase in favor of the highly disordered cubic phase. This type of destabilizing behavior is commonly observed in relaxor ferroelectrics where chemical disorder leads to cubic or pseudocubic phases.[194]

The local structure from both X-ray and neutron PDF measurements show no obvious changes in the local order of NBT due to the non-stoichiometry and doping. However, due to the small atomic percent (1% non-stoichiometry in the case of NBT 49 and NBT 51, and 2% doping on the *B*-site for NBT 50 Mg 2) of these changes they may hidden by the bulk scattering. Although there was little change in the local structure between the different compositions, the local structure of any of the NBT compositions versus temperature showed dramatic changes. These changes show a transition from monoclinic (*Cc*) to tetragonal (*P*4*bm*) to cubic ($Pm\bar{3}m$) as the temperature is increased. However, these average structure space groups do not fully encapsulate the disorder that is present in the system.

Although the average and local structure showed only minor changes that were caused by the increased temperature, the physical properties show dramatic changes. The increase in conductivity is immediately noticeable in the dielectric loss, which shows that magnesium doped (NBT 50 Mg 2) and bismuth deficient (NBT 49) have large leakage current at ~175 and ~325 °C, respectively. Both of these samples can be considered acceptor doped. For the bismuth deficient (NBT 49) sample, the following defect mechanism, in Kröger-Vink notation[195], is as follows:

$$2Bi_{Bi}^{x} + 3O_{O}^{x} \rightarrow 2V_{Bi}^{'''} + 3V_{O}^{\cdot\cdot} + Bi_2O_3$$

Whereas for the magnesium doped (NBT 50 Mg 2) sample there are two mechanisms:

$$MgO + \frac{1}{2}O_{2(g)} \rightarrow Mg''_{Ti} + 2h^{\cdot} + 2O_O^x$$

$$MgO \rightarrow Mg''_{Ti} + V_O^{\cdot\cdot} + O_O^x$$

In contrast, the 1% bismuth excess (NBT 51) sample is a much better insulator than NBT 50 and can be considered as donor doped:

$$2Na_{Na}^x + O_O^x \rightarrow 2V'_{Na} + V_O^{\cdot\cdot} + Na_2O$$

The rise in dielectric loss is directly related to the temperature at which there is a large decrease in the impedance and consequentially the resistivity (conductivity). Even in the nominal NBT 50 composition it is likely that bismuth is being lost (acceptor doping) due to the volatility of lead. For other applications, such as high temperature piezoelectric applications, where the leakage current is undesirable, a bismuth excess of as little as 1% can dramatically improve the high temperature resistivity.

From the Arrhenius plot the activation energy was calculated for each composition that was measured. The activation energy (E_a) calculations ranged from 0.72-0.75 eV which are in relative agreement to other published results for NBT 50 (E_a ~0.86 eV).[64]

5.6. Conclusions and Future Work

The average structure, local structure, and electrical properties of NBT were investigated through a number of techniques and measurements. The average structure of the parent, non-stoichiometric, and doped NBT samples were in close

agreement with the work of Aksel et al.[58,191] Furthermore the local structure of all compositions by both X-ray and neutron PDF measurements showed that there is little change between composition, but a significant change as a function of temperature. The dielectric and impedance measurements showed that acceptor doping greatly enhanced the high temperature conductivity, whereas donor doping greatly decreased it.

This work represents an on-going effort to determine the structural origins of the enhanced physical properties observed in the NBT system. To discern the true effects of non-stoichiometry and doping on the local structure, a spatially resolved technique that is sensitive to minute changes in the local structure may be required. Additionally, to capture the disorder present at the local structure, large-box modeling over large *r*-ranges maybe be more fruitful, as has been shown to be effective for the NBT parent structure.[60] Finally, to discern the nature of the enhanced conductivity, electromotive force measurements are needed. Electromotive force measurements are able to deconvolute the contributions from the ionic and electronic conductivity to the total conductivity.

5.7. Acknowledgements

The authors would like to thank the National Science Foundation for the funding (NSF DMR-1832803). Charles Culbertson would like to acknowledge Michael Bowen for his help interpreting the impedance spectroscopy data.

Chapter 6: Conclusion

6.1. Summary

In this work, the local structure and properties of a number of functional electroceramics have been explored in detail. The overriding theme is to bridge the gap between the observed physical properties and the structural phenomena that cause them.

The classical materials $MgTiO_3$, $CaTiO_3$, $SrTiO_3$, and $BaTiO_3$ were synthesized and neutron total scattering data was collected. For $MgTiO_3$, the structure crystallized in the ilmenite structure with trigonal $R\bar{3}$ symmetry. The local structure of $MgTiO_3$ was well described by the average structure model with little local disorder present. The situation was found to be the same for both $CaTiO_3$ and $SrTiO_3$, where the average structure and local structure were the same – orthorhombic *Pbnm* for $CaTiO_3$, and cubic $Pm\bar{3}m$ for $SrTiO_3$. However, in the case of $BaTiO_3$ the average structure (tetragonal *P*4*mm*) was different from the local structure (rhombohedral *R*3*m*). This difference is due to order-disorder behavior where the locally ordered rhombohedral unit cells are disordered relative to one another, and with bulk probes the structure appears to be the vector sum of the displacements. The unique properties of $BaTiO_3$ are likely due to this behavior and therefore of great interest to the community[176].

Extensive work was carried out to understand both the origin of piezoelectricity and the local structure of the lead-free material $(1-x)Ba(Zr_{0.2}Ti_{0.8})O_3$-$x(Ba_{0.7}Ca_{0.3})TiO_3$ (BZT-*x*BCT). A range of materials were synthesized: $0.45 \leq x \leq 0.60$. X-ray total scattering data was collected during the application of an electric

field. After careful analysis the PDF data was analyzed and the PDF peak shift due to the electric field was determined. The PDF peak shift was converted to the intrinsic contribution to the piezoelectricity and was found to be minimized at the morphotropic phase boundary composition ($x = 0.50$). However, the diffraction reflections were investigated and it was found that domain wall motion (extrinsic contributor) is the dominating factor for the enhanced piezoelectricity observed[169]. Furthermore, neutron total scattering and X-ray absorption spectroscopy were collected on the $x = 0.50$ sample. The titanium ions were found to be "$BaTiO_3$-like" with rhombohedral symmetry, whereas the zirconium ions were found to be undistorted with cubic symmetry. Incorporating these findings into the small-box modeling yielded the coexistence of two perovskite phases in BCT-BCZ (*R*3*m*-*Pm*$\bar{3}$*m*).

The lead-free system $Na_{0.5}Bi_{0.5}TiO_3$ (NBT) was also investigated for its strong ionic conducting properties – not its piezoelectric properties. Stoichiometric, non-stoichiometric (bismuth deficient and excess), and doped samples were synthesized. Synchrotron X-ray diffraction, synchrotron X-ray total scattering, neutron total scattering, and physical property measurements were performed. The average and local structure showed the reported phase sequence of monoclinic *Cc* to tetragonal *P*4*bm* to cubic *Pm*$\bar{3}$*m*[191]. There was little to no change between compositions in terms of the average and local structure. However it was observed that nonstoichiometry and doping caused the cubic phase to appear at lower temperatures via diffraction. Remarkably, the physical properties from the dielectric and impedance measurements showed dramatic differences. The bismuth excess decreased the high temperature

conductivity and created a much better insulator, whereas the bismuth deficiency slightly increased the conductivity, but the magnesium doping greatly enhanced it. The slopes of the Arrhenius plots for all the compositions were very similar, yielding activation energies on the order of ~0.74 eV.

6.2. Concluding Remarks

From the work detailed here a few general conclusions can be drawn. Firstly, it is clear the local structure for most materials upon slow cooling approximates the ground state configuration where the energy is minimized. As the temperature is increased, the structure is largely maintained with only the addition of thermal disorder. Some materials, that have closely related configurations – like the competing distortions for the bismuth ions in NBT, lead to different local symmetries. These phenomena can be exploited as the ground state configuration for most materials can be easily calculated via standard computational methods. Therefore to predict the structure at higher temperatures, one need only apply thermal perturbations. Secondly, this work shows that the structure at multiple levels needs to be considered, such as: the local structure, average structure, domain structure, and grain structure. As these different levels each contribute differently to the macroscopic properties we are largely interested in for applications. Finally, this work highlights the need for a new technique to replace our existing methodologies for understanding the structure of disordered materials. This new technique must have sub-Angstrom resolution, rapid data collection (for larger measurement regions), and be sensitive to light atoms such as oxygen. One of the key challenges that confounds

existing characterization techniques is the difficulty in quantitatively assessing the structure of complex solid solutions. The ideal approach would be statistical in nature, given that disorder in complex solid solutions results in spatial variability of the local structure. Additionally, large-box modeling techniques like Reverse Monte Carlo modeling should become commonplace and great advances in their software design are needed to reduce the computing cost. It is my hope that this work will contribute to the greater collective of knowledge and in some way (albeit perhaps small) aid in the plight of humanity. As J.R.R. Tolkien once wrote, "*there is good in the world. And it's worth fighting for*."[196]

Bibliography

1. Pandey, R. K. *Fundamentals of Electroceramics: Materials, Devices, and Applications*. (Wiley, 2017).
2. Electroceramics: Technologies and Global Markets Report 2017 - Research and Markets. https://www.businesswire.com/news/home/20170922005212/en/Electroceramics-Technologies-Global-Markets-Report-2017-- (2017).
3. Gagliardi, M. *Milestones in the History of Perovskite Solar Cells*. (2018).
4. Uchino, K. *Ultrasonic Transducers: Materials and Design for Sensors, Actuators, and Medical Applications*. (Woodhead, 2012).
5. McQuade, R. R. Substituitonal Effects on the Electromechanical Properties of Lead-free, Piezoelectric $(Na_{0.5}Bi_{0.5})TiO_3$-$BaTiO_3$ (NBT-BT). (Oregon State University, 2018).
6. Johnsson, M. & Lemmens, P. Crystallography and Chemistry of Perovskites. in *Handbook of Magnetism and Advanced Magnetic Materials* (eds. Kronmüller, H. & Parkin, S.) (John Wiley & Sons, Ltd, 2007). doi:10.1002/9780470022184.hmm411.
7. Goldschmidt, V. M. Die Gesetze der Krystallochemie. *Naturwissenschaften* **14**, 477–485.
8. Shannon, R. & Prewitt, C. Effective Ionic Radii in Oxides and Fluorides. *Acta Cryst.* **B25**, 925 (1969).

9. Wechsler, B. A. & Von Dreele, R. Structure refinements of Mg_2TiO_4, $MgTiO_3$ and $MgTi_2O_5$ by time-of-flight neutron powder diffraction. *Acta Cryst.* **B45**, 542–549 (1989).

10. Kay, H. F. & Bailey, P. C. Structure and properties of $CaTiO_3$. *Acta Crystallographica* **10**, 219–226 (1957).

11. Geller, S. Crystal Structure of Gadolinium Orthoferrite, $GdFeO_3$. *J. Chem. Phys.* **24**, 1236–1239 (1956).

12. Guennou, M., Bouvier, P., Kreisel, J. & Machon, D. Pressure-temperature phase diagram of $SrTiO_3$ up to 53 GPa. *Phys. Rev. B* **81**, 054115 (2010).

13. Evans, H. T. The crystal structure of tetragonal barium titanate. *Acta Crystallographica* **4**, 377–377 (1951).

14. Bartel, C. J. *et al.* New tolerance factor to predict the stability of perovskite oxides and halides. *Science Advances* **5**, eaav0693 (2019).

15. Ruddlesden, S. N. & Popper, P. New compounds of the K_2NIF_4 type. *Acta Cryst* **10**, 538–539 (1957).

16. Ruddlesden, S. N. & Popper, P. The compound $Sr_3Ti_2O_7$ and its structure. *Acta Cryst* **11**, 54–55 (1958).

17. Beznosikov, B. V. & Aleksandrov, K. S. Perovskite-like crystals of the Ruddlesden-Popper series. *Crystallography Reports* **45**, 792–798 (2000).

18. Dion, M., Ganne, M. & Tournoux, M. Nouvelles familles de phases $M^IM^{II}_2Nb_3O_{10}$ a feuillets “perovskites”. *Materials Research Bulletin* **16**, 1429–1435 (1981).

19. Harrison, W. T. A., Reis, K. P., Liu, L. & Jacobson, A. J. Barium/rare-earth/lead double perovskites. Structures of Ba_2CePbO_6, Ba_2PrPbO_6, and $Ba_2TbPbO_{5.90}$. *Materials Research Bulletin* **30**, 1455–1462 (1995).

20. Benedek, N. A. Origin of Ferroelectricity in a Family of Polar Oxides: The Dion—Jacobson Phases. https://pubs.acs.org/doi/pdf/10.1021/ic500106a (2014) doi:10.1021/ic500106a.

21. Aurivillius, B. Mixed bismuth oxides with layer lattices. I. Structure type of $CaNb_2Bi_2O_9$. *Ark. Kemi.* **1**, 463–480 (1949).

22. Aurivillius, B. Mixed bismuth oxides with layer lattices. II. Structure of $Bi_4Ti_3O_{12}$. *Ark. Kemi.* **1**, 499–512 (1949).

23. Surta, T. W. *et al.* Dielectric and Ferroelectric Properties in Highly Substituted $Bi_2Sr(A)TiNb_2O_{12}$ (A = Ca^{2+}, Sr^{2+}, Ba^{2+}) Aurivillius Phases. *Chem. Mater.* **29**, 7774–7784 (2017).

24. Chen-Glasser, M., Li, P., Ryu, J. & Hong, S. Piezoelectric Materials for Medical Applications. *Piezoelectricity - Organic and Inorganic Materials and Applications* (2018) doi:10.5772/intechopen.76963.

25. Nuffer, J. & Bein, T. Applications of Piezoelectric Materials in Transportation Industry. *October* 12 (2006).

26. Li, H., Tian, C. & Deng, Z. D. Energy harvesting from low frequency applications using piezoelectric materials. *Applied Physics Reviews* **1**, 041301 (2014).

27. Yang, F. *et al.* Defect chemistry and electrical properties of sodium bismuth titanate perovskite. *Journal of Materials Chemistry A* **6**, 5243–5254 (2018).

28. He, J. *Metal Oxide Varistors: From Microstructure to Macro-Characteristics*. (Wiley-VCH, 2019).

29. Hikami, S. & Matsuda, Y. HighT_c Superconductors of the Perovskite Structure Oxides. *Japanese Journal of Applied Physics* **26**, 1027 (1987).

30. Yusuf, S. M. Functional Magnetic Materials: Fundamental and Technological Aspects. in *Functional Materials* (eds. Banerjee, S. & Tyagi, A. K.) 111–154 (Elsevier, 2012). doi:10.1016/B978-0-12-385142-0.00003-9.

31. Neumann, F. E. Vorlesungen über die Theorie der Elastizität der festen Körper und des Lichtäthers. (1885).

32. Newnham, R. E. *Properties of Materials: Anisotropy, Symmetry, Structure*. (Oxford University Press, 2005).

33. Ahart, M. *et al.* Origin of morphotropic phase boundaries in ferroelectrics. *Nature* **451**, 545–548 (2008).

34. Wilson, J. N., Frost, J. M., Wallace, S. K. & Walsh, A. Dielectric and ferroic properties of metal halide perovskites. *APL Materials* **7**, 010901 (2019).

35. Noheda, B. & Cox, D. E. Bridging Phases at the Morphotropic Boundaries of Lead-Oxide Solid Solutions. *arXiv:cond-mat/0511256* (2005).

36. Noheda, B. *et al.* A monoclinic ferroelectric phase in the $Pb(Zr_{1-x}Ti_x)O_3$ solid solution. *Applied Physics Letters* **74**, 2059–2061 (1999).

37. Jaffe, B., Roth, R. & Marzullo, S. Piezoelectric Properties of Lead Zirconate-Lead Titanate Solid-Solution Ceramics. *Journal of Applied Physics* **25**, 809–810 (1954).

38. Schönau, K. A. *et al.* Nanodomain structure of $Pb[Zr_{1-x}Ti_x]O_3$ at its morphotropic phase boundary: Investigations from local to average structure. *Physical Review B* **75**, (2007).

39. Zhang, N. *et al.* The missing boundary in the phase diagram of $PbZr_{1-x}Ti_xO_3$. *Nature Communications* **5**, (2014).

40. *Restriction of Hazardous Substances (RoHS 1)*. 0019–0023 (2003).

41. Coondoo, I., Panwar, N. & Kholkin, A. Lead-free piezoelectrics: Current status and perspectives. *Journal of Advanced Dielectrics* **03**, 1330002 (2013).

42. Aksel, E. & Jones, J. L. Advances in Lead-Free Piezoelectric Materials for Sensors and Actuators. *Sensors* **10**, 1935–1954 (2010).

43. Damjanovic, D., Klein, N., Li, J. & Porokhonskyy, V. What Can Be Expected from Lead-Free Piezoelectric Materials? *Functional Materials Letters* **3**, 5–13 (2010).

44. Hong, C.-H. *et al.* Lead-free piezoceramics – Where to move on? *Journal of Materiomics* **2**, 1–24 (2016).

45. Koruza, J. *et al.* Requirements for the transfer of lead-free piezoceramics into application. *Journal of Materiomics* **4**, 13–26 (2018).

46. Smolenskii, G. A., Isupov, V. A., Agranovskaya, A. I. & Krainik, N. N. New Ferroelectrics of Complex Composition. *Sov. Phys. Solid State* **2**, 2651–2654 (1961).

47. Suchanicz, J. & Ptak, W. S. On the phase transition in $Na_{0.5}Bi_{0.5}TiO_3$. *Ferroelectrics Letters Section* **12**, 71–78 (1990).

48. Tu, C.-S., Siny, I. G. & Schmidt, V. H. Sequence of dielectric anomalies and high-temperature relaxation behavior in $Na_{0.5}Bi_{0.5}TiO_3$. *Phys. Rev. B* **49**, 11550–11559 (1994).

49. Suchanicz, J., Jeżowski, A. & Poprawski, R. Low-Temperature Thermal and Dielectric Properties of $Na_{0.5}Bi_{0.5}TiO_3$. *physica status solidi (a)* **169**, 209–215 (1998).

50. Hiruma, Y., Nagata, H. & Takenaka, T. Thermal depoling process and piezoelectric properties of bismuth sodium titanate ceramics. *Journal of Applied Physics* **105**, 084112 (2009).

51. Suchanicz, J. & Kwapulinski, J. X-ray diffraction study of the phase transitions in $Na_{0.5}Bi_{0.5}TiO_3$. *Ferroelectrics* **165**, 249–253 (1995).

52. Jones, G. O. & Thomas, P. A. The tetragonal phase of $Na_{0.5}$ $Bi_{0.5}TiO_3$ – a new variant of the perovskite structure. *Acta Crystallographica Section B Structural Science* **56**, 426–430 (2000).

53. Soukhojak, A. N., Wang, H., Farrey, G. W. & Chiang, Y.-M. Superlattice in single crystal barium-doped sodium bismuth titanate. *Journal of Physics and Chemistry of Solids* **61**, 301–304 (2000).

54. Jones, G. O. & Thomas, P. A. Investigation of the structure and phase transitions in the novel A-site substituted distorted perovskite compound $Na_{0.5}Bi_{0.5}$ TiO_3. *Acta Crystallographica Section B Structural Science* **58**, 168–178 (2002).

55. Isuyov, V. A., Pronin, I. P. & Kruzina, T. V. Temperature dependence of bireringence and opalescence of the sodium-bismuth titanate crystals. *Ferroelectrics Letters Section* **2**, 205–208 (1984).

56. Kreisel, J. *et al.* High-pressure x-ray scattering of oxides with a nanoscale local structure: Application to $Na_{0.5}Bi_{0.5}TiO_3$. *Phys. Rev. B* **68**, 014113 (2003).

57. Balagurov, A. M. *et al.* The rhombohedral phase with incommensurate modulation in $Na_{0.5}Bi_{0.5}TiO_3$. *Phase Transitions* **79**, 163–173 (2006).

58. Aksel, E. *et al.* Monoclinic crystal structure of polycrystalline $Na_{0.5}Bi_{0.5}TiO_3$. *Applied Physics Letters* **98**, 152901 (2011).

59. Aksel, E. *et al.* Local atomic structure deviation from average structure of $Na_{0.5}Bi_{0.5}TiO_3$: Combined x-ray and neutron total scattering study. *Physical Review B* **87**, (2013).

60. Keeble, D. S. *et al.* Bifurcated Polarization Rotation in Bismuth-Based Piezoelectrics. *Advanced Functional Materials* **23**, 185–190 (2013).

61. Takenaka, T., Maruyama, K. & Sakata, K. $(Bi_{0.5}Na_{0.5})TiO_3$-$BaTiO_3$ System for Lead-Free Piezoelectric Ceramics. *Jpn. J. Appl. Phys.* **30**, 2236 (1991).

62. Kounga, A. B., Zhang, S.-T., Jo, W., Granzow, T. & Rödel, J. Morphotropic phase boundary in $(1-x)Bi_{0.5}Na_{0.5}TiO_3–xK_{0.5}Na_{0.5}NbO_3$ lead-free piezoceramics. *Applied Physics Letters* **92**, 222902 (2008).

63. Zhang, Y.-R., Li, J.-F. & Zhang, B.-P. Enhancing Electrical Properties in NBT–KBT Lead-Free Piezoelectric Ceramics by Optimizing Sintering Temperature. *Journal of the American Ceramic Society* **91**, 2716–2719 (2008).

64. Li, M. *et al.* A family of oxide ion conductors based on the ferroelectric perovskite $Na_{0.5}Bi_{0.5}TiO_3$. *Nature Materials* **13**, 31–35 (2014).

65. Liu, W. & Ren, X. Large Piezoelectric Effect in Pb-Free Ceramics. *Physical Review Letters* **103**, (2009).

66. Hennings, D. & Schreinemacher, H. Temperature Dependence of the Segregation of Calcium Titanate from Solid Solutions of (Ba,Ca)(Ti,Zr)O_3 and its Effect on the Dielectric Properties. *Mat. Res. Bull.* **12**, 1221–1226 (1977).

67. Acosta, M., Novak, N., Jo, W. & Rödel, J. Relationship between electromechanical properties and phase diagram in the $Ba(Zr_{0.2}Ti_{0.8})O_3$– x $(Ba_{0.7}Ca_{0.3})TiO_3$ lead-free piezoceramic. *Acta Materialia* **80**, 48–55 (2014).

68. Wang, W. *et al.* Enhanced Piezoelectric Properties and Temperature Stability of 0.5BZT-0.5BCT Ceramic Induced by Using Three-Step Synthesizing Method. *ECS J. Solid State Sci. Technol.* **8**, N134 (2019).

69. Hayati, R., Fayazi, M., Diargar, H., Kaveh, M. & Tayebi, L. Electrical and mechanical properties of BZT − xBCT lead-free piezoceramics. *International Journal of Applied Ceramic Technology* doi:10.1111/ijac.13494.

70. Tuan, D. A., Tung, V., Chuong, T. V., Tinh, N. T. & Huong, N. T. M. Structure, microstructure and dielectric properties of lead-free BCT-xBZT ceramics near the morphotropic phase boundary. *APPL PHYS* **53**, 7 (2015).

71. Liu, W., Cheng, L. & Li, S. Prospective of (BaCa)(ZrTi)O_3 Lead-free Piezoelectric Ceramics. *Crystals* **9**, 179 (2019).

72. Jeong, I.-K. & Ahn, J. S. The atomic structure of lead-free $Ba(Zr_{0.2}Ti_{0.8})O_3$-$(Ba_{0.7}Ca_{0.3})TiO_3$ by using neutron total scattering analysis. *Applied Physics Letters* **101**, 242901 (2012).

73. Keeble, D. S., Benabdallah, F., Thomas, P. A., Maglione, M. & Kreisel, J. Revised structural phase diagram of $(Ba_{0.7}Ca_{0.3}TiO_3)$-$(BaZr_{0.2}Ti_{0.8}O_3)$. *Appl. Phys. Lett.* **102**, (2013).

74. Haugen, A. *et al.* Structure and phase transitions in 0.5($Ba_{0.7}Ca_{0.3}TiO_3$)-0.5($BaZr_{0.2}Ti_{0.8}O_3$) from -100C to 150C. *Journal of Applied Physics* **113**, (2013).

75. Rietveld, H. M. The Rietveld method. *Physica Scripta* **89**, (2014).

76. Gao, J. *et al.* Symmetry determination on Pb-free piezoceramic 0.5Ba($Zr_{0.2}Ti_{0.8}$)O_3-0.5($Ba_{0.7}Ca_{0.3}$)TiO_3 using convergent beam electron diffraction method. *Journal of Applied Physics* **115**, (2014).

77. Mastelaro, V. R. *et al.* Local structure and hybridization states in $Ba_{0.9}Ca_{0.1}Ti_{1-x}Zr_xO_3$ ceramic compounds: Correlation with a normal or relaxor ferroelectric character. *Acta Materialia* **84**, 164–171 (2015).

78. Gao, J. *et al.* Major contributor to the large piezoelectric response in (1 − x)Ba($Zr_{0.2}Ti_{0.8}$)O_3− x($Ba_{0.7}Ca_{0.3}$)TiO_3 ceramics: Domain wall motion. *Applied Physics Letters* **104**, 252909 (2014).

79. Rödel, J. *et al.* Transferring lead-free piezoelectric ceramics into application. *Journal of the European Ceramic Society* **35**, 1659–1681 (2015).

80. Ibn-Mohammed, T. *et al.* Life cycle assessment and environmental profile evaluation of lead-free piezoelectrics in comparison with lead zirconate titanate. *Journal of the European Ceramic Society* **38**, 4922–4938 (2018).

81. Chu, F., Reaney, I. M. & Setter, N. Role of Defects in the Ferroelectric Relaxor Lead Scandium Tantalate. *Journal of the American Ceramic Society* **78**, 1947–1952 (1995).

82. Atkins, P. *et al. Shriver and Atkins' Inorganic Chemistry*. (W.H. Freeman and Company New York, 2010).

83. Xiong, Y., Lyons, S. W., Kodas, T. T. & Pratsinis, S. E. Volatile Metal Oxide Evaporation during Aerosol Decomposition. *Journal of the American Ceramic Society* **78**, 2490–2496 (1995).

84. Sands, D. E. *Introduction to Crystallography*. (Dover, 1993).

85. Egami, T. & Billinge, S. *Underneath of Bragg Peaks: Structural Analysis of Complex Materials*. vol. 16 (Pergamon, 2012).

86. McCusker, L. B., Von Dreele, R., Cox, D. E., Louer, D. & Scardi, P. Rietveld refinement guidelines. *Journal of Applied Crystallography* **32**, 36–50 (1999).

87. Toby, B. H. *R* factors in Rietveld analysis: How good is good enough? *Powder Diffraction* **21**, 67–70 (2006).

88. Pawley, G. S. Unit-cell refinement from powder diffraction scans. *Journal of Applied Crystallography* **14**, 357–361 (1981).

89. Rietveld, H. A Profile Refinement Method for Nuclear and Magnetic Structures. *Journal of Applied Crystallography* **2**, 65–71 (1969).

90. Coelho, A. TOPAS and TOPAS-Academic: an optimization program integrating computer algebra and crystallographic objects written in C++. *J. Appl. Cryst.* **51**, 210–218 (2018).

91. *Standard Test Method for Water Absorption, Bulk Density, Apparent Porosity, and Apparent Specific Gravity of Fired Whiteware Products*. 2006.

92. Stewart, M., Battrick, W. & Cain, M. Measuring Piezoelectric d_{33} coefficients using the Direct Method. *Measurement Good Practice Guide* **44**, (2001).

93. Radiant High Voltage Displacement Measurement Fixture. (2000).

94. Schmidt, R. Impedance Spectroscopy of Electroceramics. 32.

95. Sinclair, D. C. Characterization of Electro-materials using ac Impedance Spectroscopy. **34**, 12 (1994).

96. Irvine, J. T. S., Sinclair, D. C. & West, A. R. Electroceramics: Characterization by Impedance Spectroscopy. *Advanced Materials* **2**, 132–138 (1990).

97. Sato, T., Miyamoto, R. & Fukasawa, A. Deviation of Dielectric Properties in Magnesium Titanate Ceramics. *Japanese Journal of Applied Physics* **20**, 151 (1981).

98. Deng, Y.-F., Tang, S.-D., Lao, L.-Q. & Zhan, S.-Z. Synthesis of magnesium titanate nanocrystallites from a cheap and water-soluble single source precursor. *Inorganica Chimica Acta* **363**, 827–829 (2010).

99. Thomas, S. & Thankappan, A. *Perovskite Photovoltaics: Basic to Advanced Concepts and Implementation*. (Academic Press, 2018).

100. Acosta, M. *et al.* $BaTiO_3$ -based piezoelectrics: Fundamentals, current status, and perspectives. *Applied Physics Reviews* **4**, 041305 (2017).

101. Barth, T. F. W. & Posnjak, E. The Crystal Structure of Ilmenite. *Z. Kristallogr.* **Teil A**, 271–280 (1934).

102. Henderson, C. M. B., Knight, K. S. & Lennie, A. R. Temperature Dependence of Rutile (TiO_2) and Geikielite ($MgTiO_3$) Structures Determined Using Neutron Powder Diffraction. *The Open Mineralogy Journal* **3**, 1–11 (2009).

103. Redfern, S. A. T. High-temperature structural phase transitions in perovskite ($CaTiO_3$). 9.

104. Lytle, F. W. X-Ray Diffractometry of Low-Temperature Phase Transformations in Strontium Titanate. *Journal of Applied Physics* **35**, 2212–2215 (1964).

105. Hui, Q., Tucker, M. G., Dove, M. T., Wells, S. A. & Keen, D. A. Total scattering and reverse Monte Carlo study of the 105 K displacive phase transition in strontium titanate. *Journal of Physics: Condensed Matter* **17**, S111–S124 (2005).

106. Kwei, G. H., Lawson, A. C., Billinge, S. J. L. & Cheong, S. W. Structures of the ferroelectric phases of barium titanate. *The Journal of Physical Chemistry* **97**, 2368–2377 (1993).

107. Comes, R., Lambert, M. & Guinier, A. The Chain Structure of $BaTiO_3$ and $KNbO_3$. *Solid State Communications* **6**, 715–719 (1968).

108. Senn, M. S., Keen, D. A., Lucas, T. C. A., Hriljac, J. A. & Goodwin, A. L. Emergence of Long-Range Order in $BaTiO_3$ from Local Symmetry-Breaking Distortions. *Physical Review Letters* **116**, (2016).

109. Kwei, G. H., Billinge, S. >J. L., Cheong, S.-W. & Saxton, J. G. Pair-distribution functions of ferroelectric perovskites: Direct observation of structural ground states. *Ferroelectrics* **164**, 57–73 (1995).

110. Ravel, B., Stern, E. A., Vedrinskii, R. I. & Kraizman, V. Local structure and the phase transitions of $BaTiO_3$. *Ferroelectrics* **206**, 407–430 (1998).

111. Zalar, B., Laguta, V. V. & Blinc, R. NMR Evidence for the Coexistence of Order-Disorder and Displacive Components in Barium Titanate. *Physical Review Letters* **90**, (2003).

112. Petkov, V., Gateshki, M., Niederberger, M. & Ren, Y. Atomic-Scale Structure of Nanocrystalline $Ba_xSr_{1-x}TiO_3$ (x = 1, 0.5, 0) by X-ray Diffraction and the

Atomic Pair Distribution Function Technique. *Chem. Mater.* **18**, 814–821 (2006).

113. Levin, I., Krayzman, V. & Woicik, J. C. Local structure in perovskite (Ba,Sr)TiO_3: Reverse Monte Carlo refinements from multiple measurement techniques. *Physical Review B* **89**, (2014).
114. Sears, V. Neutron scattering lengths and cross sections. *Neutron News* **3**, (1992).
115. Page, K., Kolodiazhnyi, T., Proffen, T., Cheetham, A. K. & Seshadri, R. Local Structural Origins of the Distinct Electronic Properties of Nb-Substituted $SrTiO_3$ and $BaTiO_3$. *Physical Review Letters* **101**, (2008).
116. Smith, M. B. *et al.* Crystal Structure and the Paraelectric-to-Ferroelectric Phase Transition of Nanoscale $BaTiO_3$. *Journal of the American Chemical Society* **130**, 6955–6963 (2008).
117. Usher, T.-M. *et al.* Local and average structures of $BaTiO_3$-$Bi(Zn_{0.5}Ti_{0.5})O_3$. *Journal of Applied Physics* **120**, 184102 (2016).
118. Heitmann, A. A. & Rossetti, G. A. Thermodynamics of Ferroelectric Solid Solutions with Morphotropic Phase Boundaries. *Journal of the American Ceramic Society* **97**, 1661–1685 (2014).
119. Levin, I. *et al.* Nanoscale Polar Heterogeneities and Branching Bi-Displacement Directions in $K_{0.5}Bi_{0.5}TiO_3$. *Chemistry of Materials* **31**, 2450–2458 (2019).
120. Neuefeind, J., Feygenson, M., Carruth, J., Hoffmann, R. & Chipley, K. The Nanoscale Ordered Materials Diffractometer NOMAD at the Spallation Neutron Source SNS. *Nuclear Instruments and Methods in Physics Research B* **287**, 68–75 (2012).

121. Mason, T. *et al.* The Spallation Neutron Source in Oak Ridge: A powerful tool for materials research. *Physica B* **385–386**, 955–960 (2006).

122. Coelho, A. Whole-profile structure solution from powder diffraction data using simulated annealing. *J. Appl. Cryst.* **33**, 899–908 (2000).

123. Xiao, C. J., Jin, C. Q. & Wang, X. H. Crystal structure of dense nanocrystalline BaTiO3 ceramics. *Materials Chemistry and Physics* **111**, 209–212 (2008).

124. Panda, P. K. Review: environmental friendly lead-free piezoelectric materials. *Journal of Materials Science* **44**, 5049–5062 (2009).

125. Rödel, J. *et al.* Perspective on the Development of Lead-free Piezoceramics. *Journal of the American Ceramic Society* **92**, 1153–1177 (2009).

126. Zhang, L. *et al.* Phase transitions and the piezoelectricity around morphotropic phase boundary in $Ba(Zr_{0.2}Ti_{0.8})O_3$-$x(Ba_{0.7}Ca_{0.3})TiO_3$ lead-free solid solution. *Applied Physics Letters* **105**, 162908 (2014).

127. Zhang, Q. M., Wang, H., Kim, N. & Cross, L. E. Direct evaluation of domain-wall and intrinsic contributions to the dielectric and piezoelectric response and their temperature dependence on lead zirconate-titanate ceramics. *Journal of Applied Physics* **75**, 454–459 (1994).

128. Damjanovic, D. & Demartin, M. Contribution of the irreversible displacement of domain walls to the piezoelectric effect in barium titanate and lead zirconate titanate ceramics. *Journal of Physics: Condensed Matter* **9**, 4943–4953 (1997).

129. Jones, J. L., Hoffman, M., Daniels, J. E. & Studer, A. J. Direct measurement of the domain switching contribution to the dynamic piezoelectric response in ferroelectric ceramics. *Applied Physics Letters* **89**, 092901 (2006).

130. Bertotti, G. & Mayergoyz, I. D. Hysteresis in Piezoelectric and Ferroelectric Materials. in *The Science of Hysteresis* vol. 3 337–465 (Elsevier, 2005).

131. Jones, J. L., Slamovich, E. B. & Bowman, K. J. Domain texture distributions in tetragonal lead zirconate titanate by x-ray and neutron diffraction. *Journal of Applied Physics* **97**, 034113 (2005).

132. Daniels, J. E., Jo, W., Rödel, J. & Jones, J. L. Electric-field-induced phase transformation at a lead-free morphotropic phase boundary: Case study in a 93%(Bi0.5Na0.5)TiO3–7% BaTiO3 piezoelectric ceramic. *Applied Physics Letters* **95**, 032904 (2009).

133. Hou, D. *et al.* Field-induced polarization rotation and phase transitions in $0.70Pb(Mg1/3Nb1/2)O_3 - 0.30PbTiO_3$ piezoceramics observed by *in situ* high-energy x-ray scattering. *Physical Review B* **97**, (2018).

134. Egami, T., Dmowski, W., Akbas, M. & Davies, P. K. Local structure and polarization in Pb containing ferroelectric oxides. *AIP Conference Proceedings* **436**, (1998).

135. Grinberg, I., Cooper, V. R. & Rappe, A. M. Relationship between local structure and phase transitions of a disordered solid solution. *Nature* **419**, 909–911 (2002).

136. Dmowski, W., Akbas, M. K., Davies, P. K. & Egami, T. Local structure of $Pb(Sc1/2Ta1/2)O_3$ and related compounds. *Journal of Physics and Chemistry of Solids* **61**, 229–237 (2000).

137. Jiang, L., Mitchell, D. C., Dmowski, W. & Egami, T. Local structure of NaNbO 3 : A neutron scattering study. *Physical Review B* **88**, (2013).

138. McQuade, R. R. & Dolgos, M. R. A review of the structure-property relationships in lead-free piezoelectric $(1- x)Na_{0.5}Bi_{0.5}TiO_3–(x)BaTiO_3$. *Journal of Solid State Chemistry* **242**, 140–147 (2016).

139. Page, K., Proffen, T., Niederberger, M. & Seshadri, R. Probing Local Dipoles and Ligand Structure in $BaTiO_3$ Nanoparticles. *Chemistry of Materials* **22**, 4386–4391 (2010).

140. Levin, I. *et al.* Local structure in $BaTiO_3–BiScO_3$ dipole glasses. *Physical Review B* **93**, (2016).

141. Hou, D. *et al.* Temperature-induced local and average structural changes in $BaTiO_3–xBi(Zn_{1/2}Ti_{1/2})O_3$ solid solutions: The origin of high temperature dielectric permittivity. *Journal of Applied Physics* **122**, 064103 (2017).

142. Goetzee-Barral, A. J. *et al.* Electric field dependent local structure of $(K_xNa_{1-x})_{0.5}Bi_{0.5}TiO_3$. *Physical Review B* **96**, (2017).

143. Usher, T.-M., Levin, I., Daniels, J. E. & Jones, J. L. Electric-field-induced local and mesoscale structural changes in polycrystalline dielectrics and ferroelectrics. *Scientific Reports* **5**, (2015).

144. Zhao, C. *et al.* Local structural behavior of $PbZr_{0.5}Ti_{0.5}O_3$ during electric field application via *in situ* pair distribution function study. *Journal of Applied Physics* **122**, 174102 (2017).

145. Hou, D., Zhao, C., Paterson, A. R., Li, S. & Jones, J. L. Local structures of perovskite dielectrics and ferroelectrics via pair distribution function analyses. *Journal of the European Ceramic Society* **38**, 971–987 (2018).

146. Gao, J. *et al.* Microstructure basis for strong piezoelectricity in Pb-free $Ba(Zr_{0.2}Ti_{0.8})O_3$-$(Ba_{0.7}Ca_{0.3})TiO_3$ ceramics. *Applied Physics Letters* **99**, 092901 (2011).

147. Woodward, D. I., Knudsen, J. & Reaney, I. M. Review of crystal and domain structures in the $PbZr_xTi_{1-x}O_3$ solid solution. *Physical Review B* **72**, (2005).

148. Damjanovic, D., Biancoli, A., Batooli, L., Vahabzadeh, A. & Trodahl, J. Elastic, dielectric, and piezoelectric anomalies and Raman spectroscopy of $0.5Ba(Ti_{0.8}Zr_{0.2})O_3$-$0.5(Ba_{0.7}Ca_{0.3})TiO_3$. *Applied Physics Letters* **100**, 192907 (2012).

149. Damjanovic, D. A morphotropic phase boundary system based on polarization rotation and polarization extension. *Applied Physics Letters* **97**, 062906 (2010).

150. Ochoa, D. A. *et al.* Extensive domain wall contribution to strain in a $(K,Na)NbO_3$ -based lead-free piezoceramics quantified from high energy X-ray diffraction. *Journal of the European Ceramic Society* **36**, 2489–2494 (2016).

151. Tutuncu, G. *et al.* Domain wall and interphase boundary motion in $(1-x)Bi(Mg_{0.5}Ti_{0.5})O_3–xPbTiO_3$ near the morphotropic phase boundary. *Journal of Applied Physics* **120**, 044103 (2016).

152. Tutuncu, G., Damjanovic, D., Chen, J. & Jones, J. L. Deaging and Asymmetric Energy Landscapes in Electrically Biased Ferroelectrics. *Physical Review Letters* **108**, (2012).

153. Hinterstein, M. *et al.* Structural Description of the Macroscopic Piezo- and Ferroelectric Properties of Lead Zirconate Titanate. *Physical Review Letters* **107**, (2011).

154. Daniels, J. E., Jo, W., Rödel, J., Honkimäki, V. & Jones, J. L. Electric-field-induced phase-change behavior in $(Bi_{0.5}Na_{0.5})TiO_3$–$BaTiO_3$–$(K_{0.5}Na_{0.5})NbO_3$: A combinatorial investigation. *Acta Materialia* **58**, 2103–2111 (2010).

155. Tutuncu, G., Li, B., Bowman, K. & Jones, J. L. Domain wall motion and electromechanical strain in lead-free piezoelectrics: Insight from the model system $(1 - x)Ba(Zr_{0.2}Ti_{0.8})O_3$–$x(Ba_{0.7}Ca_{0.3})TiO_3$ using *in situ* high-energy X-ray diffraction during application of electric fields. *Journal of Applied Physics* **115**, 144104 (2014).

156. Ehmke, M. C., Khansur, N. H., Daniels, J. E., Blendell, J. E. & Bowman, K. J. Resolving structural contributions to the electric-field-induced strain in lead-free $(1-x)Ba(Zr_{0.2}Ti_{0.8})O_3-x(Ba_{0.7}Ca_{0.3})TiO_3$ piezoceramics. *Acta Materialia* **66**, 340–348 (2014).

157. Chupas, P. J., Chapman, K. W. & Lee, P. L. Applications of an amorphous silicon-based area detector for high-resolution, high-sensitivity and fast time-resolved pair distribution function measurements. *Journal of Applied Crystallography* **40**, 463–470 (2007).

158. Hammersley, A. P. FIT2D: An Introduction and Overview. *ESRF Internal Report* (1997).

159. Juhás, P., Davis, T., Farrow, C. & Billinge, S. PDFgetX3: a rapid and highly automatable program for processing powder diffraction data into total scattering pair distribution functions. *Journal of Applied Crystallography* **46**, 560–566 (2013).

160. Guo, H., Zhou, C., Ren, X. & Tan, X. Unique single-domain state in a polycrystalline ferroelectric ceramic. *Physical Review B* **89**, (2014).

161. Iamsasri, T., Tutuncu, G., Uthaisar, C., Pojprapai, S. & Jones, J. L. Analysis methods for characterizing ferroelectric/ferroelastic domain reorientation in orthorhombic perovskite materials and application to Li-doped $Na_{0.5}K_{0.5}NbO_3$. *Journal of Materials Science* **48**, 6905–6910 (2013).

162. Khatua, D. K., K. V., L., Fancher, C. M., Jones, J. L. & Ranjan, R. Coupled domain wall motion, lattice strain and phase transformation in morphotropic phase boundary composition of $PbTiO_3$-$BiScO_3$ piezoelectric ceramic. *Journal of Applied Physics* **120**, 154104 (2016).

163. Zakhozheva, M. *et al. In situ* electric field induced domain evolution in $Ba(Zr_{0.2}Ti_{0.8})O_3$-$0.3(Ba_{0.7}Ca_{0.3})TiO_3$ ferroelectrics. *Applied Physics Letters* **105**, 112904 (2014).

164. Shirane, G. & Hoshino, S. Crystal Structure of the Ferroelectric Phase in $PbZrO_3$ Containing Ba or Ti. *Physical Review* **86**, 248–249 (1952).

165. Sawaguchi, E. Ferroelectricity versus Antiferroelectricity in the Solid Solutions of $PbZrO_3$ and $PbTiO_3$. *Journal of the Physical Society of Japan* **8**, (1953).

166. Jaffe, B., Cook Jr., W. R. & Jaffe, H. *Piezoelectric ceramics*. (Academic Press, 1971).

167. Sung, Y. S. *et al.* Roles of lattice distortion in $(1-x)(Bi_{0.5}Na_{0.5})TiO_3$-$xBaTiO_3$ ceramics. *Applied Physics Letters* **96**, 202901 (2010).

168. Berlincourt, D., Cmolik, C. & Jaffe, H. Piezoelectric Properties of Polycrystalline Lead Titanate Zirconate Compositions. *Proceedings of the IRE* **48**, 220–229 (1960).

169. Manjon-Sanz, A., Culbertson, C., Hou, D., Jones, J. & Dolgos, M. Total scattering and diffraction studies of lead-free piezoelectric (1-x)$Ba(Zr_{0.2}Ti_{0.8})O_3$-x$(Ba_{0.7}Ca_{0.3})TiO_3$ deconvolve intrinsic and extrinsic contributions to electromechanical strain. *Acta Mater.* **171**, 79–91 (2019).

170. Glazer, A. M. The classification of tilted octahedra in perovskites. *Acta Crystallographica Section B Structural Crystallography and Crystal Chemistry* **28**, 3384–3392 (1972).

171. Stokes, H. T., Kisi, E. H., Hatch, D. M. & Howard, C. J. Group-theoretical analysis of octahedral tilting in ferroelectric perovskites. *Acta Crystallographica Section B Structural Science* **58**, 934–938 (2002).

172. Aroyo, M. *et al.* Crystallography online: Bilbao Crystallographic Server. *Bulg. Chem. Commun.* **43**, 183–197 (2011).

173. Aroyo, M. *et al.* Bilbao Crystallographic Server I: Databases and crystallographic computing programs. *Z. Krist.* **221**, 15–27 (2006).

174. Aroyo, M., Kirov, A., Capillas, C., Perez-Mato, J. & Wondratschek, H. Bilbao Crystallographic Server II: Representations of crystallographic point groups and space groups. *Acta Cryst.* **A62**, 115–128 (2006).

175. Ivantchev, S., Kroumova, E., Madariaga, G., Perez-Mato, J. & Aroyo, M. SUBGROUPGRAPH - a computer program for analysis of group-subgroup relations between space groups. *J. Appl. Cryst.* **33**, 1190–1191 (2000).

176. Culbertson, C. M. *et al.* Neutron Total Scattering Studies of Group II Titanates ($ATiO_3$, A^{2+} = Mg, Ca, Sr, Ba). *Scientific Reports* **10**, (2020).

177. Ravel, B. & Newville, M. ATHENA, ARTEMIS, HEPHAESTUS: data analysis for X-ray absorption spectroscopy using IFEFFIT. *Journal of Synchrotron Radiation* **12**, 537–541 (2005).

178. Wang, M., Árnadóttir, L., Xu, Z. J. & Feng, Z. In Situ X-ray Absorption Spectroscopy Studies of Nanoscale Electrocatalysts. *Nano-Micro Letters* **11**, (2019).

179. Lorch, E. Neutron diffraction by germania, silica and radiation-damaged silica glasses. *Journal of Physics C: Solid State Physics* **2**, 229–237 (1969).

180. Soper, A. & Barney, E. On the use of modification functions when Fourier transforming total scattering data. *Journal of Applied Crystallography* **45**, 1314–1317 (2012).

181. Farrow, C. *et al.* PDFfit2 and PDFgui: computer programs for studying nanostructure in crystals. *J. Phys.: Condens. Matter* **19**, (2007).

182. Farrow, C. *et al.* PDFgui user guide. (2016).

183. Kamon-in, O., Pattanasiriwisawa, W., Yangthaisong, A. & Srilomsak, S. Structural studies of $Ba_{1-x}La_xTiO_3$ using X-ray absorption near-edge spectroscopy. *Journal of Physics: Conference Series* **190**, 012082 (2009).

184. Yoshii, K. *et al.* Electronic structure of $BaTiO_3$ using resonant X-ray emission spectroscopy at the Ba-L_3 and Ti-K absorption edges. *Journal of Physics and Chemistry of Solids* **75**, 339–343 (2014).

185. Phaktapha, P. *et al.* Temperature dependent local structure in $BaTiO_3$ single crystal. *Integrated Ferroelectrics* **177**, 74–78 (2017).

186. Deguchi, H., Yoshida, H., Inagaki, T. & Horiuchi, M. EXAFS study of doped ceria using multiple data set fit. *Solid State Ionics* **176**, 1817–1825 (2005).

187. Yang, J. *et al.* Retention Mechanisms of Citric Acid in Ternary Kaolinite-Fe(III)-Citrate Acid Systems Using Fe K-edge EXAFS and $L_{3,2}$-edge XANES Spectroscopy. *Scientific Reports* **6**, (2016).

188. Laulhé, C., Hippert, F., Bellissent, R., Simon, A. & Cuello, G. J. Local structure in $BaTi_{1-x}Zr_xO_3$ relaxors from neutron pair distribution function analysis. *Physical Review B* **79**, (2009).

189. Yang, F. *et al.* Optimisation of oxide-ion conductivity in acceptor-doped $Na_{0.5}Bi_{0.5}TiO_3$ perovskite: approaching the limit? *Journal of Materials Chemistry A* **5**, 21658–21662 (2017).

190. Li, M. *et al.* Dramatic Influence of A-Site Nonstoichiometry on the Electrical Conductivity and Conduction Mechanisms in the Perovskite Oxide $Na_{0.5}Bi_{0.5}TiO_3$. *Chemistry of Materials* **27**, 629–634 (2015).

191. Aksel, E., Forrester, J. S., Kowalski, B., Jones, J. L. & Thomas, P. A. Phase transition sequence in sodium bismuth titanate observed using high-resolution x-ray diffraction. *Applied Physics Letters* **99**, 222901 (2011).

192. Aksel, E. *et al.* Local atomic structure deviation from average structure of $Na_{0.5}Bi_{0.5}TiO_3$: Combined x-ray and neutron total scattering study. *Physical Review B* **87**, (2013).

193. Rao, B. N. *et al.* Local structural disorder and its influence on the average global structure and polar properties in $Na_{0.5}Bi_{0.5}TiO_3$. *Physical Review B* **88**, (2013).

194. McQuade, R., Rowe, T., Manjón-Sanz, A., de la Puente, L. & Dolgos, M. R. An investigation into group 13 (Al, Ga, In) substituted $(Na_{0.5}Bi_{0.5})TiO_3$-$BaTiO_3$ (NBT-BT) lead-free piezoelectrics. *Journal of Alloys and Compounds* **762**, 378–388 (2018).

195. Kröger, F. A. & Vink, H. J. Relations between the Concentrations of Imperfections in Crystalline Solids. in *Solid State Physics* (eds. Seitz, F. & Turnbull, D.) vol. 3 307–435 (Academic Press, 1956).

196. Tolkien, J. R. R. *The Lord of the Rings: The Two Towers*. (George Allen & Unwin, 1954).

197. Shannon, R. Revised Effective Ionic Radii and Systematic Studies of Interatomic Distances in Halides and Chalcogenides. *Acta Cryst.* **A32**, 751 (1976).

198. Giacovazzo, C. *et al. Fundamentals of Crystallography*. (Oxford University Press, 2011).

Appendices

Appendix A. Supplemental Information for Chapter 2:

Supplementary Note A.I. Diffraction Patterns

The phase pure diffractograms from a bench-top X-ray diffractometer (Miniflex 600) for each compound are shown in Figure A.1(a-d). There was a Tungsten L-α reflection observed in all samples, denoted by †. Furthermore, there was a minor $MgTi_2O_5$ impurity phase denoted by * in Figure A.1.

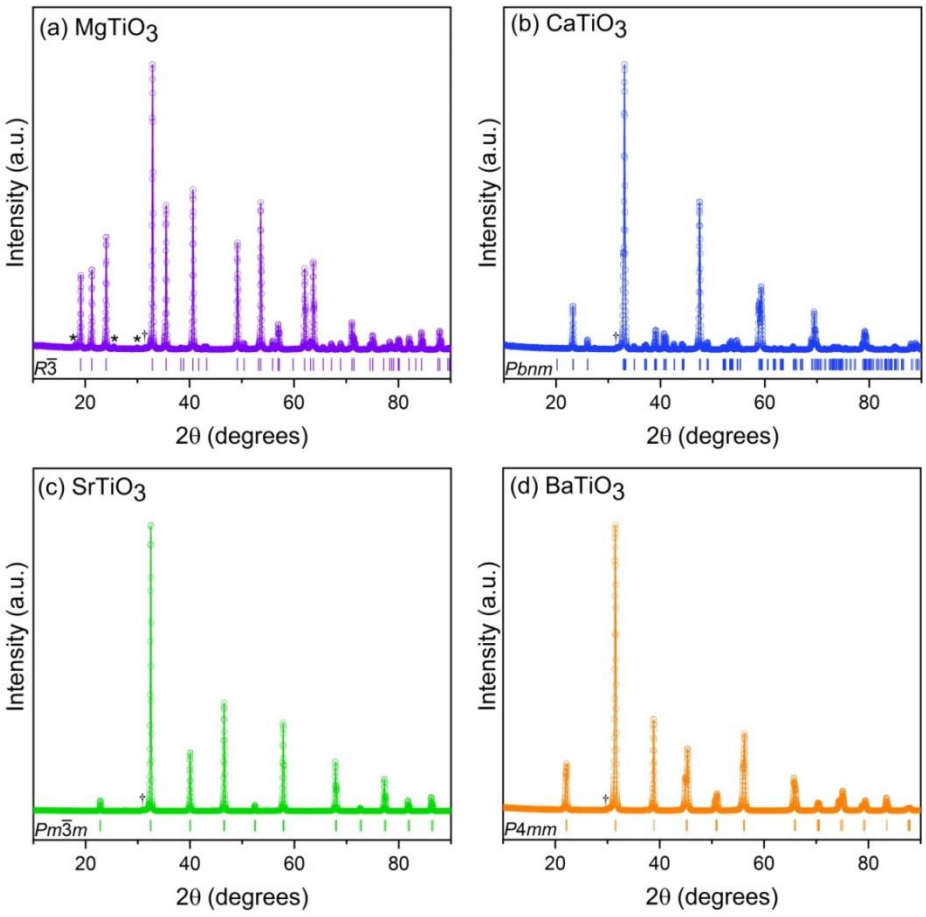

Figure A.1. Benchtop X-ray diffraction results for (a) $MgTiO_3$, (b) $CaTiO_3$, (c) $SrTiO_3$, and (d) $BaTiO_3$, with *hkl* ticks shown below with the corresponding space group labels. *$MgTi_2O_5$ impurity phase. †Tungsten L-α reflection as determined from a Silicon standard.

Supplementary Note A.II. Neutron Total Scattering Results for $MgTiO_3$

For $MgTiO_3$ the data at 225 and 290 K was well modelled in the trigonal $R\bar{3}$ space group. The results at 225 K are shown in Figure A.2 and tabulated in Table A1. The tabulated results for $MgTiO_3$ at 290 K are shown in Table A.2.

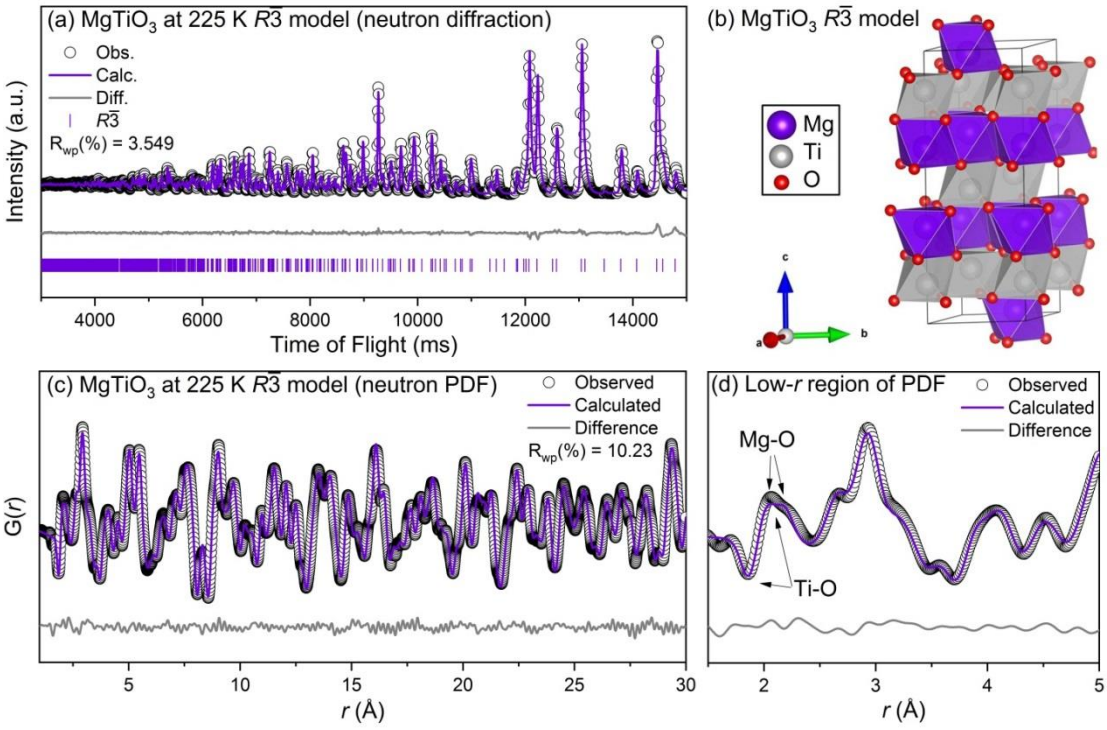

Figure A.2. (a) Rietveld refinement of neutron diffraction, (b) refined model, (c) small-box modeling of neutron PDF, and (d) zoom-in of neutron PDF for $MgTiO_3$ at 225 K with the $R\bar{3}$ space group. Data (identified by black circles) and refined models (continuous lines) are shown, along with the difference pattern and *hkl* indices below (diffraction data only).

Table A1. Rietveld and neutron PDF (1-30 Å) refinement parameters for $MgTiO_3$ at 225 K with the $R\bar{3}$ space group.

$MgTiO_3$ at 225 K											
Neutron Diffraction Refinement:						Neutron PDF Refinement:					
a (Å)	5.0554(1)	α (°)	90	R_p	2.688	a (Å)	5.0571(6)	α (°)	90		
b (Å)	5.0554(1)	β (°)	90	R_{wp}	3.549	b (Å)	5.0571(6)	β (°)	90	R_{wp}	10.226
c (Å)	13.8966(1)	γ (°)	120	red. χ^2	2.010	c (Å)	13.9031(1)	γ (°)	120	red. χ^2	0.1774
Atomic Position	x	y	z	Occ.	Beq	Atomic Position	x	y	z	Occ.	Beq
Mg	0	0	0.3554(5)	1	0.383(1)	Mg	0	0	0.355(9)	1	0.43(6)
Ti	0	0	0.1448(7)	1	0.580(5)	Ti	0	0	0.144(8)	1	0.35(4)
O	0.3159(6)	0.0214(4)	0.2463(9)	1	0.485(1)	O	0.315(9)	0.020(9)	0.246(6)	1	0.44(3)

Table A.2. Rietveld and neutron PDF (1-30 Å) refinement parameters for $MgTiO_3$ at 290 K with the $R\bar{3}$ space group.

$MgTiO_3$ at 290 K											
Neutron Diffraction Refinement:						Neutron PDF Refinement:					
a (Å)	5.0574(2)	α (°)	90	R_p	3.208	a (Å)	5.0591(2)	α (°)	90		
b (Å)	5.0574(2)	β (°)	90	R_{wp}	4.146	b (Å)	5.0591(2)	β (°)	90	R_{wp}	10.012
c (Å)	13.9044(3)	γ (°)	120	red. χ^2	2.027	c (Å)	13.9118(6)	γ (°)	120	red. χ^2	0.2022
Atomic Position	x	y	z	Occ.	Beq	Atomic Position	x	y	z	Occ.	Beq
Mg	0	0	0.3554(2)	1	0.430(2)	Mg	0	0	0.356(1)	1	0.47(6)
Ti	0	0	0.1448(1)	1	0.639(3)	Ti	0	0	0.144(9)	1	0.39(8)
O	0.3159(6)	0.0215(5)	0.2463(4)	1	0.543(1)	O	0.316(2)	0.021(2)	0.246(6)	1	0.49(1)

Supplementary Note A.III. Neutron Total Scattering Results for $CaTiO_3$

For $CaTiO_3$ the data at 225 and 290 K was well modelled in the orthorhombic *Pbnm* space group. The results at 225 K are shown in Figure A.3 and tabulated in Table A.3. The tabulated results for $CaTiO_3$ at 290 K are shown in Table A.4.

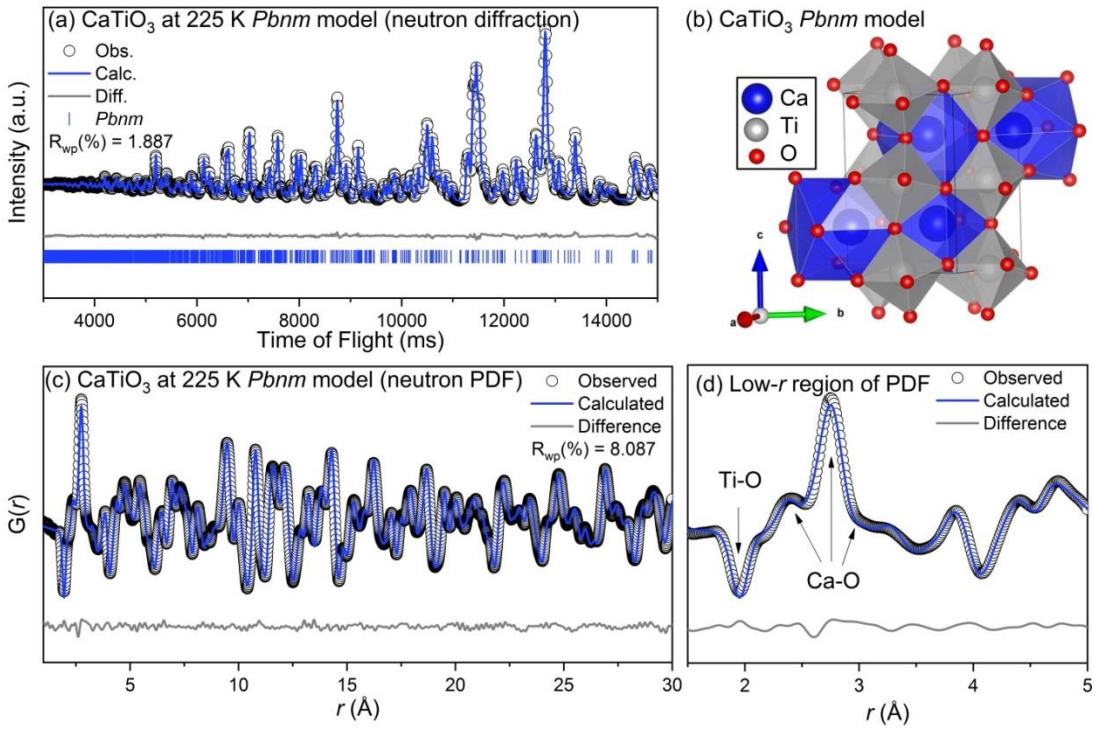

Figure A.3. (a) Rietveld refinement of neutron diffraction, (b) refined model, (c) small-box modeling of neutron PDF, and (d) zoom-in of neutron PDF for $CaTiO_3$ at 225 K with the *Pbnm* space group. Data (identified by black circles) and refined models (continuous lines) are shown, along with the difference pattern and *hkl* indices below (diffraction data only).

Table A.3. Rietveld and neutron PDF (1-30 Å) refinement parameters for $CaTiO_3$ at 225 K with the orthorhombic *Pbnm* space group.

$CaTiO_3$ at 225 K											
Neutron Diffraction Refinement:						Neutron PDF Refinement:					
a (Å)	5.3774(5)	α (°)	90	R_p	1.438	a (Å)	5.3769(7)	α (°)	90		
b (Å)	5.4424(3)	β (°)	90	R_{wp}	1.887	b (Å)	5.4440(5)	β (°)	90	R_{wp}	8.087
c (Å)	7.6385(6)	γ (°)	90	red. χ^2	2.236	c (Å)	7.6438(3)	γ (°)	90	red. χ^2	0.1235
Atomic Position	x	y	z	Occ.	Beq	Atomic Position	x	y	z	Occ.	Beq
Ca	0.9932(1)	0.0361(1)	0.25	1	0.565(2)	Ca	0.992(1)	0.036(2)	0.25	1	0.48(6)
Ti	0	0.5	0	1	0.386(9)	Ti	0	0.5	0	1	0.33(3)
O1	0.0729(6)	0.4831(2)	0.25	1	0.451(1)	O1	0.072(5)	0.482(1)	0.25	1	0.39(1)
O2	0.7109(7)	0.2892(2)	0.0378(3)	1	0.482(4)	O2	0.711(3)	0.288(6)	0.038(4)	1	0.44(3)

Table A.4. Rietveld and neutron PDF (1-30 Å) refinement parameters for $CaTiO_3$ at 290 K with the orthorhombic *Pbnm* space group.

$CaTiO_3$ at 290 K											
Neutron Diffraction Refinement:						Neutron PDF Refinement:					
a (Å)	5.3822(5)	α (°)	90	R_p	2.187	a (Å)	5.3814(8)	α (°)	90		
b (Å)	5.4437(7)	β (°)	90	R_{wp}	3.108	b (Å)	5.4456(3)	β (°)	90	R_{wp}	8.051

c (Å)	7.6438(5)	γ (°)	90	red. χ^2	3.399	c (Å)	7.6491(5)	γ (°)	90	red. χ^2	0.1263
Atomic Position	x	y	z	Occ.	Beq	Atomic Position	x	y	z	Occ.	Beq
Ca	0.9961(4)	0.0360(8)	0.25	1	0.689(2)	Ca	0.992(6)	0.035(3)	0.25	1	0.59(5)
Ti	0	0.5	0	1	0.447(4)	Ti	0	0.5	0	1	0.37(5)
O1	0.0728(3)	0.4829(8)	0.25	1	0.497(7)	O1	0.072(1)	0.482(1)	0.25	1	0.42(2)
O2	0.7112(8)	0.2895(6)	0.0371(5)	1	0.481(2)	O2	0.711(9)	0.288(1)	0.038(2)	1	0.50(1)

Supplementary Note A.IV. Neutron Total Scattering Results for $SrTiO_3$

For $SrTiO_3$ the data at 225 and 290 K was well modelled in the cubic $Pm\bar{3}m$ space group. The results at 225 K are shown in Figure A.4 and tabulated in Table A.5. The tabulated results for $SrTiO_3$ at 290 K are shown in Table A.6.

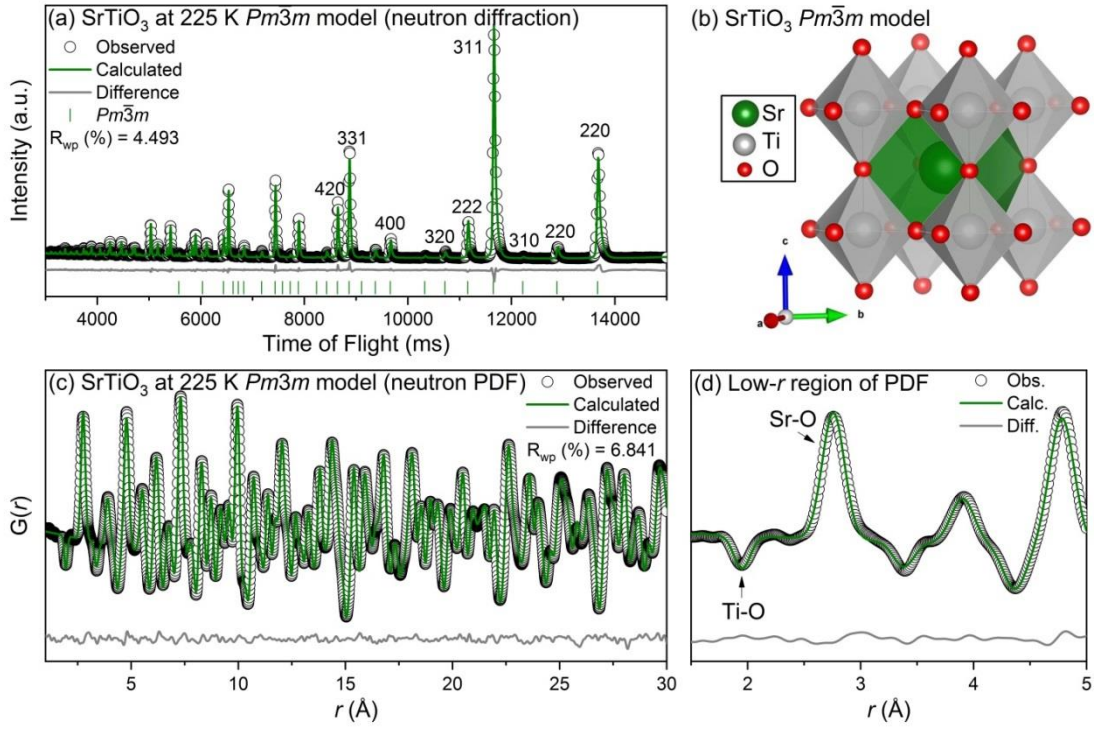

Figure A.4. (a) Rietveld refinement of neutron diffraction, (b) refined model, (c) small-box modeling of neutron PDF, and (d) zoom-in of neutron PDF for $SrTiO_3$ at 225 K with the $Pm\bar{3}m$ space group. Data (identified by black circles) and refined models (continuous lines) are shown, along with the difference pattern and *hkl* indices below (diffraction data only).

Table A.5. Rietveld and neutron PDF (1-30 Å) refinement parameters for $SrTiO_3$ at 225 K with the cubic $Pm\bar{3}m$ space group.

$SrTiO_3$ at 225 K

Neutron Diffraction Refinement: $Pm\bar{3}m$						Neutron PDF Refinement: $Pm\bar{3}m$					
a (Å)	3.9046(4)	α (°)	90	R_p	3.572	a (Å)	3.9064(2)	α (°)	90		
b (Å)	3.9046(4)	β (°)	90	R_{wp}	4.493	b (Å)	3.9064(2)	β (°)	90	R_{wp}	6.841
c (Å)	3.9046(4)	γ (°)	90	red. χ^2	4.028	c (Å)	3.9064(2)	γ (°)	90	red. χ^2	0.2268
Atomic Position	x	y	z	Occ.	Beq	Atomic Position	x	y	z	Occ.	Beq
Sr	0	0	0	1	0.408(3)	Sr	0	0	0	1	0.44(6)
Ti	0.5	0.5	0.5	1	0.332(4)	Ti	0.5	0.5	0.5	1	0.32(1)
O	0.5	0.5	0	1	0.555(2)	O	0.5	0.5	0	1	0.54(5)

Table A.6. Rietveld and neutron PDF (1-30 Å) refinement parameters for $SrTiO_3$ at 290 K with the cubic $Pm\bar{3}m$ space group.

$SrTiO_3$ at 290 K											
Neutron Diffraction Refinement: $Pm\bar{3}m$						Neutron PDF Refinement: $Pm\bar{3}m$					
a (Å)	3.9067(9)	α (°)	90	R_p	3.481	a (Å)	3.9085(8)	α (°)	90		
b (Å)	3.9067(9)	β (°)	90	R_{wp}	4.309	b (Å)	3.9085(8)	β (°)	90	R_{wp}	6.969
c (Å)	3.9067(9)	γ (°)	90	red. χ^2	3.548	c (Å)	3.9085(8)	γ (°)	90	red. χ^2	0.2386
Atomic Position	x	y	z	Occ.	Beq	Atomic Position	x	y	z	Occ.	Beq
Sr	0	0	0	1	0.506(4)	Sr	0	0	0	1	0.52(4)
Ti	0.5	0.5	0.5	1	0.396(1)	Ti	0.5	0.5	0.5	1	0.37(5)
O	0.5	0.5	0	1	0.637(8)	O	0.5	0.5	0	1	0.62(7)

Supplementary Note A.V. Neutron Total Scattering Results for $BaTiO_3$

For $BaTiO_3$ (BT) the tabulated results for the refinements at 225 K in the orthorhombic *Amm*2 space group are show in Figure A.4. Similarly, the tabulated results for the refinements at 290 K in the tetragonal *P*4*mm* space group are shown in Table A.8. The tabulated results from the local structure refinement (from 1-10 Å) at 290 K in the rhombohedral *R*3*m* space group are shown in Table A.9. Furthermore, the results of the box-car refinements are shown in Figure A.5.

Table A.7. Rietveld and neutron PDF (1-30 Å) refinement parameters for $BaTiO_3$ at 225 K.

$BaTiO_3$ at 225 K											
Neutron Diffraction Refinement: *Amm*2						Neutron PDF Refinement: *Amm*2					
a (Å)	3.9886(4)	α (°)	90	R_p	2.327	a (Å)	3.991(1)	α (°)	90		
b (Å)	5.6749(3)	β (°)	90	R_{wp}	3.421	b (Å)	5.678(9)	β (°)	90	R_{wp}	6.454
c (Å)	5.6926(1)	γ (°)	90	red.	5.057	c (Å)	5.694(4)	γ (°)	90	red. χ^2	0.2026

			χ^2								
Atomic Position	x	y	z	Occ.	Beq	Atomic Position	x	y	z	Occ.	Beq
Ba	0	0	0	1	0.292(7)	Ba	0	0	0	1	0.38(5)
Ti	0.5	0	0.511(3)	1	0.596(5)	Ti	0.5	0	0.514(1)	1	0.29(5)
O1	0	0	0.487(1)	1	0.341(4)	O1	0	0	0.487(1)	1	0.31(2)
O2	0.5	0.255(4)	0.233(8)	1	0.516(1)	O2	0.5	0.253(5)	0.231(7)	1	0.46(8)

Table A.8. Structural parameters from the neutron PDF (1-10 Å) refinement for $BaTiO_3$ at 225 K.

$BaTiO_3$ at 225 K Neutron PDF Refinement: *R*3*m*					
a (Å)	4.0141(8)	α (°)	89.63(6)		
b (Å)	4.0141(8)	β (°)	89.63(6)	R_{wp}	4.203
c (Å)	4.0141(8)	γ (°)	89.63(6)	red. χ^2	0.1463
Atomic Position	x	y	z	Occ.	Beq
Ba	0.012(1)	0.012(1)	0.012(1)	1	0.28(3)
Ti	0.5	0.5	0.5	1	0.36(2)
O	0.523(2)	0.523(2)	0.029(2)	1	0.40(1)

Table A.9. Rietveld and neutron PDF (1-30 Å) refinement parameters for $BaTiO_3$ at 290 K.

$BaTiO_3$ at 290 K											
Neutron Diffraction Refinement: *P*4*mm*						Neutron PDF Refinement: *P*4*mm*					
a (Å)	3.9976(8)	α (°)	90	R_p	3.604	a (Å)	3.999(4)	α (°)	90		
b (Å)	3.9976(8)	β (°)	90	R_{wp}	4.841	b (Å)	3.999(4)	β (°)	90	R_{wp}	6.714
c (Å)	4.0347(6)	γ (°)	90	red. χ^2	6.754	c (Å)	4.038(9)	γ (°)	90	red. χ^2	0.2087
Atomic Position	x	y	z	Occ.	Beq	Atomic Position	x	y	z	Occ.	Beq
Ba	0	0	0	1	0.029(6)	Ba	0	0	0	1	0.36(3)
Ti	0.5	0.5	0.508(5)	1	1.08(4)	Ti	0.5	0.5	0.514(8)	1	0.51(6)
O1	0.5	0.5	0.023(3)	1	1.22(1)	O1	0.5	0.5	-0.028(4)	1	0.59(3)
O2	0.5	0	0.506(1)	1	0.481(6)	O2	0.5	0	0.485(8)	1	0.46(1)

Table A.10. Structural parameters from the neutron PDF (1-10 Å) refinement for $BaTiO_3$ at 290 K.

$BaTiO_3$ at 290 K Neutron PDF Refinement: *R*3*m*					
a (Å)	4.0155(8)	α (°)	89.58(4)		
b (Å)	4.0155(8)	β (°)	89.58(4)	R_{wp}	4.349
c (Å)	4.0155(8)	γ (°)	89.58(4)	red. χ^2	0.1504
Atomic Position	x	y	z	Occ.	Beq
Ba	0.009(9)	0.009(9)	0.009(9)	1	0.35(3)
Ti	0.5	0.5	0.5	1	0.48(8)

O	0.521(7)	0.521(7)	0.027(2)	1	0.44(9)

Supplementary Note A.VI. Box-Car Refinements

The box-car refinement results for $BaTiO_3$ at 225 K for the 20-30, 25-35, and 30-40 Å boxes is shown in supplementary Figure A.5 with the rhombohedral *R*3*m* and orthorhombic *Amm*2 fits. As mentioned in the main text, at low-*r* the rhombohedral model fit best, then at intermediate distances the orthorhombic model fits best. Surprisingly though for the 25-35 and 30-40 Å boxes the rhombohedral model fit significantly better. Visually it is difficult to determine a significant difference between the fits, but in general the orthorhombic model provides sharper features that are not observed and thus yields a poorer fit. At higher-r ranges, the average orthorhombic structure yields the better fit as expected.

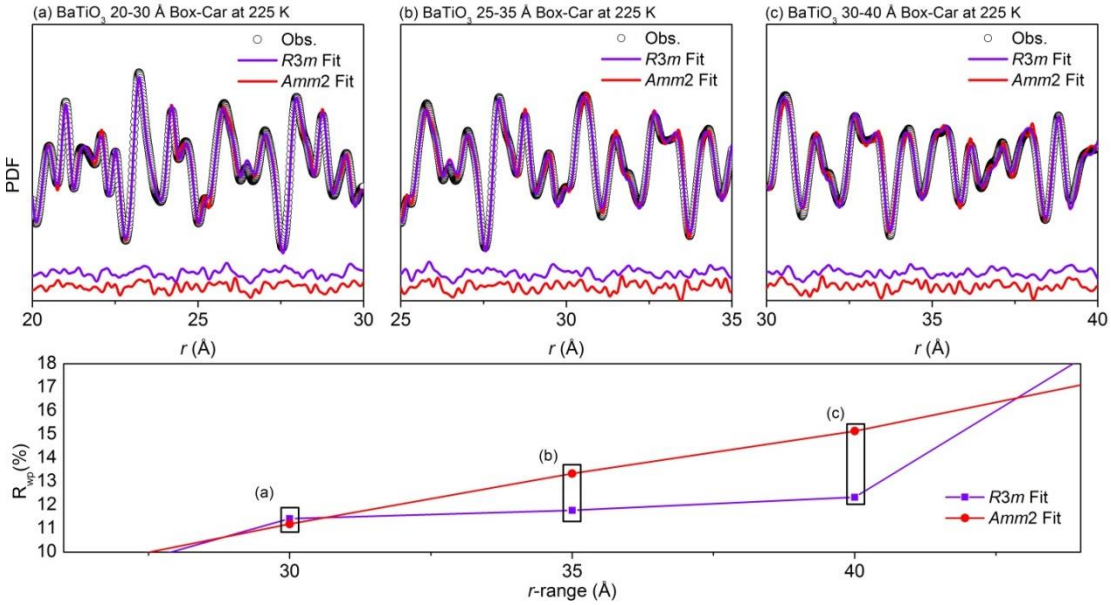

Figure A.5. Box-car refinement results (below) and fits (above) for $BaTiO_3$ at 225 K for the (a) 20-30, (b) 25-35, and (c) 30-40 Å boxes.

Appendix B. Supplemental Information for Chapter 3:

Supplementary Note B.I. Polarization and Strain Measurements

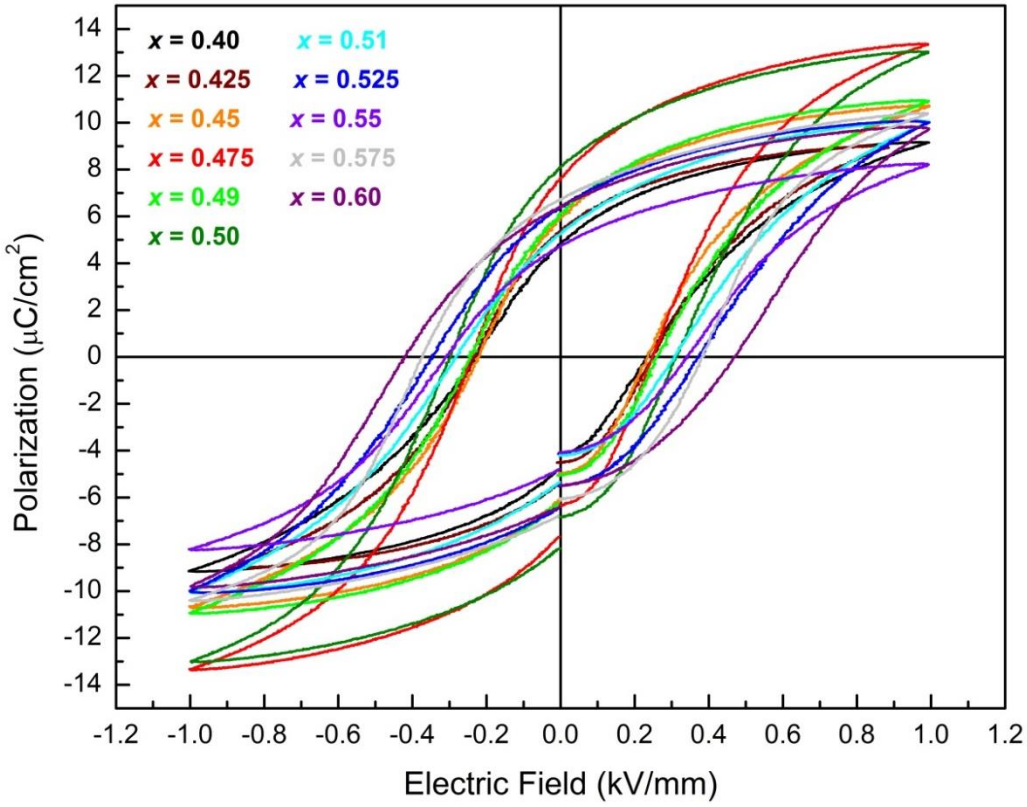

Figure A.6. Room temperature *P-E* hysteresis loops measured at 0.1 Hz for BZT-*x*BCT ceramics.

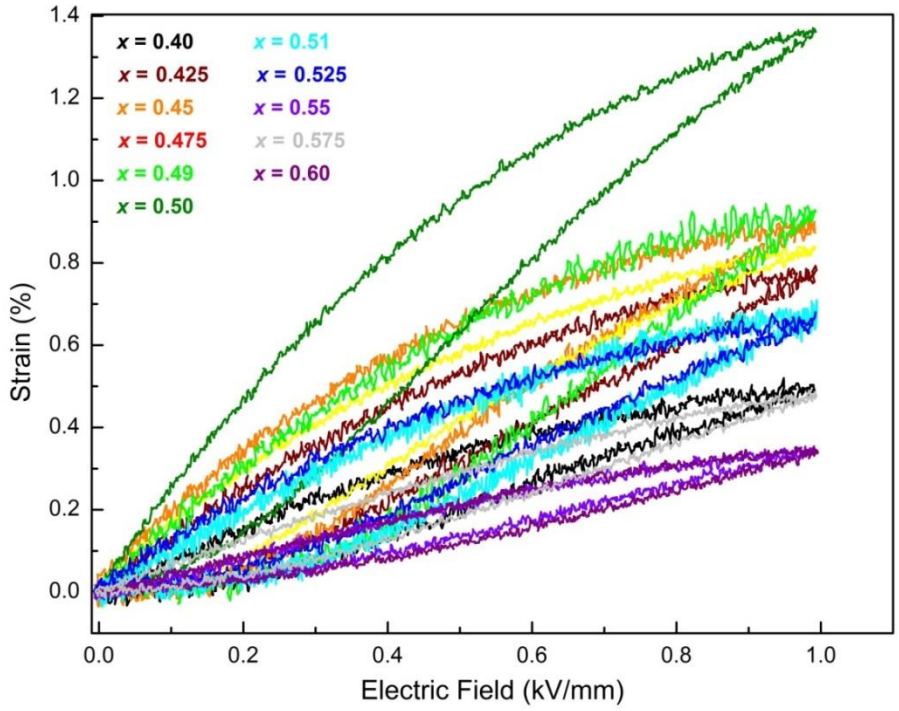

Figure A.7. Room temperature *S*-*E* hysteresis loops measured at 0.1 Hz for BZT-*x*BCT ceramics.

Supplementary Note B.II. Diffraction Patterns versus Electric Field

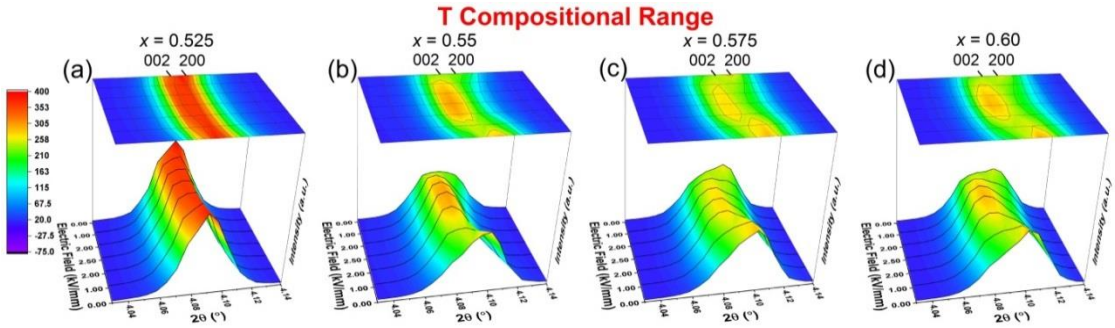

Figure A.8. Sections of the diffraction patterns for compositions with T structure, x = 0.525, 0.55, 0.575 and 0.60: a-d) in the $\{002\}_{pc}$ region, when E = 0.00, 1.00, 2.00, 2.50, 2.00, 1.00, and 0.00 kV/mm, in the parallel direction from the electric field.

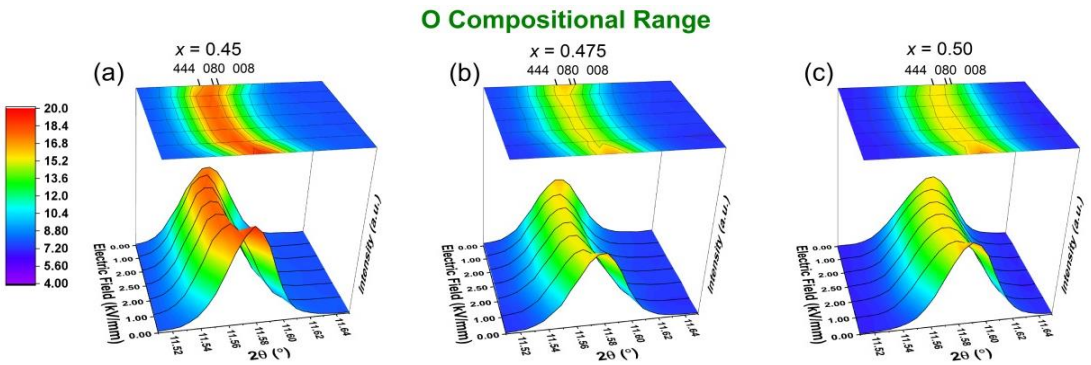

Figure A.9. Sections of the diffraction patterns for compositions x = 0.45, 0.475, and 0.50 in the O compositional range: (a-c) in the $\{440\}_{pc}$ region when E = 0.00, 1.00, 2.00,2.50, 2.00, 1.00, and 0 kV/mm, in the parallel direction from the electric field.

Supplementary Note B.III. Pawley Fitting

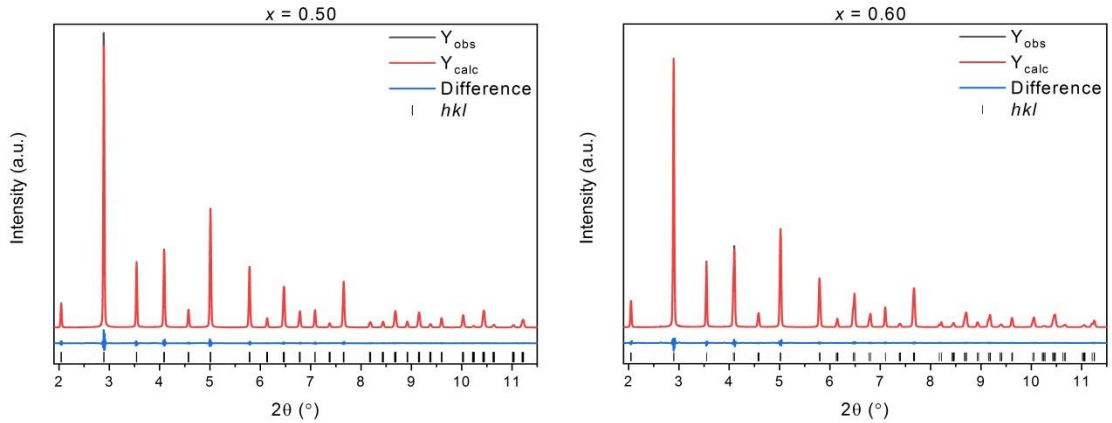

Figure A.10. Pawley fits of x = 0.50 and 0.60 in *Amm*2 (left) and *P*4*mm* (right) respectively carried out against SXRD data in the parallel direction to the electric field. The black solid represents the observed data; the red solid line represents the model while the blue difference curve is below. The tick marks below the difference curve give the positions of the Bragg reflections.

Table A.11. Lattice parameters from Pawley fits performed in *Amm*2 for unpoled compositions in the O range x = 0.45, 0.475, and 0.50.

x	**Lattice parameters (Å)**
0.45	*a* = 4.0162(7) *b* = 5.668(3) c = 5.666(3)
0.475	*a* = 4.0168(5) *b* = 5.672(9) *c* = 5.662(8)
0.50	*a* = 4.0154(4) *b* = 5.665(1) *c* = 5.661(1)

Table A.12. Lattice parameters from Pawley fits performed in *P*4*mm* for unpoled compositions in the T range x = 0.525, 0.55, 0.575, and 0.60.

x	**Lattice parameters (Å)**
0.525	a = 4.0028(2) c = 4.01438(2)
0.55	a = 3.99879(1) c = 4.01841(1)
0.575	a = 3.99573(9) c = 4.01517(9)
0.60	a = 3.99334(8) c = 4.01475(9)

Supplementary Note B.IV. PDF Results for All Compositions

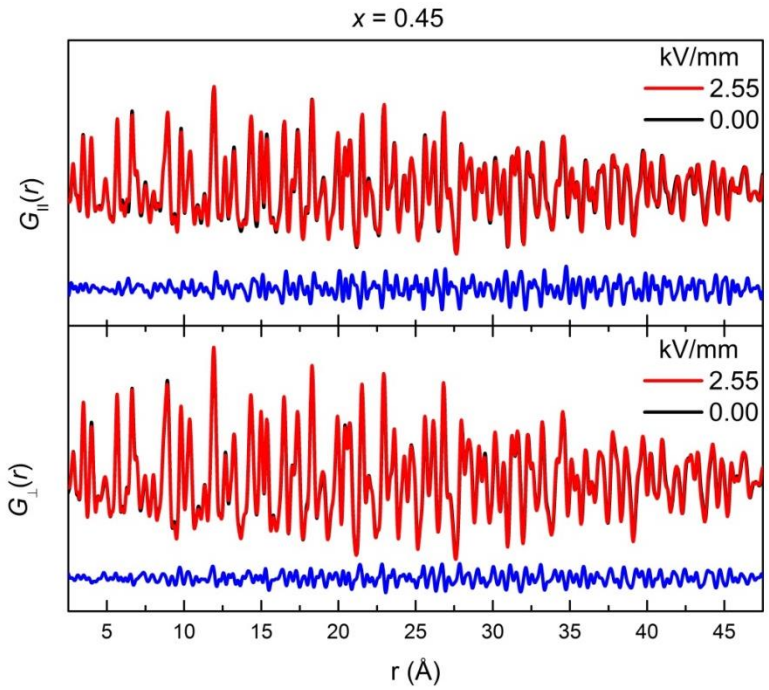

Figure A.11. $G_{\parallel}(r)$ and $G_{\perp}(r)$ for x = 0.45 at E = 0.00 (black), E = 2.55 kV/mm (red), and the difference ($\Delta G_{\parallel}(r)$) in blue.

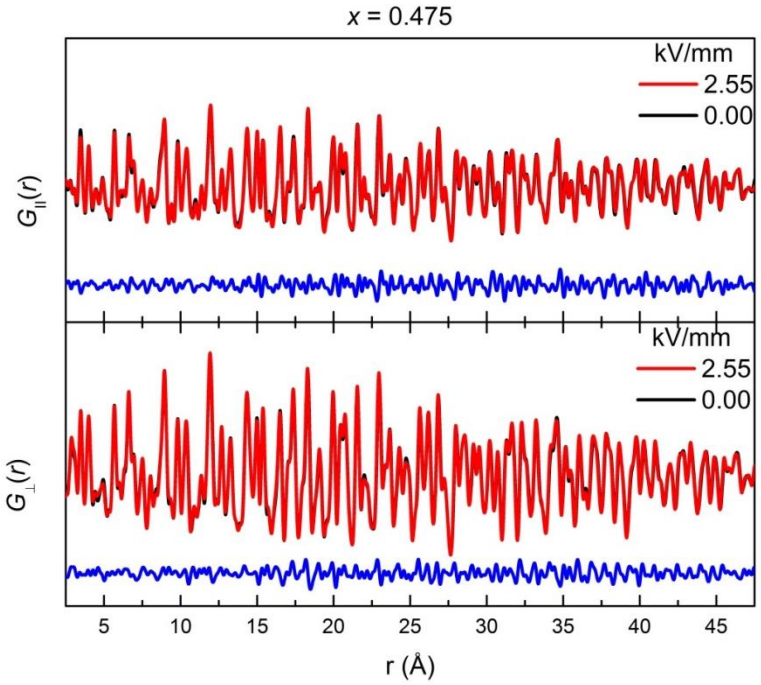

Figure A.12. $G_{\parallel}(r)$ and $G_{\perp}(r)$ for x = 0.475 at E = 0.00 (black), E = 2.55 kV/mm (red), and the difference ($\Delta G_{\parallel}(r)$) in blue.

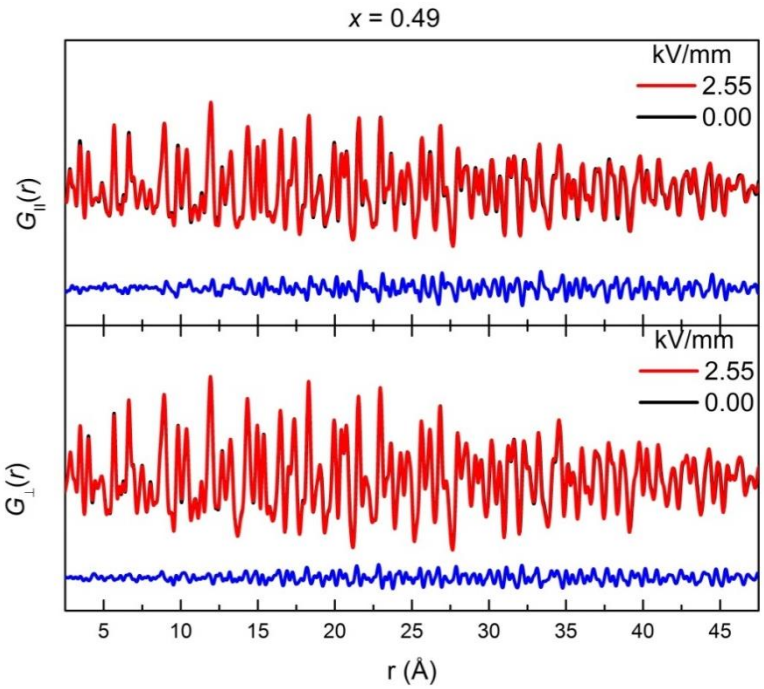

Figure A.13. $G_{\parallel}(r)$ and $G_{\perp}(r)$ for x = 0.49 at E = 0.00 (black), E = 2.55 kV/mm (red), and the difference ($\Delta G_{\parallel}(r)$) in blue.

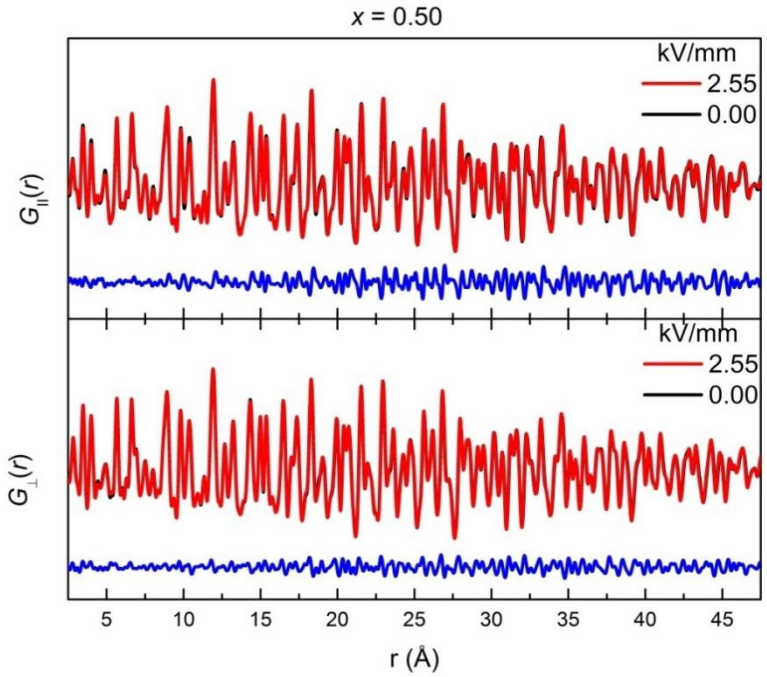

Figure A.14. $G_{\parallel}(r)$ and $G_{\perp}(r)$ for x = 0.50 at E = 0.00 (black), E = 2.55 kV/mm (red), and the difference ($\Delta G_{\parallel}(r)$) in blue.

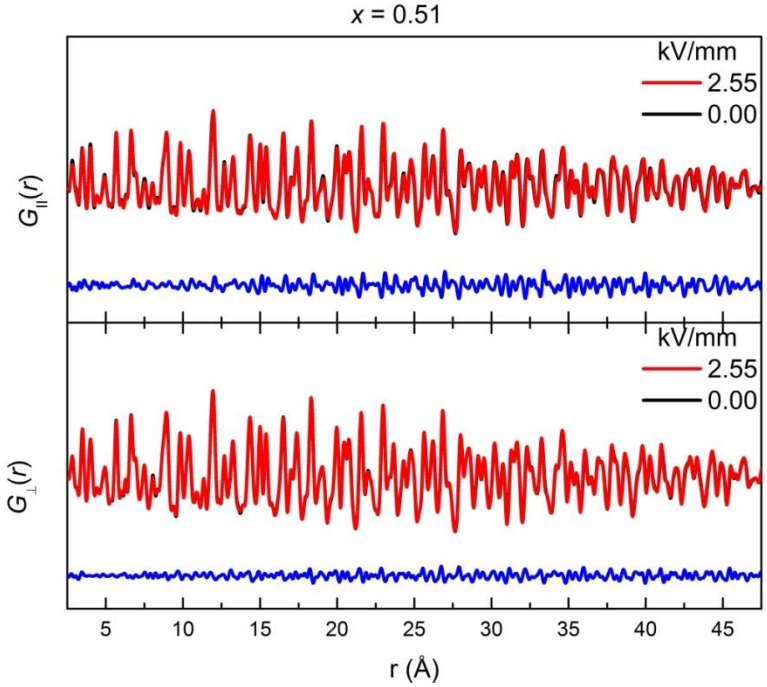

Figure A.15. $G_{\parallel}(r)$ and $G_{\perp}(r)$ for x = 0.51 at E = 0.00 (black), E = 2.55 kV/mm (red), and the difference ($\Delta G_{\parallel}(r)$) in blue.

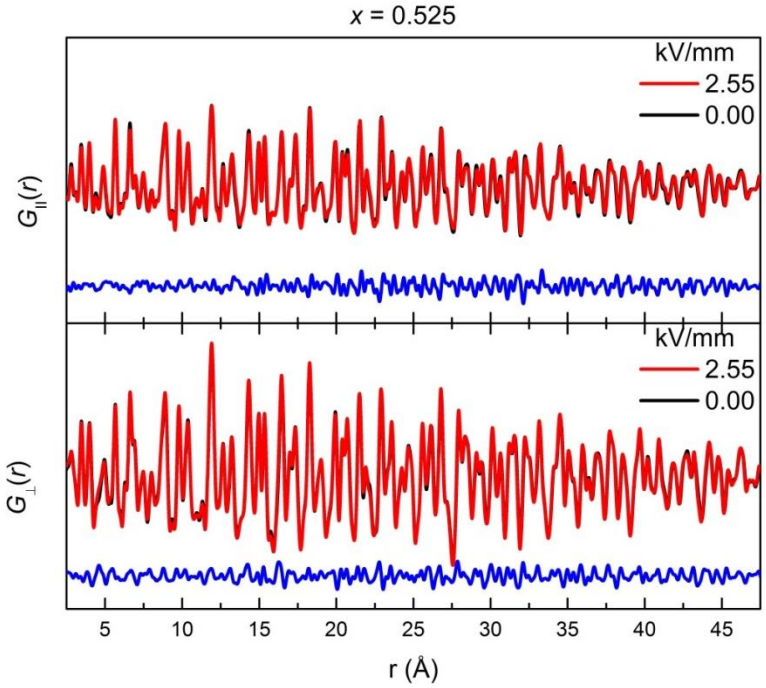

Figure A.16. $G_{\parallel}(r)$ and $G_{\perp}(r)$ for x = 0.525 at E = 0.00 (black), E = 2.55 kV/mm (red), and the difference ($\Delta G_{\parallel}(r)$) in blue.

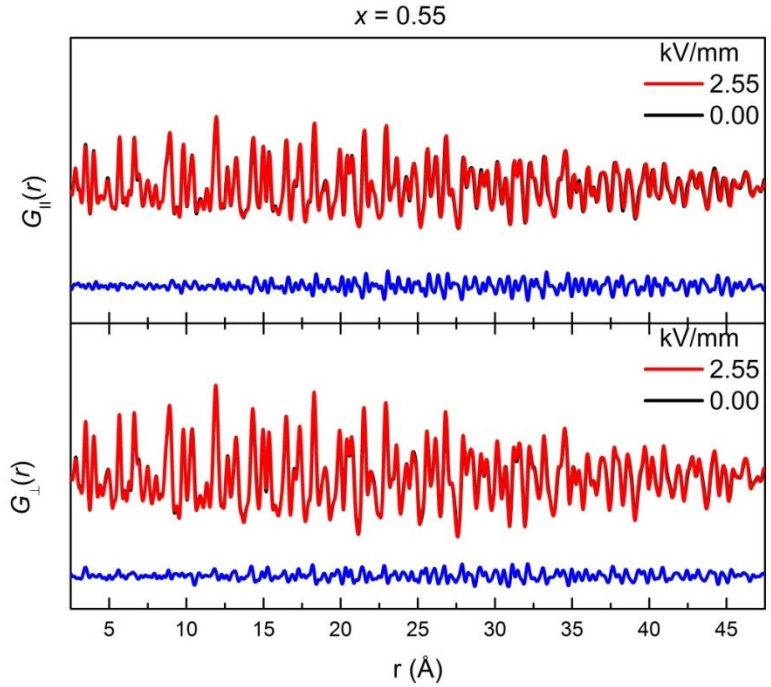

Figure A.17. $G_{\parallel}(r)$ and $G_{\perp}(r)$ for x = 0.55 at E = 0.00 (black), E = 2.55 kV/mm (red), and the difference ($\Delta G_{\parallel}(r)$) in blue.

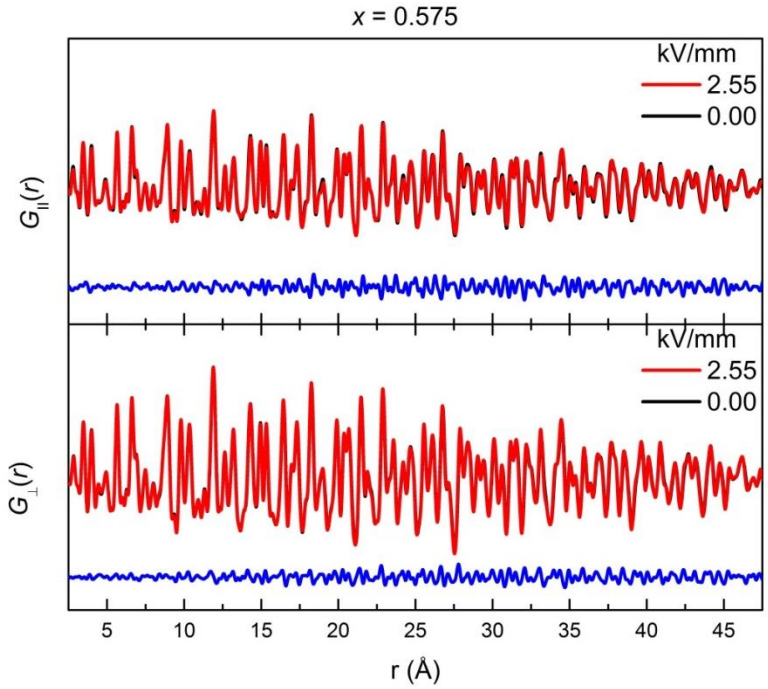

Figure A.18. $G_{\parallel}(r)$ and $G_{\perp}(r)$ for x = 0.575 at E = 0.00 (black), E = 2.55 kV/mm (red), and the difference ($\Delta G_{\parallel}(r)$) in blue.

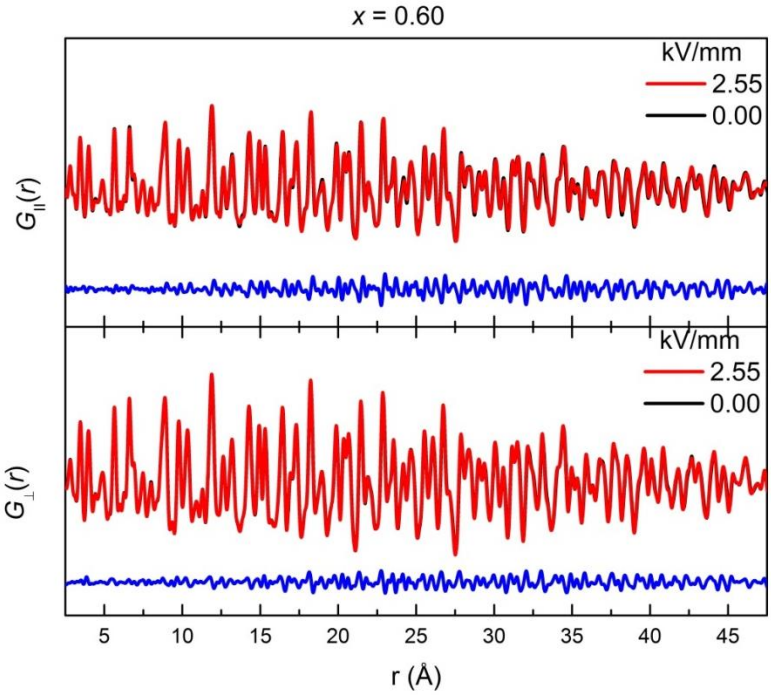

Figure A.19. $G_{\parallel}(r)$ and $G_{\perp}(r)$ for x = 0.60 at E = 0.00 (black), E = 2.55 kV/mm (red), and the difference ($\Delta G_{\parallel}(r)$) in blue.

Appendix C. Supplemental Information for Chapter 4:

Supplementary Note C.I. Ionic Radii, Neutron Scattering Lengths, and Z

In a typical diffraction experiment, X-rays are scattered by electrons surround the nucleus of an atom. Consequently, heavier atoms with more electrons scatter X-rays more effectively and the scattering power of X-rays from a material is therefore dependent on the atomic number (Z). However, neutron scattering, which involves scattering from the atomic nuclei, is not dependent on the atomic number and is particularly useful for materials that contain low-Z elements, like oxygen. The ions in BZT-0.5BCT are tabulated in Table A.13 with the ionic radii, coherent neutron scattering length (coh *b*), and atomic number listed for each.

Table A.13. Effective ionic radii,[8,197,198] coherent neutron scattering length,[114] and atomic number for cation and ions in BZT-*x*BCT compositions.

Ion	Ionic radii (Angstroms)	Coherent neutron scattering length (fm)	Atomic Number (Z)
Ba^{2+}	1.61	5.07	56
Ca^{2+}	1.34	4.70	20
Zr^{4+}	0.72	7.16	40
Ti^{4+}	0.605	-3.44	22
O^{2-}	1.40	5.80	8

Supplementary Note C.II. X-ray Diffraction

X-ray diffraction data were collected from a lab diffractometer (Miniflex 600) using Cu K-α radiation (λ = 1.541 Å) and is shown in Figure A.20. The X-ray diffraction pattern was indexed to the orthorhombic *Amm*2 space group as has been reported by Keeble et al.[73] The data were collected from 10 to 60° 2θ with a step size of 0.02°.

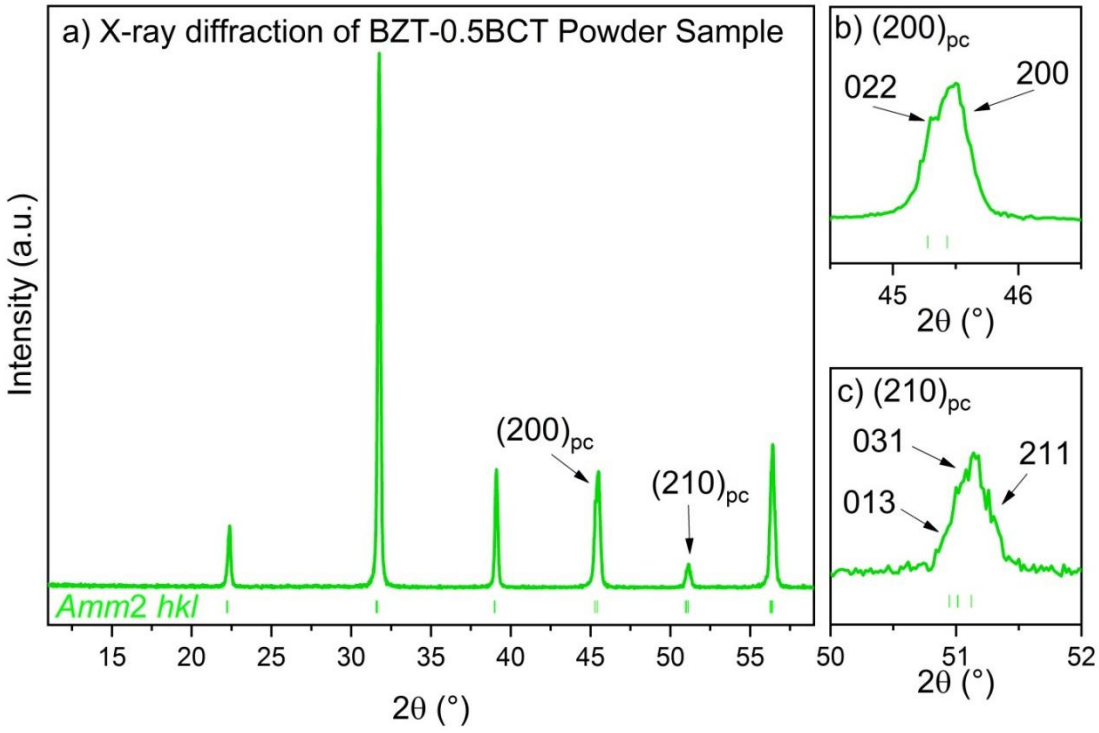

Figure A.20. X-ray diffraction pattern of BZT-0.5BCT powder sample indexed in the orthorhombic *Amm*2 space group (*hkl* ticks shown below the collected diffractogram).

To investigate the neutron diffraction data of BZT-0.5BCT at 305 K, single and two phase refinements were conducted in a number of relevant space groups and combination of space groups.[73] The R_{wp} value for the refinement in the *Amm*2 space group was 8.44% (shown in Figure A.21). Although, this single phase model was able to account for all of the observed peaks, both two-phase models, *R*3*m*-*P*4*mm* (Rwp = 6.57%) and *R*3*m*-*Amm*2 (7.25%), yielded lower weighted-profile *R* values (R_{wp}). It should be cautioned that performing a refinement with two phases will naturally yield a lower fit criterion as more variables are being refined and one must carefully inspect the observed reflections to determine if a secondary phase is actually necessary to improve the fit. A summary of all of the Rietveld refinement results is provided in the supplementary information.

The symmetry of BZT-0.5BCT is defined by the *B*-site distortions present. The magnitudes of these distortions are small, which leads to peak splitting that is difficult to detect via diffraction techniques. This phenomena has lead researchers to coin the phrase "pseudocubic" (pc), where the structure appears cubic via diffraction techniques – but is known or later found by other techniques (dielectric measurements, PDF, high resolution diffraction, etc.) to not be cubic (centrosymmetric). As such, the neutron diffraction data for BZT-0.5BCT was modelled well with nearly all of the reported space groups and combinations thereof.

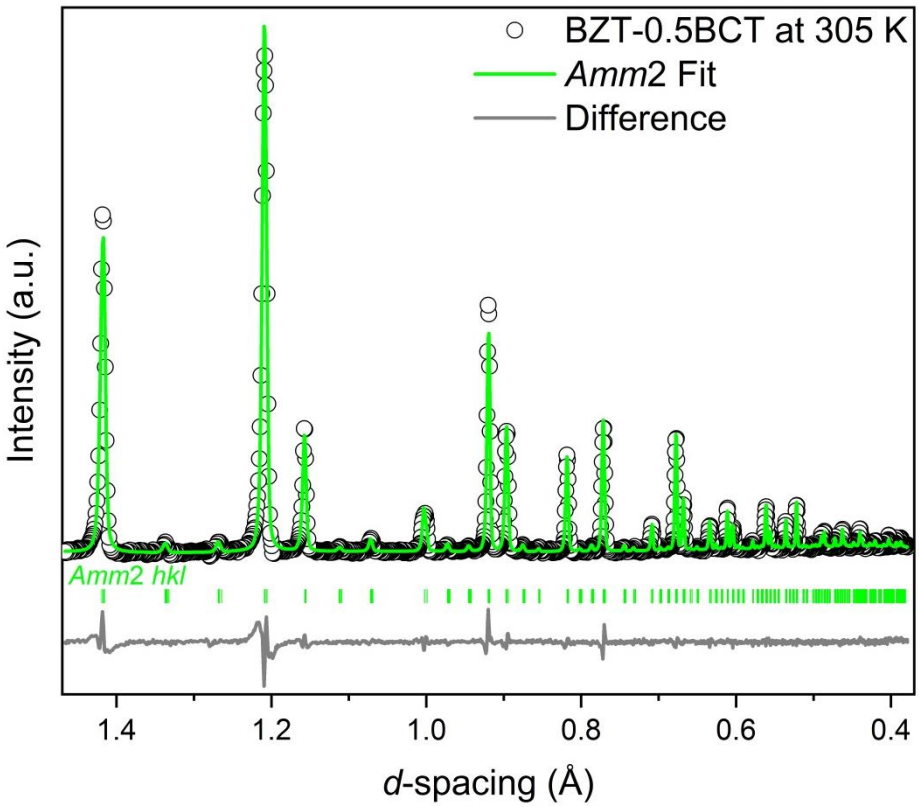

Figure A.21. Rietveld refinement of BZT-0.5BCT at 305 K with the orthorhombic *Amm*2 space group where the observed data is shown as open circles, the fit in green, the difference (Y_{obs}-Y_{calc}) in grey, and the *hkl* ticks are shown below.

The problem with the pseudocubic nature of BZT-0.5BCT is compounded by the limited diffraction resolution of the NOMAD beamline. The NOMAD beam line is

designed for total scattering measurements which require a large *Q*-range. The increased *Q*-range comes at the cost of diffraction resolution. Another consequence of neutron total scattering using a spallation neutron source is peak asymmetric, where the low time of flight (TOF) side of each peak is Lorenztian, whereas the high TOF side is more Gaussian in nature. Currently, the authors are preparing for a follow up study to better understand the average structure of BZT-0.5BCT using high resolution neutron diffraction data from the POWGEN beamline at ORNL.

Table A.14. Comparison of fit criterion (R_{wp}) for Rietveld refinements of neutron diffraction data.

R_{wp} (%)					
*R*3*m*	*Amm*2	*P*4*mm*	$Pm\bar{3}m$	*R*3*m*-*P*4*mm*	*R*3*m*-*Amm*2
11.04	8.44	7.27		6.57	7.25

Table A.15. Rietveld refinement results for BZT-0.5BCT at 305 K in the rhombohedral *R*3*m* space group.

*R*3*m* (Hex)					
a (Å)	5.649		*α* (°)	90	
b (Å)	5.649		*β* (°)	90	
c (Å)	6.937		*γ* (°)	120	
Atomic Position	x	y	z	Occ.	Beq
Ba	0	0	0	0.85	0.63
Ca	0	0	0	0.15	0.63
Ti	0	0	0.5013	0.90	1.25
Zr	0	0	0.5013	0.10	1.25
O	0.1658	-0.1658	0.3468	1	0.86
R_{wp} (%)			Reduced χ^2		
11.04			3.345		

Table A.16. Rietveld refinement results for BZT-0.5BCT at 305 K in the orthorhombic *Amm*2 space group.

*Amm*2					
a (Å)	3.989		*α* (°)	90	
b (Å)	5.656		*β* (°)	90	
c (Å)	5.664		*γ* (°)	90	
Atomic Position	x	y	z	Occ.	Beq

Ba	0	0	0	0.85	0.44
Ca	0	0	0	0.15	0.44
Ti	0.5	0	0.479	0.90	1.01
Zr	0.5	0	0.479	0.10	1.01
O1	0	0	0.484	1	1.06
O2	0.5	0.251	0.252	1	0.89
R_{wp} (%)			Reduced χ^2		
8.43			2.56		

Table A.17. Rietveld refinement results for BZT-0.5BCT at 305 K in the tetragonal *P*4*mm* space group.

*P*4*mm*					
a (Å)	3.993		*α* (°)	90	
b (Å)	3.993		*β* (°)	90	
c (Å)	4.007		*γ* (°)	90	
Atomic Position	x	y	z	Occ.	Beq
Ba	0	0	0	0.85	0.63
Ca	0	0	0	0.15	0.63
Ti	0.5	0.5	0.497	0.90	1.18
Zr	0.5	0.5	0.497	0.10	1.18
O1	0.5	0.5	0.019	1	1.59
O2	0	0.5	0.507	1	0.67
R_{wp} (%)			Reduced χ^2		
7.27			2.20		

Table A.18. Rietveld refinement results for BZT-0.5BCT at 305 K in the cubic $Pm\bar{3}m$ space group.

$Pm\bar{3}m$					
a (Å)	3.993		*α* (°)	90	
b (Å)	3.993		*β* (°)	90	
c (Å)	4.007		*γ* (°)	90	
Atomic Position	x	y	z	Occ.	Beq
Ba	0	0	0	0.85	0.57
Ca	0	0	0	0.15	0.57
Ti	0.5	0.5	0.5	0.90	1.15
Zr	0.5	0.5	0.5	0.10	1.15
O	0.5	0.5	0	1	0.97
R_{wp} (%)			Reduced χ^2		
9.69			2.94		

Supplementary Note C.III. Neutron PDF

Small-box modeling was performed on the neutron pair distribution function that was treated with the Lorch function. A comparison of the different *r*-range fits (1.5-4.5 and 1.5-35) in the various space groups fit of the low-r range is shown in Figure A.22. The refined parameters for the two-phase *R*3*m*-*Pm*$\bar{3}$*m* BCT-BCZ model of BZT-0.5BCT at 305 K are shown in Table A.19.

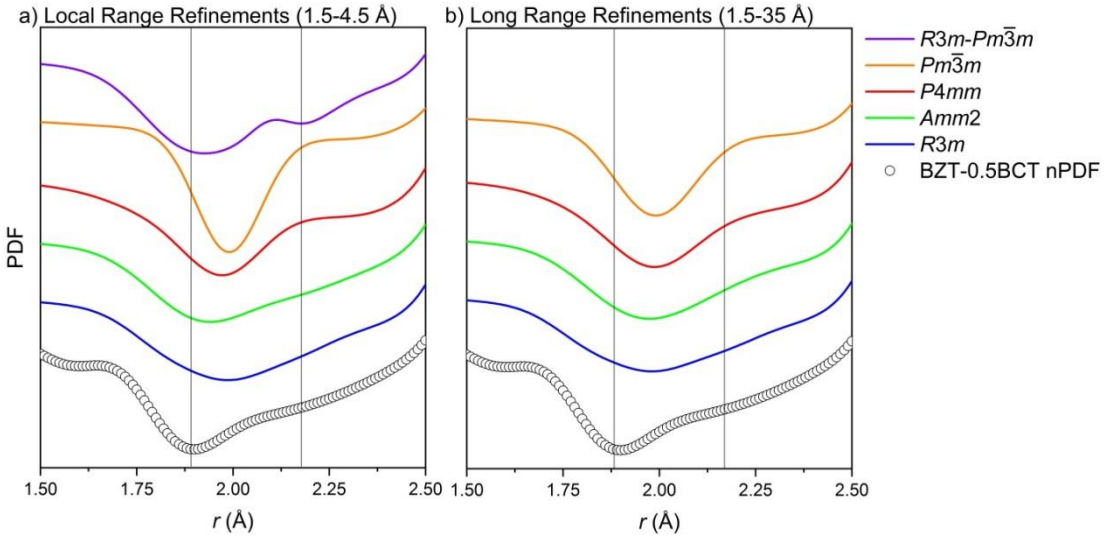

Figure A.22. Comparison of the calculated B-O bond distances for the a) local range refinements (1.5-4.5 Å) and the b) long range refinements (1.5-35 Å) to the BZT-0.5BCT neutron PDF data at 305 K (black, open circles).

Table A.19. Refined parameters for two-phase *R*3*m*-*Pm*$\bar{3}$*m* BCT-BCZ model for the local structure of BZT-0.5BCT at 305 K from 1.5 to 4.5 Å.

$Ba_{0.85}Ca_{0.15}TiO_3$ (BCT): *R*3*m*						$Ba_{0.85}Ca_{0.15}ZrO_3$ (BCZ): *Pm*$\bar{3}$*m*					
a (Å)	3.9871(3)	*α* (°)	89.99(3)	Phase fraction		*a* (Å)	4.20	*α* (°)	90	Phase fraction	
b (Å)	3.9871(3)	*β* (°)	89.99(3)	0.90		*b* (Å)	4.20	*β* (°)	90	0.10	
c (Å)	3.9871(3)	*γ* (°)	89.99(3)			*c* (Å)	4.20	*γ* (°)	90		
Atomic Position	x	y	z	Occ.	Beq	Atomic Position	x	y	z	Occ.	Beq
Ba	0.023(1)	0.023(1)	0.023(1)	0.85	0.27	Ba	0	0	0	0.85	0.32
Ca	0.023(1)	0.023(1)	0.023(1)	0.15	1.00	Ca	0	0	0	0.15	0.96
Ti	0.5	0.5	0.5	1	0.80	Zr	0.5	0.5	0.5	1	0.1
O	0.533(2)	0.533(2)	0.029(7)	1	0.96	O	0.5	0.5	0	1	0.25
R_{wp} (%)						6.074					
Reduced χ^2						0.3072					